DESIGNING ARTIFICIAL ENZYMES: SUPPORTED [FeFe]-HYDROGENASE MIMICS WITH ENHANCED CATALYTIC HYDROGEN PRODUCTION AND OXYGEN STABILITY IN AQUEOUS MEDIA

by

William P. Brezinski

Copyright © William P. Brezinski 2018

A Thesis Submitted to the Faculty of the

DEPARTMENT OF CHEMISTRY AND BIOCHEMISTRY

In Partial Fulfillment of the Requirements

For the Degree of

DOCTOR OF PHILOSOPHY

WITH A MAJOR IN CHEMISTRY

In the Graduate College

THE UNIVERSITY OF ARIZONA

2018

THE UNIVERSITY OF ARIZONA

GRADUATE COLLEGE

As members of the Dissertation Committee, we certify that we have read the dissertation prepared by William P. Brezinski, titled Designing Artificial Enzymes: Supported [FeFe]-Hydrogenase Mimics with Enhanced Catalytic Hydrogen Production and Oxygen Stability in Aqueous Media and recommend that it be accepted as fulfilling the dissertation requirement for the Degree of Doctor of Philosophy.

Date: 24th July, 2018

Professor Richard S. Glass

Date: 24th July, 2018

Professor Dennis L. Lichtenberger

Date: 24th July, 2018

Professor Jeffrey Pyun

Date: 24th July, 2018

Professor John Jewett

Final approval and acceptance of this dissertation is contingent upon the candidate's submission of the final copies of the dissertation to the Graduate College. I hereby certify that I have read this dissertation prepared under my direction and recommend that it be accepted as fulfilling the dissertation requirement.

Date: 24th July, 2018

Dissertation Director: Professor Richard S. Glass

STATEMENT BY AUTHOR

This dissertation has been submitted in partial fulfillment of the requirements for an advanced degree at the University of Arizona and is deposited in the University Library to be made available to borrowers under rules of the Library.

Brief quotations from this dissertation are allowable without special permission, provided that an accurate acknowledgement of the source is made. Requests for permission for extended quotation from or reproduction of this manuscript in whole or in part may be granted by the head of the major department or the Dean of the Graduate College when in his or her judgment the proposed use of the material is in the interests of scholarship. In all other instances, however, permission must be obtained from the author.

SIGNED: William P. Brezinski

ACKNOWLEDGEMENTS

The author would like to thank all the family and friends that supported him through the completion of this work. First and foremost, his parents William and Carrie Brezinski for fostering scholarship and encouraging his personal and professional development as well as being generally amazing parents. Thanks to my wife, Meredith, for endless patience and emotional support over the last nine years, and for helping to raise LD, who has been an unwavering source of comfort and happiness. Thanks to RSG and DLL for their unmitigated genius and infectious enthusiasm for chemistry, and to JP for pushing me when I needed it most. To all of my graduate school friends, GJM, GBH, PKD, EV, RFV, EA, AD, BRS, RG, PD, MH, DCF, KG, TK, MK, LH and KEC, who above all others were able to understand and commiserate with the stress and frustration of of research, orals, and peer review, and everything else that can make graduate student life seem so interminable, but who took it in stride and held each other up through it all. Each and every one of you made this possible.

TABLE OF CONTENTS

List of Tables

List of Schemes

List of Figures

Abstract

Hydrogen is an attractive clean fuel for the storage and transport of energy generated by clean energy sources. It is energy dense, storable, and its use as a fuel produces no carbonaceous by-products whether used in a conventional means as a combustible fuel, or preferably, used in a fuel cell to directly generate electricity from the oxidation of molecular hydrogen. Currently, the vast majority of hydrogen is produced through steam reforming of natural gas. This process is useful for the production of hydrogen as a chemical feedstock, but requires very high temperatures (>700 °C) and utilizes natural gas as a feedstock, which is obtained via fracking and other extractive methods which are detrimental to the environment and human health. Further, stream reforming produces approximately ten tons of carbonaceous by-products (primarily CO_2 and CO) for every ton of hydrogen produced. The hydrogen produced in this process also generally contains significant amounts of carbon monoxide, a contaminant known to poison the catalysts used in conventional hydrogen fuel cells. The other method used for hydrogen production is the electrolysis of water, in which protons from the water molecules are reduced with electrons supplied by an electrode to generate hydrogen gas which is of high purity – but it also comes at high cost. The electrolyzers used in this process depend on expensive nano-structured platinum catalysts for the cathodic reaction (that is, the reduction of protons to molecular hydrogen) which operates at essentially diffusion limited rates in acidic media.[1] Platinum is both expensive and rare, limiting its application and preventing the use of platinum cathodes in large scale production of hydrogen as a fuel. Accordingly, a large body of research has emerged around developing new catalysts using inexpensive, earth abundant materials to enable large scale production of hydrogen for the storage and transport of clean energy.

Hydrogenase metalloenzymes are a class of naturally occurring enzymes which are capable of producing or metabolizing hydrogen gas in anaerobic bacteria as a metabolic process. There are several classifications of these metalloenzymes, the most active of which are the [FeFe]-hydrogenases, which has been found to catalyze the hydrogen evolution reaction at rates on the order to 10^4 molecules of hydrogen per second, with very low overpotential requirements.[2,3] Accordingly, mimicking this activity has been an active thrust of research for over 25 year, thanks in part to the synthetic accessibility of structurally similar [2Fe-2S] butterfly organometallic complexes, first synthesized over 50 years ago.[4,5] To date, hundreds of structural analogs of the active site of the [FeFe]-hydrogenases have been synthesized, but none have managed to replicate the performance of the enzyme.[6,7] More recently, some research groups have begun to focus on mimicking not only the active site of the enzyme, but also the macromolecular environment around the active site – in part because of a growing body of work which indicates the protein architecture around the active site plays several key roles in its stability and activity.[8–11] In our work, we were inspired to use polymer supports to improve the stability and activity of small molecule [2Fe-2S] complexes.

Our first attempt to incorporate [2Fe-2S] complexes in a polymer matrix centered around the synthesis of oligothiophene-[2Fe-2S] complexes which we hoped could be electropolymerized into electrocatalytic films on the surface of electrodes. While these systems were not amenable to such an electropolymerization, we did discover an intriguing and extensive level of electronic communication between the oligothiophene ligands and the diiron system, which enabled their use as photo-catalysts for hydrogen evolution, without the need for an expensive external photosensitizer (such as an iridium or ruthenium complex, or cadmium-chalcogenide based quantum dots which are undesirable due to the use of highly toxic

cadmium) which virtually all other photocatalytic [2Fe-2S] systems require. Undeterred, we developed a new system based in modern polymer chemistry – an initiator for a controlled radical polymerization was functionalized with a [2Fe-2S] moiety and successfully incorporated into several methacrylic metallopolymers and metallo(co)-polymers using atom transfer radical polymerization (ATRP). Extensive electrocatalytic studies on these polymers revealed that an amine rich, water soluble metallopolymer polydimethylaminoethylmethylmethacylate-*graft*-[2Fe-2S] (**PDMAEMA-*g*-[2Fe-2S]**) is able to catalyze the reduction of protons from neutral water with a low overpotential requirement (0.33 V to reach 0.1 mA cm^{-2} current density) extremely high turn over frequency (in excess of 200,000 molecules of hydrogen produced per second), is stable to operating voltages for up to six days with each molecule of catalyst producing approximately 40,000 molecules of hydrogen before becoming deactivated, and exhibits complete aerobic stability under optimized operating conditions – a feat which in unprecedented by either the enzyme or any other [2Fe-2S] mimic.[12–16] These catalytic figures of merit put it in a league of its own, as it has in many ways (rate, aerobic stability) surpassed the activity of the enzyme which inspired the work.

To elucidate the reason for such astounding activity, we synthesized a second water soluble metallopolymer poly(oligoethyleneglycolmethylmethacylate-*graft*-[2Fe-2S] (**POEGMA-*g*-[2Fe-2S]**) which lack the amine functional groups of PDMAEMA. We found that while it is an active electrocatalyst, it is outperformed in every way by the **PDMAEMA-*g*-[2Fe-2S]** system. Random metallo(co)-polymers composed of approximately 50/50 and 70/30 ratios of DMAEMA/OEGMA monomers exhibited intermediate electrcatalytic activity in terms of overpotential, electrocatalytic current density (and therefore rate) and oxygen stability, with the **POEGMA-*g*-[2Fe-2S]** homopolymer losing all activity under ambient aerobic conditions.

Finally, in a side project preformed in collaboration with the Heien lab, low order oligoethylenedioxythiophene (OEDOT) chains were found to form in the presence of Nafion upon slow evaporation of dilute solution of the two Nafion and EDOT in acetonitrile. Thorough characterization and a mechanistic investigation revealed that a cationic oligomerization mechanism is likely the cause for the formation of the OEDOT chains, and once they grown to a certain size, the formation of polaron on the OEDOT chain led to a strong electrostatic interaction between OEDOT and negatively charge Nafion, in which Nafion entangles the OEDOT chain and forms a stable colloidal dispersion in acetonitrile. These colloidal polymer particles were found to be sensitive probes for the water content of acetonitrile solutions, as they undergo an irreversible conformational change upon encountering water in solution, resulting in a bathochromic shift. We found dispersions of these particles are able to accurately and rapidly detect water concentrations between 125 and 2500 ppm using a simple UV-Vis measurement, at a cost of less than $2 USD per measurement.

Chapter 1 - Designing Artificial Enzymes: Supported [FeFe]-Hydrogenase Mimics with Enhanced Catalytic Hydrogen Production and Oxygen Stability in Aqueous Media

1. Introduction

1.1 Motivation for the Development of Hydrogen Evolution Catalysts

As renewable energy technologies – most notably wind and solar – rapidly decrease in cost ($/kWh), the main impediment to large scale utilization is the lack of efficient energy storage methods. The electricity generated by renewable sources such as wind and solar is intermittent and requires storage methods for load balancing and release of excess energy to the grid when production and demand are not temporally matched.[17] An ideal storage system will use excess energy during peak production times to drive a process which will store some of the energy as some form of potential energy. For example, pumped hydroelectric energy storage uses excess electricity generated by renewable sources to pump water uphill to a holding reservoir.[18] When grid demand exceeds capacity, the water is released from the upper reservoir and used to drive a hydroelectric turbine, converting the stored gravitational potential energy into electricity. This method is not particularly efficient and requires expensive, large scale construction of reservoirs and hydroelectric dams, but it is readily accessible with existing technologies and helps conceptualize the goal of renewable energy storage.

One solution for the next generation of energy storage methods is based on a hydrogen economy in which electricity that is generated in excess of grid demand is used to run and electrocatalytic fuel cells which split water into hydrogen and oxygen, $2H_2O \rightarrow O_2 + 2H_2$.[19,20] These fuels can either be burned as a mixture to release the energy stored in their chemical bonds, or preferably, the reaction can be run in reverse in a proton exchange membrane fuel cell (PEMFC) to generate electricity more efficiently as there are far lower losses to heat evolution.[21] Additionally, hydrogen offers an extremely high gravimetric energy density of 142 MJ/kg, almost three times higher than gasoline, and although its volumetric energy density is lower as a gas, efficient storage methods are a very active area of investigation.[22–24] These factors combine to make hydrogen an attractive option for fuel cell vehicles as it is energy dense, portable, and its use generates no carbonaceous by-products. The current state-of-the-art electrocatalyst for the hydrogen evolution reaction (HER) is platinum, which is both rare and expensive, limiting its usefulness in large scale energy storage. Due to the sensitive nature of the catalysts used in existing fuel cells which are easily poisoned by trace CO found in hydrogen produced via steam reforming, highly pure hydrogen from photo- or electrocatalytic water splitting is preferred.[25]

A complementary option for the production of hydrogen is focused on cutting out ‘the middle man’ of solar cells and instead using a photocatalytic system which directly converts sunlight into molecular hydrogen in a photosynthetic process.[26] The key advantage to this approach is that by cutting out solar cells, higher conversion efficiencies could theoretically be achieved as you no longer compound the inefficiencies of a solar cell with the inefficiencies of the HER catalyst. In practice, artificial photosynthetic systems have proven quite challenging as they face many of the same problems seen in photovoltaic cells, namely, increasing the lifetime and stability of the photoexcited states and preventing charge recombination by balancing electron transfer and hole filling rates, all while still needing to address the complex problem

of HER catalysis. Additionally, since the reduction of protons to hydrogen is a two electron process, the initial product of photoreduction (*i.e.* the $Fe^{I}Fe^{0}$ oxidation state or protonated $Fe^{II}Fe^{I}$-H product thereof in [2Fe-2S] complexes) must be stable long enough to be reduced by a second photoelectron in order to complete the catalytic cycle.

1.2 [FeFe]-Hydrogenase Enzymes, [2Fe-2S] Small Molecule Mimics and Their Limitations

Nature has provided a template for HER catalysis using earth abundant iron and sulfur in the[FeFe]-hydrogenase metalloenzymes produced by anaerobic bacteria, which function as HER catalysts at rates up to 10^4 s^{-1} in aqueous media, with a low overpotential requirement, similar to that of platinum.[2,3,27] The reactivity of these enzymes is centered around a [2Fe-2S] butterfly moiety in the active site, which is both synthetically accessible and easily modified by changing the ligands on the iron, or the identity of the organic moiety attached to the bridging μ-thiolate ligands. Studies on the structure and mechanism of the [FeFe]-hydrogenases have shown that the polypeptide structure in which the organometallic active site resides is crucial to the activity of the enzyme by *1) stabilizing a mixed valence, rotated open [2Fe-2S] cluster, 2) shuttling electrons to the active site via [4Fe-4S]-cubane moieties and 3) shuttling protons to the active site via amino acid residues, including a highly conserved cysteine residue which is implicated in hydrogen bonding with the nitrogen bridgehead of the active site*, *which is thought to be the species which protonates the* Fe_d *atom where catalysis occurs.*[8,9,11,28–33] Small molecule [2Fe-2S] mimetics have demonstrated high turnover frequencies (TOFs) in organic media with added acid, but exhibit low turnover numbers (TONs), are rapidly and irreversibly deactivated by oxygen, and are generally incompatible with the aqueous media of interest for a water splitting device.[13,34] Despite the wide structural variety synthesized to date, small molecule [2Fe-2S] catalysts have thus far failed to recreate the high levels of activity and low overpotential seen in the enzyme. Taken together, these findings suggest that mimicking only the active site is not sufficient to achieve the desired HER catalytic activity, stability, and solvent compatibility; tuning the macromolecular architecture is crucial to the development of highly active and robust [2Fe- 2S] HER catalysts.

1.3 Supported [FeFe]-Hydrogenase Mimics

Supported [2Fe-2S] systems, defined here as well defined [2Fe-2S] complex(es) incorporated into a macromolecular architecture via *covalent* or *non-covalent* intermolecular interactions have been explored in hopes of utilizing a macromolecular support to enhance the water compatibility, stability, HER catalysis rate, processability, and aerobic stability that has largely eluded unsupported [2Fe-2S] complexes. Using a fully synthetic supported [2Fe-2S] system offers a handful of advantages over using the enzyme, including scalability which is limited by the cost and difficultly of purifying an oxygen sensitive membrane enzyme. Further, the extreme oxygen sensitivity of the enzyme would require protection from even the small amounts of O_2 that would inevitably diffuse through the membrane of a water splitting device. Finally, chemical methods provide an opportunity to change the macromolecular architecture to address the shortcoming of both small molecule systems and the enzyme, which evolved along different design requirements to that of our ideal HER catalyst. Use of a macromolecular architecture provides a new way to address the systematic problems of small molecule [2Fe-2S] systems, provide water compatibility for use in water splitting applications, and improve the catalytic figures of merit.

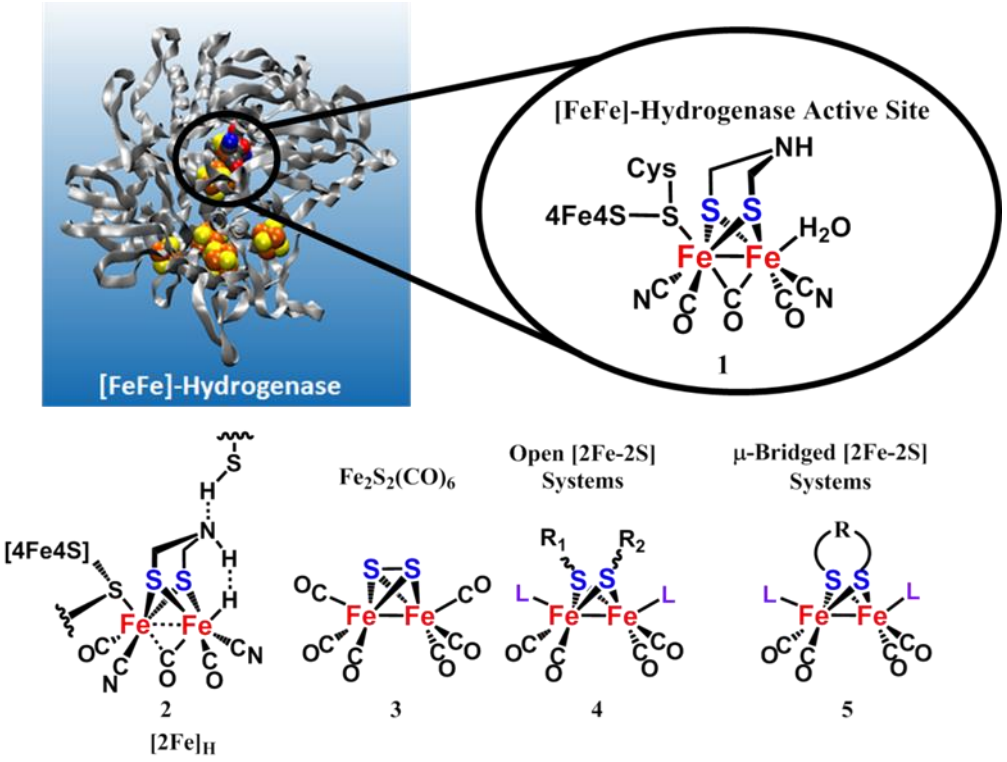

Figure 1.1. Ribbon structure of [FeFe]-hydrogenase enzyme, the [2Fe-2S] active site, and general structures of synthetic mimics. Structures of the [FeFe] hydrogenase enzyme and active site (1), a proposed catalytic intermediate for the enzyme catalytic cycle $[2Fe]_H$ (2), as well as the parent organometallic complex $Fe_2S_2(CO)_6$ (3) , and the general structure of open (4), and μ-bridged (5) synthetic [2Fe-2S] organometallic complexes which have been investigated as mimics of the active site of [FeFe]-hydrogenase enzymes. The [FeFe]-hydrogenase structure[8] is taken from the deposit PDB ID 5LA3 in the Protein Data Bank (http://www.rcsb.org/).[35] and is a partial recreation of material from [FeFe]-Hydrogenase Mimetic Metallopolymers with Exceptional Catalytic Activity for Hydrogen Production in Water Angew. Chem. Int. Ed. 2018 DOI: 10.1002/anie.201804661 (ASAP article) online only. Copyright Wiley-VCH Verlag GmbH & Co. KGaA. Reproduced with permission.

The catalytic figures of merit include the lifetime of a catalyst, defined by a turnover number (TON, on the order of 10^4 for the longest lived synthetic [2Fe-2S] systems)[12,36–38], which may be increased by sterically inhibiting associative mechanisms with a bulky macromolecular support.[39] In photocatalytic systems the Fe^IFe^0 and $Fe^{II}Fe^I$-H photocatalytic intermediates may be stabilized by the supporting macromolecule, much as the protein support stabilize the mixed valence $Fe^{II}Fe^I$ active site in the metalloenzyme. The rate of catalysis, defined as a turnover frequency (TOF, on the order of 10^3-10^5 for the fastest reported [2Fe-2S] systems)[12,40,41] may be improved by the inclusion of basic functional groups to either transport protons from the bulk solution to the active site or to provide a high local concentration of protons for reduction. Theoretically, 'molecular wires' (such as ferrocene, cobaltocene, viologens, quinones and other redox active molecules) may be incorporated into such systems to also facilitate electron transport. In photocatalytic systems, co-localization of photosensitizer (PS), sacrificial electron donor (SD), and catalyst with the support can help to promote rapid electron transfer to the catalyst, and inhibit back electron transfer by increasing the rate of hole filling on the photosensitizer, increasing the quantum efficiency of photocatalysts. Using a support which is redox active or rich in amine functional groups has been shown to improve the oxygen tolerance of the enzyme and [2Fe-2S] mimics which are rapidly and irreversibly deactivated under aerobic conditions.[13,14,42–46] Finally, a smaller

overpotential requirement (η†, the overpotential required to reach a specified current density, 0.1 mA cm^{-2} in this work) may be obtained in electrocatalytic systems if the macromolecular architecture enables a proton coupled electron transfer (PCET) mechanism which has been shown to decrease the potential requirement for the second reduction step by coupling a protonation event with an electron transfer.[47–50] Additionally, these fully synthetic systems lend themselves well to scalable synthesis and may be produced at much lower cost than the tedious and delicate purification of strictly anaerobic membrane-bound enzymes – a process which typically limits the scale of purified enzyme to hundreds of micrograms or a few milligrams at most.

In this review, we will focus on approaches that are based in the application of chemical methods to stabilize and improve the immobilization, or conjugation [2Fe-2S] complexes onto synthetic materials. Systems which contain macromolecular/nanoscale components (*e.g.* QD's) which only have a transient interaction (*i.e.* electron transfer from an excited photosensitizer) with a small molecule [FeFe]-H_2ase mimic are not covered in this review, nor are approaches to enzyme engineering including the design and synthesis of modified enzymes, selective mutation of [FeFe]-hydrogenases, and the use of polymers and other materials to stabilize the enzyme have been reviewed recently and fall outside of the scope of this review.[6,31,51–55] Broadly, supported [2Fe-2S] systems may be classified by the type of macromolecular support that is used. Carbohydrate systems such as cyclodextrins and chitosan have been employed to improve the photocatalytic hydrogen evolution catalysis, as well as improving water solubility via host-guest interactions.[56–60] Similarly, micelle solutions have been used to bring insoluble, or sparingly soluble small molecule [2Fe-2S] complexes into aqueous solutions where they have been demonstrated to drastically increase the lifetime of charge separated states in photocatalytic system.[40,61–63] Polymer and low molecular weight peptide hydrogels have also been employed in the pursuit of water compatibility and intramolecular stabilization of the reduced diiron systems active in HER catalysis.[60,64,65] Functionalized electrodes have been fabricated in which [2Fe-2S] sites are covalently or non-covalently bound to the surface of the electrode to facilitate rapid electron transfer and anchor the diiron systems to prevent associative deactivation mechanisms.[38,50,66] Finally, we will review the promising field of [2Fe-2S] metallopolymers from which the highest TON photocatalytic system has been reported. Most recently a metallopolymers system has been shown to display electrocatalytic HER performance and stability that exceeds that of [FeFe]-hydrogenases.

2. Supported [2Fe-2S] Systems

2.1 Carbohydrates

One of the earliest approaches to supramolecular stabilization and improved water compatibility of [2Fe-2S] systems focused on using water soluble carbohydrates (cyclodextrins and chitosan) to form host-guest complexes of [2Fe-2S] catalysts in hopes of improving catalytic rates and catalyst stability. In photocatalytic systems, it is envisioned that a photosensitizer species could also be entangled in the host-guest complex, keeping the photosensitizer and catalyst close together to increase the chances of interaction between the two species. This approach has indeed been effective for photocatalytic systems in which the inclusion of the supramolecular carbohydrate scaffolds has increased quantum efficiency, charge separated state lifetimes, TON, and TOF of the photocatalytic systems. Licheng Sun *et al.* incorporated halogenated fluorescein dyes Erythrosin B (EB) and Rose Bengal (RB) into

β-CyD (7 glucose units) and γ-CyD (8 glucose units) (see Fig 1.2) along with catalyst ((μ-adt-N-(p-phenylsulfonate))$Fe_2(CO)_6$ complex (**6**).[58] Cyclodextrins increased TON by nine-fold, quantum efficiency by sixteen fold, and tripled active lifetime of that catalyst without the addition of CyD species. These effects are attributed to stabilization of the reduced $Fe^{I}Fe^{0}$ intermediate. In contrast, electrochemical studies on cyclodextrin – [2Fe-2S] systems have shown a decrease in electrocatalytic performance with the addition of cyclodextrin or chitosan supports.[56,59] The decrease in activity was initially attributed to a restriction of the geometric reorganization required for [2Fe-2S] catalyst to proceed through the catalytic cycle, but the success of photocatalytic systems casts some doubt on this hypothesis and would seem to indicate electron transfer from the electrode is inhibited by the inclusion large, relatively insulating carbohydrates.

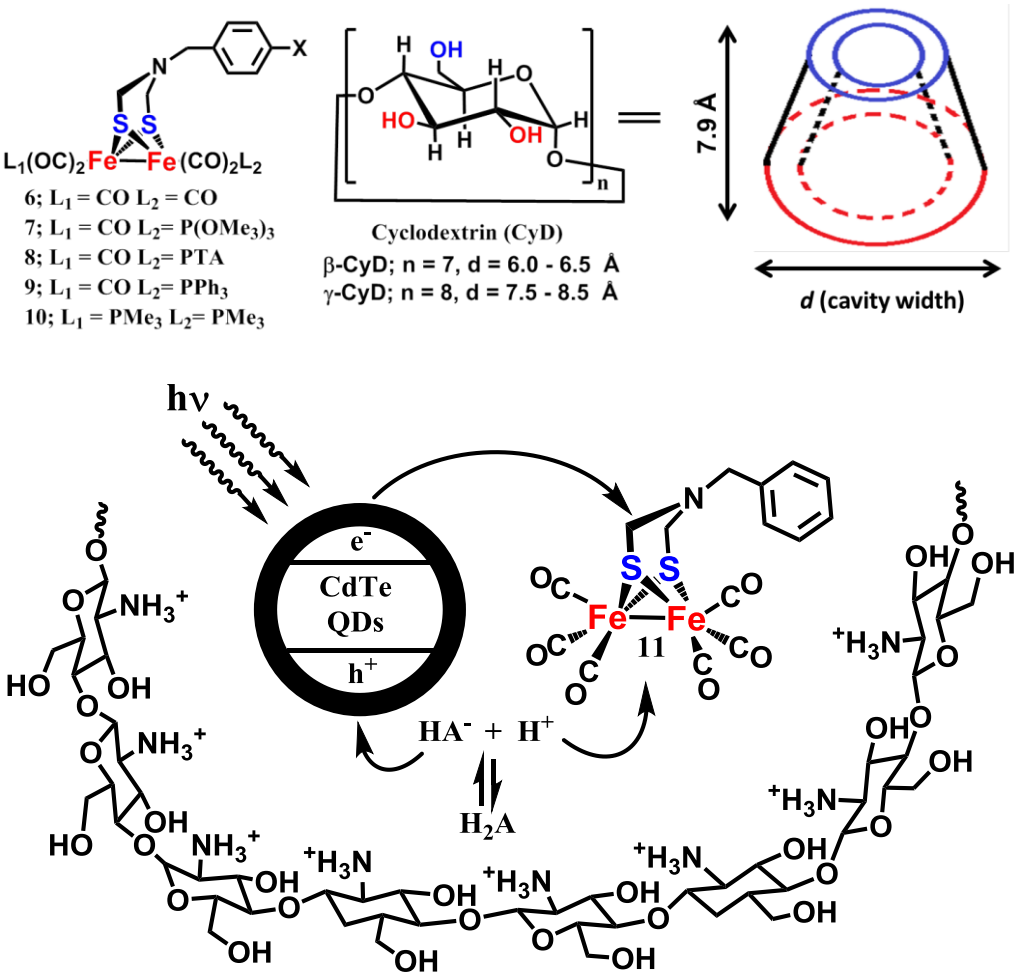

Figure 1.2. Structure of [2Fe-2S] catalysts 6-11 used in carbohydrate supported system as well as the structure of cyclodextrins and a schematic view of the chitosan/(11) photocatalytic system. H_2A is ascorbic acid, HA^- is ascorbate

The first study on the use of cyclodextrin – [2Fe-2S] host-guest complexes was reported by Darensbourg *et al.* in 2010 using (**6**) which is somewhat water soluble by virtue of the sulfonate group attached to the bridgehead. [67] Crystal structures showed two β-cyclodextrin (β-CyD) rings assemble around one [2Fe-2S] molecule in the solid state. Variable temperature NMR spectroscopic studies found that in solution, a 1:1 CyD/[2Fe-2S] complex forms in which the diiron complex rapidly exchanges in and out of cyclodextrin. Unfortunately, the presence of CyDs actually inhibits electrocatalysis. The catalytic peak shifts 200 mV negative upon

addition of β-CyD to a solution of (**6**) with no benefit to catalytic current density. A follow-up study the next year found this electrocatalytic deactivation effect was general to four other diiron systems with one or two of the carbonyl ligands substituted by $P(OMe)_3$ (**7**), 1,3,5-triaza-7-phosphatricyclo[3.3.1.1]decane (PTA) (**8**), PPh_3 (**9**), or two PMe_3 ligands (**10**). The disubstituted PMe_3 complex (**10**) displayed the best electrocatalytic activity in acetonitrile (ACN) with added acetic acid, but was not catalytic within the solvent window in aqueous solution. All complexes showed a decrease in electrocatalytic current upon addition of β-CyD. They did however, note greatly increased stability in air-free water following the addition of CyD to the solution. This is consistent with the increased photostability and photocatalytic activity observed in the aforementioned cyclodextrin-[2Fe-2S] host-guest complexes, which is perhaps a better application for the cyclodextrin motif.

A high performance photocatalytic [2Fe-2S] system using $[Fe_2(CO)_6(\mu\text{-adt-Bn})]$ (11) and cadmium telluride (CdTe) quantum dots (as a photosensitizer) in a methanol-water solution (25% MeOH) buffered at pH 4.5 with ascorbic acid (H_2A) buffer has demonstrated a *4,000 fold* increase in TON with the addition of chitosan – reaching 52,800 moles H_2 evolved per mole of active site under optimized conditions and increased the photocatalytic lifetime from 8 to 60 hours.[56] Spectroscopy and dialysis experiments were confirmed tight incorporation of (**11**) into the chitosan matrix. It is postulated that chitosan wraps around QDs, stabilizing them and preventing aggregation, as well as attracting a high local concentration of HA^- the active electron donor which fills holes formed in the QDs. These effects nearly double the photoluminescent lifetime (10.9 ns to 18.3 ns), increase photoluminescent intensity, and greatly improve quantum yield (5.1% -without chitosan to 38.3% with chitosan). Though this level of activity is impressive, it is confined to a fairly tight pH window between pH 4-5.and controlling pH is demonstrated to be the most important factor governing photocatalytic performance. Activity below pH 4 cannot be investigated as the 3-mercaptopropionic acid (MPA) coating on the CdTe QDs becomes unstable, resulting in precipitation and the formation of defects which will inhibit electron transfer. The activity drops off quickly at higher pH values - with only ~50-60% of its peak activity at pH 6.0, which the authors attribute to deprotonation of the amine in the glucosamine residues, reducing the solubility of chitosan and inhibiting any stabilization or proton shuttling role it may have played. Control experiments using micelles achieved low TONs (37 ± 3 and 36 ± 4 for sodium dodecylsulfate (SDS) and cetyltrimethylammonium bromide (CTAB) micelle solutions, respectively), so the rate enhancements are entirely due to presence of and interaction with chitosan support. A tight interaction between catalyst, quantum dot photosensitizer and chitosan has been demonstrated, and shown to improve electron transfer to the catalyst system via pump-probe measurements. The positively charged chitosan scaffold will also attract a high concentration of HA^- species nearby to fill holes in the QDs and prevent photo-corrosion.

2.2 Micelles

Micellar systems have also been investigated; they offer the benefit of quickly and easily screening a variety of small molecules and micelle systems in aqueous media with minimal synthesis required, improving throughput. The first study on [2Fe-2S] complexes encapsulated in micelles came in 2010 from Wu *et al.* in which (**6**) and (**11**) were incorporated into a three part photocatalytic system utilizing a Re(I) photosensitizer and ascorbic acid as both electron donor and proton source in an aqueous solution of SDS micelles.[62] These systems exhibited extremely long lived mixed valence Fe^IFe^0 state – with a lifetime of 697 ns achieved with (**11**) and $[Re(phen)(CO)_3Br]$ photosensitizer. In comparison, a self-assembled

photo-dyad of (**12**) with the same photosensitizer typically gives $Fe^{I}Fe^{0}$ lifetimes on the order of 30-40 ns.[68] Unfortunately, this did not translate into exceptional catalytic activity, with a sub-catalytic TON of 0.13 reported under optimized conditions.

In 2016, the same laboratory followed up with the first report of a micellar [2Fe-2S] system which achieved a catalytic TONs (that is TON > 1).[61] A polymeric micelle agent **P-NB** allowed a maximum loading of $[Fe_2(CO)_6(\mu\text{-pdt})]$ (**12**) of 0.188 mM, which correlates to a mass loading of 48 mg of PDT per gram of polymer.[69] In practice, best performance was obtained using a much lower catalyst concentration with $Ru(bpy)_3^{2+}$ (30 μM) and excess ascorbic acid (45 mM) to get a TON of 133 under irradiation from a 450 nm LED – a thirty-fold increase over the system without **P-NB**. Mechanistically, the excited $^{*}Ru(bpy)^{2+}$ is not reductive enough ($E^{1/2}$ = -0.60 V vs NHE) to reduce Fe system only after excitation *and* trapping the excited state. The $^{*}Ru(bpy)_3^{+}$ species generated has a reduction potential of -1.30 V vs NHE, negative enough to transfer an electron to the iron system.[70] This results in a mechanism where the Ru system is excited, then reduced by HA^{-} to generated the active reductant, $^{*}Ru(bpy)_3^{+}$, which interacts with the [2Fe-2S] system. The micelle functions as a cage to co-localize the reagents and ensure adequate collision between the catalyst and reducing $^{*}Ru(bpy)_3^{+}$ species. The resulting $Fe^{I}Fe^{0}$ species is thought to then undergo a protonation and generate a $Fe^{I}Fe^{II}$-H bridging hydride species which can then undergo a second reduction with $Ru(bpy)_3^{+}$ before reacting with a second proton to produce hydrogen.

In all of these aqueous micellar systems, one must wonder how water, protons, and other polar protic substrates are going to interact with a catalyst system that is buried in the hydrophobic interior of a micelle. This question was addressed nicely in a study by Pickett and Hunt *et al.* who used IR, 2D-IR, and ultrafast pump-probe measurements were used to study a system of (**12**) in a heptane-dodecyltrimethylammonium bromide (DTAB)-water microemulsion.[71] PDT was found to be partitioned between two different environments. The first can be thought of as the greasy, alkane rich, hydrophobic interior which is essentially identical to the same molecules in heptane solution. The second environment is located closer to the edge of the micelle, where water molecules intercalated and participated in hydrogen bonding with the Fe system which resulted in new spectral features. The amount of water accessible catalyst can be tuned by tuning micelle size, with smaller micelles having more accessible catalyst and larger micelles having most catalyst in a heptane-like environment. Intermediate micelles had behavior intermediate to the very large and very small micelles. This suggests that catalytic micellar systems will benefit from either *a)* targeting small micelles to increase water-catalyst activity or *b)* designing micellar systems that allow a high degree of water intercalation even at large micelles sizes. In either approach the goal is to leverage the co-localization of reagents from the micellar system without shutting down beneficial catalyst – water interactions.

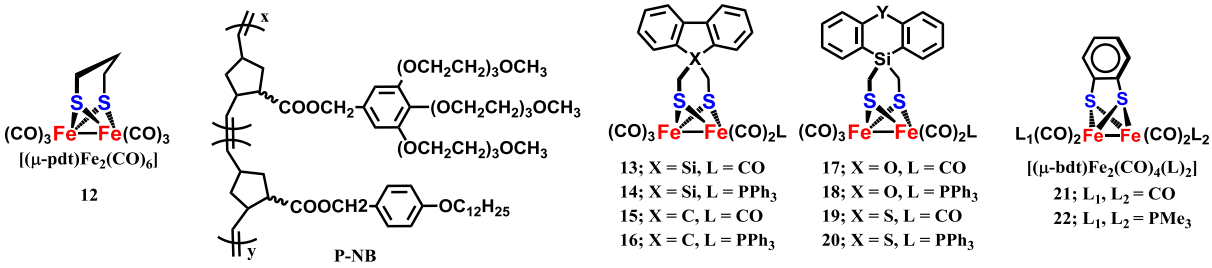

Figure 1.3 Structure of [2Fe-2S] complexes **12-22** used in micelle supported systems as well as the polymeric amphiphile **P-NB.**

Most recently Weigand *et al.* published a study on [2Fe-2S] complexes tethered to fluorene and silafluorene photosensitizers via the dithiolate ligands (compounds **13**-**20**), which are capable of intermolecular electron transfer from the tethered organic chromophore to the diiron system.[72] A maximum TON of 539 was obtained in ACN with 10 µM catalyst, 100 mM triethylamine as a sacrificial electron donor and 50 mM trifluoroacetic acid as a proton source. This represents the best performance to date using micelles to achieve water compatibility with [2Fe-2S] mimics. Aqueous photochemical experiments were conducted in micellar solutions of SDS and CTAB at an optimized pH of 10 gave a maximum TON of 148 using the CTAB micelle solution, and 139 for the SDS micelle solution, *indicating the identity of the amphiphile is not important in this case.*

Far less time has gone into studying micellar systems in an electrocatalytic context. The well-studied, benzene annulated catalyst,[(µ-bdt)$Fe_2(CO)_6$] (**21**) was examined electrochemically in a solution of SDS micelles.[40] The catalyst was found to be functional at pH values below 6. The authors assert the 'turn-on' of catalytic activity below pH 6 is due to a proton coupled electron transfer mechanism operating in the aqueous environment. A maximum TOF of 2600 s^{-1} was calculated using the Dubois method – a rate which approaches the performance of the enzyme itself.[73] A TON of 52 mol H_2 mol^{-1} cat was determined using controlled potential electrolysis at However, inclusion of the surfactant had a detrimental effect on overpotential, with an overpotential of ~0.5 V required to reach a current density of 0.5 mA cm^{-2}. A follow-up study by the same lab found that replacement of two of the CO ligands with $P(OMe)_3$ ligands **22** gave a higher TOF (4600 s^{-1}) using Delahay's method but lower TON of only 23 mol H_2 mol^{-1} cat at pH 3 using a dropping mercury electrode.[74,75] They also report instability to the presence of acetate ions without SDS, but once the micelles are formed, the catalyst is relatively insensitive to the presence of acetate.

2.3 Hydrogels, Peptides, and MOFs

Peptide and polymer gels have been used to support [2Fe-2S]-photocatalysts in a macromolecular architecture via non-covalent interactions. Redox active hydrogels have been shown to stabilize [FeFe]-, [NiFe]-, and [NiFeSe]- hydrogenases and protect them from oxidation and high potential deactivation mechanisms.[42–44] A low molecular weight Fmoc-Leu-Leu hydrogel was loaded with (µ-pdt)$Fe_2(CO)_4(PMe_3)_2$ (**23**).[64] IR and dynamic studies suggest this hydrogel support locks the Fe system in a solvent cage with a rigid hydrogen bonding network. The small molecule alone is reported to be extremely unstable in aqueous solution, but the hydrogel (90% water) was stable for up to two weeks, however catalysis was not demonstrated. In 2007, Darensbourg *et al.* showcased a series of three catalysts that utilized different bonding motifs to attach carboxylic acids via substitution of an Fe-CO with $P((CH_2)_2COOH)_3$ (**24**) and attachment to a bridged (**25**), unbridged system (**26**) via the µ-

thiolate ligand, and These molecules are amenable to surface immobilization via the carboxylic acid groups, but catalysis was not demonstrated.[76] In 2009, Darensbourg *et al.* used N,N'-diisopropylcarbodiimide (DIC) coupling to anchor these three small molecule mimics to PEG-rich polystyrene Tentagel beads via amide bond formation.[77] Unfortunately, the PEG environment was found to facilitate photochemical loss of a CO ligand and subsequent catalyst degradation. The addition of acid to the aqueous solution was found to degrade the [2Fe-2S] complex and release the degraded complexes from the beads. In 2007, a 36 chain peptide SynHyd1 with a well-defined α-helical structure was synthesized with an open [2Fe-2S] mimic attached via two cysteine residues and in 2011, on resin modification of a short chain peptide was performed by Jones *et al*. [78,79] The synthesis and characterization of these two peptide supported [2Fe-2S] system was demonstrated and but catalysis was not presented in either case. In 2012, a 19-residue helical polypeptide used an artificial dithiol leucine residue in the 16 position to incorporate a [2Fe-2S] cluster.[80] This helical peptide (**27**) was used in pH 4.5 ascorbic acid buffer with $Ru(bpy)^{2+}$ buffer to achieve a TON of 84 over 2.3 hours.

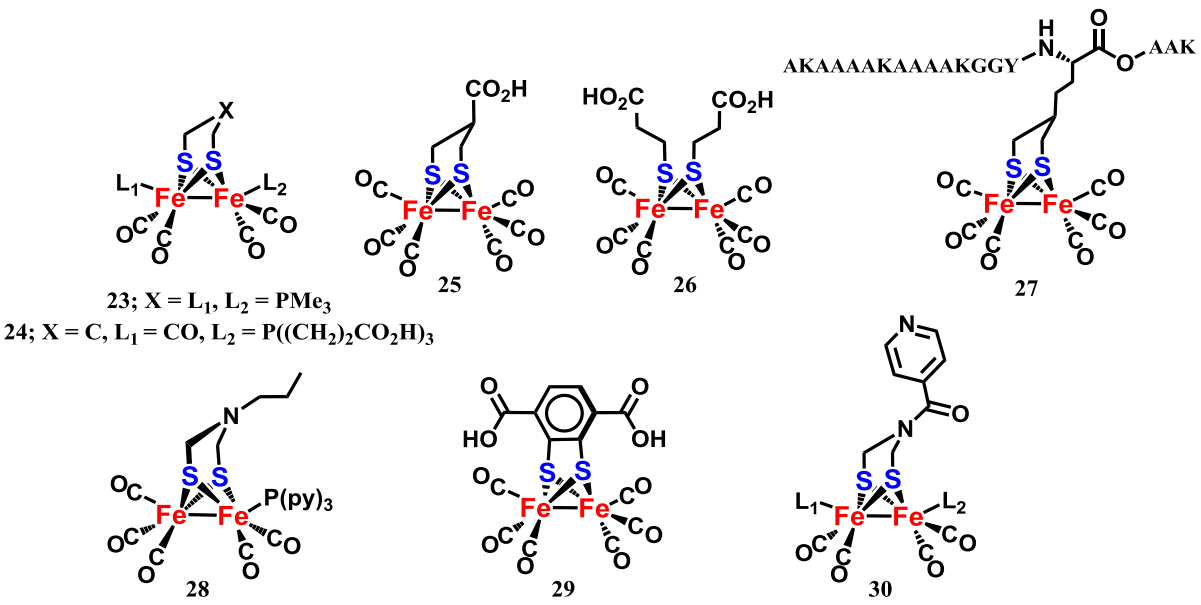

Figure 1.4. Structure of [2Fe-2S] complexes used in hydrogels (**23**, **28**), attached to Tentagel beads (**24-26**) a synthetic peptides (**27**), and incorporated into MOFs (**29**, **30**).

A [2Fe-2S] complex has also been assembled into vesicular structures, but no attempt was made to characterize the photo- or electrocatalytic performance of the assembly.[81] The most active reported photocatalytic hydrogel system comes from the laboratory of Yang and Li.[60] A PVP hydrogel loaded with [(μ-adt-N-^{n}Pr)$Fe_2(CO)_5P(pyr)_3$] (**28**) dissolved in methanol was dried and swollen with an aqueous solution of photosensitizer $Ru(bpy)_3^{2+}$ and ascorbic acid which acts as both an electron donor and proton source. They demonstrated a four-fold increase in the lifetime of the excited state after incorporation into the gel when compared with free $Ru(bpy)_3^{2+}$. Addition of the diiron system progressively quenches the characteristic 505 nm emission, providing evidence for electron transfer (ET) to the iron system from PS^*. A TON of 780 was reported when operating in pH 4 ascorbate buffer. Unfortunately, this activity is confined to a tight pH window, with the TON dropping to *ca.* 200 moles H_2 mol^{-1} catalyst when the pH is lowered to 3 and approximately 100 moles of H_2 mol^{-1} catalyst when increased to pH 5. Increasing the pH to 6 renders the system almost entirely inactive.

Two examples MOF supported [2Fe-2S] have been reported. The first came in 2013 by Ott *et al.* in which two molecules of (**29**) were incorporated into a Zr based UiO-66 MOF.[82] The resulting system catalyzed HER at pH 5 in an aqueous acetate/ascorbate buffer system using $Ru(bpy)_3^{2+}$ as a PS with a TON of ~6, a threefold enhancement over (**29**) alone and an increase in both initial rate of H_2 production and a longer lifetime for H_2 evolution. The authors suggested three complementary mechanistic reasons for this enhancement (1) stabilization of the reduced catalyst forms, (2) preventing charge recombination with an oxidized ascorbate molecule, and (3) promoting as disproportionation mechanism between two monoanions in the same MOF to generate a catalytically competent dianion. The next year, a zirconium-porphyrin based MOF ([ZrPF) was used to support an ADT complex (**30**) which coordinated a zinc atom in the porphyrins via a pyridine attached at the bridgehead.[83] This MOF system ([FeFe]@ZrPF) functions as a photocatalyst with a TON of 7 in pH 5.0 acetate buffer with added ascorbic acid without the need for an external photosensitizer – the MOF bound porphyrins serve as intramolecular photosensitizers.

Table 1.1. Selected results from photocatalytic [2Fe-2S] systems. Φ is the quantum efficiency, KET is the electron transfer rate from PS* to the [2Fe-2S] complex, τ FeIFe0 is the lifetime of the mixed valence species generated by one electron reduction of the [2Fe-2S] complex is the absence of acid. Conditions and light source refer to the optimized methods used to obtain the turn over number (TON) value.

[2Fe-2S]	Support	PS	TON (mol H_2/mol cat)	Run time (h)	Φ (@ λ)	K_{ET} $M^{-1}s^{-1}$	τ Fe^IFe^0 (μs)	Conditions	Ref
6	γ-CyD	Eosin Y (EY)	190	24	1.95% (520 nm)	2.13 x 10^{11}	---	10% TEA (aq), pH 10, 500 W Xe lamp, >450 nm	**[58]**
11	Chitosan	MPA-CdTe QDs	52800	60	38.3% (405 nm)	2.26 x 10^{4}	---	H_2A (0.2M, pH 4.5), 1:3 MeOH/H_2O 410 nm LED	**[56]**
11	SDS	[Re(I)(4,4'-diMebpy)$(CO)_3$Br]	0.13	1	35.30%	2.3 x 10^{11}	619	H_2A (0.1M, pH 7.4), ACN/H_2O, 500 W Hg lamp, >400 nm	**[62]**
12	P-NB	Ru(bpy)3^{2+}	133	2	2.3% (400 nM)	8.68 x 10^{7}	128	H_2A (45 mM, pH 4.1), 450 nm LED	**[84]**
12	Helical peptide	Ru(bpy)3^{2+}	84	2.3	---	---	---	H_2A (50 mM pH 4.5), 450 W Xe lamp >410 nm	**[80]**
28	PVP hydrogel	Ru(bpy)3^{2+}	780	12	0.45%	5.2 x10^{3}	664	H_2A (0.2 M, pH 4.0 Xe lamp, 200 mW cm-2)	**[60]**
29	UiO-66 MOF	Ru(bpy)3^{2+}	6	2.5	---	1 x 10^{7}	---	H_2A (0.1M) acetate buffer (1 M, pH 5.0) Blue LED, 470 nm	**[85]**
30	ZrPF MOF	Zn-TPP in MOF	7	2	--	--	--	H_2A (20 mM) acetate buffer (1 M, pH 5.0)	**[83]**
3	InP	InP	---	---	---	---	---	0.1 M aqueous NaBF4 (pH 7.0) LED array 395 nm	**[86]**
49	PAA	MPA-CdSe QDs	27135	8	5.07%	6.15 x 10^{12}	449	H_2A (0.2 M, pH 4.0), 450 nm LED	**[87]**
51	PEI	MPA-CdSe QDs	10600	45	2.10%	8.46 x 10^{11}	---	H_2A (0.125 M, pH 6.5), 3 W LED lamp 410 nm	**[88]**
53	PAA/PEI	MPA-CdSe QDs	83600	28	---	4.5 x 10^{11}	---	H_2A (0.1 M, pH 4.1), 3 W 450 nm LED	**[46]**

2.4. Functionalized Electrodes

Direct attachment of [2Fe-2S] systems to an electrode surface approach promises several benefits including rapid electron transfer to surface bound diiron systems, mitigation of associative deactivation mechanisms by anchoring the diiron systems so they cannot interact, and it is a more practical design for a water splitting device, which are typically constructed with heterogeneous catalysts. The first effort came in 2005 when an electrode was functionalized with aniline by electrochemically depositing a layer on the surface of the electrode.[89] Amide bond formation with (**21**) formed a functionalized electrode surface which was characterized by CV and found to be stable in acetonitrile. Unfortunately the addition of acid resulted in broad, featureless voltammograms which did not indicate a clear catalytic wave. CV in water (0.1 M, pH 7 sodium phosphate buffer) did not find any reduction events within the solvent window.

In 2007, Pickett *et al.* reported the non-covalent incorporation of (μ-pdt)$Fe_2(CO)_4(CN)_2^{2-}$ (**31**) into a polycationic polypyrrole film via a strong coulombic interaction between the dianionic diiron system and the positively charged polymer, but catalysis was not demonstrated.[90] In a follow up paper in 2011, the same group reported the results of a stopped-flow FTIR study film-bound (**31**) and a solution of the same complex in acetonitrile.[91] Initially, both had similar Fe-CO stretching frequencies, but after exposure to acid, the spectrum of the film did not change significantly when exposed to HCl vapor, while the small molecule forms a spectroscopically distinct μ-hydride species upon exposure to HBF_4•Et_2O in acetonitrile. This

result indicates the film does not form a μ-hydride intermediate like the solution species does. Additionally, the film was stable to HCl vapor for several hours, while a solution of (**31**) degraded rapidly in the presence of HCl.

An elegant hybrid photo-electrocatalytic system was published by Pickett *et al.* in 2010.[86] In this hybrid nano-photocathode, a crosslinked layer of nanocrystalline indium phosphide (InP) was deposited layer by layer on the surface of a gold electrode, then the electrode was soaked in a solution of $Fe_2S_2(CO)_6$ to incorporate the [2Fe-2S] complex. A potential of -0.19 V vs SHE was applied to the electrode, and a 395 nm LED was used to illuminate the electrode surface. The overall mechanism can be said to be photocatalytic in nature, with the InP acting as a photosensitizer for the [2Fe-2S] system. Viewing the system this way, the gold electrode takes on the function of the sacrificial electron donor typically employed in a photocatalytic system. The system displayed a 60% Faradaic efficiency and showed degradation of photocurrent over one hour under a bias of -190 mV vs SHE. The main drawbacks to the system are in the relatively low HER current density, the use of expensive gold and indium materials, and the tedious, stepwise fabrication of the photoelectrode using vapor deposition, however the use of an electrode to fill holes in a photocatalytic system is an interesting and under-utilized concept in the field of photocatalytic [2Fe-2S] systems.

In 2012 a very promising membrane electrode was fabricated with electrospun fibrous membranes (EFMs) composed of cellulose acetate (CA), carboxylated multi-walled carbon nanotubes (MWCNTs, added to improve conductivity), polyvinyl pyrrolidone (PVP), and [(Fe_2(edt)$(CO)_6$)] (**32**).[92] The resulting EFM demonstrated HER catalysis in water, which improved with the addition of acetic acid. This electrode also demonstrated a higher degree of function and stability than previous functional electrode systems, with freshly fabricated electrodes giving about 40% of the HER catalytic current density as that of a platinum disk electrode at an increased overpotential requirement of 400 mV. Furthermore, *ca.* 50% of this activity was retained after 150 cycles. The system still requires refinement however, as the electrodes are not suitable for bulk electrolysis due to mechanical deformation of the delicate membrane by bubbles of evolved hydrogen. Despite these drawbacks, the impressive activity of these membrane electrodes invited further investigation.

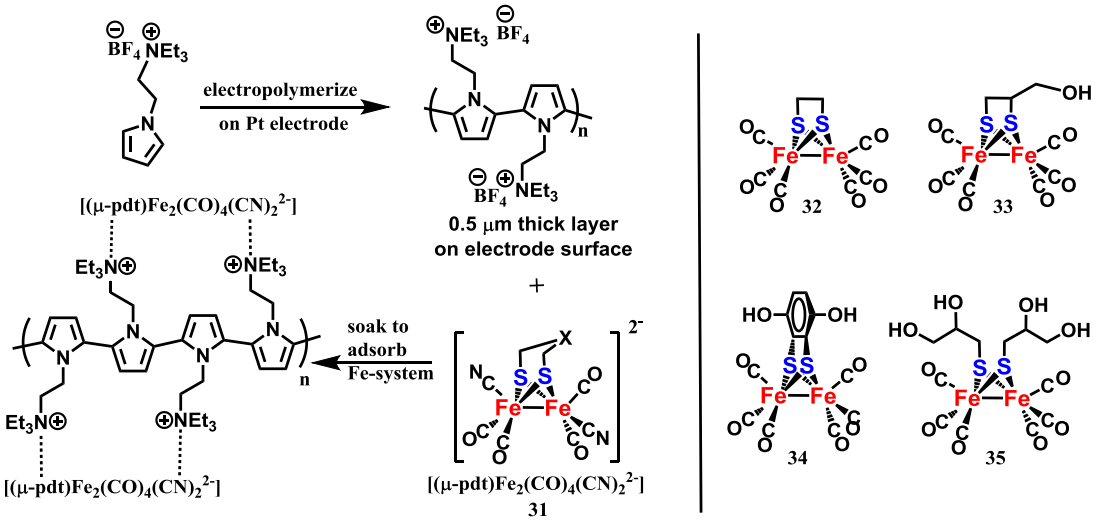

Figure 1.5. Structure of [2Fe-2S] dianion (**31**) and its non-covalent incorporation into cationic polypyrrole films. [2Fe-2S] compounds (**31-35**) incorporated into cellulose acetate electrospun fibers, used in membrane electrodes.

Three years later, a follow-up paper by the same laboratory used four different hydroxy-functionalized [2Fe-2S] complexes [(μ-edt)$Fe_2(CO)_6$], (**32**); [(μ-edt-CH_2OH)$Fe_2(CO)_6$], (**33**) with one hydroxy functional group; a hydroquinone bridged catalyst [(μ-hqdt)$Fe_2(CO)_6$], (**34**); and an unbridged [2Fe-2S] system functionalized with two polyethylene glycol functionalities [Fe_2(μ-$SCH_2EG)_2(CO)_6$], (**35**).[93] Graphene oxide was added as a dopant for conductivity. Electrodes assembled with fibers made with **35** produced excellent catalytic currents but were found to bleach rapidly in acid solution, likely due to the high solubility of **35** in water. Fibers made with **34** gave messy electrochemical results upon addition of acid. The best performance was obtained using membranes assembled with fibers containing **33** which also had the highest resistance to bleaching in aqueous media. The hydrophobicity of **32** was thought to inhibit substrate and electron transport to the active site in aqueous systems, explaining the drastic improvement in the activity of **33** just by the addition of a hydroxyl group. Membranes assembled with **33** were doped with polyethyleneimine (PEI) with the goal of increasing proton transport via the *inclusion of basic amine groups. PEI was found to drastically increase the catalytic current of the electrode*, and the electrocatalytic performance of the membrane electrode assemblies was found to improve as more PEI was added. The maximum loading attempted doubled the peak catalytic current density compared with an electrode with no PEI. They note the addition of PEI makes the 1st reduction indistinguishable. All electrodes still suffer from some amount of bleaching upon cycling, worse for the more soluble ones which just leach out of the fiber into water since they are not tightly bound. Despite their outstanding performance, the CA-PEI-[2Fe-2S] systems demonstrated one of the pitfalls of non-covalent incorporation of the [2Fe-2S] site, degradation via catalyst bleaching due to a lack of strong interactions with the supporting matrix. Covalently bonding the [2Fe-2S] system to the surface of the electrode, or into the supporting matrix, would prevent such catalyst loss, and may serve to stabilize reduced catalytic intermediates.

Table 1.2. Catalytic figures of merit for selected functionalized electrode systems. All electrode potentials have been converted to values vs SHE for ease of comparison, and all current values converted to current density using the geometric area of the electrode used. $t_{1/2}$ is the half-life of the electrode catalyst, defined by the number of cyclic voltammetry (CV) cycles that the system can be used for before 50% (or more) of the catalytic activity is lost. E^o_{IPc} is the potential at which peak catalytic current was observed under optimized conditions in a cyclic voltammogram (CV) at a given scan rate, v, under given in the conditions column. Overpotential (η) is given as an absolute value calculated from the half wave potential ($E_{1/2}$) of the catalytic wave in a CV. In many cases, potential values were not explicitly given and had to be extracted from figures. Despite considerable care in this process, a small error (no more than 50 mV) may be present in the numbers presented here. All potentials reported vs SHE.

[2Fe-2S]	Support	$t_{1/2}$	J_{max} (mA cm^{-2})	v (mV/s)	E^o_{Ipc} (V)	$E_{1/2}$ (V)	η (V)	Conditions	Ref
40	polypyrroles	--	-0.23	100	-1.15	-1	---	16 mM Lutidine-H+ in ACN	**[90]**
42	GC	1	-3.8		-1.91	-1.54	---	15 eq HBF4 Et_2O in ACN	**[94]**
45	PVC-Nafion-MWCNTs	1	-3.5	100	-1.25	--	0.19	4 uL AcOH in ACN	**[95]**
44	polyene	1	-6	5	-1.65	-1.3	0.24	5 uL AcOH in 3 mL ACN	**[96]**
32	CA-PVP-cMWCNTs	150	-1.24		-1.25	-1.06	0.18	Dilute Aq acetic acid (pH ~ 3.1)	**[97]**
33	CA-GO	150	-2.36		-1	--	0.20	Dilute Aq acetic acid (pH ~ 3.4)	**[98]**
36	PEI-RGO-Nafion	3	-7.2	100	-1.55	-1.13	0.17	8 uL AcOH in 0.1 M KCl (aq), 0.1 M KCl	**[99]**

2.5. Metallopolymers

One of the most promising approaches for a covalently bound, supported [2Fe-2S] system is the field of metallopolymers.[100–103] Metallopolymers have already found application in other energy conversion and storage materials.[104] Metallopolymer systems are classically subdivided into two categories based on the location of the metal in the polymer chain in either the main chain or appended on as side chain moieties. For the purpose of this discussion, it is useful to consider a third classification of metallopolymers which incorporate a single metal center in the polymer chain. In the field of [2Fe-2S]-metallopolymers, poly(acrylic acid)-*g*-[2Fe-2S] and PEI-*g*-[2Fe-2S] have been shown to dramatically improve the performance of a photocatalytic [2Fe-2S] system, by helping to co-localize catalysts and substrate, facilitate use in aqueous media, sterically isolate the reduced diiron clusters, and stabilize the rotated geometries of catalytic intermediates.[37,46,105] More recently, PDMAEMA-*g*-[2Fe-2S] systems have demonstrated extremely potent electrocatalytic activity, with TOFs exceeding that of the parent enzyme (10^8 s^{-1}) with a similar overpotential requirement (0.3 V to reach 0.1 mA cm^{-1} compared with 0.2 V for the enzyme on a TiO_2 electrode), and most strikingly, is able to operate under aerobic conditions – a crucial property for any practical HER catalyst to be used in a water splitting application. These discoveries combine the high activity of small molecule [2Fe-2S] mimics with tunable macromolecular architectures to replicate many of the functions of the protein matrix in [FeFe]-hydrogenase enzymes including site isolation, proton transport via basic functional groups (*i.e.* carboxylate and amines), and stabilization of the active site relative to 'free' small molecules.

I. Main Chain Metallopolymers

Gold electrodes have been modified with a self-assembled monolayer (SAM) of thiol tethered azides.[99] An unbridged [2Fe-2S] complex, $[Fe_2(\mu\text{-}SCH_2CCH)_2(CO)_6]$ (**36**) was then 'clicked' into a metallopolymer coating on the surface of the gold electrode. IR, thermo-gravimetric analysis (TGA), and cyclic voltammetry in acetonitrile all provide evidence for the incorporation of [2Fe-2S] systems into the polymer film on the electrode. Cyclic voltammetry showed a broad reduction shifted to about 400 mV positive of the reduction events of **36** and repetitive scanning was found to slowly deplete the electrochemical response of the system, with *ca.* 25% of current lost after 20 scans. Catalysis was not demonstrated with this electrode, and systems specific to gold electrodes are not particularly attractive for practical applications.

The most recent example of a main-chain metallopolymer system comes from the laboratory of Liu in 2016[106] who used **36** as a monomer unit in an azide-alkyne 'click' polymerization with 2,6-bis(azidomethyl)pyridine, bis(2-azidoethyl)amine, or sodium bis(2-azidoethyl)glycinate to generate polymers **37**, **38**, and **39** respectively. A [2Fe-2S] moiety was present in each repeating unit of the polymer, and various potential proton transport moieties (pyridine, diethylamine, and a carboxylate) were present in the azide unit. Solution electrochemistry in DMSO showed all metallopolymers were electrocatalytically active, but the carboxylate containing polymer was found to be unstable, decomposing rapidly in DMSO solution. However, once assembled into membrane electrodes using polyethyleneimine-reduced graphene oxide (PEI-RGO) and Nafion, the carboxylate containing polymer was stable and achieved catalytic current densities as high as 2.08 mA cm^{-2} in extremely dilute aqueous acetic acid. This work demonstrated it was possible to improve catalysis by modifying the outer coordination sphere of the [2Fe-2S] system via incorporation of functional groups capable of proton transport in the macromolecular support. Unfortunately, like most

membrane electrodes, the system suffers from a significant loss of activity after successive cycling of the electrode.

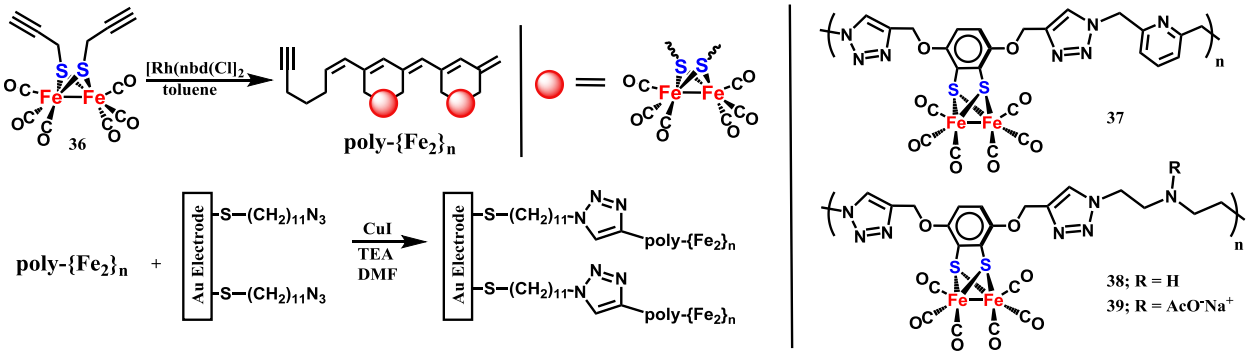

Figure 1.6. Synthesis of **Poly-{Fe2}n** from (**36**) and subsequent attachment to an azide functionalized electrode via azide-alkyne 'click' chemistry. Structure of main chain metallopolymer systems (**37-39**) synthesized by Liu et al.

II. Side Chain Metallopolymers

Pickett *et al.* reported the first metallopolymers incorporating [2Fe-2S] complexes.[90] They demonstrated control over the structure of the incorporated diiron system by changing the ratio of comonomers in the electropolymer films. Electrocatalytic response was demonstrated by a homopolymer of pyrrole N-ethypropionate-[$Fe_2S_3(CO)_5$] (**40**) with a current density of *ca.* 0.25 mA cm^{-2} with 16 mM 2,6-dimethylpyridium in acetonitrile. This study was the first proof of concept demonstrating it was possible to incorporate [2Fe-2S] complexes into electropolymer films on inexpensive carbon electrodes, and that such assemblies can electrocatalytically reduce protons to hydrogen gas. The same laboratory also demonstrated the synthesis and characterization of an elaborate polypyrrole system which incorporates both the [2Fe-2] cluster (**41**) but also linked it to a $[Fe_4S_4]^{2+}$-cubane assembly in a film on an electrode surface.[107] The film is characterized by IR and CV, but catalysis was not demonstrated.

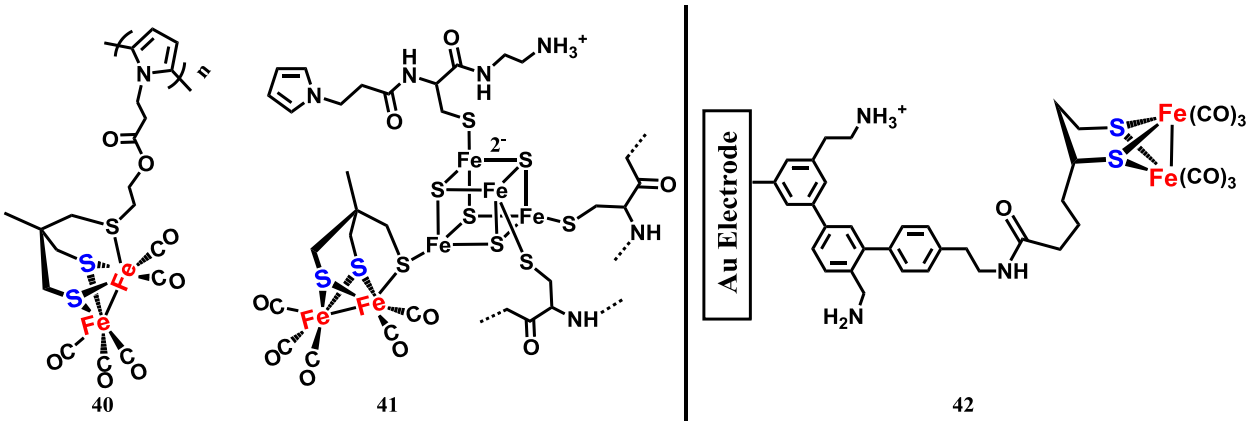

Figure 1.7. Structure of polypyrrole-*g*-$Fe_2S_3(CO)_5$ (**40**), and a 'complete' model [FeFe]-hydrogenase mimic (**41**) which includes a $[4Fe\text{-}4S]^{2-}$ cluster attached via the apical sulfur ligand as in the parent enzyme. **42** shows one possible bonding mode for a [(μ-pdt)$Fe_2(CO)_6$] complex attached to a polyphenyleneamine coated gold electrode via amide bond linkage.

In 2010 Artero and Jousselme decorated gold and glassy carbon electrodes with a polyphenyleneamine layer, and a PDT complex was attached via amide bond formation to a five-carbon flexible linker attached to the 1-positon of the three carbon bridge.[108] This functional electrode (**42**) demonstrated a maximum current density of 3.8 mA.cm^{-2} at a formal potential of -1.2 V vs $Ag/AgClO_4$ with 15 equivalents of HBF_4, but the activity was completely lost after the first scan, indicating the as-formed catalyst layer is not stable to the potentials required for HER.

Subsequently, an open system bearing an alkyne (**43**) was polymerized with $WCl_6/SnPh_4$ to generate a polyacetylene backbone with pendant $Fe_2S_2(CO)_6$ groups (**44**) which has two dominant confirmations, a *cis*-cisoidal and *trans*-cisoidal confirmation, of which the *cis*-transoidal is believed to dominate in both $CDCl_3$ solution (supported by ^{1}H NMR spectroscopy) and on the surface of vitreous carbon electrode (as evidenced by the observation of evenly spaced linear arrays via TEM). A film electrode was spin coated onto vitreous carbon electrodes, and the addition of MWCNTs increased catalytic current density by improving the conductivity of the film electrode.[96] However, like most functional electrodes, these film electrodes are significantly degraded by cycling to catalytically active potentials. This electrode is particularly sensitive, with 50% of activity lost after the first scan, and almost all activity lost after 70 scans.

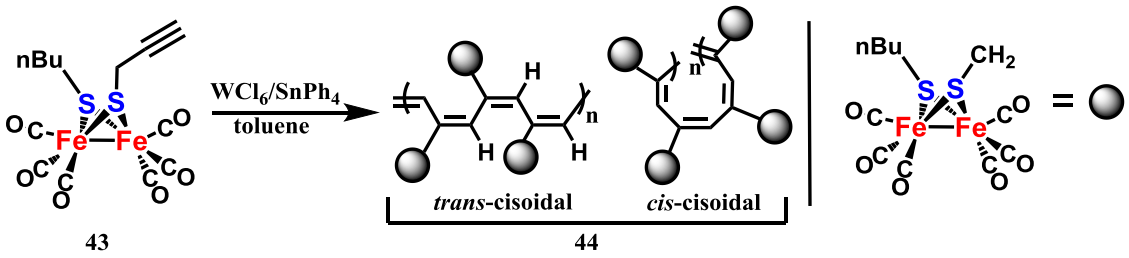

Figure 1.8. Synthesis of [2Fe-2S]-polyene metallopolymer (**44**) (which predominately exists in the *trans*-cisoidal confirmation) from monomer (**43**).

In 2011, Xiaoming Liu *et al.* reduced $Fe_2S_2(CO)_6$ with $LiHBEt_3$ to generate the open dithiolate $[Fe_2S_2(CO)_6]^{2-}$ which is then reacted with polyvinyl chloride (PVC), which generates an inseparable mixture of forms of [2Fe-2S] functionalized PVC – one intrachain form, one crosslinking interchain form, and an incomplete intrachain form which reacts with the quenching agent, MeI. This mixture was named **PVC-Fe-A**.[109] They also functionalized PVC with sodium azide, then the azide functionalized PVC polymer was 'clicked' with diyne complex (**36**). This was found to generate both inter- and intrachain functionalized [2Fe-2S] systems, however they also found one of the carbonyl groups was substituted off by a nitrogen in the 3 – nitrogen in the resulting 1,2,3-triazole ring, this mixture is named **PVC-Fe-B**. In their final system, they used **43** instead of **36** so that only one form of metallopolymer would result from the 'click' reaction with PVC-N_3. As hoped, this gave one main product, **PVC-Fe-C** (**45**) in which one of the carbonyl ligands has again been substituted by the 3 – nitrogen on the 1,2,3 – triazole ring formed in the azide-alkyne click reaction. All of the polymers exhibited poor solubility in organic solvents which inhibited good film formation, and were not natively conductive, but the addition of Nafion (to improve film formation) and MWCNTs (to improve conductivity) allowed acceptable film electrodes of 10-30 μm to be spin coated onto vitreous carbon electrodes. Despite good current densities (> 3 mA cm^{-2}) obtained from films of **PVC-Fe-C** (**45**) in dilute acetic acid in acetonitrile, the activity is almost

fully lost after the first scan, even though IR showed 40% of Fe-CO intensity is retained after 30 scans.

Two years later, the same laboratory published a study on a series of ten polyethyleneimine (PEI) polymers which were functionalized with diphenylphosphine. The phosphine functionalized polymer (PEI-P) was refluxed in THF with $Fe_2S_2(CO)_6$ **3** or **32** to displace a CO ligand and anchor the diiron complex to the polymer chain, generating PEI-P-Fe.[110] Solution electrochemisty in DMF demonstrated better performance with **3** than **32**. The system was improved by increasing the length and flexibility of the alkyl-linker attaching the phosphorus ligand to the polymer chain. The best performance was achieved via inclusion of carboxylate functionalities on the PEI chain. This demonstrated a major improvement in catalytic activity *from the same [2Fe-2S] cluster* by modulating functional groups macromolecular support.

Weigand and Shubert *et al.* reported the first demonstration of a controlled radical polymerization with a diiron system in 2013.[111] Three styrenic [2Fe-2S] monomers [(μ-S-CH_2-Sty)$_2Fe_2(CO)_6$] (**46**), [(μ-pdt-CH_2-Sty)$Fe_2(CO)_6$] (**47**), and [(μ-adt-CH_2-Sty)$Fe_2(CO)_6$] (**48**) were synthesized and copolymerized with 'naked' styrene monomers using reversible addition-fragmentation transfer polymerization (RAFT) with a maximum incorporation of 11% [2Fe-2S] monomer, though lower loadings (0.5-4%) were more practical as the [2Fe-2S] system was found to slow the rate of polymerization, and too many diiron centers on in the polymer would increase the likelihood of two nearby sites forming catalytically inactive Fe_xS_y clusters. Interestingly, attempts to co-polymerize styrene with the nitogen containing monomer (**48**) failed under all polymerization conditions attempted. Retention of the diiron system after exposure to the radical conditions of RAFT polymerization was proven using IR of the Fe-CO stretching frequencies as well as size exclusion chromatography (SEC) coupled to a 460 nm UV-Vis detector – a wavelength characteristic of the [2Fe-2S] system but not polystyrene. The living nature of the polymerization was demonstrated by chain extension of macroinitiators to form block copolymers to increase the molecular weight from $M_{n,SEC}$ = 2800 g mol^{-1} to $M_{n,SEC}$ = 6000 g mol^{-1}.

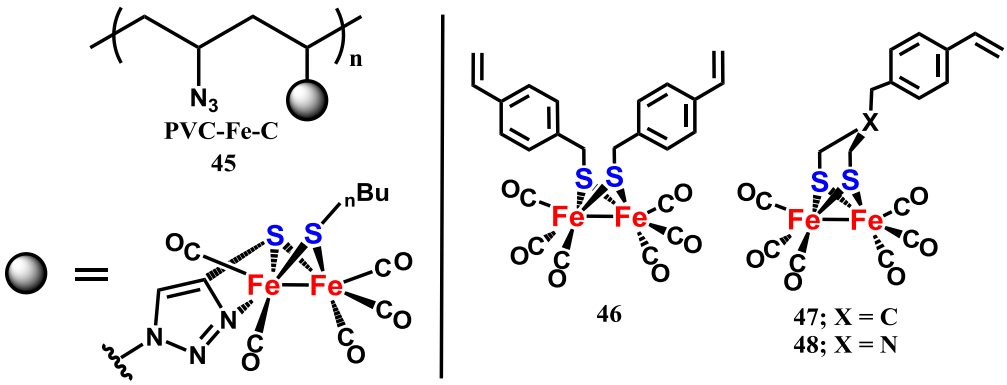

Figure 1.9. . Structure of side chain metallopolymer PVC-C (**45**) and styrenic-[2Fe-2S] monomers (**46-48**) used in reversible addition-fragment transfer (RAFT) polymerization with styrene to generate styrenic metallopolymers.

The *r*-poly(styrene)-*g*-[2Fe-2S] (poly(Sty)-*g*-[2Fe-2S]) polymers demonstrated electrocatalytic behavior in DCM and DMF upon the addition of acetic acid, but the catalysis was inhibited in the metallopolymers relative to the monomers. This is likely due to inhibition of electron transfer to the [2Fe-2S] sites and the relatively non-polar polystyrene matrix inhibiting the polar substrate (AcOH) from accessing the diiron sites. A slower diffusion rate (due to a much

larger radius of gyration) may also be at play in the reduced electrocatalytic activity. Despite the electrochemical results, this important work demonstrated the ability to use controlled radical polymerization (CRP) methods with an [FeFe]-hydrogenase mimic without either a) destroying or decomposing the [2Fe-2S] system under radical conditions or b) disrupting the delicate balance of reaction rates that CRP methods rely on. Future systems may seek to apply such techniques to incorporate the [2Fe-2S] system into more advantageous polymer architectures.

One of the most impressive photocatalytic [FeFe]-hydrogen systems come from the laboratory of Wu *et al*. Their first venture into [2Fe-2S] photocatalysts was a (μ-pdt)$Fe_2(CO)_5L$ system with a CN-Ph-yne-Ph ligand substitution (**49**).[112] This ligand was used to anchor a benzene ring bearing three short polyethyleneglycol chains to impart water solubility. Using CdTe quantum dots as the photoelectron donor rather than a molecular photosensitizer, a very respectable TON of 505 was obtained in pH 4 ascorbic acid (H_2A) buffer under optimized conditions. Subsequently, they used the same ligand bonding motif to graft the iron system onto poly(acrylic acid) (PAA) via amide bond formation between PAA and **50**.[113] The resulting **PAA-*g*-[2Fe-2S]** (**51**) system achieved a TON in excess of 27,135 from an aqueous pH 4 ascorbic acid solution using CdSe quantum dots as a photosensitizer – easily the best [2Fe-2S] based photocatalytic system at the time of publication. The dramatic increase in activity is attributed to the PAA support which serves three roles in this system. The first is to bring the hydrophobic [2Fe-2S] system into water. Secondly, PAA interacts with the Cd atoms on the surface of the dots and reduces the formation of QD aggregates which is promoted by the mildly acidic condition. Preventing aggregate formation is desirable as the aggregates efficiently quench excited states, preventing electron transfer to the Fe system. Finally, the PAA chains hold the iron system in close proximity to the electron donor species, ascorbate (HA^-) improving the electron transfer rate (measured at a blistering $k_{et} = 6.15 \times 10^{12}\ M^{-1}\ s^{-1}$). A pH study was also conducted and concluded that pH 4 is optimal for this photocatalytic system, a finding that seems to be general to photocatalytic systems which use ascorbic acid buffers because the equilibrium is fairly balanced, giving similar concentrations of [H_2A] and [HA^-], both of which play an important role in the catalytic cycle (H_2A as acid, HA^- as SD). Interestingly, *the best H_2 production efficiency is obtained from the polymer with the lowest grafting density of [2Fe-2S] systems*, while the highest grafting density results in a polymer system that is barely active. This trend points to deactivation via clustering or association of reduced [2Fe-2S] active sites when too many are incorporated into the polymer chain.

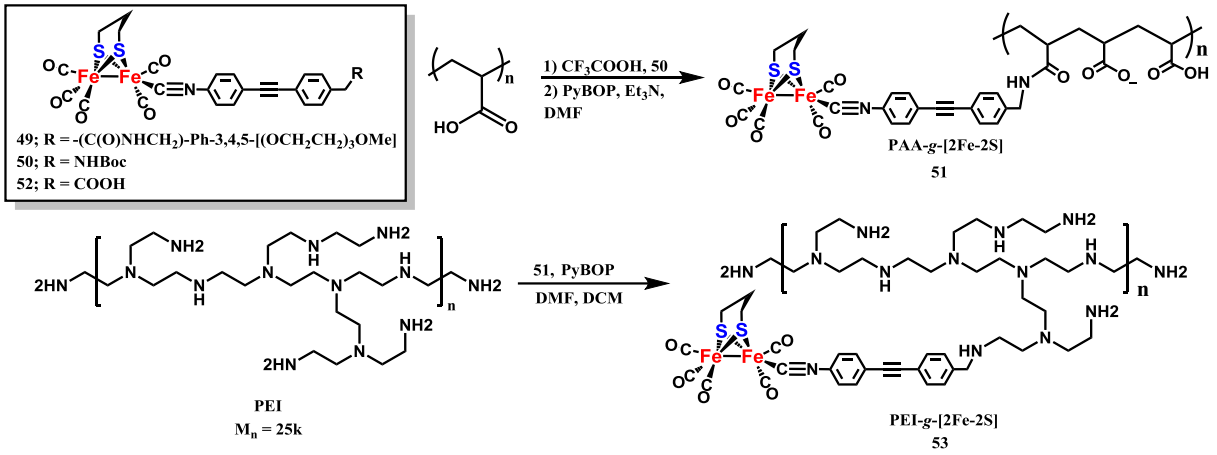

Figure 1.10. Synthesis and structure of **PAA-*g*-[2Fe-2S]** (**51**) and **PEI-*g*-[2Fe-2S]** (**53**). Water soluble small molecule [2Fe-2S] compound (**49**) is shown for comparison with the metallopolymer systems. Polyethylene imine (PEI, **50**) is not only as a synthetic precursor, but also plays a key role in a mixed photocatalytic system with (**51**)/PEI.

To follow up their groundbreaking **PAA-*g*-[2Fe-2S]** paper, Wu *et al.* chose to interrogate the activity of a diiron system grafted to a polymer rich in amines rather than carboxylic acid functionalities.[88] The amine rich polymer polyethyleneimine (PEI) was chosen and using a carboxylic acid functionalized **52**, PEI-*g*-[2Fe-2S] (**53**) was synthesized via amide bond formation between the amine side chains and –COOH group on **52**. This gave a metallopolymer with [2Fe-2S] moieties grafted to side chains along the PEI backbone in a method very similar to that employed in the synthesis of **PAA-*g*-[2Fe-2S]**, (**51**). The resulting photocatalytic system reached TONs on the order of 10,000, and did so at pH 6.5 instead of pH 4-5, where most photocatalytic systems utilizing ascorbic acid/ascorbate buffer find peak activity. This indicates involvement of the polymer chain in proton transport, as the amine containing polymer (which will have higher pKa functional groups) reaches peak performance 2.5 pH units higher than the polymer rich in carboxylic acid groups. In fact, **PEI-*g*-[2Fe-2S]** (**53**) operates more efficiently at pH 9.5 than pH 4 – while the **PAA-*g*-[2Fe-2S]** (**51**) system has loses almost all of its activity by increasing the pH from 4 to 5.1. Overall, the self-buffering capacity of the PEI system seems to improve its stability and function across wide range of pH values, with some activity retained at pH values as high as 11.5.

Most recently, a combined system that leverages the benefits of both the PEI and PAA polymers has demonstrated the highest photocatalytic TON reported thus far. The self-assembled photocatalytic system consisting of PEI added to a solution of **PAA-*g*-[2Fe-2S]** (**51**) and CdSe quantum outperforms all other reported [2Fe-2S] photocatalytic mimics.[46] Zeta potential measurements showed zeta potential of the surface of the quantum dots changed from -8.7 mV to +25.7 mV after the addition of PEI to a dispersed solution of CdSe QDs **and PAA-*g*-[2Fe-2S]** (**51**) in pH 4.1 ascorbate buffer. At this pH, PEI is heavily protonated, while the PAA chain bears negatively charged carboxylates. Columbic attraction between the two polymer chains results in a close chain-chain interaction with PEI now largely on the outside of the quantum dot. Subsequent to this association, the potential of the surface of the QDs is positively charged due to the heavily protonated, polycationic PEI, and the positively charged surface encourages close association of HA^- molecules (the electron donor), which increases the rate of hole trapping in the CdSe quantum dots and reduces photo-corrosion. Indeed, the rate of hole transfer is increased 30-fold by the addition of PEI. When run at pH 4.1, the

system achieved a TON of 83,600 over 28 hours– the highest reported TON for a photocatalytic [2Fe-2S] system of any kind.

III. Single Active Site Metallopolymers

The first single active site [2Fe-2S]-macromolecular supported system came from Li *et al.* who constructed a benzyl-ether based dendrimer around the $Fe_2S_2(CO)_6$ core, Hy-$G_{1\text{-}4}$.[36] The dendrimers architecture guaranteed a single active site per dendrimer, the steric bulk of which should help shut down deactivating associative mechanisms. These dendrimer catalysts were then used in a photocatalytic system in 9:1 acetone/water with an $Ir(ppy)_2(bpy)^{2+}$ photosensitizer and triethylamine as a sacrificial electron donor. Water was the only proton source, and extremely low catalyst loadings (1 µM) are possible. The charge separated state lifetime was found to increase with increasing dendrimer generations from 27.2 µs for G_1 to 86.3 µs for G_4. As in the **P-NB/12** micelle system, thermodynamic calculations indicated the $Ir(ppy)_2(bpy)^+$ photosensitizer must be reduced by TEA to form the active reductant $Ir(ppy)_2(bpy)$. The resulting Fe^IFe^0 species must then undergo protonation to form an $Fe^{II}Fe^I$-H species before a second reduction even can take place. Li's dendrimer system displayed the highest quantum yields reported at the time for a [2Fe-2S] based photocatalytic system, increasing from 18% to 28% over the G_1-G_4 series. These effects are thought to be responsible for the increase in TON from 18,100 for G_1 to 22,200 for G_4, a value competitive with the **PAA-*g*-[2Fe-2S]** system which was published contemporaneously. However, incompatibility with purely aqueous systems, use of an expensive iridium-based photosensitizer, and the tedious stepwise synthesis of high generation dendrimers which limits scalability all represent major drawbacks to the dendrimer approach.

One of the most recent [2Fe-2S] metallopolymer systems has taken a new approach by attaching only a single [2Fe-2S] moiety to a polymer chain via chain-end functionalization to generate (**55**).[114] The polymer chain was designed with pendant anthracene moieties which undergo a (4 + 4) photo-promoted interchain cyclization with another anthracene to contract the polymer into a single chain nanoparticle (SCNP) via irradiation with 350 nm light. The advantages of this metallopolymer design is total site isolation of the diiron site, which protects it from associative deactivation mechanisms, in a macromolecular support that is reminiscent of the single active site buried in the protein support of the metalloenzyme. Unfortunately, the use of 350 nm light likely decomposes the [2Fe-2S] sites via decarbonylation, and catalysis is not demonstrated with the SCNP system.

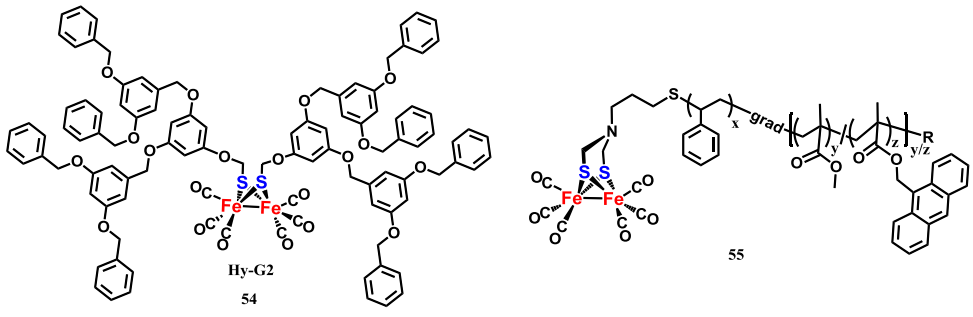

Figure 1.11. Structure of second generation Frechét type [2Fe-2S] dendrimer Hy-G2 (**54**) and [2Fe-2S]-polystyrene-*grad*-PMMA/AMMA metallopolymer (**55**) before folding into a single chain nanoparticle.

Table 1.3. Catalytic figures of merit for selected functionalized electrode systems. All electrode potentials have been converted to values vs SHE for ease of comparison, and all current values converted to current density using the geometric area of the electrode used. E^{o}_{IPc} is the potential at which peak catalytic current was observed under optimized conditions in a cyclic voltammogram (CV) at a given scan rate, v, under given in the conditions column. Overpotential (η) is given as an absolute value calculated from the half wave potential ($E_{1/2}$) of the catalytic wave in a CV. In many cases, potential values were not explicitly given and had to be extracted from figures. Despite considerable care in this process, a small error (no more than 50 mV) may be present in the numbers presented here. When considering the reported TOF, the calculation method has been indicated where [a] used the Dubois Ic/Ip method, [b] used the Delahey method[74], and [c] used foot of the wave analysis (FOWA) described by Constentin and Savéant.[115] [d] used a unique monolayer Langmuir adsorption model which assumed complete, close packed surface coverage based similar to a method reported by Long and Chang.[116] [a] TON is given in units mol H_2 mol $^{-1}$ catalyst. All potentials given vs SHE.

[2Fe-2S]	Support	J_{max} (mA cm^{-2})	E^{0}_{IPc} (V)	$E_{1/2}$ (V)	η (V)	TOF (s^{-1})	TON[a]	η† (V)	V_{hold} (V)	FY (%)	Conditions	Ref
21	SDS	-0.5	--	--	0.34	[a]2600	52	--	-0.66	100	AcOH (aq) pH 3	**[117]**
22	SDS	-0.26	-0.68	-0.59	0.37	[b]4600	23	--	-0.69	100	HCl (aq) pH 3, 0.1 M NaCl	**[118]**
3	PEI	-7.6	-1.74	-1.44	0.35	--	--	--	--	--	DMF/AcOH	**[110]**
12	β-CyD	-0.45	-1.25	-1.10	0.59	---	--	--	--	--	0.01 M KCl (aq)	**[67]**
57	PMMA	-2.32	-1.62	-1.36	0.44	[a]22000	<10	--	-1.26	--	AcOH in ACN	**[12]**
59	P(OEGMA)	-2.67	-1.29	-1.16	0.75	[c]5000	--	0.7	--	--	pH 7.0 phosphate buffer, 1 M	**[45]**
58	PDMAEMA	-70±3	-1.29	-1.13	0.69	[d]250000	40,000 ±20,000	0.33	-0.95	100	pH 7.0 tris buffer 1 M	**[12]**

Recent work in our laboratory has focused on developing a versatile, modular synthetic method that enables the synthesis of metallopolymers with one [2Fe-2S] active site per chain in which water solubility, aerobic stability, and electrocatalytic HER rates can be enhanced by tuning the macromolecular support. Taking lessons from the preceding work, we believe a modular approach is crucial, as it allows screening of many different polymer supports with minimal synthetic development, as opposed to the synthesis of [2Fe-2S]-monomers, which has been the dominant approach to [2Fe-2S]-metallopolymers up to now. Using the design approach a metallopolymer catalyst **PDMAEMA-*g*-[2Fe-2S]** (**58**) has demonstrated electrocatalytic HER rates an order of magnitude faster (250,000 s^{-1}) than the fastest rates reported for the enzyme have been achieved, as well as an overpotential requirement that is only *ca.* 0.1 V higher and an operational lifetime of up to six days (with a TON on the order of $4 \pm 2 \times 10^4$) and remarkable aerobic stability.[12] This metallopolymer is synthesized using atom transfer radical polymerization (ATRP), a controlled radical polymerization method never before applied to [2Fe-2S] systems.[119–121] Our approach is centered on an ATRP initiator functionalized with a [2Fe-2S] system (**56**), in contrast with previous efforts which have largely focused on using [2Fe-2S] functionalized monomers. This provides a variety of advantages including 1) inclusion of only one active site per chain – mimicking the enzyme structure and providing a bulky macromolecular structure which should inhibit aggregation or homoassociation of reduced iron sites, 2) the most expensive component of the polymerization, the [2Fe-2S] initiator, is nearly quantitatively incorporated into the final polymer whereas a [2Fe-2S]-monomer will be statistically incorporated into the polymer and a large amount lost in removal of unreacted monomer unless the polymerization is run to very high conversion, and 3) modularity – many metallopolymer systems can be synthesized simply by changing the monomer used in ATRP, as it has already been demonstrated that

catalytic activity of a [2Fe-2S] active site can be tuned via modulation of the macromolecular support in which it is bound.

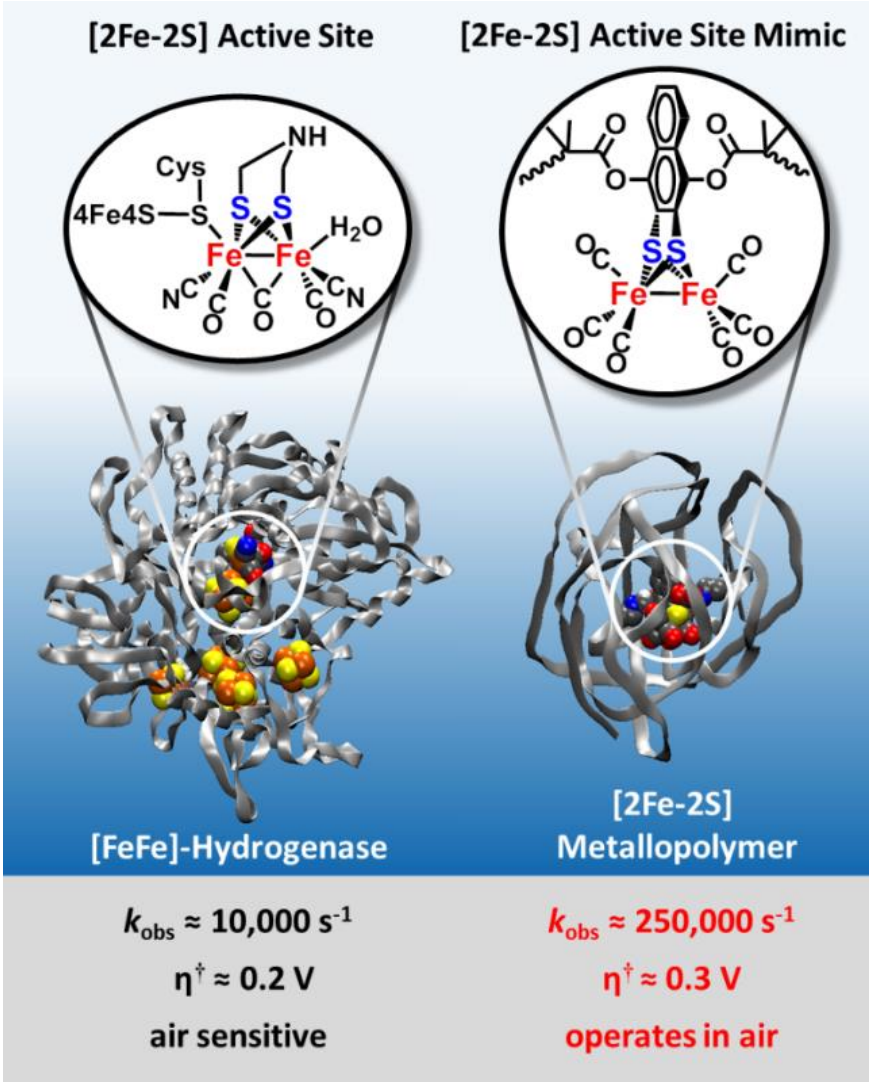

Scheme 1.1. Comparison of a new class of metallopolymer-[2Fe-2S] HER catalysts vs. [FeFe]-hydrogenase at the same scale.

Metallopolymer HER catalyst **PDMAEMA-*g*-[2Fe-2S]** (**58**) is remarkably faster than the enzyme AND is air stable at neutral pH. In addition, current densities greater than 300 mA cm^{-2} are achieved with 75 μM catalyst loading. $\eta^{\dagger}$ is the overpotential requirement to achieve an operating cell current density of 0.1 mA cm^{-2}.

The [FeFe]-hydrogenase structure[25] is taken from the deposit PDB ID 5LA3 in the Protein Data Bank (http://www.rcsb.org/).[26]

The molecular images were created with the Virtual Molecular Dynamics program[27] (http://www.ks.uiuc.edu/Research/vmd/) version 1.9.3.

The figure above is from [FeFe]-Hydrogenase Mimetic Metallopolymers with Exceptional Catalytic Activity for Hydrogen Production in Water Angew. Chem. Int. Ed. 2018 DOI: 10.1002/anie.201804661 (ASAP article) online only. Copyright Wiley-VCH Verlag GmbH & Co. KGaA. Reproduced with permission.

Using this method, a difunctional metalloinitiator for atom transfer radical polymerization (ATRP) bearing a [2Fe-2S] group (**56**) is used to initiate ATRP with methacrylic monomers to generate metallopolymers with controlled molecular weights and polydispersity. Methylmethacrylate (MMA), 2-(dimethylamino)ethyl methacrylate (DMAEMA), and oligo(ethylene glycol)methacrylate (OEGMA) to generate a **PMMA-*g*-[2Fe-2S]** (**57**), **PDMAEMA-*g*-[2Fe-2S]** (**58**), and **P(OEGMA)-*g*-[2Fe-2S]** (**59**), the latter two being water soluble. Polymer chains of approximately 5k MW grown symmetrically from both sides of the initiator, resulting in buried active site motif reminiscent of the enzyme. In our initial study, we found the amine containing **PDMAEMA-*g*-[2Fe-2S]** catalyst was a superior electrocatalyst in comparison with **PMMA-*g*-[2Fe-2S]** when operating in a 50 mM acetic acid solution in acetonitrile, operating with both higher current densities and lower overpotential. Moving into aqueous media, we found **PDMAEMA-*g*-[2Fe-2S]** (**58**) was a highly active electrocatalyst in neutral aqueous media. Operating in pH 7 buffer, we found current densities similar to those obtained from a cathodically conditioned planar platinum electrode, with an overpotential requirement[50,122] of only 0.33 V at a current density of 0.1 mA cm^{-2}, a similar Tafel slope to platinum and the current density matches that of platinum in the range from about 1 to 200 mA cm^{-2} with less than 0.2 V greater overpotential requirement than platinum.[12] Further, we were able to demonstrate under optimized conditions, the system retains full activity under aerobic conditions. The final figures of merit determined for this system were a TOF of 2.5 x 10^5 s^{-1}, a TON of 4 ± 2 x 10^4 mol H_2 mol^{-1} catalyst, an operational lifetime of six days, and an overpotential requirement only 0.13 V larger than that of an [FeFe]-hydrogenase enzyme on a TiO_2 electrode. In follow up work, we investigated the impact of the polymer architecture on the remarkable activity of this metallopolymer HER catalyst by comparison with another water soluble metallopolymer **P(OEGMA)-*g*-[2Fe-2S]** (**59**) which does not contain basic functional groups in the side chains, in contrast with the tertiary amines in the side chain of **PDMAEMA-*g*-[2Fe-2S]** (**58**) which have a pKa of approximately 8.3 in our conditions.[45] **P(OEGMA)-*g*-[2Fe-2S]** (**59**) was found to be an active electrocatalyst for HER, but operated with much lower current densities and higher overpotential in pH 7 sodium phosphate buffer. Random metallo(co)-polymers (**60**) and (**61**) were found to have intermediate activity which increased as the proportion of DMAEMA monomer was increased. Additionally, **P(OEGMA)-*g*-[2Fe-2S]** (**59**) was found to be completely inactive when operated under aerobic conditions, while the random copolymers operated with increasing efficiency under aerobic conditions as the percentage of DMAEMA units was increased. With a 50/50-feed ratio random copolymer (**60**) retaining approximately 60% of its catalytic efficiency under aerobic conditions, and a 70/30-feed ratio random copolymer (**61**) retaining approximately 80% under the same conditions. Taken together, these results demonstrate that the macromolecular support is *crucial* to the activity of the these systems, imparting not only water solubility, but also increasing the activity of the catalyst, reducing the overpotential requirement, and imparting aerobic stability to the **PDMAEMA-*g*-[2Fe-2S]** (**58**) system.

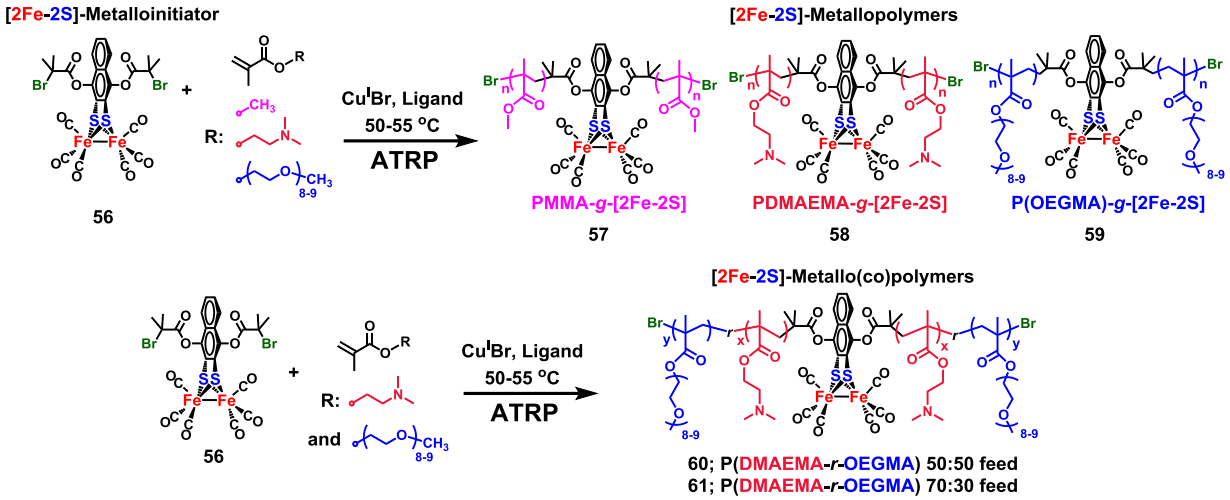

Figure 1.12. Metalloinitiator (**56**) and synthesis of homo-metallopolymers **PMMA-*g*-[2Fe-2S]** (**57**), **PDMAEMA-*g*-[2Fe-2S]** (**58**), and **P(OEGMA)-*g*-[2Fe-2S]** (**59**) as well as random metallo(co)polymers (**60**) and (**61**) via atom transfer radical polymerization (ATRP).

3. Summary and Outlook

Despite being a relatively new field of active research, with the bulk of work done in the last 5 years, supported [2Fe-2S] systems have already surpassed the stability and catalytic activity of small molecule [2Fe-2S] systems in both photo- and electrocatalytic hydrogen evolution. While it is generally accepted that enzymes will have superior activity to that of any mimic system, **PDMAEMA-*g*-[2Fe-2S]** (**58**) has shown superior electrocatalytic rates and oxygen resistance to that of any the enzyme which inspired it. While this is a surprising result, one must consider the different design goals of the enzyme developed for hydrogen production and metabolism in anaerobic bacteria, and those of an artificial HER catalyst for use in a water splitting device. Anaerobes have no need to evolve towards oxygen stability, while any practical HER catalyst will need to resist poisoning by O_2 due to the inevitability of some diffusion of oxygen across a membrane from the complementary oxygen evolution reaction. Further, the hydrogenase enzyme is evolved to work with chemical reductants (such as NADH, NADPH) rather than an electrode, and the rate may well have been tuned in consideration of other upstream or downstream metabolic events, or even to prevent hydrogen production from being too fast, which could lead to deformation of the membrane in which theses enzymes are bound.

It is clear a macromolecular support can provide myriad benefits beyond simple site isolation, water compatibility, or intramolecular stabilization of catalytic intermediates. In photo-HER systems such as **PAA-*g*-[2Fe-2S]** (**51**)/PEI and chitosan/(**11**) a charged macromolecular architecture ensure co-localization of electron donors to fill holes in the quantum dot photosensitizer, increasing the rate of hole filling which in turn suppresses back electron transfer. The role of charged macromolecular supports in electrocatalytic systems is less well understood, but it has been demonstrated in multiple systems (CA-PEI-**33** electrospun fibers, carboxylated azide-alkyne click polymer **39**, and **PDMAEMA-*g*-[2Fe-2S]** (**58**)) that the inclusion of basic moieties improve electrocatalytic performance, perhaps by improving proton transport to the active site.

While the activity achieved so far is impressive, the highest TONs achieved in both photo- and electrocatalytic systems are on the order of 10^4 with lifetimes on the order of several days.

These number which will need significant improvement before such catalysts can find large scale application in water splitting devices. For example, DOE projections for large scale hydrogen production assume replacement of the cell materials only once per seven years.[123] Mechanism of catalyst degradation, and how to circumvent these degradation processes, will be essential in progressing [2Fe-2S] catalysts towards practical application. One well known mechanism for degradation of small molecule [2Fe-2S] systems is likely at work in supported [2Fe-2S] systems as well. Loss of the most weakly bound, apical CO ligands creates reactive vacant sites on the iron atoms, and opens many possible degradation pathways such as Fe_xS_y cluster formation, or irreversible oxidation of the iron atoms to an Fe^{II} or Fe^{III} oxidation state. It would be wise to investigate supported systems in which these ligands are replaced with phosphines, cyanides or other more strongly bound ligands which may also have the advantage of being more stable at elevated temperatures. Another approach that should be considered is designing some sort of intramolecular stabilization of the primary ligands on the iron atoms, in much the same way as the polypeptide structure of the [FeFe]-hydrogenase enzyme stabilizes an otherwise quite unstable mixed valence active site.[124] Further, all of the highest preforming [2Fe-2S] catalytic systems have used soluble catalysts. This has the advantage of simplifying the study of the activity and mechanism of these systems, but complicates their use in practical devices. Solution based catalysts have the distinct disadvantage of requiring a costly recovery step (precipitation, dialysis, centrifugation, etc) to avoid being discarded with any waste solution. A much better option would be to use these materials to fabricate a heterogeneous catalyst by isolating the [2Fe-2S] material on the surface of an electrode or photovoltaic material. This would allow aqueous solutions to be flowed over the active catalyst and continuously replaced with fresh media, with no need for catalyst recycling. In photocatalytic systems, applying a mild potential to the photovoltaic material may also eliminate the need for a sacrificial electron donor – an unfortunate necessity in almost all photocatalytic systems to date. Immobilization of [2Fe-2S] materials on a surface may offer benefits to stability as well by completely inhibiting Fe_xS_y cluster formation by anchoring the diiron sites in place. Two serious concerns that should be kept in mind by researchers wishing to attempt such film systems are (1) substrate access *i.e.* using a swellable material so that water molecules and ions can still intercalate the film and interact with the diiron sites and (2) maintaining mechanical stability in a swellable film. As demonstrated by the cellulose acetate membrane electrodes balancing these two factors can be tricky, and bubble formation can degrade films that are not sufficiently robust due to being too porous. In electrocatalytic films, conductive doping agents such as carbon nanotubes or graphene oxide will also be required, however several systems have shown this is achievable and conductive dopants are well studied.

In conclusion, it has been demonstrated that, in the case of [FeFe]-hydrogenase mimics, small molecule organometallic chemistry is severely limited despite a long history of excellent research and hundreds of structural analogues. Taking further inspiration from nature and making more complete ‘artificial enzymes’ in which the active [2Fe-2S] sites are supported, stabilized, and enabled by a macromolecular architecture provides a fresh new approach to these promising systems which have seen a decrease in interest lately due to the seemingly intractability of several crucial flaws that have prevented the high levels of HER catalytic activity from being translated into useful, practical catalyst systems. Caution should be used in learning from the enzyme however, because as mentioned above it evolved to meet a different set of design goals than those of the artificial catalysts which seek to mimic its activity, and while the native enzyme likely has an essentially infinite TON until replaced or

repaired by the cell, when isolated on electrode surfaces and held at an operating potential the catalytic activity of the enzyme has been found to degrade over the course of mere hours. Accordingly, while the enzymes are a good source of inspiration, they should not be regarded as blueprints for the ideal catalyst. In just over ten years and less than one hundred examples, supported [2Fe-2S] systems have outstripped the performance of their small molecule predecessors with several systems achieving TONs on the order of 10^4, TOFs that far outpace that of the native catalyst, acceptably low overpotential requirements, function in neutral water, and exhibit a level of aerobic stability which has long eluded the fields of both small molecules and protein engineering. Further, the most impressive of these systems – the grafted metallopolymers - are easily scalable, processable, and tunable via the polymer architecture. The mechanism by which the macromolecular support enables such activity is not yet well understood and will certainly be an active area of debate in the coming years. The polymer chemistry used to develop these systems is rich and well understood and provides so many opportunities the hardest part for researchers in this area may be deciding which path to take. The future for these systems is practically bubbling over with opportunity to develop new solutions to the problem of practical, inexpensive, earth abundant HER catalysts.

Chapter 2 - Synthesis and Characterization of μ-3,4-dithiolato-oligothiophene Catalysts

Previous studies on [(μ-bdt)$Fe_2(CO)_6$] (**21**) (**Figure 2.1**) showed that the bridging hydride formed in the electrocatalytic cycle of **21** is not hydridic enough to react with another proton from acetic acid and form molecular hydrogen without the need for a third electron introduced at a more negative potential. The requirement to inject this third electron increases the overpotential of the catalyst. This inspired a follow-up study on **62** to see if a more electron rich, thiophene ring provided the [2Fe-2S] system with enough electron density to increase the basicity of the hydride intermediate. Studies carried out by Dr. Laura Stratton demonstrated via IR, PES, and cyclic voltammetry that the electronic structure, specifically the electron density on the iron centers, had not been significantly altered[125]. Undeterred, we chose to increase the chain length and electron richness of the thiophene ligand as it is well documented that increasing thiophene chain lengths increases their electron donor ability, reducing their electrochemical oxidation potential[126,127]. We envisioned two benefits to these larger, oligothiophene ligands. *1) Increase electron donation into the [2Fe-2S] system to increasing the electron density on the Fe centers* and *2) reducing the oxidation potential of the thiophene ligands may result in t a crossover at some sufficiently large thiophene chain which allows for electropolymerization of the thiophene ligands to generate [2Fe-2S]-metallopolymers without oxidation of the [2Fe-2S] system.* The two target molecules chosen are **63** – which features a 2,2'-5,5'-terthiophene ligand and **64** in which the thiophene rings on the 2,5-position of the central μ-thiophene ligand are 3,4-ethylenedioxythiophenes (EDOTs). EDOT was chosen because the 3,4-ethylenedioxy substituent adds electron density to the thiophene ring, and polymers of EDOT (called PEDOT) are well known electron donor materials for organic photovoltaic cells, so it was hoped that incorporating EDOT units would afford better electron donation to the iron center.

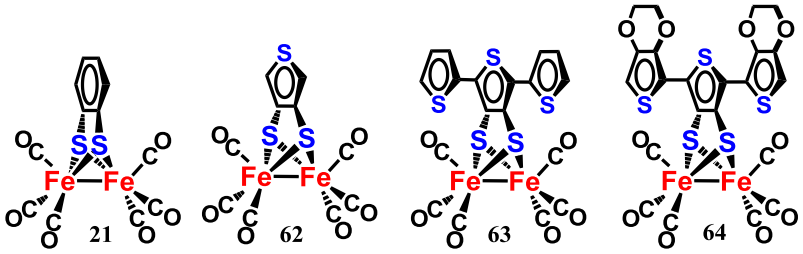

Figure 2.1. Structures of previously studied compound **21** and **62** as well as extended thiophene systems **63** and **64**.

Synthesis μ-3,4-dithiolato-oligothiophene Catalysts

Five small molecule thiophene catalysts were synthesized in this work. Catalyst system **62** was prepared from thiophene-3,4-dithiol by refluxing in THF with $Fe(CO)_5$, in the same method as reported for **21** (scheme 2.1).[128] To approach the extended systems, we initially envisioned a convergent synthesis of compounds **62**-**64**, first synthesizing a dibromo cross coupling 'core' thiophene **10** bearing a dithiocarbonate moiety bridging the 3,4 positions. Various thiophene derivatives could then be attached at the 2,5 positions via a transition metal mediated cross coupling reactions.

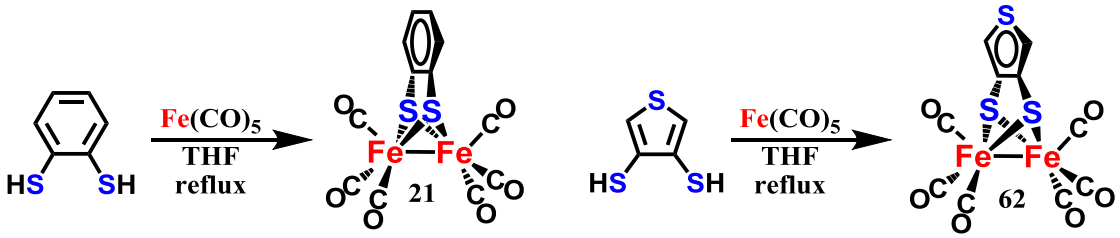

Scheme 2.1. Synthesis of [2Fe-2S] catalysts **21** and **62**.

Starting from methyl-ethyl ketone, reaction with bromine and potassium isopropyl xanthoate in the presence of K_2CO_3 produced **65** which was immediately cyclized under strong acid conditions to generate 2-propanol and dithiocarbonate **66** (see Scheme 2.2). Photo promoted radical bromination with NBS produced **67** which was then cyclized with Na_2S to give **68** as an intermediate before aromatization was achieved with DDQ to give thiophene-3,4-dithiocarbonate **69**. Bromination of **69** with elemental bromine went in very high yields to give the target cross coupling reagent, **70.** Unfortunately, once the dithiocarbonate core **70** was in hand, we were unable to achieve any carbon-carbon bond formation from Suzuki, Stille, or Kumada coupling with a wide variety of catalysts, additives, solvents, and conditions. In several cases using $Pd(PPh_3)_4$ catalyst, we were recovered primarily **69** the hydrogen substituted adduct of **70** This indicated an oxidative addition to the catalyst likely took place to cleave the C-Br bonds, but did not result in coupling with either Stille or Suzuki reagents.[129–131] Due to a lack of success in achieving the desired C-C bond forming reactions, this route was eventually abandoned in favor of a procedure published by Skabara and coworkers[132,133].

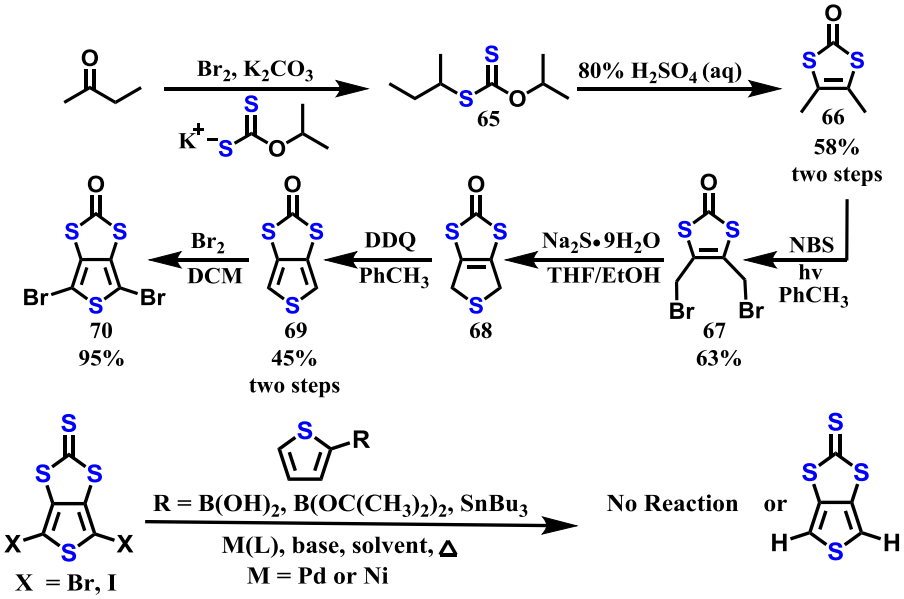

Scheme 2.2. Synthesis of cross coupling partner **70** and general scheme of the convergent synthetic route initially envisioned for synthesis of oligothiophene ligands.

As shown in Scheme 2.3, vinylene trithiocarbonate (VTC, **71**) is deprotonated with LDA at -78 °C. The anion is then quenched with a formyl thiophene reagent. This stepwise process is repeated and the desired diol product is obtained upon aqueous workup. VTC is commercially available, but expensive (ca. $100/g) and better yields were obtained with material easily made in house according to a procedure outlined by Melby and coworkers[134]

The formyl thiophene reagents **12a** and **12b** could be synthesized in one step from Vilsmeier-Haack formylation in refluxing 1,2-dichloroethane, which gave quantitative yields of both compounds. The crude material is oxidized with MnO_2 deposited on silica gel[135]. We had great difficulty reproducing the efficient oxidation reported by Skabara who reports quantitative conversion of the diol intermediate to diketone **13** in 2 minutes. In our hands however, the reaction was far less efficient, generally resulting in 10-20% yields, at both short and long reaction times. Several alternative oxidation methods including DMP, Swern, PDC, PCC, Oppenheimer, etc. resulted in decomposition of the starting material. Further, we found fresh MnO_2 is required for reaction, with old material giving little to no product. It is therefore necessary to prepare a new batch and activate it for 18-24 hours at 125 °C each time the reaction is performed. The major side product of the reaction is the mono-alcohol, indicating that the second deprotonation is not proceeding as desired. Longer reaction times with the second equivalent of LDA have not been found to help and stronger bases, such as alkyl lithiums have been found to decompose the starting material, likely via nucleophilic attack on the thiocarbonyl carbon. Isolation of the mono-alcohol followed by treatment with 2 equivalents of LDA followed by quenching with a formyl thiophene has also failed to produce the desired diol. If further optimization was to be attempted, trapping the first alkoxide produced with a silicon based protecting group such as TBDPS-Cl may stabilize the compound enough to prevent decomposition, and the second deprotonation should proceed more easily if the first anion is trapped. Subsequent to the second addition, the protected diol could be deprotected with KF in situ in the presence of an oxidizing agent. This route was not explored however due to a lack of interest in scaling the synthesis beyond what was already easily achievable.

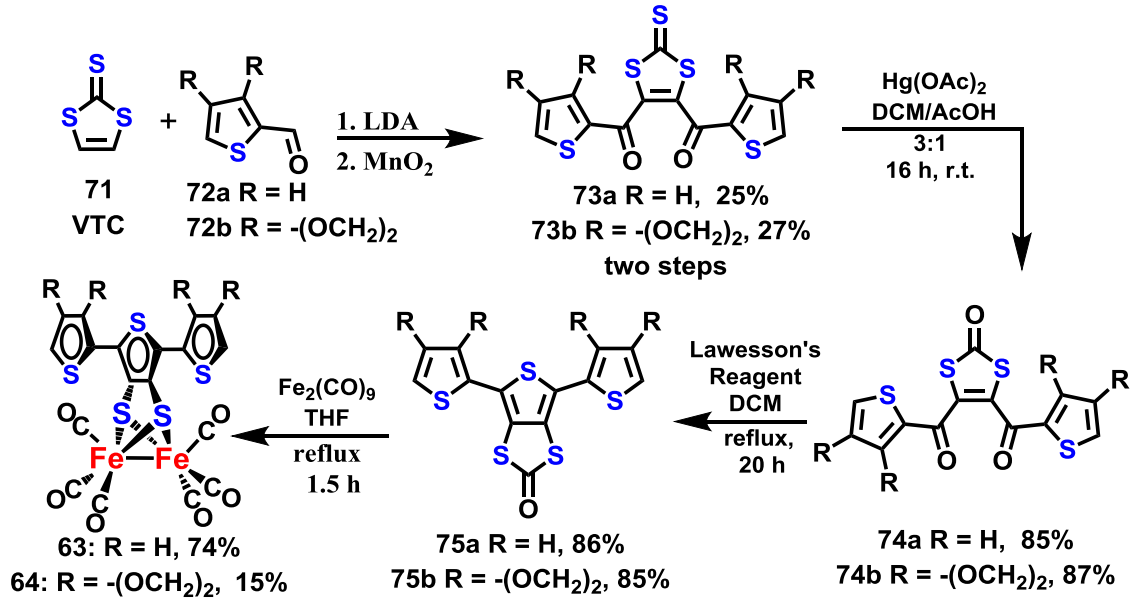

Scheme 2.3. Full synthetic route to oligothiophene ligands **75a**, **75b** and their respective [2Fe-2S] complexes **63** and **64**. It should be noted that the addition of the formyl thiophene reagent in step one happens sequentially, not concomitantly

Once in hand, the 1,4-diketone system could be cyclized into a thiophene ring with the use of P_4S_{10} in dioxane at elevated temperatures, but yields were low – only 39% for **75b**. We have improved upon this reaction by using Lawesson's Reagent in refluxing DCM, which provides numerous advantages. Chief among these is the increased hydrolytic stability of Lawesson's Reagent when compared with P_4S_{10} which reacts violently with water to produce highly toxic

H_2S and makes handling the reagent outside of a drybox difficult. Additionally, the reaction gives improved yields, likely due to the lower temperature (42 ˚C vs 90 ˚C) which does not degrade the starting material. The cyclized terthiophene complexes **75a** and **75b** have very low solubility, especially in polar solvents. This made purification by column chromatography impractical on any useful scale. Crude NMR seemed to indicate the main side product was the aryl phosphoxide formed by the oxidation of Lawesson's reagent. This compound had limited solubility in methanol, in which both **75a** and **75b** were found to be completely insoluble. Soxhlet extraction with methanol was found to be the optimal purification method and resulted in ligands that were completely pure as analyzed on ^{1}H NMR (see appendix A for spectra).

Initially, the trithiocarbonate compound analogue of **75** was synthesized. Direct reaction with diiron nonacarbonyl gives the desired product as the major product, but forms several side products which can only be removed by slow recrystallization to obtain **64** in high purity. This is consistent with published studies on the reaction of thioketones with $Fe_2(CO)_9$[136] which have shown a large number of viable side reactions exist. Hydrolyzing the trithiocarbonate to a dithiocarbonate using $Hg(OAc)_2$ and subsequent reaction with $Fe_2(CO)_9$ yields a pure, crystalline product after a quick column purification, albeit in very slightly reduced yields due to the two step nature of the process. In consideration of the low solubility of the fully cyclized, terthiophene species, we chose to move this reaction to an earlier phase of the synthesis – before the cyclization with Lawesson's reagent – to see if we could improve yields, and retain the C=O bond in the cyclization reaction, which is a concern because Lawessons reagent has primarily been used for the thiation of carbonyl complexes[137].

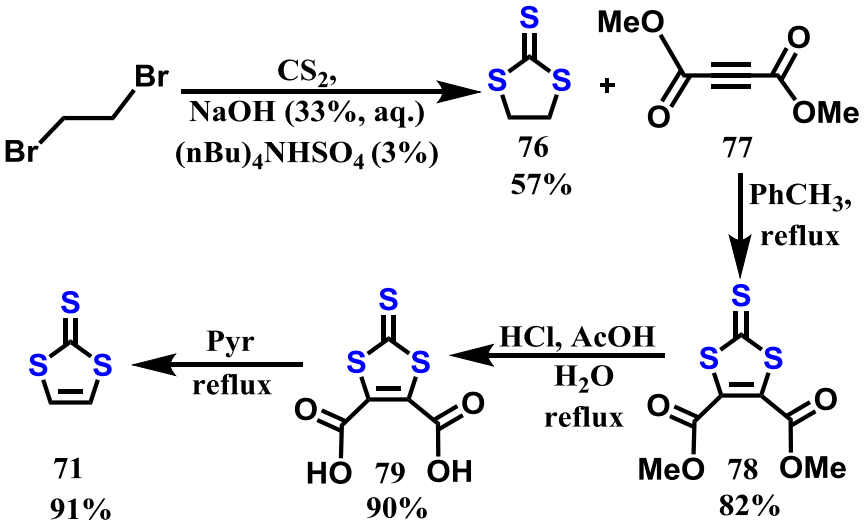

Scheme 2.4. Four step synthesis of starting material vinylene trithiocarbonate **71** from inexpensive starting materials.

As mentioned previously once we determined this synthetic route was viable, we investigated the synthesis of vinylene trithiocarbonate as it was cost prohibitive (~$100/gram) as a starting material due in part to the low yielding first reaction, and the desire to pursue as many extended systems as possible. Additionally, we found the commercially available reagent to be of low quality and were concerned it was negatively impacting our yields. Fortunately, a high yielding, four step preparation from very inexpensive materials was developed using a literature preparation of ethylene trithiocarbonate from 1,2-dibromoethane. [134] A solution of 33% KOH is stirred with an equal volume of carbon disulfide and a small amount of phase

transfer catalyst. A blood red color forms at the interface, which the authors assert is trithiocarbonate dianion which then performs an intermolecular attack on 1,2-dibromoethane, followed by a second intramolecular attack to form ethylene trithiocarbonate **76**. Yields have been steadily increased with scale, as very slow addition of 1,2-dibromoethane is key to increased yield and becomes easier on large scale. Slow addition of the electrophile is important because after the first intermolecular attack of 1,2-dibromoethane, a second intramolecular attack is required to form the ethylene trithiocarbonate ring **76**. By very slowly dropping the 1,2-dibromoethane into the dianion solution the concentration of 1,2-dibromoethane is low at any given point, promoting intramolecular attack to give the ring over intermolecular attack to yield oligomeric and polymeric products. Subsequent installation of the double bond by reaction of ethylene trithiocarbonate with dimethyl acetylenedicarboxylate **77** to provide diester **78**, which was hydrolyzed in aqueous acid to give the diacid **79**, subsequent decarboxylation in refluxing pyridine gives the final product vinylene trithiocarbonate **71**[134]. This preparation was found to be scalable to yield **71** on a scale of tens of grams and the synthetic method was amenable to preparation by relatively inexperienced undergraduate research assistants.

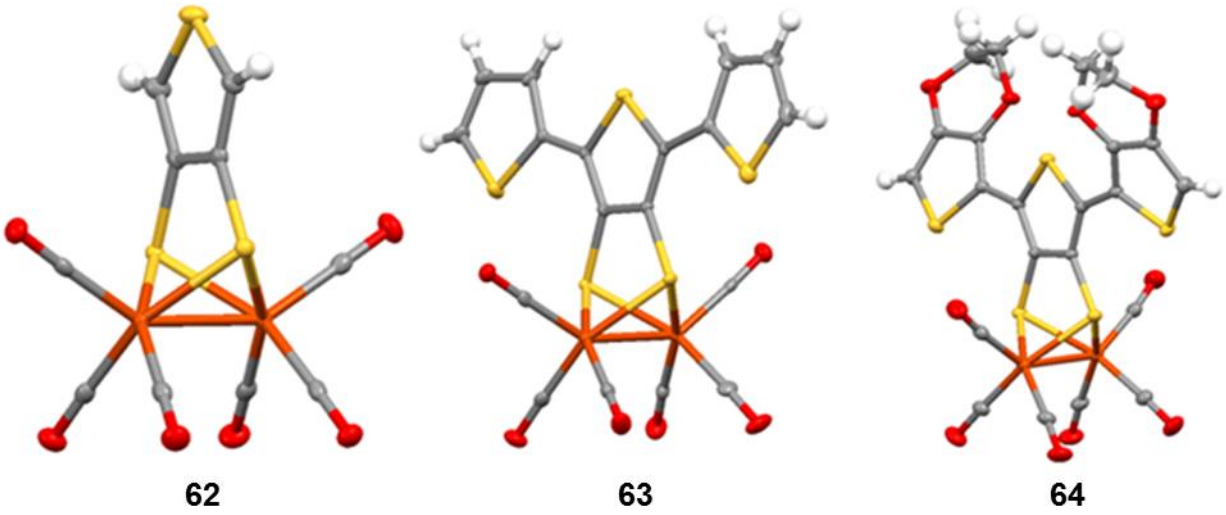

Figure 2.2. Oak Ridge thermal ellipsoid plot (ORTEP) diagram of **62**-**64** with thermal ellipsoids shown at 50% probability level. CCDC 1559397 contains the supplementary crystallographic data for **62** (synthesized, crystalized, and collected by Dr. Laura Stratton), CCDC 1834278 contains the supplementary crystallographic data for **63** (synthesized and crystalized by Steven Sill, structure by Dr. Gabriel Hall), CCDC 1834277 contains the supplementary crystallographic data for **64** (synthesized, crystalized, and collected by William Brezinski). These data are provided free of charge by The Cambridge Crystallographic Data Centre.

Single Crystal X-Ray Crystallography of μ-3,4-dithiolato-oligothiophene Catalysts

The thiophene rings on the 2,5 positions of TTcat are twisted slightly out of plane from central thiophene ring, 8.3° on one ring and -5.1° twist on the other ring. In comparison, the thiophene rings on EDOT bent much further out of plane from central ring – a 20.7° twist on each ring, with significant torsion in the 3,4-ethylenedioxy bridge. The effects of ring torsion has been studied previously in oligothiophene systems, and shown to reduce the effective pi-

conjugation length.[138] Reduced pi-conjugation length will, to an extent, negate the desired effects of increasing the length of the oligothiophene chain i.e. lower oxidation potential, high molar absorptivity, and a bathochromic shift. Incorporation of alkyl chains on the 3 or 4 position of the rings can increase planarity, and therefore effective pi-conjugation length.[139] It may be worthwhile to examine such substituted complexes in the future. The Fe-Fe bond distance is 2.49 Å, identical to the Fe-Fe bond length found in **63** and just slightly longer than the Fe-Fe bond distance in **62**, which is 2.48 Å. The apical Fe-CO is bent a little over 3° further away from linear with respect to the Fe-Fe bond – with a Fe-Fe-C_{apical} bond angle of 146.0°. Overall, the ligand series shown here has minor effects on the bond angles and lengths in the $Fe_2S_2(CO)_6$ cluster, but no large geometric changes are observed in comparing the [2Fe-2S] cluster in each structure. See the experimental section below for crystal data tables for **62**-**64**.

IR Spectroscopy of μ-3,4-dithiolato-oligothiophene Catalysts

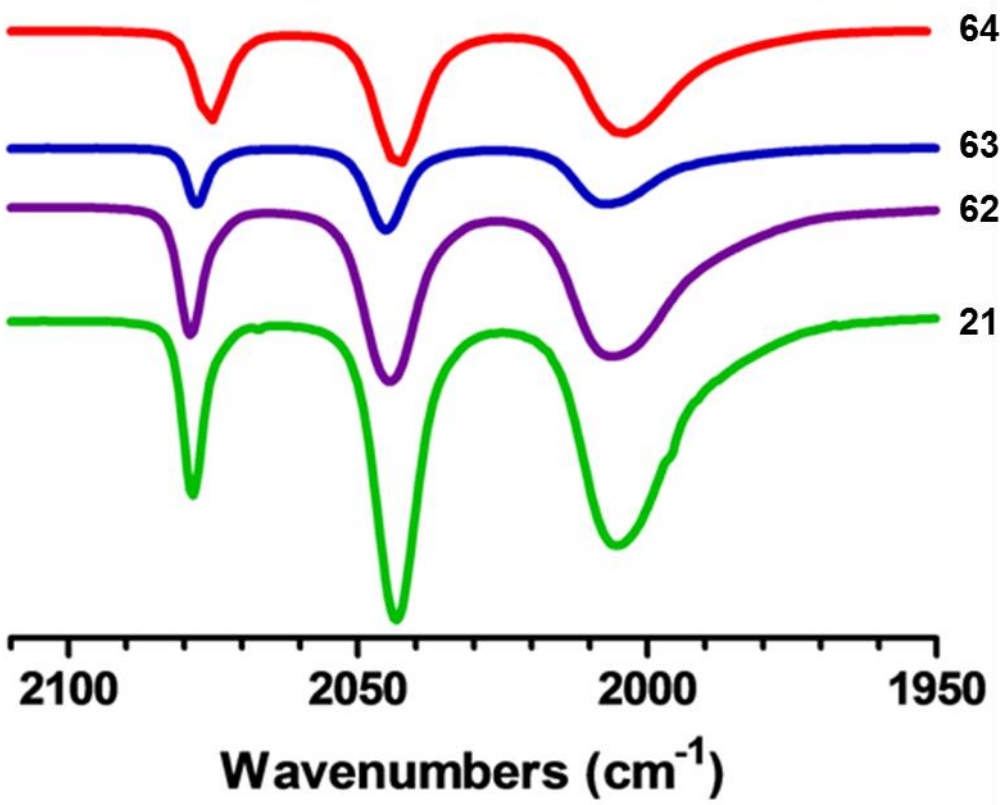

Figure 2.3 Overlay of Fe-CO stretching region of the IR spectra of **21**, **62-64**. Thin films of a solution of catalyst in $CHCl_3$ between NaCl plates.

The Fe-CO stretching frequencies of these molecules provide a very sensitive method for comparing the electron richness of the iron centers. An overlay of the complexes **21** and **62**-**64** shows **21** and **62** have essentially identical Fe-CO frequencies with three peaks at 2079 cm^{-1}, 2043 cm^{-1}, and 2005 cm^{-1}. **63** is shifted slightly to 2078 cm^{-1}, 2045 cm^{-1}, and 2008 cm^{-1}. **64** shows a the largest shift to lower wavenumbers (2075 cm^{-1}, 2042 cm^{-1}, and 2004 cm^{-1}) consistent with the expected trend in which the most electron rich thiophene ligand, the EDOT-thiophene-EDOT ligand on **64**, has increased the electron density on the Fe system the most. This is also consistent with the reduced oxidation potential seen in subsequent cyclic voltammetry experiments.

Electrochemical Characterization of μ-3,4-dithiolato-oligothiophene Catalysts

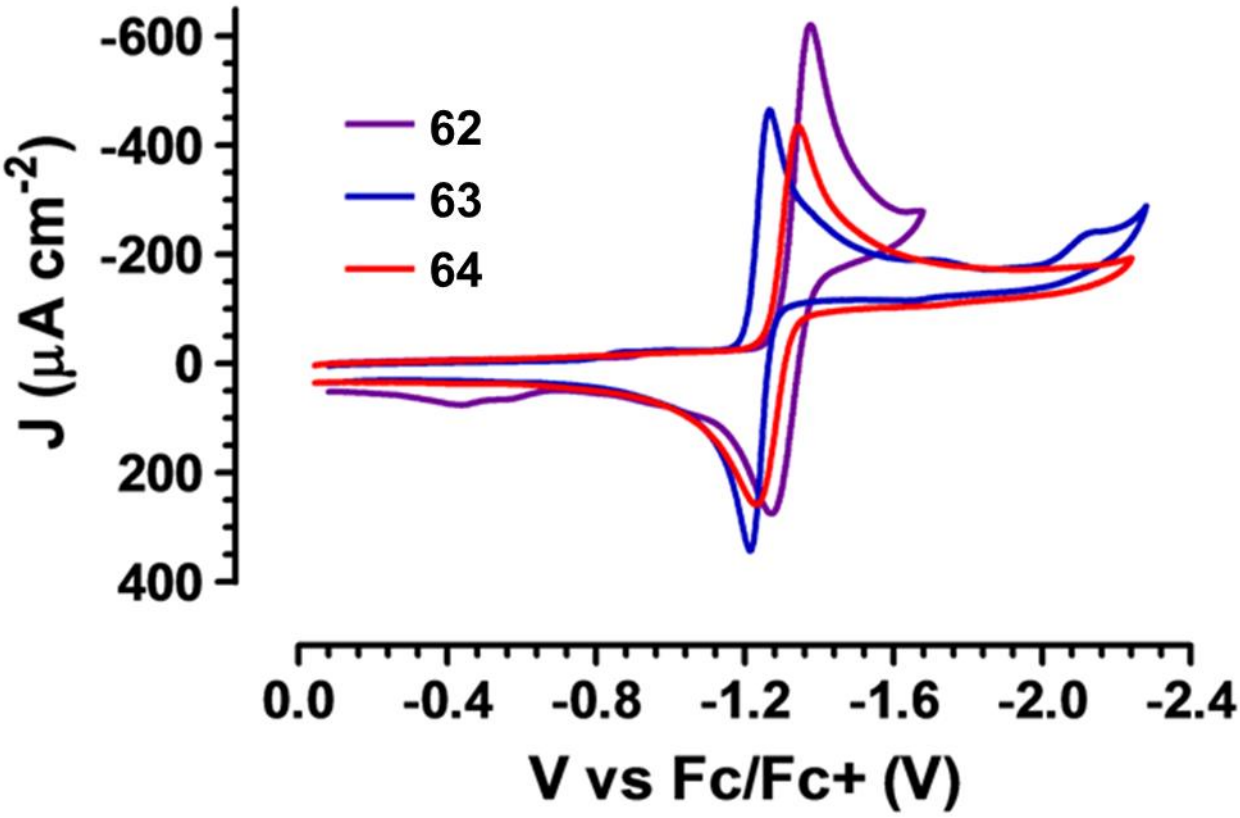

Figure 2.4. Overlay of reductive CV scans of **62-64** in acetonitrile (0.1 M n-Bu_4NPF_6) in the absence of added acid. Glassy carbon working electrode (ϕ = 3 mm), scan rate 100 mV/s.

A comparison of the electrocatalysts begins with characterization of the reductive chemistry of the catalyst. All electrochemical results are reported in tabular form in Table 2.1. Cyclic voltammetry experiments in acetonitrile show an electrochemically reversible reduction at $E_{1/2}$ = -1.32 V vs Fc/Fc^+ for **2**, $E_{1/2}$ = -1.24 V vs Fc/Fc^+ for **63**, $E_{1/2}$ = -1.28 V vs Fc/Fc^+ for **64**. This shift in redox potentials can be rationalized by considering the electronics of the two terthiophene ligand systems. On the one hand, the larger pi-system in terthiophene catalysts **63** and **64** should help delocalize electron density from the Fe-system, making the system easier to reduce overall. However, the electron donating 3,4-ethylenedioxy substituent would make the EDOT substituents on **64** worse at stabilizing negative charge, as it is a more electron rich system, resulting in the observed order of redox potentials for the first reduction where **63** < **64** < **62.**

The reductions appear to be completely reversible for **63** and **64**, with full recovery of current on the oxidative scan and no peak seen for the reoxidation of a homoassociated 4Fe-4S complex[140] (seen near -0.5 V in **62**). This increase in reversibility may indicate the increased steric bulk of the extended thiophene systems is sufficient to suppress the homoassociation mechanism.

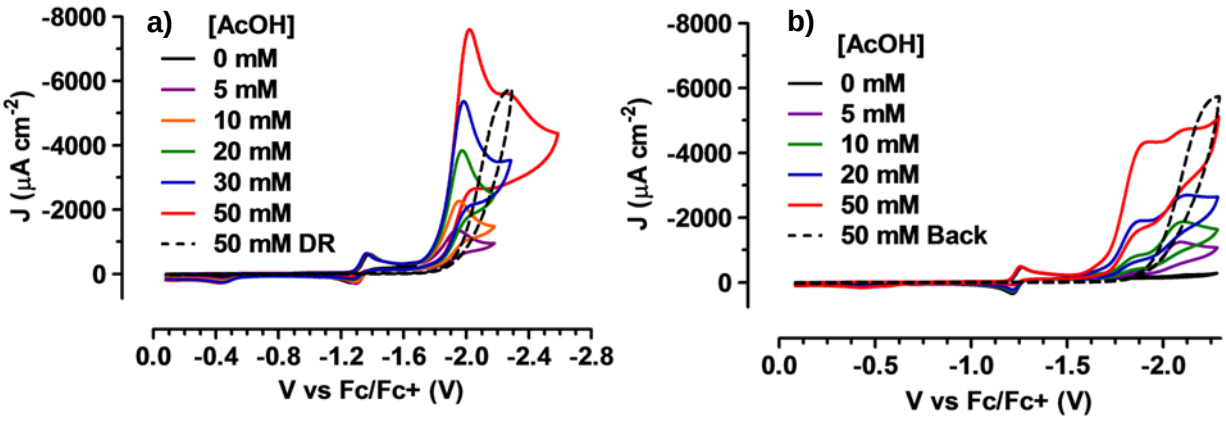

Figure 2.5 Cyclic Voltammetry of 62 and 63 in acetonitrile with increasing AcOH concentration. **a)** Cyclic voltammetry of **62** in acetonitrile with increasing acetic acid concentrations. Data collected by Meghan Talbott. **b)** Cyclic voltammetry of **63** in acetonitrile with increasing acetic acid concentrations. The dashed black line shows direct reduction of acetic acid on the glassy carbon working electrode in 50 mM acetic acid in both voltammograms. See experimental for more information on electrochemical setup.

Subsequently, acetic acid was added in aliquots to the electrochemical solution to provide protons for the hydrogen evolution reaction (HER). The expectation for an HER electrocatalysts is that the addition of acid will reveal a new peak corresponding to the catalytic reduction of protons from the acetic acid to molecular hydrogen. This peak should increase linearly with increasing acid concentration, up to the point where substrate concentration (i.e. acetic acid concentration) is no longer limiting the rate of catalysis. In practice, exceeding 50 mM acetic acid in acetonitrile is of little use, as the background generated by direct reduction of acetic acid at the glassy carbon electrode surface becomes very large and less well separated from the catalytic wave generated by the [2Fe-2S] system. In comparing **62** to the well-studied[141] benzcat system **21** which was the inspiration for the synthesis of **62**, we find that **62** is indeed catalytic (see Figure 2.6a) though not as fast as **21** under the same conditions[125]. Acetic acid titration studies from 0-50 mM confirm the catalytic prowess of **63** and **64** (see Figures 2.6b, 2.7). In comparison to **62**, extended terthiophene system **63** has a reduced overpotential (ca. 320 mV for **63** compared to 450 mV for **62**), though this is balanced by a weaker catalytic response, with only about 65% of the peak catalytic current observed in **62**. The EDOT system **64** manages to combine the best of both systems, by improving on the overpotential of **62** (η = 380 mV for **64** compared to 450 mV for **62**) and a peak catalytic current density of 1 ca. 13.5 mA – nearly double the peak current density of **62** and at a similar applied potential (see Figure 2.8 for a comparison of catalysis in 50 mM acetic acid). This 'goldilocks' behavior seems to nod to where the EDOT substituents have provided enough electron density to increase the reactivity of the reduced, active catalytic species without imposing a large penalty on the energy required to reduce the neutral pre-catalyst to the active species. This demonstrates the benefits of including a tunable, aromatic system. **64** demonstrates such ligands can 'push back' as well. Strong electron donating substituents increase the reactivity of **64** compared to **63**, and we know from the crystal structures that these compounds have very similar $Fe_2S_2(CO)_6$ geometries, so this effect is attributed to the increased electron donation ability of the EDOT-Thiophene-EDOT ligand in **64** compared to the terthiophene system **63**.

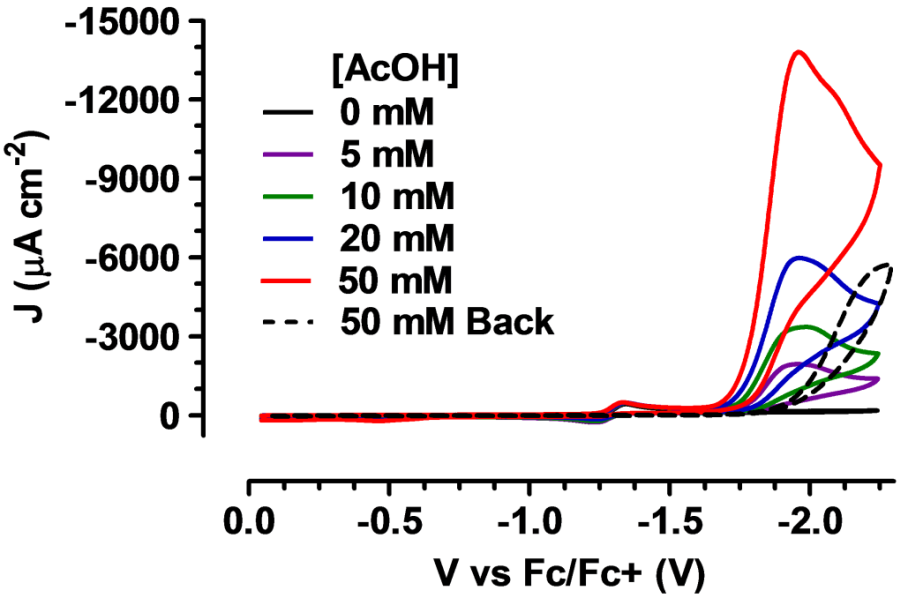

Figure 2.6. Cyclic voltammetry of ETEcat 64 in acetonitrile (0.1 M $TBAPF_6$) with increasing acetic acid concentrations. Data collected at 0.5 mM catalyst concentration due to low solubility in ACN, then normalized to 1 mM catalyst concentration for comparison with the other two data sets. Black dotted trace shows the background current at a glassy carbon electrode in 50 mM acetic acid without catalyst. Initial $2e^-$ reduction occurs at $E_{1/2}$ = 1.28 V, $E_{1/2}$ for catalysis -1.84 V.

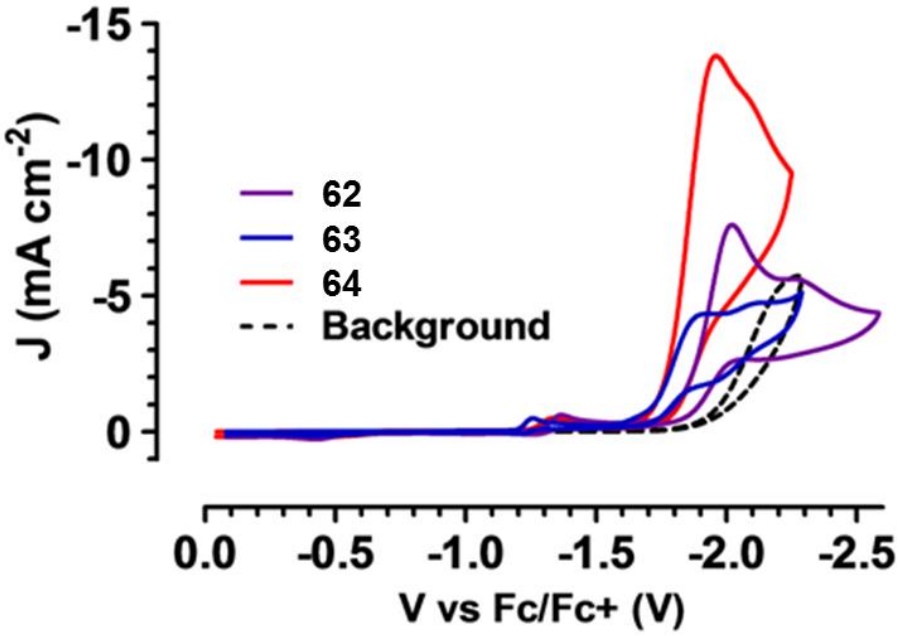

Figure 2.7. CV comparison of 62-64 in 50 mM AcOH in ACN. Cyclic voltammetry of 1.0 mM **62** (purple), 1.0 mM **63** (blue), and 0.5 mM TTcat **64** (red,) in acetonitrile with 50 mM acetic acid added. Data for **64** normalized to 1 mM catalyst concentration for comparison with other two data sets as **64** is not soluble enough in acetonitrile to achieve 1 mM. See experimental (page 59) for more information on electrochemical setup.

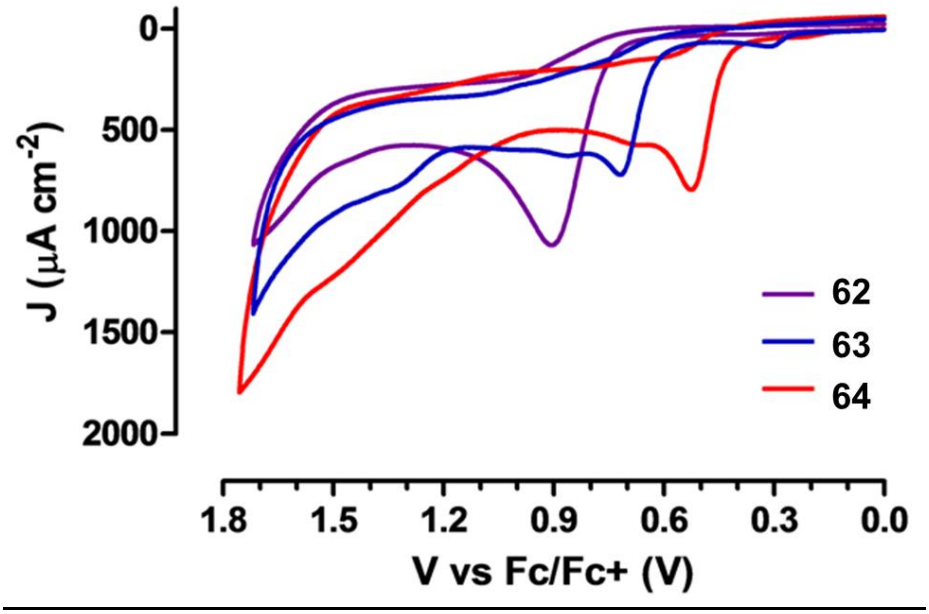

Figure 2.8. Oxidative CV scans of 62-64. Cyclic voltammetry of **62** (1.0 mM) **63** (1.0 mM) and **64** (0.5 mM, normalized to 1.0 mM) in acetonitrile (0.1 M TBAPF6) scanning positive to observe the oxidation of the [2Fe-2S] system (observed at 0.81 V, 0.66 V, and 0.47 V for **62**, **63**, and **64** respectively) as well as the electrochemical polymerization of the thiophene ligands (observed at 1.53 V, 1.29 V, and 1.19 V for **62**, **63**, and **64** respectively).

One hope for the extended thiophene systems was that there would be a chain length, n, at which the thiophene ligand would be oxidatively polymerized at a less positive potential than the $Fe^{I} \rightarrow Fe^{II}$ oxidation of the iron system which is typically irreversible. Unfortunately, once we had the compounds in hand, we found that while the thiophene system does indeed become easier to oxidize along the trend E_{ox} **64** < E_{ox} **63** < E_{ox} **62**. However, due to the excellent electronic communication between the (ter)thiophene ligands and the iron system, the $Fe_2S_2(CO)_6$ system also becomes easier to oxidize as the electron donor ability of the (ter)thiophene ligand increases. The $Fe^{I} \rightarrow Fe^{II}$ oxidation of **62** occurs as ~0.81 V vs Fc/Fc^{+} and the formal potential for the electropolymerization of thiophene is approximately 1.53 V. In **63** the terthiophene system oxidizes 0.24 V more positive at ~1.29 V, but the $Fe^{I} \rightarrow Fe^{II}$ oxidation has also moved positive by 0.15 V to a formal potential of 0.66 V. Finally, **64** shows the easiest electrochemical polymerization of the oligothiophene chain with a formal potential of approximately 1.19 V, 0.1 V positive of **63**, but also the easiest $Fe^{I} \rightarrow Fe^{II}$ oxidation, which occurs at a formal potential of 0.47 V, a 0.19 V shift positive of the $Fe^{I} \rightarrow Fe^{II}$ oxidation seen in **63**. This is consistent with the idea that the EDOT substituents will help push electron density onto the iron system, and a more electron rich iron system will be easier to oxidize. This is also consistent with the observed Fe-CO stretching frequencies, which indicate a marked increase in the electron density in the iron system of **64** relative to **21**, **62**, and **63**.

Table 2.1. Tabulated summary of electrochemical results for thiophene catalyst 62-64. All potentials given are referenced to an internal Fc/Fc^+ couple. E_{ox}^1 is assigned to the oxidation of the [2Fe-2S] system, while E_{ox}^2 is assigned to the oxidative polymerization of the thiophene ligands. The values ΔE_{ox}^1 and ΔE_{ox}^2 for **63** is calculated relative to the potentials observed in **62**, and the values for **64** is calculated relative to the values for **62**, to examine the trend. Overpotential (η) calculated using -1.46 V vs Fc/Fc^+ as the formal potential for reduction of acetic acid in acetonitrile. I_{pc} values are based on current obtained in acetonitrile with 50 mM acetic acid added.

Catalyst	E_{ox}^1 (V)	E_{ox}^2 (V)	ΔE_{ox}^1 (mV)	ΔE_{ox}^2 (mV)	E_{red}^1 (V)	E_{red}^2 (V)	η (mV)	J_{pc} (mA cm^{-2})
62	0.81	1.53	--	--	-1.32	-1.91	450	-7.25
63	0.66	1.29	150	240	-1.24	-1.78	320	-4.00
64	0.47	1.19	190	100	-1.28	-1.84	380	-13.4

Photocatalytic-H_2 Experiments

A second goal for extended thiophene systems **63** and **64** was to investigate their use as photocatalysts. Using photocatalysts for HER has some distinct advantages, namely that it circumvents the constant struggle to achieve lower overpotentials because the energy input is sunlight, which is naturally occurring and abundant – at least in Tucson, AZ. Photocatalysis does come with its own host of problems such as photostability of the catalysts, proper selection of a good sacrificial electron donor, and preventing charge recombination in the excited state[139,142,143]. The last problem is of particular importance as the charge separated intermediate must react before recombination occurs, or the excited state will decay via fluorescence from the singlet state, or intersystem crossing to the triplet state, followed by phosphorescence to the ground state. In most systems reported to photo-produce hydrogen, the triplet state does not have sufficient energy to reduce the iron system. Therefore, maximizing the lifetime of the singlet state is crucial to improving a photocatalytic system. Electrocatalytic systems with an aryl bridging ligand typically undergo a geometric rearrangement after one electron reduction of the iron system, resulting in a monoanion which is more easily reduced than the neutral species, which appears in the cyclic voltammetry experiment as a two electron initial reduction, even at fast scan rates[144]. In contrast, alkyl-bridged systems typically exhibit two separated one electron reductions at slow scan rates, which shifts to an apparent two electron process as the scan rate in increased[145]. The monothiophene complex **62** has demonstrated an electrochemical inversion similar to **21**[125], as has **63**[146] and **64** (see Figure 2.4). This suggests that the excited state may be able to conduct two electron transfers to the iron system. It is also possible that the singly reduced iron system will react with a proton before undergoing the second photoinduced electron transfer step as has been shown in other photocatalytic [FeFe]-hydrogenase mimics. The order of these steps and identity of the intermediates has not been studied in this work, this discussion is only intended to point out the need for at least two photoinduced electron transfers per molecule of hydrogen produced. Additionally, the oxidized form of the thiophene ligand will require reduction by a sacrificial electron donor to return to the neutral state which may then preform a second photoinduced electron transfer. Figure 2.9 provides a cartoon representation of the steps required for one photocatalytic cycle, without intending to suggest any particular order of steps or the structure of the intermediates. Ott *et al.* provide a thorough discussion of the possible mechanistic pathways for photocatalysis from a [2Fe-2S] system[143].

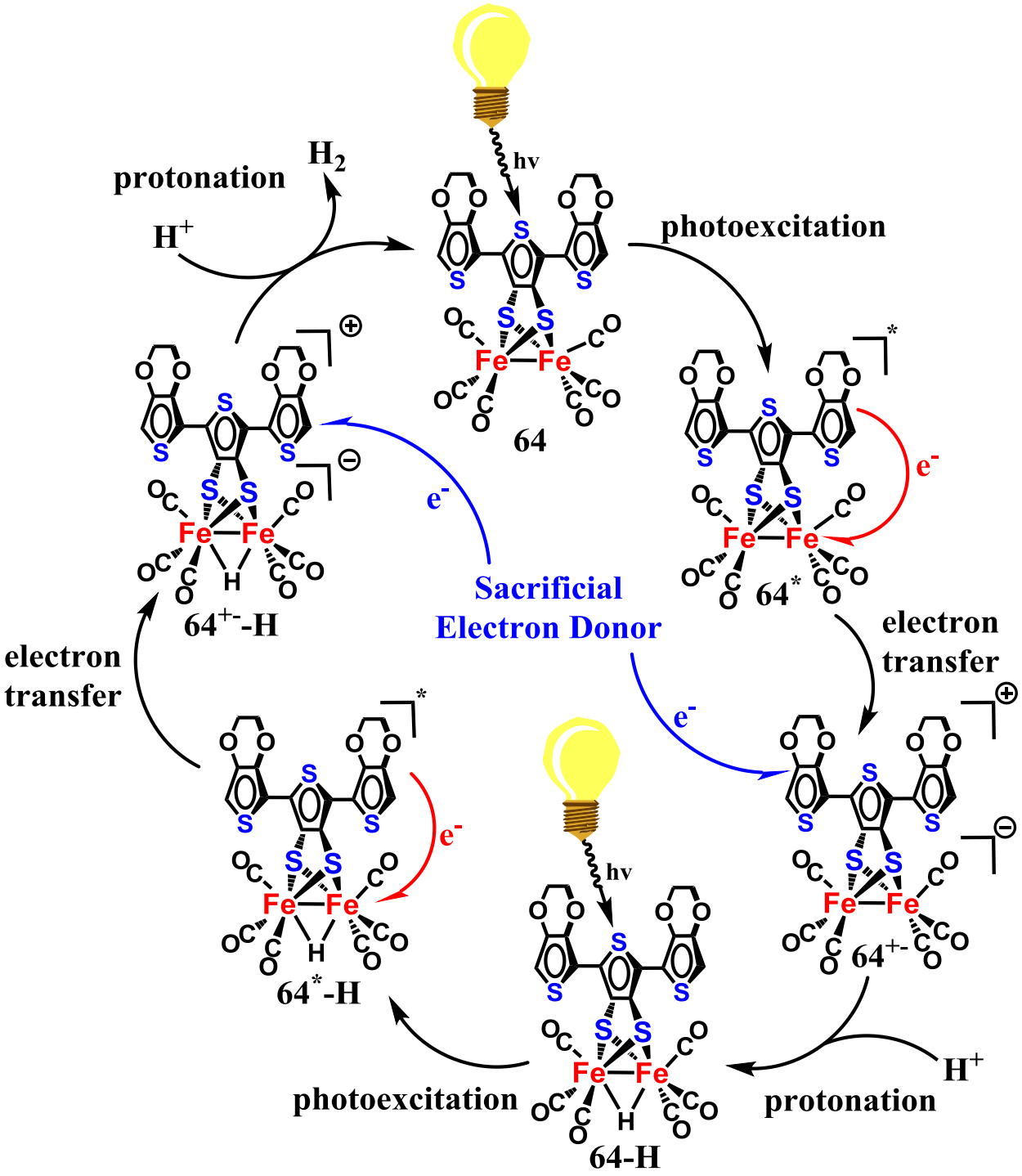

Figure 2.9. Schematic representation of the general steps required for photogeneration of H2. This scheme is not intended to imply any specific mechanism for the photoproduction of hydrogen gas from **64** or any specific structure for the intermediates, rather it is intended to give the reader an understanding of the fundamental steps which must occur in such a process, and the need for a sacrificial electron donor.

To increase the chance of two excitation events happening temporally close together, it is desirable to increase the molar absorptivity, ε, of the catalyst so that more photons are absorbed per unit solar flux. It is also beneficial to shift the absorbance profile of the catalyst toward the red and near IR portions of the electromagnetic spectrum as that portion of the

spectrum is where peak solar flux occurs on the surface of Earth, yet they still carry sufficient energy to drive the reaction[142]. Both of these effects are anticipated to occur with increased oligothiophene chain length and electron density.

The extended thiophene systems elegantly address both of these 'wants' for a photocatalytic HER system. Oligo- and polythiophene materials have long been used in organic photovoltaics[139,147] as electron donor materials. Poly-EDOT (PEDOT) in particular is a well-known donor material with a broadband absorption on the red portion of the spectrum, giving PEDOT films a characteristic blue color[148]. This well documented behavior warrants investigation of the photocatalytic ability of at least EDOT-thiophene-EDOT complex **64**.

UV-Vis Spectroscopy of μ-3,4-dithiolato-oligothiophene Catalysts

The UV-Vis spectra of compounds **62**-**64** shows that some of the proposed benefits of extended thiophene chains – namely increased ε and a bathochromic shift of λ_{max} for complexes **63** and **64** compared with **62**. Compounds **63** and **64** both exhibit a strong UV absorption at 338 nm with **3** having a substantially larger ε, but complex **64** also has distinct shoulders at 369 nm and 391 nm that are weak or absent in the absorption profile of **63**. In the visible region, **63** has a slightly higher ε, but λ_{max} for **64** has been red shifted 38 nm towards the region of maximum solar flux. Given that wavelengths below ~400 nm are thought to promote decomposition of the Fe system via dissociation of a CO ligand. Limiting analysis to the region above 400 nm (see inset in **figure 2.10**) shows both **63** and **64** have good absorbance in the region between 400-500 nm with the absorbance of **3** falling off by 550 nm and **64** falling off around 600 nm. Both compounds display much higher molar absorptivity (($\varepsilon \approx 5700$ M^{-1} cm^{-1} for **3** and $\varepsilon \approx$. 4900 M^{-1} cm for 4) than the monothiophene compound **62** which has only a weak absorbance between 400-550 nm ($\varepsilon \approx 1000$ M^{-1} cm^{-1}) which is typical of other small molecule mimics lacking photoactive ligands[142]. This demonstrates that we have achieved one of the stated project goals – increasing and red-shifting the absorption profile of the catalyst towards the region of most intense solar flux and invites investigation into photocatalytic activity.

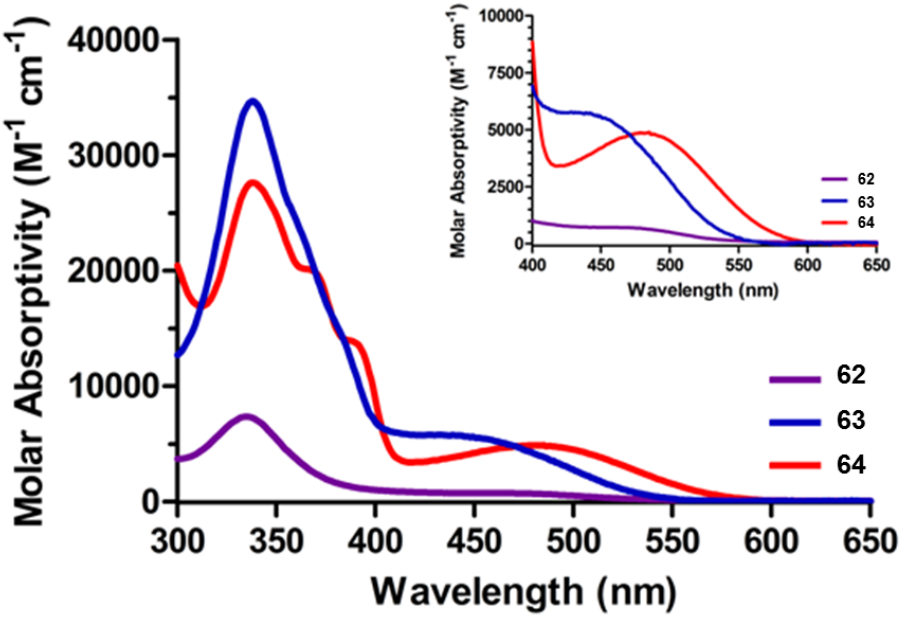

Figure 2.10. UV-Vis data of compounds **62-64** in toluene. Data has been normalized to molar absorptivity ε (M^{-1} cm^{-1}) using Beers Law.

Photoexcitation of a neutral molecule **64** allows electron donation from the excited state (**64***) of the thiophene system into the iron center. The resulting species **64**$^{+-}$ is now reactive toward protons, but must react before the charge separated exciton can recombine. This may happen via either a) trapping the anion on the iron center by reducing the thiophene system with an external reductant or b) protonation, followed by reduction of the thiophene system by and external reductant. It is least likely that protonation and excitation happen simultaneously, as this would obey three-body kinetics. It is possible that both pathways (a) and (b) occur in competition with each other. Once protonated and reduced, **64-H** can undergo another excitation event followed by electron transfer and protonation to liberate hydrogen.

As previously mentioned, a photocatalytic system requires a sacrificial electron donor regenerate the catalyst by filling the holes left behind by electrons promoted to the LUMO by photoexcitation, then used for proton reduction. Common sacrificial electron donors include ascorbic acid, amines, and thiols. If the reaction is carried out in organic solvents, an external acid will also need to be added. In our initial study, we chose thiophenol as both an acid source and sacrificial electron donor. A second major consideration for the experimental design was how to handle the effusion of molecular hydrogen. Due to its small size and high root mean square speed, H_2 has an extremely high rate of effusion. This problem is compounded by our method of sampling – headspace analysis – which necessitates multiple needle punctures in whatever septum is being used on the reaction flask, which will increase the rate of H_2 effusion over time. The best way to address these problems is by using an internal standard that will have comparable effusion rates. Methane was chosen based on literature precedence, and was found to be a suitable internal standard which elutes reasonably close to hydrogen under our gas chromatography conditions.

Figure 2.11 shows the photocatalytic hydrogen evolution of a 1 mM solution of **64** in toluene with 1 M PhSH acting as both electron donor and proton source. Photocatalysis was evident with an increase in H_2/CH_4 ratio for the first ~16 hours, after which point catalysis has stopped and the H_2/CH_4 declines over time as hydrogen escapes the cell more quickly than the methane internal standard. There was also a detectable amount of hydrogen at t = 0, which is attributed to photo production of H_2 from the overhead lights present in the laboratory. The initially translucent red solution darkens quickly over the course of catalysis and is completely black by the end of the run. Interestingly, a large amount of crystalline material forms in the reaction flask. This material was subsequently analyzed via ^{1}H NMR and mass spectrometry and confirmed to be diphenyl disulfide. The iron system had all been decomposed into a black precipitate which is commonly observed with [2Fe-2S] systems. This material is both paramagnetic and insoluble in common organic solvents, which prevents NMR analysis and complicates mass spectral analysis. As such, it has not been rigorously characterized.

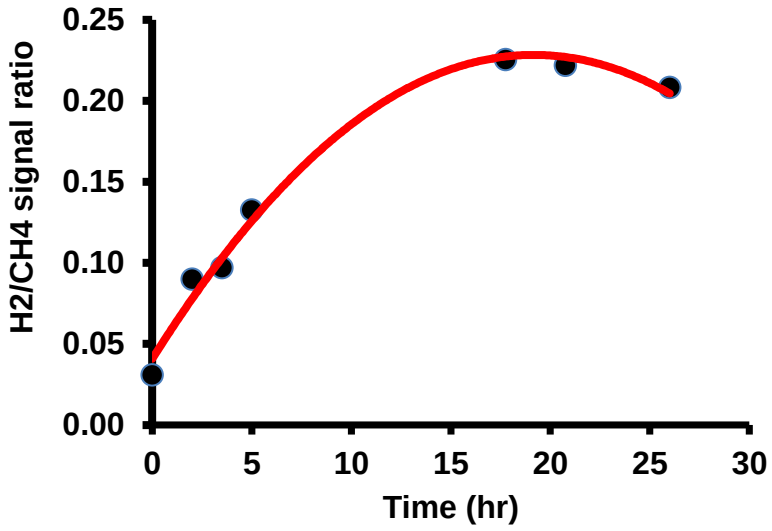

Figure 2.11. Photo-H_2 evolution plot of GC headspace measurements obtained from an irradiated sample of 1 mM **64** in toluene with 1 M PhSH added as electron donor and acid. Y-axis is plotted as a ratio of peak areas from headspace GC comparing the area of a methane internal standard with the H_2.

Experimental

Materials

Unless otherwise noted, solvents were received from Fischer Scientific as ACS grade and used without further purification. $Fe(CO)_5$ (99.5 %,Alfa-Aesar), NaOH (EMD, ACS grade), NH_4Cl (EMD, ACS grade), S_8 (Mallinckrodt, sublimed), Na_2SO_4 (EMD, ACS grade), Br_2 (Strem Chemicals), K_2CO_3 (Alfa Aesar, ACS grade), H_2SO_4 (Alfa Aesar, ACS grade), $Na_2S \bullet 9H_2O$ (Sigma Aldrich, ACS reagent grade), DDQ (Sigma Aldrich, ≥98%), thiophene (Sigma Aldrich, ≥99%), 3,4-ethylenedioxythiopene (Accela ChemBio, 97%), $POCl_3$ (Sigma Aldrich, sure seal *Reagent Plus*), dimethylformamide (Sigma Aldrich, 99.8%, anhydrous), Celite 545 (VWR), and Silica Gel (SiliaFlash F60, 230-400 mesh, Silicycle) were used as received without further purification. $Fe_2S_2(CO)_6$ was prepared according to literature procedures[149] and sublimed before use. $Fe_2(CO)_9$ was prepared photochemically[150] according to published methods. Potassium isopropyl xanthoate was prepared using a published procedure.[151] Vinylene trithiocarbonate (Sigma-Aldrich, 98%) N-bromosuccinimide (Tokyo Chemical Industry, ≥98%) was recrystallized from water to obtain a white crystalline solid before use as described in *e-Eros Reagents for Organic Chemistry.*[152]. LDA (Sigma Aldrich, 2.0 M solution in THF) was titrated with diphenyl ditelluride[153] in triplicate prior to use. Dichloromethane (DCM) (Fischer Chemical, ACS grade), methanol (Fischer Chemical, ACS grade,), hexanes (Fischer Chemical, ACS grade), and toluene (EMD, ACS grade), $CDCl_3$ (EMD) were used as received. Tetrahydrofuran (THF) (EMD, GC grade), was either distilled from Na-benzophenone (after first distilling until the solution turned purple) or dried by standing for at least 24 hours over 3 Å molecular sieves (Sigma-Aldrich) activated at 300 °C. Acetonitrile (Fischer Chemical, HPLC grade) was dried over 3 Å molecular sieves (Sigma-Aldrich, activated at 300 °C for a minimum of 24 hours) for 24-48 hours before use. ^1H and ^{13}C nuclear magnetic resonance (NMR) spectra were obtained using a Bruker DRX 500 MHz or a Bruker Avance III 400 MHz

spectrometer. Chemical shifts were referenced to $Si(Me)_4$ (δ 0.00 ppm) for ^1H NMR and $CDCl_3$ (δ 77.0 ppm) for ^{13}C NMR. MestReNova 10.0 software was used for spectral processing. IR spectra were obtained on a Nicolet Avatar 360 FT-IR with EZ-OMNIC software using H_2O and CO_2 correction. Resolution set to 0.964 cm^{-1} for all IR spectra. A Fisher Scientific FT-30 30specRFL500700*L IRSEC cell with 0.5 mm Teflon spacer (total path length = 1 mm) and CaF_2 window (Alfa-Aesar) was used for quantitative IR measurements. Qualitative IR was performed using solutions in $CHCl_3$ in thin films between NaCl plates (Fisher Scientific). Spectral processing and graphing were performed using Microsoft Excel, Origin Pro 8.0, and Prism Graph Pad 5.0.

Electrochemical Procedures

General Procedures and Materials

A Gamry Reference 3000 was used for all data collections with Gamry Framework 6 software. A custom airtight cell was designed and fabricated in-house and is pictured below (**Figure 2.12**). All potentials were referenced to an internal Fc/Fc^+ couple. A scan rate of 100mV/s was used unless otherwise noted. Solution resistance was measured and compensated at 90% of measured cell resistance (typical solution resistance measured to be between 120-150 ohms). The glassy carbon (GC) working electrode with a diameter of 0.3 cm (calculated area = 0.071 cm^2) was obtained from BASi. The electrode surface areas was confirmed experimentally by means of the current of the oxidation peak of ferrocene in acetonitrile (diffusion coefficient 2.20 x 10^{-5} cm^2/s; 0.070(3) cm^2). The working electrode was polished between scans in a figure eight pattern on a Buehler microcloth polishing cloth with 1.0 then 0.05 micron alumina mircopolish (1 minute each) suspended in de-ionized water. A Pt Wire (Sigma-Aldrich, 99.9%) was used as a counter electrode. Silver wire (99.999% Alfa Aesar), $AgNO_3$ (99.9% Sigma-Aldrich ACS reagent) and Vycor frits were used to fabricate reference electrodes to fit the cell. Once fabricated, a reference electrode was stored for up to 7 days before being remade. Acetonitrile (anhydrous, 99.8%, Sigma-Aldrich GC-MS grade) and tetrabutylammonium hexafluorophosphate ($TBAPF_6$, Fluka, puriss electrochemical grade) were used to prepare acetonitrile solutions. Acid experiments were performed by adding acetic acid (Alfa-Aesar, 99.998%) degassed via three cycles of freeze-pump-thaw using 10 µL or 100 µL Eppendorf auto pipettes. Acid concentrations given based on 10 mL solution volume, assuming negligible solvent evaporation 0.57 µL AcOH = 1 mM [AcOH]. Acetonitrile was degassed by sparging with argon for 30 minutes prior to preparation of solutions. The cell was assembled and flushed with argon before solution deoxygenated solution was added through a 14/20 rubber septum via deoxygenated syringe. An initial scan is taken to ensure no oxygen ($E^o \approx$ -1.0 V vs ref) is present. If O_2 is detected, the solution is bubbled with argon in five minute increments until O_2 reduction is no longer detected.

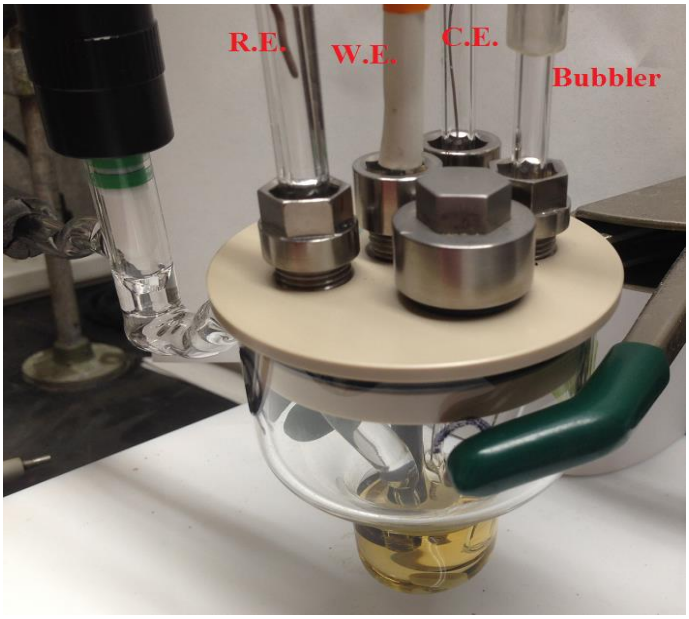

Figure 2.12. Photograph of custom cyclic voltammetry cell. The reference electrode (R.E.), working electrode (W.E.), counter electrode (C.E.) and bubbler are all labeled. The bubbler and Kontes valve (seen on the left) are attached to an argon line to allow bubbling with argon or maintenance of positive pressure of argon atmosphere at user discretion.

Synthesis

4,6-di(thiophen-2-yl)thieno[3,4-d][1,3]dithiole-2-thione (73a)

71 (927 mg, 6.90 mmol) was added to a dry, argon purged 100 mL Schlenk flask and dissolved in 30 mL anhydrous THF cooled in a dry-ice acetone bath to -55 °C. 1.45 M lithium diisopropylamide (LDA) in THF (5.25 mL, 7.71 mmol) was added quickly dropwise over 1 minute then stirred 30 minutes. Simultaneously, thiophene-2-carboxaldehyde **72a** (1.70 g, 15.2 mmol) was dissolved in 10 mL THF, resulting in a total solution volume of approximately 11.5 mL. 5.75 mL of this solution was added dropwise over 5 minutes to the solution of **71** after it had stirred with LDA for 30 minutes. The solution was then stirred 30 minutes. A second addition of LDA (5.75 mL, 7.71 mmol) was added and stirred for 30 minutes after which time the remaining 5.75 mL of thiophene-2-carboxaldehyde solution was added and the mixture was stirred for another hour in the cold bath. The cold bath was then removed and the reaction stirred at room temperature for 1.5 hours. The solvent was removed under reduced pressure and the residue was redissolved in DCM (50 mL) and MnO_2 on silica gel (50 g) was added. The solution was stirred at room temperature under argon for 24 hours. The solution was then filtered to remove the MnO_2 and the solvent removed via rotovap. Column chromatography (10% hexanes in DCM → DCM → 2% EtOAc in DCM) elutes two spots. The top spot is **73a**, while the lower spot is the mono-substituted ketone product, which was not easily separable from the desired product. Total mass 609 mg, (25%) ^{1}H NMR (CDCl3) δ 7.72 (dd, *J* = 1.1 and 4.9 Hz, 2H), 7.71 (dd, *J* = 1.1 and 3.9 Hz, 2H), 7.10 (dd, *J* = 3.9 and 4.9 Hz, 2H).

4,6-di(thiophen-2-yl)thieno[3,4-d][1,3]dithiol-2-one (74a)

To a solution of **73a** (0.609 g, 1.72 mmol) in dichloromethane/glacial acetic acid (3:1 v/v, 10 mL) was added mercuric acetate (766 mg, 2.41 mmol). The resulting mixture was stirred at room temperature for 16 h and filtered over a 2” silica pad, washing with dichloromethane, then 10% EtOAc in DCM (20 mL) to elute a yellow band. The solvent was removed under

reduced pressure to afford **74a** as an off-white solid (523 mg, 85%). ^{1}H NMR ($CDCl_3$) δ 7.71 (dd, *J* = 1.1 and 4.9 Hz, 2H), 7.68 (dd, *J* = 1.1 and 3.9 Hz, 2H), 7.09 (dd, *J* = 3.9 and 4.9 Hz, 2H).

Preparation of 4,6-di-thiophene-2-yl-thieno[3,4-d][1,3]dithiol-2-one (75a)

In a two neck round bottom flask with condenser, **74a** and the mono-substituted analogue (628 mg, 1.86 mmol) was dissolved in DCM (40 mL) and Lawesson's reagent (788 mg, 1.95 mmol) was added as a solid in one portion. The reaction mixture was heated to reflux for two hours in a preheated oil bath then cooled to room temperature and filtered to isolate 326 mg mustard yellow powder from the green filtrate. The filtrate was concentrated on rotovap and run through a short silica gel plug column, eluted with DCM. A red band was found to contain **74b,**,which was further purified by dissolving in 4 mL DCM, adding to 50 mL stirred methanol and rotovaping at 30 ºC and 400 torr to selectively remove the DCM. Filtration recovered another 87 mg mustard yellow solid. Total yield of **75a** = 66% without accounting for the imurties in the starting material. Using NMR integrations to estimate the purity of the starting material bring the yield up to 86%. ^{1}H NMR ($CDCl_3$) δ 7.38 (dd, *J* = 1.1 and 5.1 Hz, 2H), 7.24 (dd, *J* = 1.1 and 3.7 Hz, 2H), 7.11 (dd, *J* = 3.7 and 5.1 Hz, 2H). MS (MALDI) m/z: 338 (M+, 6%), 310 (M+ - CO, 100%).

(2,5-bis-(2',2''-thiophen-2-yl)-thiophene-μ-3,4-dithiolato)diiron hexacarbonyl, (63)

In a round bottom flask with a condenser attached was dissolved **13** (50 mg, 0.148 mmol) and $Fe_2(CO)_9$ (108 mg, 0.295 mmol) in dry THF degassed via argon sparge (10 mL). This mixture was heated to reflux for 1.5 h in a preheated oil bath and then cooled to room temperature. The solvent was removed under reduced pressure, and the product was isolated by column chromatography (silica, 15% DCM in Hexanes (v/v)) to afford **3** as a dark red solid (64.6 mg, 74%). ^{1}H NMR (CDCl3) δ 7.35 (dd, *J* = 1.1 and 5.1 Hz, 2H), 7.32 (dd, *J* = 1.1 and 3.7 Hz, 2H), 7.04 (dd, *J* = 3.7 and 5.1 Hz, 2H). See Steven Sill's thesis for full characterization data. CCDC 1834278 contains the supplementary crystallographic data for **3**. These data are provided free of charge by The Cambridge Crystallographic Data Centre.

2-formyl-3,4-ethylenedioxythiophene (72b)

EDOT (0.30 mL, 2.81 mmol) was dissolved in 1,2-dichloroethane (12 mL) in a flame dried three neck 25 mL round bottom flask and the resulting solution cooled to 0 ^{o}C in an ice bath. $POCl_3$ (0.29 mL, 3.09 mmol), and DMF (0.24 mL, 3.09 mmol) were added dropwise, sequentially. The reaction was stirred for 1 hour at 0 ^{o}C, slowly taking on a light yellow color. The mixture is then heated to reflux for 18 hours. The reaction was then cooled to room temperature and 10 mL of aqueous NaOAc solution (1 M) was added. Organic layer removed and aqueous layer washed with ethyl acetate (3 x 10 mL) and DCM (2 x 10 mL). Combined organic layers washed with brine (40 mL) then dried ($MgSO_4$) and concentrated on rotovap to yield *ca.* 1 g crude red-white solid. Separation on column (Sigel, 30% EtOAc in Hexanes) yielded 540 mg white crystalline solid (quantitative yield). Larger scale preparations employed recrystallization from 95% ethanol for purification, yielding very fine, hair like crystals. Very large scale reactions (~10 g) employed stirring in ethyl acetate with activated carbon followed by filtration, removal of solvent, and recrystallization from 95% ethanol to avoid column chromatography.

4,6-bis(2,3-dihydrothieno[3,4-b][1,4]dioxin-5-yl)thieno[3,4-d][1,3]dithiole-2-thione (73b)

A flame dried, 500 mL Schlenk flask was fitted with an argon inlet and equipped with a stir bar before cooling under vacuum. The flask is placed in a dry-ice acetone bath and charged with LDA (10.25 mL, 1.7 M, 17.4 mmol). In a separate flame dried flask VTC (2.13 g, 15.8 mmol) was dissolved in degassed THF (59 mL, [VTC] = 0.34 M). The VTC solution was then added dropwise to the cold LDA solution over 5 minutes and the mixture stirred 30 minutes. In a third Schlenk flask, 2-formyl EDOT **72b** (5.92 g, 34.8 mmol) is dissolved in degassed THF (51 mL) with sonication then 25.5 mL of this solution was added dropwise to the cold VTC anion solution. The solution is stirred for 30 minutes then a second portion of LDA is added (10.25 mL, 1.7 M, 17.4 mmol) and the solution stirred 45 minutes. The remaining 25.5 mL of **72b** 2-formyl EDOT solution is added dropwise, and the solution was stirred 1.5 hours in the cold bath then allowed to stir without external cooling for 1 hour. Saturated aqueous $NaHCO_3$ (75 mL) is added, causing the light orange solution to darken to red-black with a yellow aqueous layer. Organic layer removed and aqueous layer washed with DCM (4 x 40 mL) and ethyl acetate (1 x 40 mL) and the combined organic layers were dried ($MgSO_4$) and concentrated on rotovap to yield an orange-red film that foams under vacuum. This solid was redissolved in DCM (150 mL) and fresh MnO_2 on silica gel (88 g) was added portionwise while the solution was vigorously stirred. The flask was shielded from light and allowed to stir for 48 h. At the end of this period, the mixture was filtered over Celite to remove MnO_2 and the pad washed with ethyl acetate until no more yellow color is visible. Concentration on rotovap and column chromatography (Sigel, 45% ethyl acetate in hexanes) yielded 2.013 g yellow solid (27%, two steps). ^{1}H NMR (499 MHz, $CDCl_3$) δ 6.68 (s, 2H), 4.26 (ddd,(*J* = 8.4, 3.7, 0.6 Hz), 4H), 4.18 (ddd,(*J* = 8.3, 3.7, 0.5 Hz, 4H) ^{13}C NMR ($CDCl_3$, 298K, 126 MHz) δ 209.0 (Cq, 1, C=S) , 173.6 (Cq, 2, C=O), 145.8 (Cq, 2, 4-thiophene), 145.2 (3-thiophene), 141.7(Cq, 2, -S-C=C-S), 117.6 (Cq, 2, 2-thiophene), 111.7 (Cq, 2, 5-thiophene), 65.4, 63.9 (-OCH_2CH_2O-) IR (KBr pellet, cm^{-1}) 3086 (w), 2952 (w), 2915 (w), 2859 (w), 1601 (s), 1594 (s), 1483 (vs), 1429 (s) 1368 (s), 1289 (s), 1160 (s), 1063 (vs), 911 (s), 763 (s), 705 (s) m.p. 187.5-188.7 ^{o}C MS (ESI): m/z = 470 (M + H^+, 24%), 328 (MH^+ - EDOT, 100%) HRMS: m/z = 470.91537 = $C_{17}H_{11}O_6S_5$ calculated = MH^+

4,6-bis(2,3-dihydrothieno[3,4-b][1,4]dioxin-5-yl)thieno[3,4-d][1,3]dithiol-2-one (74b)

73b (150 mg, 0.317 mmol) was dissolved in DCM/AcOH (3:1, 7 mL) with stirring and sonication. $Hg(OAc)_2$ was added as a solid in one portion (152 mg, 0.476 mmol) and the clear yellow solution became cloudy. The reaction was stirred overnight in ambient conditions, then filtered over a 2" pad of silica gel, eluted with DCM until yellow color was no longer present. Combined filtrates were extracted with deionized water (2 x 40 mL), saturated $NaHCO_3$ solution (2 x 40 mL), and brine (1 x 40 mL) then dried with $MgSO_4$ and the solvent removed on a rotary evaporator. The pure product can be isolated via column chromatography (Silica gel, 2% EtOAc in DCM, r.f. 0.28) to give a waxy solid. Crystalline material was obtained by dissolving in a minimum amount of DCM and diluting with hexanes to *c.a.* five times original volume in a jacketed recrystallizing dish (being careful to not mix the layers excessively). This solution was then cooled to -5 $^{\circ}$C using a cold recirculating pump and allowed to evaporate in ambient air. Yield 130 mg yellow orange crystalline solid (87%). ^{1}H NMR (499 MHz, 298K, CDCl3) δ 6.68 (s, 2H) 4.26 (m, 4H), 4.18 (m, 4H) ^{13}C NMR (126 MHz, 298K, $CDCl_3$) δ 188.0 (C=O, central ring),, 175.4 (C=O, peripheral), 145.7 (C_q, 3-posn on EDOT) 141.7 (CH=CH, central ring) 136.4 (C_q, 4-posn on EDOT), 117.9 (CH, 2-posn on EDOT), 111.2 (5-posn on EDOT), 65.4 (CH_2 , -OCH_2CH_2O-) 63.9 (CH_2 , -OCH_2CH_2O-) IR (KBr pellet, cm^{-1}) 3097 (w),

2920 (w), 2848 (w), 1684 (m), 1628 (s), 1533 (w) 1487 (vs), 1450 (s) 1431 (s), 1369, (m), 1290 (s), 1186 (w), 1068 (s), 912 (m), 829 (w), 729 (w)

4,6-bis(2,3-dihydrothieno[3,4-b][1,4]dioxin-5-yl)thieno[3,4-d][1,3]dithiol-2-one (75b)

74b (150 mg, 0.329 mmol) was dissolved in 8 mL anhydrous DCM to give a light yellow translucent solution. Lawesson's reagent (140 mg 0.345 mmol) was added in one portion as a solid, and the flask was immediately fitted with a reflux condenser and placed in a preheated oil bath to reach reflux in <1 minute. Over the course of the reflux, the light yellow solution darkens to an opaque black color. After 16 hours, the solution was poured into 200 mL methanol. The flask was rinsed with methanol, using sonication to suspend all black solid left in the flask, then adding the bulk solution. The solution was filtered to separate the black solid (crude product) from the green solution. After Soxhlet extraction of the black solid 127.5 mg of **75b** (85%) was obtained as a yellow-brown solid. ^{1}H NMR (499 MHz, 298K, CDCl3) δ 6.43 (2, 2H) 4.39 (m, 4H), 4.29 (m, 4H) ^{13}C NMR (126 MHz, 298K, $CDCl_3$) was not obtained for this compound due to the extremely low solubility of the compound in all organic solvents tested. IR (Thin film on PET, cm^{-1}) 3094 (vw), 1686 (wv), 1637 (m), 1504 (s) 1369 (m), 1288 (w), 1171 (s), 1068 (s), 910 (m), 860 (m)

(2,5-bis(2,3-dihydrothieno[3,4-*b*][1,4]dioxin-5-yl)thiophen-μ-3,4-dithiolato)diiron hexacarbonyl (64)

75b (125.3 mg, 0.276 mmol) was added to a dry, two neck round bottom flask followed by degassed THF (80 mL) and the solution was sonicated and stirred for 20 minutes to disperse reagents. $Fe_2(CO)_9$ (602 mg, 1.65 mmol) was then added and the solution was heated to reflux for 2 hours in a preheated oil bath. The solution is cooled to room temperature then filtered over a 2" pad of silica gel eluted with DCM until the red color dissipates (ca. 150 mL). Concentration on rotovap gives a dark red film which is purified via column chromatography (Sigel, 15% → 35% DCM in hexanes → 50% DCM in hexanes) to elute a green band followed by a red band which was concentrated on the rotovap to obtain the product as a powdery red solid (30.2 mg, 15%) in the second red band, which is pure by ^{1}H NMR analysis. Crystals of suitable quality for XRD were obtained via vapor diffusion of ethanol or isopropyl alcohol into a saturated solution of toluene. CCDC 1834277 contains the supplementary crystallographic data for **64** These data are provided free of charge by The Cambridge Crystallographic Data Centre. ^{1}H NMR (499 MHz, 298K, $CDCl_3$) δ 6.38 (s, 2H) 4.31 (m, 4H) 4.22 (m, 4H) ^{13}C NMR (126 MHz, 298K, $CDCl_3$) δ 209.0 (Fe-C=O), 173.6, 145.8, 144.2, 141.7, 117.6, 111.7, 65.4 (CH_2-O), 63.9(CH_2-O), IR (KBr pellet, cm^{-1}) 2931 (m), 2871 (m), 2075 (s), 2042(vs), 2004 (s) 1499 (vs), 1437 (vs), 1361 (vs), 1116 (m), 1068 (vs), 862 (s)

X-Ray Crystallography of 64

Crystal structures for **62** and **63** were previously obtained by Dr. Laura Stratton and Steven Sill respectively. A single crystal of **64** was grown via vapor diffusion of ethanol into a solution of **64** in toluene under an argon atmosphere. A large, rectangular red block was obtained after several weeks, rinsed with a small amount of ethanol and suspended in Paratone® oil to minimize O_2 exposure. The crystal was found to be suitable for X-ray diffraction at 150 K.

Data was collected at the University of Arizona X-ray Diffraction Facility. Crystals were mounted onto a *MiTeGen* micromount under a protective film of Paratone® oil and diffraction data for all crystals were measured using a Bruker Kappa APEX II DUO diffractometer, with graphite-monochromated Mo-Kα radiation (λ = 0.71073 Å) generated by a sealed tube, and an APEX II CCD area detector. The diffractometer was fitted with an Oxford Cryostream low-

temperature device and data sets were collected using the *APEX2* software package (Bruker AXS Inc., Madison, WI, 2007). The data were corrected for absorption effects using a multi-scan method in *SADABS*[154]. CCDC 1577155 contains the supplementary crystallographic data for this paper. These data are provided free of charge by The Cambridge Crystallographic Data Centre. All structures were solved by direct methods (*SHELXS-97*)[155], and developed by full least-squares refinement based upon F^2 (*SHELXL*)[156] interfaced *via X-Seed*[157] and *OLEX2*[158] Crystallographic figures were prepared using *Mercury* (Version 3.9).

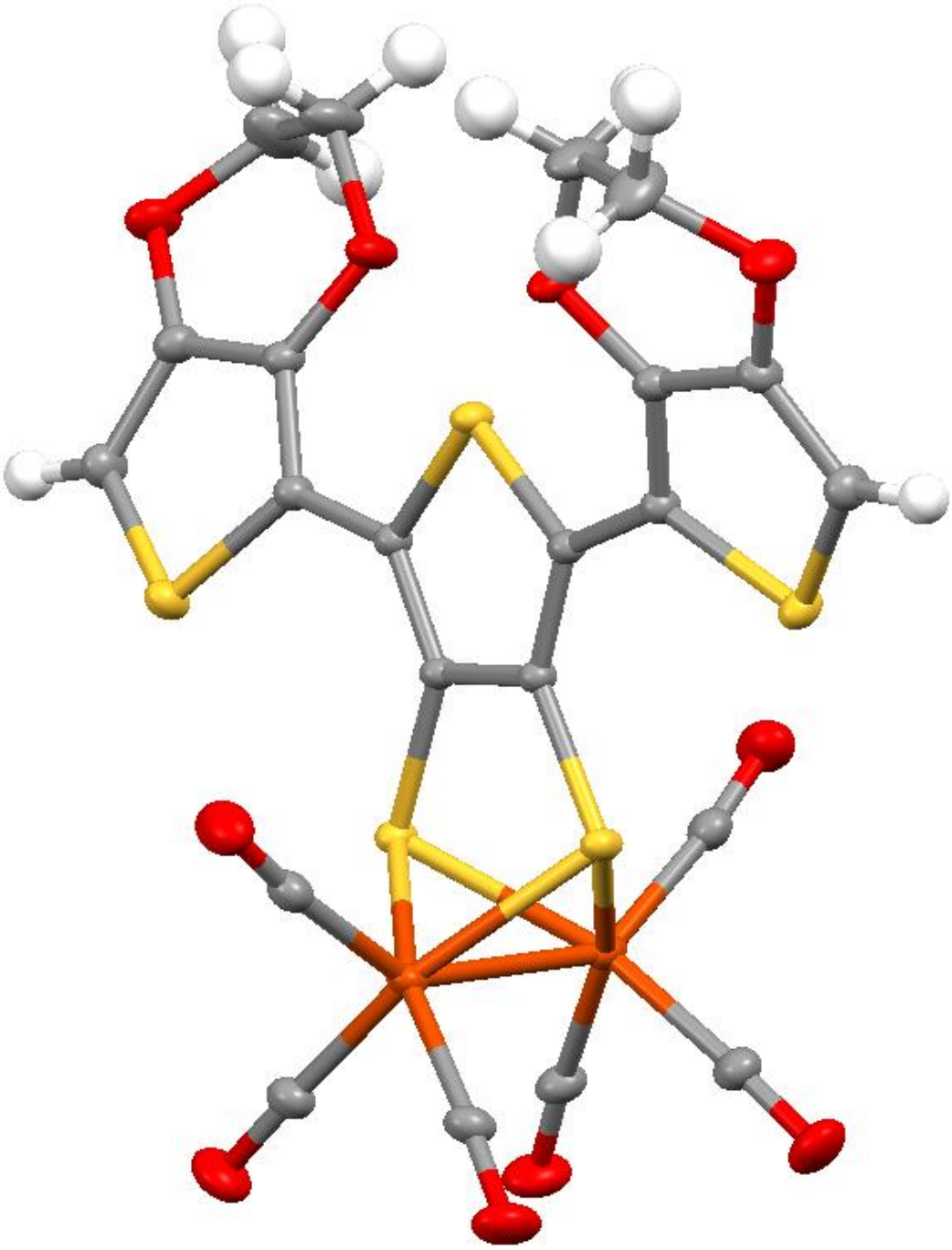

Figure 2.13. Oak Ridge thermal ellipsoid plot (ORTEP) diagram of **64** with thermal ellipsoids shown at 50% probability level. CCDC 1834277 contains the supplementary crystallographic data for 64 (synthesized, crystalized, and collected by William Brezinski). These data are provided free of charge by The Cambridge Crystallographic Data Centre

NMR Spectra of New Compounds

4,6-bis(2,3-dihydrothieno[3,4-b][1,4]dioxin-5-yl)thieno[3,4-d][1,3]dithiole-2-thione (73b)

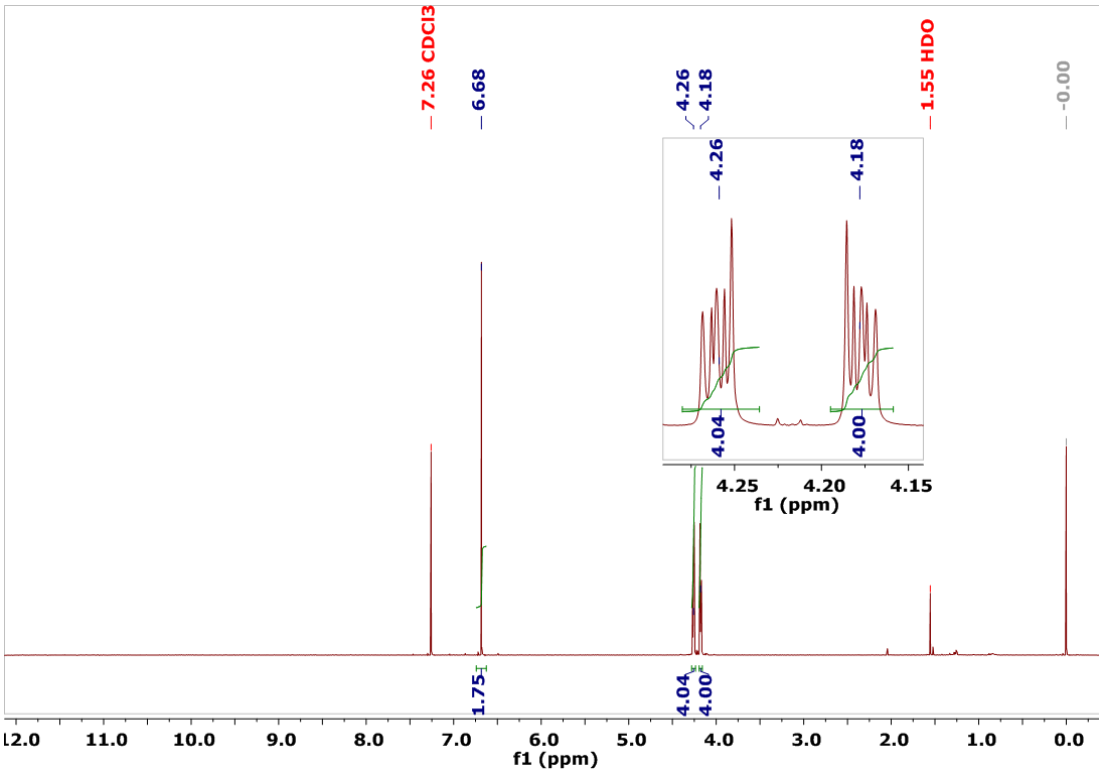

Figure 2.14. ^{1}H NMR spectrum of triketone **73b**

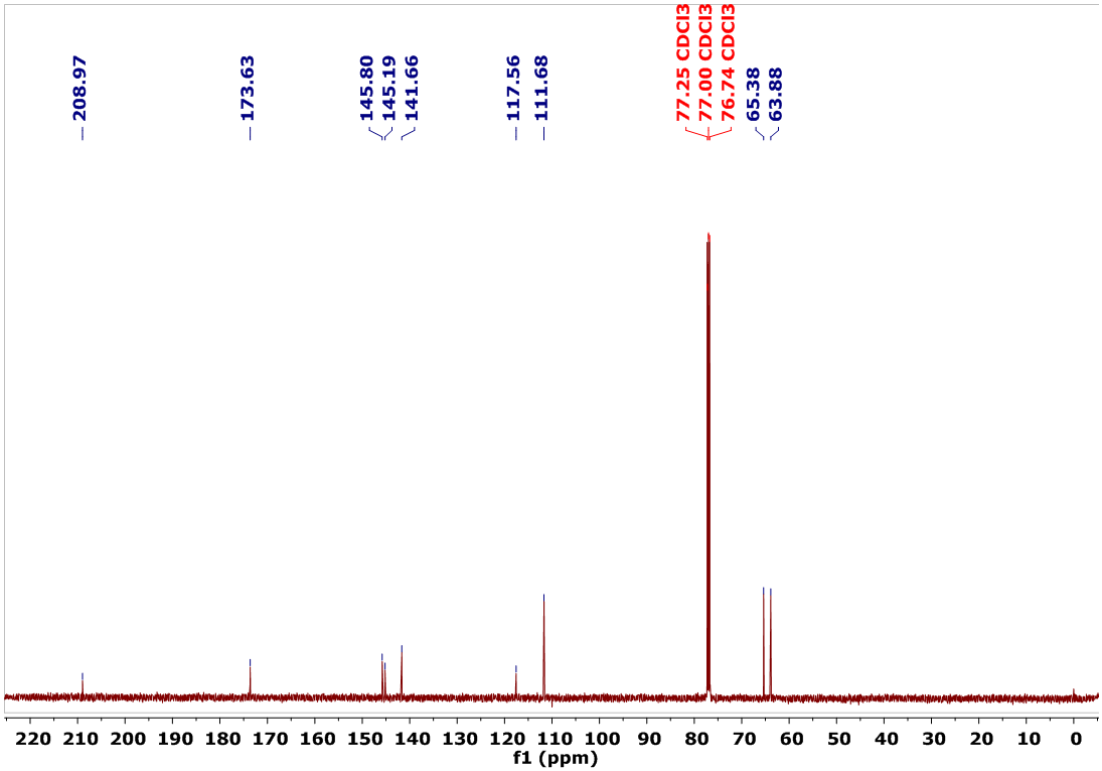

Figure 2.15. ^{13}C NMR spectrum of triketone **73b**

4,6-bis(2,3-dihydrothieno[3,4-b][1,4]dioxin-5-yl)thieno[3,4-d][1,3]dithiol-2-one (74b)

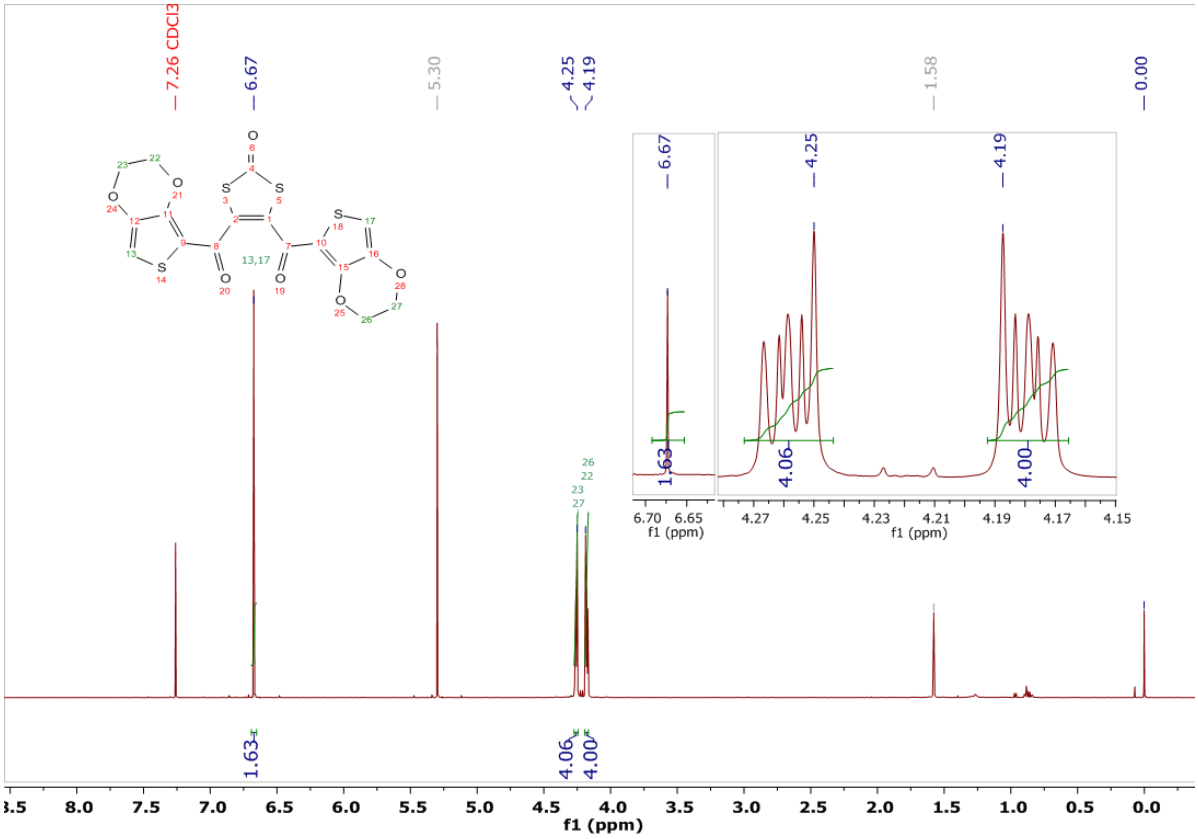

Figure 2.16. ^{1}H NMR spectrum of triketone **74b**

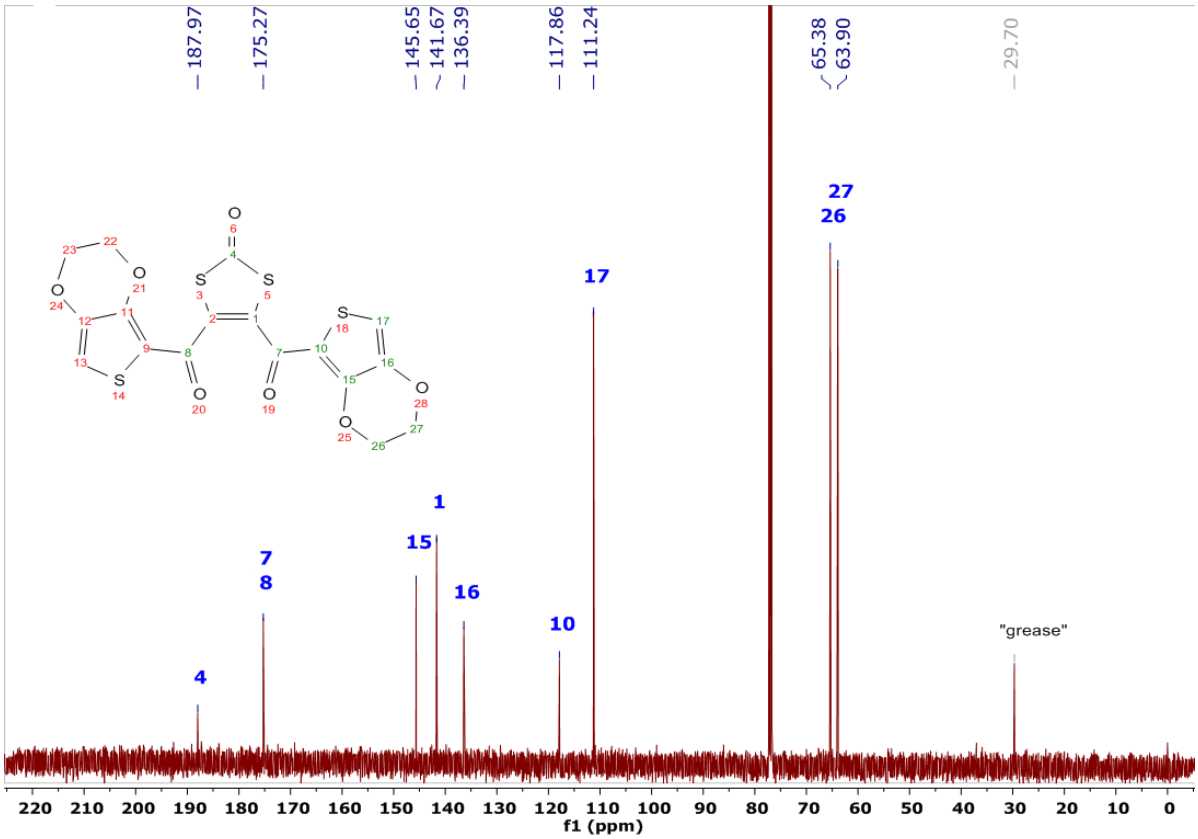

Figure 2.17. ^{13}C NMR spectrum of triketone **74b**

4,6-bis(2,3-dihydrothieno[3,4-b][1,4]dioxin-5-yl)thieno[3,4-d][1,3]dithiol-2-one (75b)

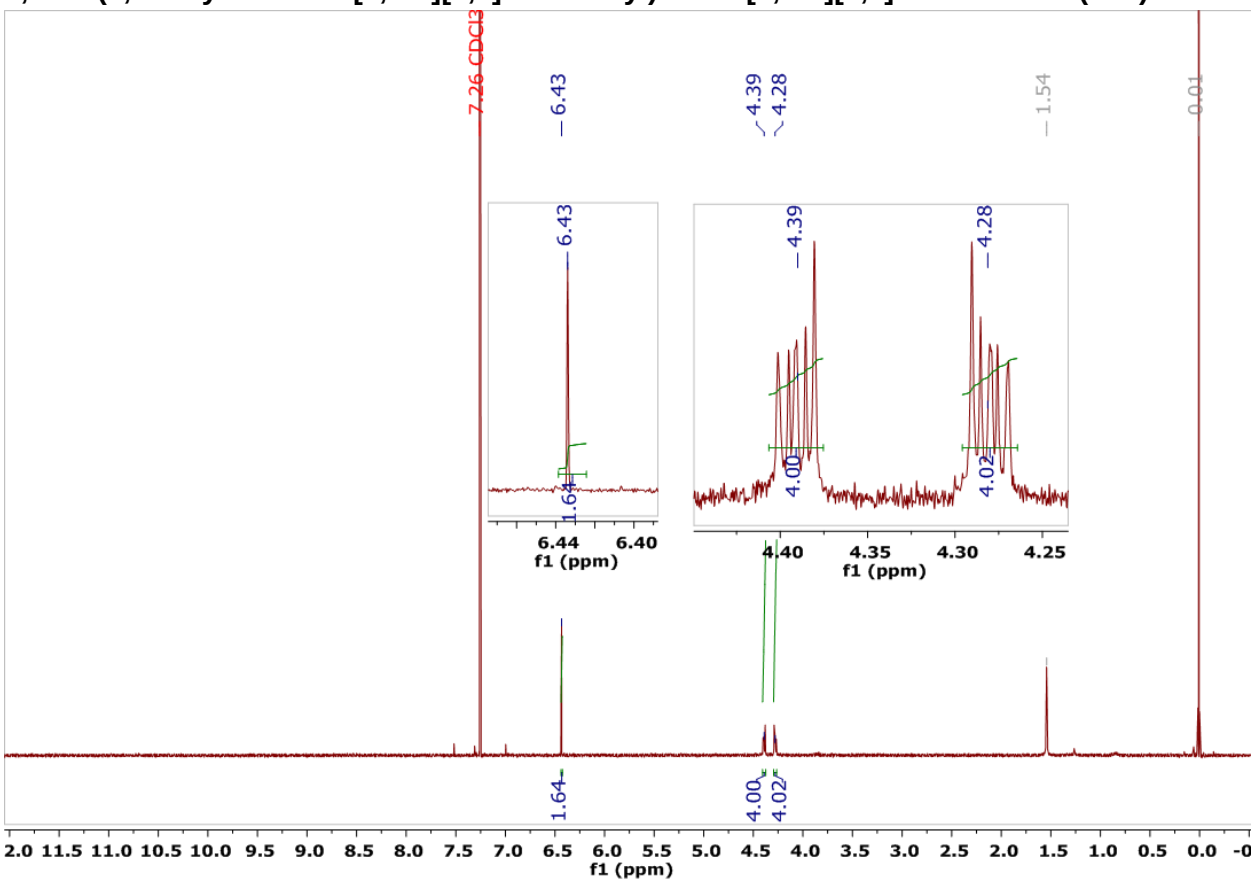

Figure 2.18. ^{1}H NMR spectrum of EDOT-Thiophene-EDOT ligand **75b**

(2,5-bis(2,3-dihydrothieno[3,4-*b*][1,4]dioxin-5-yl)thiophen-μ-3,4-dithiolato)diiron hexacarbonyl (64)

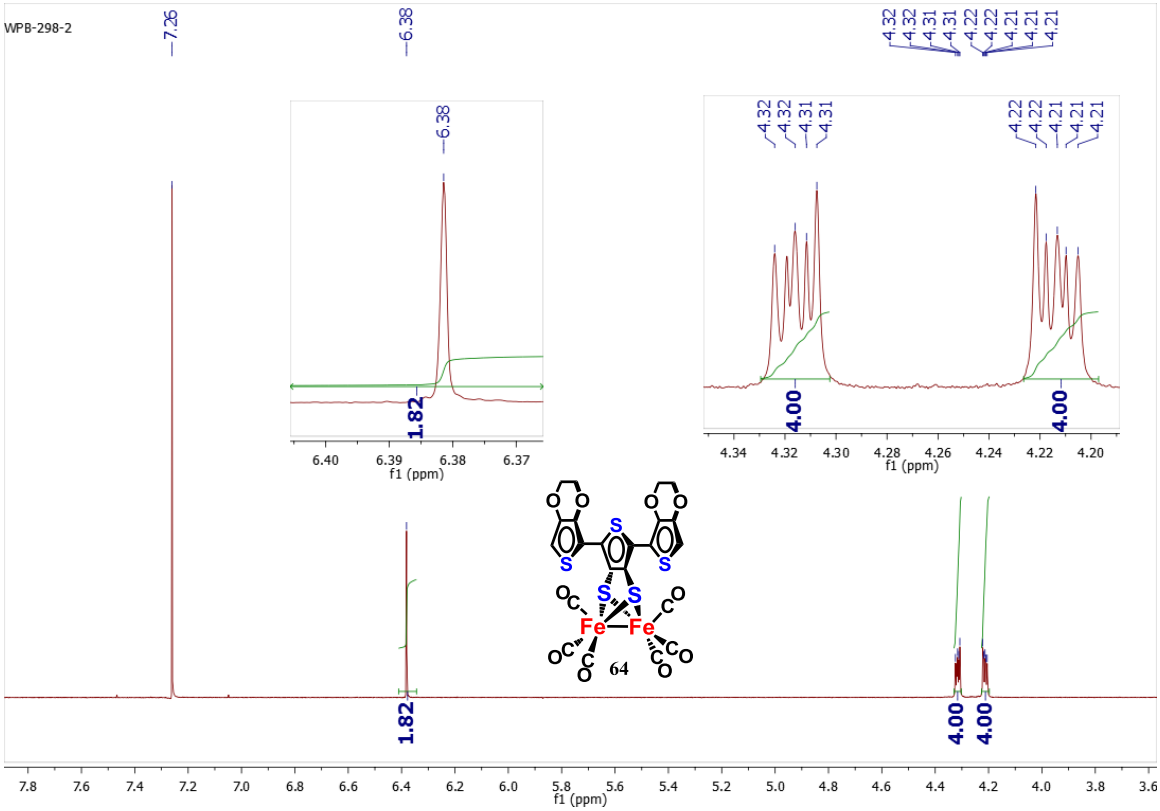

Figure 2.19. ^{1}H NMR spectrum (499 MHz, CDCl3, 298K) of **64.**

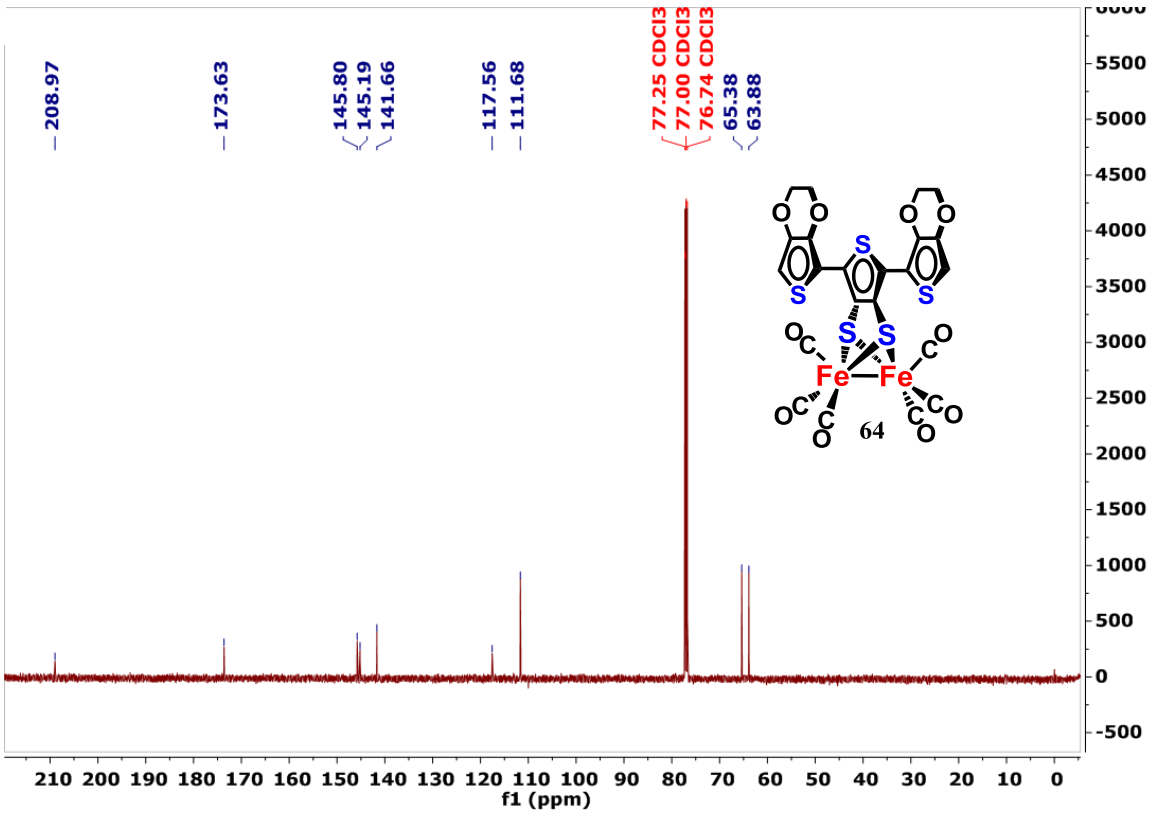

Figure 2.20. ^{13}C NMR spectrum (126 MHz, $CDCl_3$, 298K) of **64**.

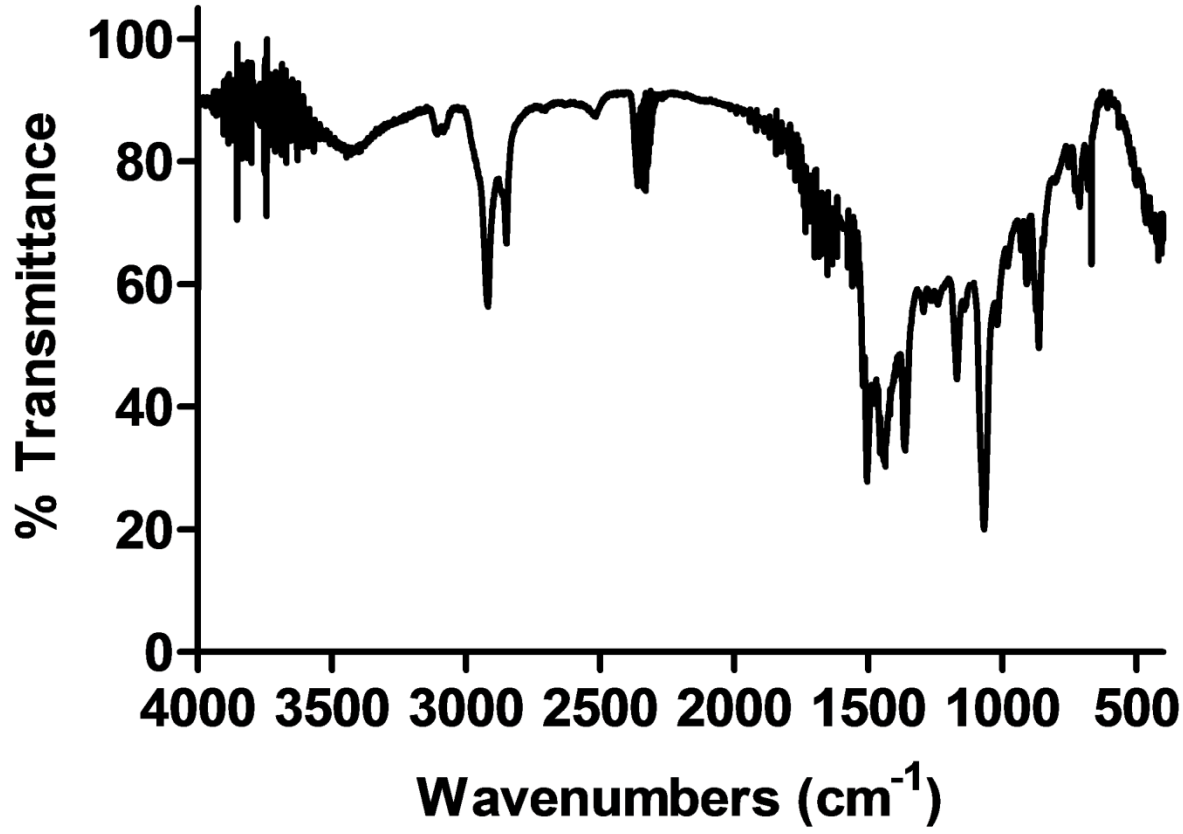

Figure 2.21. Full IR spectrum of ETEcatalyst **64**.

X-Ray Crystal Data Tables

i. Thiophene-μ-3,4-dithiolato)diiron hexacarbonyl (62)

Table 2.2. Fractional Atomic Coordinates (×10^4) and Equivalent Isotropic Displacement Parameters (Å^2×10^3) for 62.

Table 2 Fractional Atomic Coordinates (×10^4) and Equivalent Isotropic Displacement Parameters (Å^2×10^3) for(62). U_{eq} is defined as 1/3 of of the trace of the orthogonalised U_{IJ} tensor.				
Atom	***x***	***y***	***z***	**U(eq)**
Fe1	2060.2(2)	5247.7(3)	6814.5(2)	11.77(7)
Fe2	2027.0(2)	5234.0(3)	4955.9(2)	11.33(7)
S1	3093.1(3)	6773.5(6)	6025.7(3)	12.7(1)
S2	2482.5(3)	2627.8(6)	5949.4(3)	12.18(10)
S3	5294.4(3)	2854.6(7)	6335.8(3)	19.67(11)
O1	2997.3(8)	4633.9(17)	3227.2(9)	20.0(3)
O2	368.8(8)	3175.5(18)	4323.1(9)	23.1(3)
O3	1150.4(8)	8974.7(18)	4409.9(9)	23.0(3)
O4	3074.7(8)	4754.5(17)	8836.9(10)	23.1(3)
O5	434.5(8)	3176.1(18)	7071.2(9)	24.5(3)
O6	1198.7(8)	9022.2(18)	7022.0(9)	20.7(3)
C1	2607.9(11)	4855(2)	3886.6(13)	14.1(4)

C2	1017.9(11)	3965(2)	4551.9(12)	15.3(4)
C3	1498.3(11)	7536(3)	4621.0(12)	15.7(4)
C4	2675.9(12)	4939(2)	8058.5(14)	16.0(4)
C5	1069.1(11)	3978(3)	6983.6(12)	16.0(4)
C6	1534.9(11)	7570(3)	6952.0(12)	15.0(4)
C7	4806.3(11)	5126(3)	6270.2(13)	15.7(4)
C8	3922.1(11)	4959(2)	6145.0(12)	13.2(4)
C9	3630.2(10)	2994(2)	6101.1(12)	12.2(3)
C10	4292.0(11)	1693(3)	6190.8(13)	18.2(4)

Table 2.3. Anisotropic Displacement Parameters ($Å^2×10^3$) for (62)

Table 3 Anisotropic Displacement Parameters ($Å^2×10^3$) for (62). The Anisotropic displacement factor exponent takes the form: $-2\pi^2[h^2a^{*2}U_{11}+2hka^*b^*U_{12}+\ldots]$.						
Atom	**U_{11}**	**U_{22}**	**U_{33}**	**U_{23}**	**U_{13}**	**U_{12}**
Fe1	11.58(13)	12.22(14)	11.63(13)	-0.32(9)	2.05(10)	-0.55(9)
Fe2	11.19(13)	11.28(14)	11.22(13)	0.24(9)	0.44(10)	0.29(9)
S1	12.2(2)	10.9(2)	14.9(2)	-0.35(17)	1.51(16)	-0.91(16)
S2	11.2(2)	11.2(2)	13.8(2)	0.22(16)	0.71(16)	-0.61(16)
S3	12.3(2)	19.2(2)	27.1(2)	3.55(19)	1.14(18)	1.97(18)
O1	20.6(7)	23.0(7)	17.5(7)	-2.4(5)	5.9(6)	-0.8(5)
O2	16.5(7)	20.4(7)	30.7(7)	-1.3(6)	-2.9(6)	-2.1(6)
O3	24.7(7)	16.9(7)	26.9(7)	3.2(6)	1.4(6)	4.7(6)
O4	26.6(7)	24.7(8)	16.3(7)	2.7(5)	-3.5(6)	-4.1(6)
O5	18.8(7)	22.3(7)	34.2(8)	0.8(6)	9.8(6)	-3.7(6)
O6	19.3(7)	16.4(7)	26.6(7)	-3.2(6)	4.0(5)	2.6(6)
C1	12.9(9)	11.2(9)	16.2(9)	1.6(7)	-4.7(7)	-0.2(7)
C2	18.6(9)	12.3(9)	15.1(9)	-0.2(7)	2.1(7)	5.2(8)
C3	14.4(9)	19.8(10)	12.8(8)	-0.5(7)	1.9(7)	-3.4(8)
C4	16.1(9)	12.5(9)	20.8(10)	-1.1(7)	7.4(8)	-1.2(7)
C5	18.6(9)	14.1(9)	15.6(9)	-0.7(7)	3.2(7)	5.4(8)
C6	13.4(9)	20.2(10)	11.3(8)	-1.2(7)	1.9(7)	-5.5(8)
C7	15.0(9)	16(1)	16.2(9)	1.7(7)	2.0(7)	-2.4(7)
C8	15.6(9)	14.1(9)	9.8(8)	1.4(7)	1.2(7)	0.9(7)
C9	11.4(8)	14.8(9)	10.1(8)	1.2(7)	0.2(6)	-1.6(7)
C10	16.1(9)	15(1)	23.2(10)	3.0(8)	1.5(7)	-1.6(8)

Table 2.4. Bond Lengths for (62).

Table 4 Bond Lengths for (62).						
Atom	**Atom**	**Length/Å**		**Atom**	**Atom**	**Length/Å**
Fe1	Fe2	2.4753(3)		S2	C9	1.7693(16)
Fe1	S1	2.2790(5)		S3	C7	1.7250(18)
Fe1	S2	2.2772(5)		S3	C10	1.7240(18)
Fe1	C4	1.8083(19)		O1	C1	1.142(2)

Fe1	C5	1.7980(18)		O2	C2	1.141(2)
Fe1	C6	1.8059(18)		O3	C3	1.138(2)
Fe2	S1	2.2812(5)		O4	C4	1.139(2)
Fe2	S2	2.2769(5)		O5	C5	1.141(2)
Fe2	C1	1.8050(18)		O6	C6	1.131(2)
Fe2	C2	1.7978(18)		C7	C8	1.354(2)
Fe2	C3	1.8031(18)		C8	C9	1.418(2)
S1	C8	1.7734(17)		C9	C10	1.347(2)

Table 2.5. Bond Angles for (62)

Table 5 Bond Angles for (62).								
Atom	**Atom**	**Atom**	**Angle/°**		**Atom**	**Atom**	**Atom**	**Angle/°**
S1	Fe1	Fe2	57.167(12)		C3	Fe2	Fe1	101.05(5)
S2	Fe1	Fe2	57.070(13)		C3	Fe2	S1	90.71(5)
S2	Fe1	S1	82.005(16)		C3	Fe2	S2	157.36(5)
C4	Fe1	Fe2	148.93(6)		C3	Fe2	C1	100.70(7)
C4	Fe1	S1	99.62(6)		Fe1	S1	Fe2	65.752(14)
C4	Fe1	S2	102.92(5)		C8	S1	Fe1	100.18(6)
C5	Fe1	Fe2	102.90(5)		C8	S1	Fe2	100.34(6)
C5	Fe1	S1	159.82(5)		Fe2	S2	Fe1	65.851(14)
C5	Fe1	S2	89.37(5)		C9	S2	Fe1	100.40(6)
C5	Fe1	C4	100.08(8)		C9	S2	Fe2	100.27(5)
C5	Fe1	C6	90.78(7)		C10	S3	C7	91.92(9)
C6	Fe1	Fe2	99.06(5)		O1	C1	Fe2	178.00(15)
C6	Fe1	S1	89.64(5)		O2	C2	Fe2	177.87(15)
C6	Fe1	S2	155.41(5)		O3	C3	Fe2	178.79(15)
C6	Fe1	C4	101.26(7)		O4	C4	Fe1	178.98(16)
S1	Fe2	Fe1	57.081(13)		O5	C5	Fe1	178.66(15)
S2	Fe2	Fe1	57.080(13)		O6	C6	Fe1	178.84(15)
S2	Fe2	S1	81.962(16)		C8	C7	S3	110.75(13)
C1	Fe2	Fe1	148.16(5)		C7	C8	S1	130.66(13)
C1	Fe2	S1	99.76(5)		C7	C8	C9	113.14(15)
C1	Fe2	S2	101.64(5)		C9	C8	S1	116.20(12)
C2	Fe2	Fe1	101.57(5)		C8	C9	S2	116.46(12)
C2	Fe2	S1	158.37(5)		C10	C9	S2	130.39(14)
C2	Fe2	S2	88.85(5)		C10	C9	C8	113.14(15)
C2	Fe2	C1	101.26(7)		C9	C10	S3	111.05(14)
C2	Fe2	C3	90.36(7)					

Table 2.6. Torsion Angles for (62)

Table 6 Torsion Angles for (62).										
A	**B**	**C**	**D**	**Angle/°**		**A**	**B**	**C**	**D**	**Angle/°**
Fe1	S1	C8	C7	-146.23(16)		S1	C8	C9	C10	179.65(12)
Fe1	S1	C8	C9	34.03(13)		S2	C9	C10	S3	-179.35(10)
Fe1	S2	C9	C8	-32.97(13)		S3	C7	C8	S1	-179.72(10)
Fe1	S2	C9	C10	146.54(16)		S3	C7	C8	C9	0.02(19)
Fe2	S1	C8	C7	146.81(16)		C7	S3	C10	C9	-0.14(14)
Fe2	S1	C8	C9	-32.93(13)		C7	C8	C9	S2	179.46(12)
Fe2	S2	C9	C8	34.11(13)		C7	C8	C9	C10	-0.1(2)
Fe2	S2	C9	C10	-146.38(16)		C8	C9	C10	S3	0.18(19)
S1	C8	C9	S2	-0.75(17)		C10	S3	C7	C8	0.07(14)

Table 2.7. Hydrogen Atom Coordinates (Å×10^4) and Isotropic Displacement Parameters (Å^2×10^3) for (62).

Table 7 Hydrogen Atom Coordinates (Å×10^4) and Isotropic Displacement Parameters (Å^2×10^3) for (62).				
Atom	***x***	***y***	***z***	**U(eq)**
H7	5145(12)	6250(30)	6325(13)	23(5)
H10	4254(13)	450(30)	6184(14)	26(6)

ii. (2,5-bis-(2',2"-thiophen-2-yl)-thiophene-μ-3,4-dithiolato)diiron hexacarbonyl (63)

Table 2.8. Fractional Atomic Coordinates (×10^4) and Equivalent Isotropic Displacement Parameters (Å^2×10^3) for (63)

Table 8 Fractional Atomic Coordinates (×10^4) and Equivalent Isotropic Displacement Parameters (Å^2×10^3) for (63). U_{eq} is defined as 1/3 of of the trace of the orthogonalised U_{IJ} tensor.				
Atom	***x***	***y***	***z***	**U(eq)**
Fe1	4507.6(6)	2872.18(19)	1009.9(3)	11.04(12)
Fe2	4013.4(6)	2896.08(19)	2702.0(3)	11.04(12)
S1	6334.6(10)	2321.3(3)	2298.2(5)	10.82(16)
S2	2117.1(10)	2346.8(3)	1429.7(5)	10.64(16)
S4	4066.8(10)	470.0(3)	2004.7(5)	12.27(16)
C2	6471(4)	3390.2(15)	1056(2)	16.6(6)
O5	6875(3)	3824.3(11)	3636(2)	29.5(6)
O3	1756(3)	3835.1(11)	80.3(17)	22.9(5)
C11	2353(4)	1032.3(13)	1524(2)	10.1(6)
C3	2818(4)	3457.3(14)	428(2)	15.4(6)
C5	5772(4)	3456.0(15)	3283(2)	17.7(7)
O2	7715(3)	3720.5(11)	1074.8(17)	25.8(5)
C14	5879(4)	1018.3(13)	2397(2)	10.2(6)
O6	1035(3)	3825.6(12)	2687.9(18)	28.3(6)
C10	400(4)	847.6(13)	1065(2)	10.3(6)
C15	7768(4)	807.1(14)	2929(2)	12.2(6)
C1	4714(4)	2431.7(14)	-54(2)	13.9(6)
C6	2158(4)	3457.8(15)	2675(2)	17.1(6)
C18	11179(5)	720.0(17)	3816(2)	22.2(7)
C12	3175(4)	1607.3(14)	1666(2)	10.3(6)
C7	-3009(4)	796.0(15)	135(2)	16.5(6)
C13	5171(4)	1595.8(13)	2133(2)	9.5(5)
O4	3605(3)	2138.3(10)	4383.3(16)	20.2(5)
O1	4858(3)	2146.7(10)	-710.3(16)	18.8(5)
C4	3760(4)	2441.8(14)	3748(2)	14.2(6)
S3	-1309.0(11)	1365.2(4)	439.1(6)	16.52(17)
S5	9691.4(11)	1299.2(4)	3284.4(6)	19.59(18)
C9	-362(4)	255.7(15)	1044(2)	16.0(6)
C8	-2321(4)	238.5(15)	501(2)	17.0(6)
C16	8263(4)	182.2(16)	3275(2)	20.7(5)
C17	10268(4)	170.5(16)	3749(2)	20.7(5)

Table 2.9. Anisotropic Displacement Parameters ($Å^2×10^3$) for (63)

Table 9 Anisotropic Displacement Parameters ($Å^2×10^3$) for (63). The Anisotropic displacement factor exponent takes the form: $-2\pi^2[h^2a^{*2}U_{11}+2hka^*b^*U_{12}+\ldots]$.						
Atom	**U_{11}**	**U_{22}**	**U_{33}**	**U_{23}**	**U_{13}**	**U_{12}**
Fe1	10.1(2)	8.7(2)	12.2(2)	0.57(16)	-0.93(16)	-1.96(15)
Fe2	9.6(2)	8.9(2)	12.5(2)	-2.43(16)	-1.01(16)	0.58(16)
S1	8.3(3)	8.8(3)	13.4(3)	-1.0(3)	-0.5(3)	-1.0(3)
S2	7.8(3)	8.5(3)	13.4(3)	-0.2(3)	-1.3(3)	-0.3(3)
S4	11.1(3)	8.2(3)	16.6(4)	-0.2(3)	2.0(3)	-0.4(3)
C2	18.8(16)	14.1(16)	13.3(15)	0.6(12)	-2.3(12)	0.8(13)
O5	19.4(12)	18.5(13)	44.8(15)	-13.1(12)	-2.1(11)	-3.2(10)
O3	19.5(12)	16.9(12)	29.8(13)	7.3(10)	1.6(10)	3.5(10)
C11	9.0(13)	11.8(14)	9.5(13)	-0.2(11)	2.4(10)	-0.1(11)
C3	16.2(15)	13.5(15)	15.9(15)	-1.8(12)	2.8(12)	-7.2(13)
C5	14.3(15)	12.0(15)	25.1(17)	-2.2(13)	1.7(13)	4.8(13)
O2	22.8(12)	25.7(14)	24.9(13)	3.5(10)	-1.3(10)	-13.0(11)
C14	9.9(13)	11.2(15)	9.6(13)	-1.4(11)	2.8(11)	-0.1(11)
O6	23.9(13)	27.6(14)	28.0(13)	-6.9(11)	-3.1(10)	12.5(11)
C10	10.5(13)	10.5(14)	9.9(13)	-0.7(11)	2.6(11)	-0.9(11)
C15	10.4(14)	14.8(15)	10.7(13)	-0.8(12)	1.3(11)	1.1(11)
C1	7.3(13)	14.5(16)	16.7(15)	3.5(13)	-2.4(11)	-2.3(11)
C6	17.9(15)	16.2(16)	13.1(15)	-2.6(12)	-3.4(12)	0.7(13)
C18	12.1(15)	34(2)	18.0(16)	-3.1(14)	-0.6(12)	7.1(14)
C12	9.8(13)	10.2(14)	10.4(13)	0.5(11)	1.3(11)	0.7(11)
C7	12.6(14)	16.5(16)	18.9(15)	-0.8(13)	1.3(12)	-6.6(12)
C13	9.5(13)	9.1(14)	9.9(13)	-0.8(11)	2.4(11)	-1.0(11)
O4	23.1(12)	20.6(12)	16.3(11)	2.9(10)	3.9(9)	2.3(10)
O1	18.3(11)	18.0(12)	17.4(11)	-1.3(9)	-0.1(9)	-1.9(9)
C4	9.4(14)	12.7(15)	17.9(15)	-7.8(13)	-1.4(11)	1.7(11)
S3	12.1(4)	14.5(4)	19.4(4)	4.0(3)	-2.5(3)	-3.4(3)
S5	14.7(4)	22.5(4)	20.0(4)	-0.8(3)	1.5(3)	2.3(3)
C9	10.5(14)	16.5(16)	21.8(16)	-9.0(13)	5.4(12)	-4.8(12)
C8	13.6(15)	14.5(16)	22.1(16)	-3.9(13)	2.9(12)	-5.2(12)
C16	14.0(11)	16.1(12)	27.9(12)	0.1(10)	-2.0(9)	8.5(9)
C17	14.0(11)	16.1(12)	27.9(12)	0.1(10)	-2.0(9)	8.5(9)

Table 2.10. Bond Lengths for (63)

Table 10 Bond Lengths for (63).						
Atom	**Atom**	**Length/Å**		**Atom**	**Atom**	**Length/Å**
Fe1	Fe2	2.4889(6)		C11	C10	1.449(4)
Fe1	S1	2.2810(8)		C11	C12	1.370(4)
Fe1	S2	2.2679(8)		C14	C15	1.452(4)
Fe1	C2	1.796(3)		C14	C13	1.363(4)
Fe1	C3	1.802(3)		O6	C6	1.140(4)
Fe1	C1	1.808(3)		C10	S3	1.730(3)
Fe2	S1	2.2729(8)		C10	C9	1.390(4)
Fe2	S2	2.2844(8)		C15	S5	1.720(3)
Fe2	C5	1.793(3)		C15	C16	1.448(4)
Fe2	C6	1.802(3)		C1	O1	1.134(4)
Fe2	C4	1.813(3)		C18	S5	1.694(3)
S1	C13	1.766(3)		C18	C17	1.350(5)
S2	C12	1.766(3)		C12	C13	1.424(4)
S4	C11	1.743(3)		C7	S3	1.714(3)
S4	C14	1.748(3)		C7	C8	1.353(4)
C2	O2	1.144(4)		O4	C4	1.135(4)
O5	C5	1.145(4)		C9	C8	1.426(4)
O3	C3	1.141(4)		C16	C17	1.432(4)

Table 2.11. Bond Angles for (63)

Table 11 Bond Angles for (63).								
Atom	**Atom**	**Atom**	**Angle/°**		**Atom**	**Atom**	**Atom**	**Angle/°**
S1	Fe1	Fe2	56.71(2)		C12	S2	Fe2	100.33(9)
S2	Fe1	Fe2	57.17(2)		C11	S4	C14	92.88(14)
S2	Fe1	S1	81.85(3)		O2	C2	Fe1	179.2(3)
C2	Fe1	Fe2	104.93(10)		C10	C11	S4	119.6(2)
C2	Fe1	S1	90.27(10)		C12	C11	S4	109.7(2)
C2	Fe1	S2	161.89(10)		C12	C11	C10	130.6(3)
C2	Fe1	C3	90.95(14)		O3	C3	Fe1	178.3(3)
C2	Fe1	C1	97.27(13)		O5	C5	Fe2	178.3(3)
C3	Fe1	Fe2	99.86(10)		C15	C14	S4	118.6(2)
C3	Fe1	S1	155.91(10)		C13	C14	S4	109.7(2)
C3	Fe1	S2	89.76(10)		C13	C14	C15	131.7(3)
C3	Fe1	C1	100.68(13)		C11	C10	S3	122.3(2)
C1	Fe1	Fe2	149.31(10)		C9	C10	C11	126.8(3)
C1	Fe1	S1	103.01(10)		C9	C10	S3	110.9(2)
C1	Fe1	S2	100.37(9)		C14	C15	S5	122.6(2)
S1	Fe2	Fe1	57.02(2)		C16	C15	C14	125.8(3)
S1	Fe2	S2	81.67(3)		C16	C15	S5	111.5(2)
S2	Fe2	Fe1	56.54(2)		O1	C1	Fe1	178.8(3)
C5	Fe2	Fe1	100.89(10)		O6	C6	Fe2	177.2(3)
C5	Fe2	S1	89.94(10)		C17	C18	S5	112.1(2)
C5	Fe2	S2	156.85(11)		C11	C12	S2	130.0(2)
C5	Fe2	C6	89.56(14)		C11	C12	C13	113.7(3)
C5	Fe2	C4	101.82(14)		C13	C12	S2	116.2(2)
C6	Fe2	Fe1	106.37(10)		C8	C7	S3	112.0(2)
C6	Fe2	S1	162.91(10)		C14	C13	S1	130.1(2)
C6	Fe2	S2	92.24(10)		C14	C13	C12	114.0(3)
C6	Fe2	C4	98.78(14)		C12	C13	S1	115.9(2)
C4	Fe2	Fe1	146.00(9)		O4	C4	Fe2	177.5(3)
C4	Fe2	S1	98.04(9)		C7	S3	C10	92.04(15)
C4	Fe2	S2	100.70(9)		C18	S5	C15	92.62(16)
Fe2	S1	Fe1	66.26(2)		C10	C9	C8	111.7(3)
C13	S1	Fe1	101.54(10)		C7	C8	C9	113.4(3)
C13	S1	Fe2	99.24(9)		C17	C16	C15	107.8(3)
Fe1	S2	Fe2	66.29(2)		C18	C17	C16	115.8(3)
C12	S2	Fe1	100.35(9)					

Table 2.12. Torsion Angles for (63).

Table 12 Torsion Angles for (63).										
A	**B**	**C**	**D**	**Angle/°**		**A**	**B**	**C**	**D**	**Angle/°**
Fe1	Fe2	S1	C13	-98.62(10)		C11	S4	C14	C13	-1.9(2)
Fe1	Fe2	S2	C12	96.85(9)		C11	C10	S3	C7	178.2(2)
Fe1	Fe2	C5	O5	57(10)		C11	C10	C9	C8	-178.2(3)
Fe1	Fe2	C6	O6	-122(7)		C11	C12	C13	S1	177.9(2)
Fe1	Fe2	C4	O4	-2(6)		C11	C12	C13	C14	-3.0(4)
Fe1	S1	C13	C14	152.5(3)		C3	Fe1	Fe2	S1	-173.91(10)
Fe1	S1	C13	C12	-28.6(2)		C3	Fe1	Fe2	S2	83.27(10)
Fe1	S2	C12	C11	-147.0(3)		C3	Fe1	Fe2	C5	-91.15(14)
Fe1	S2	C12	C13	37.5(2)		C3	Fe1	Fe2	C6	1.62(14)
Fe2	Fe1	S1	C13	95.12(9)		C3	Fe1	Fe2	C4	137.68(19)
Fe2	Fe1	S2	C12	-96.83(9)		C3	Fe1	S1	Fe2	14.8(2)
Fe2	Fe1	C2	O2	-161(100)		C3	Fe1	S1	C13	110.0(3)
Fe2	Fe1	C3	O3	31(10)		C3	Fe1	S2	Fe2	-101.92(10)
Fe2	Fe1	C1	O1	-32(13)		C3	Fe1	S2	C12	161.25(13)
Fe2	S1	C13	C14	-140.0(3)		C3	Fe1	C2	O2	-60(22)
Fe2	S1	C13	C12	38.9(2)		C3	Fe1	C1	O1	-163(13)
Fe2	S2	C12	C11	145.4(3)		C5	Fe2	S1	Fe1	-103.05(10)
Fe2	S2	C12	C13	-30.1(2)		C5	Fe2	S1	C13	158.33(14)
S1	Fe1	Fe2	S2	-102.81(3)		C5	Fe2	S2	Fe1	14.0(3)
S1	Fe1	Fe2	C5	82.76(10)		C5	Fe2	S2	C12	110.9(3)
S1	Fe1	Fe2	C6	175.54(11)		C5	Fe2	C6	O6	-21(7)
S1	Fe1	Fe2	C4	-48.41(17)		C5	Fe2	C4	O4	-133(6)
S1	Fe1	S2	Fe2	55.43(3)		C14	S4	C11	C10	-179.7(2)
S1	Fe1	S2	C12	-41.40(9)		C14	S4	C11	C12	0.2(2)
S1	Fe1	C2	O2	144(22)		C14	C15	S5	C18	179.8(3)
S1	Fe1	C3	O3	18(10)		C14	C15	C16	C17	179.2(3)
S1	Fe1	C1	O1	12(13)		C10	C11	C12	S2	5.8(5)
S1	Fe2	S2	Fe1	-55.76(3)		C10	C11	C12	C13	-178.7(3)
S1	Fe2	S2	C12	41.09(9)		C10	C9	C8	C7	-0.5(4)
S1	Fe2	C5	O5	114(10)		C15	C14	C13	S1	3.0(5)
S1	Fe2	C6	O6	-110(6)		C15	C14	C13	C12	-176.0(3)
S1	Fe2	C4	O4	-42(6)		C15	C16	C17	C18	3.5(4)
S2	Fe1	Fe2	S1	102.81(3)		C1	Fe1	Fe2	S1	54.67(18)
S2	Fe1	Fe2	C5	-174.42(10)		C1	Fe1	Fe2	S2	-48.15(18)
S2	Fe1	Fe2	C6	-81.65(11)		C1	Fe1	Fe2	C5	137.4(2)
S2	Fe1	Fe2	C4	54.41(17)		C1	Fe1	Fe2	C6	-129.8(2)
S2	Fe1	S1	Fe2	-55.87(3)		C1	Fe1	Fe2	C4	6.3(2)
S2	Fe1	S1	C13	39.25(9)		C1	Fe1	S1	Fe2	-154.70(9)
S2	Fe1	C2	O2	-152(22)		C1	Fe1	S1	C13	-59.58(13)
S2	Fe1	C3	O3	87(10)		C1	Fe1	S2	Fe2	157.26(10)

S2	Fe1	C1	O1	-71(13)		C1	Fe1	S2	C12	60.43(13)
S2	Fe2	S1	Fe1	55.30(3)		C1	Fe1	C2	O2	41(22)
S2	Fe2	S1	C13	-43.32(10)		C1	Fe1	C3	O3	-172(100)
S2	Fe2	C5	O5	45(10)		C6	Fe2	S1	Fe1	-14.7(3)
S2	Fe2	C6	O6	-178(100)		C6	Fe2	S1	C13	-113.3(4)
S2	Fe2	C4	O4	41(6)		C6	Fe2	S2	Fe1	108.19(10)
S2	C12	C13	S1	-5.9(3)		C6	Fe2	S2	C12	-154.96(14)
S2	C12	C13	C14	173.2(2)		C6	Fe2	C5	O5	-49(10)
S4	C11	C10	S3	-171.85(15)		C6	Fe2	C4	O4	135(6)
S4	C11	C10	C9	7.2(4)		C12	C11	C10	S3	8.3(4)
S4	C11	C12	S2	-174.12(18)		C12	C11	C10	C9	-172.7(3)
S4	C11	C12	C13	1.5(3)		C13	C14	C15	S5	-5.1(4)
S4	C14	C15	S5	175.96(15)		C13	C14	C15	C16	171.3(3)
S4	C14	C15	C16	-7.7(4)		C4	Fe2	S1	Fe1	155.02(9)
S4	C14	C13	S1	-177.98(18)		C4	Fe2	S1	C13	56.40(13)
S4	C14	C13	C12	3.0(3)		C4	Fe2	S2	Fe1	-152.43(9)
C2	Fe1	Fe2	S1	-80.25(11)		C4	Fe2	S2	C12	-55.58(13)
C2	Fe1	Fe2	S2	176.93(11)		C4	Fe2	C5	O5	-148(10)
C2	Fe1	Fe2	C5	2.51(14)		C4	Fe2	C6	O6	81(7)
C2	Fe1	Fe2	C6	95.28(15)		S3	C10	C9	C8	1.0(3)
C2	Fe1	Fe2	C4	-128.66(19)		S3	C7	C8	C9	-0.2(4)
C2	Fe1	S1	Fe2	107.77(10)		S5	C15	C16	C17	-4.1(3)
C2	Fe1	S1	C13	-157.11(13)		S5	C18	C17	C16	-1.3(4)
C2	Fe1	S2	Fe2	-9.6(3)		C9	C10	S3	C7	-1.0(2)
C2	Fe1	S2	C12	-106.4(3)		C8	C7	S3	C10	0.7(3)
C2	Fe1	C3	O3	-75(10)		C16	C15	S5	C18	3.0(2)
C2	Fe1	C1	O1	104(13)		C17	C18	S5	C15	-1.0(3)
C11	S4	C14	C15	177.3(2)						

Table 2.13. Hydrogen Atom Coordinates (Å×10^4) and Isotropic Displacement Parameters (Å^2×10^3) for (63)

Table 13 Hydrogen Atom Coordinates (Å×10^4) and Isotropic Displacement Parameters (Å^2×10^3) for (63).				
Atom	***x***	***y***	***z***	**U(eq)**
H18	12501	775	4124	27
H7	-4283	864	-245	20
H9	335	-94	1354	19
H8	-3070	-128	405	20
H16	7410	-159	3200	25
H17	10916	-201	4000	25

iii.(2,5-bis(2,3-dihydrothieno[3,4-*b*][1,4]dioxin-5-yl)thiophen-μ-3,4-dithiolato)diiron hexacarbonyl (64)

Table 2.14. Fractional Atomic Coordinates (×10^4) and Equivalent Isotropic Displacement Parameters (Å^2×10^3) for 64

Table 14 Fractional Atomic Coordinates (×10^4) and Equivalent Isotropic Displacement Parameters (Å^2×10^3) for 64. U_{eq} is defined as 1/3 of of the trace of the orthogonalised U_{IJ} tensor.

Atom	*x*	*y*	*z*	U(eq)
Fe1	6192.71(19)	2414.25(13)	7483.86(10)	15.30(5)
S2	5000	6395.8(3)	7500	15.61(8)
S3	4606.3(3)	3322.4(2)	6689.23(16)	15.24(6)
S1	3425.2(3)	5041.9(2)	5353.90(17)	19.43(7)
C6	4810.9(12)	4528.5(8)	7113.2(6)	13.78(19)
O2	5234.9(12)	7488.7(7)	6206.7(6)	22.8(2)
C3	4541.5(13)	6736.0(9)	5785.3(7)	16.2(2)
C4	4290.4(13)	5803.4(9)	6057.0(6)	15.3(2)
C5	4670.7(12)	5482.2(9)	6810.1(6)	14.09(19)
O1	4251.7(13)	7684.1(8)	4649.2(6)	25.4(2)
C9	6204.3(15)	1406.6(10)	6844.6(8)	21.4(2)
C1	3429.5(15)	5967.8(11)	4711.4(7)	21.2(2)
C2	4058.4(14)	6822.5(10)	5019.4(7)	17.9(2)
O5	6213.6(14)	714.7(9)	6480.2(7)	32.9(3)
C8	6931.5(15)	1558.3(11)	8203.2(8)	22.3(2)
O3	8415.7(12)	3711.1(10)	7289.6(8)	34.0(3)
C7	7603.7(14)	3180.2(10)	7380.3(8)	21.2(2)
C1aa	5253(2)	8425.4(12)	5820.1(9)	33.3(4)
C0aa	5345(2)	8259.1(14)	5056.7(9)	36.3(4)
O4	7341.2(13)	997.5(10)	8670.2(7)	34.6(3)

Table 2.15. Anisotropic Displacement Parameters ($Å^2×10^3$) for 64

Table 15 Anisotropic Displacement Parameters ($Å^2×10^3$) for 64. The Anisotropic displacement factor exponent takes the form: $-2\pi^2[h^2a^{*2}U_{11}+2hka^*b^*U_{12}+\ldots]$.						
Atom	**U_{11}**	**U_{22}**	**U_{33}**	**U_{23}**	**U_{13}**	**U_{12}**
Fe1	18.89(9)	11.38(7)	15.14(8)	0.61(5)	3.05(6)	2.15(6)
S2	22.6(2)	10.11(15)	13.38(16)	0	2.75(14)	0
S3	21.49(14)	11.15(11)	12.41(11)	-0.81(9)	2.62(10)	0.4(1)
S1	25.00(16)	16.61(13)	14.92(13)	-0.64(10)	1.17(11)	-4.78(11)
C6	17.6(5)	10.5(4)	12.8(4)	-0.2(3)	2.8(4)	-0.1(4)
O2	36.9(6)	13.3(4)	15.5(4)	0.7(3)	0.6(4)	-4.8(4)
C3	21.8(5)	12.7(4)	13.6(4)	0.2(4)	3.1(4)	0.1(4)
C4	19.6(5)	12.8(4)	13.0(4)	0.0(3)	2.7(4)	-0.1(4)
C5	17.5(5)	11.6(4)	12.5(4)	0.0(3)	2.2(4)	-0.4(4)
O1	40.0(6)	18.4(4)	16.7(4)	4.3(3)	4.4(4)	-3.4(4)
C9	27.8(7)	15.5(5)	21.3(6)	1.2(4)	6.6(5)	4.0(5)
C1	27.9(6)	20.3(5)	13.6(5)	0.3(4)	1.3(4)	-1.7(5)
C2	24.9(6)	14.9(5)	13.7(5)	1.9(4)	3.9(4)	1.1(4)
O5	52.8(8)	18.4(5)	28.5(6)	-4.1(4)	11.6(5)	4.7(5)
C8	23.6(6)	17.7(5)	25.1(6)	2.3(5)	4.5(5)	3.2(5)
O3	28.4(6)	28.0(6)	45.7(7)	8.5(5)	8.9(5)	-1.9(5)
C7	21.7(6)	18.0(5)	23.0(6)	2.2(4)	3.4(5)	3.9(4)
C1aa	55.0(11)	16.9(6)	24.3(7)	3.2(5)	1.7(7)	-9.4(6)
C0aa	49.8(11)	31.8(8)	25.1(7)	6.6(6)	4.6(7)	-17.4(8)
O4	37.9(7)	29.0(6)	34.2(6)	14.4(5)	3.0(5)	7.5(5)

Table 2.16. Bond Lengths for 64

Table 16 Bond Lengths for 64						
Atom	**Atom**	**Length/Å**		**Atom**	**Atom**	**Length/Å**
Fe1	Fe1[1]	2.4891(5)		C6	C5	1.3747(16)
Fe1	S3	2.2895(4)		O2	C3	1.3669(16)
Fe1	S3[1]	2.2787(4)		O2	C1aa	1.4376(18)
Fe1	C9	1.8000(14)		C3	C4	1.3803(17)
Fe1	C8	1.7967(14)		C3	C2	1.4261(17)
Fe1	C7	1.8257(15)		C4	C5	1.4531(17)
S2	C5[1]	1.7515(12)		O1	C2	1.3738(16)
S2	C5	1.7515(12)		O1	C0aa	1.430(2)
S3	Fe1[1]	2.2788(4)		C9	O5	1.1451(17)
S3	C6	1.7705(12)		C1	C2	1.3617(19)
S1	C4	1.7398(12)		C8	O4	1.1550(18)
S1	C1	1.7252(14)		O3	C7	1.1384(19)
C6	C6[1]	1.428(2)		C1aa	C0aa	1.491(3)

[1]1-X,+Y,3/2-Z

Table 2.17. Bond Angles for 64

Table 17 Bond Angles for 64								
Atom	**Atom**	**Atom**	**Angle/°**		**Atom**	**Atom**	**Atom**	**Angle/°**
S3	Fe1	Fe1[1]	56.779(11)		C5	C6	C6[1]	114.00(7)
S3[1]	Fe1	Fe1[1]	57.193(11)		C3	O2	C1aa	113.07(11)
S3[1]	Fe1	S3	81.836(16)		O2	C3	C4	123.11(11)
C9	Fe1	Fe1[1]	100.44(5)		O2	C3	C2	123.27(11)
C9	Fe1	S3[1]	155.84(5)		C4	C3	C2	113.58(11)
C9	Fe1	S3	93.38(5)		C3	C4	S1	109.57(9)
C9	Fe1	C7	101.64(7)		C3	C4	C5	126.52(11)
C8	Fe1	Fe1[1]	103.27(5)		C5	C4	S1	123.91(9)
C8	Fe1	S3[1]	88.00(5)		C6	C5	S2	109.38(8)
C8	Fe1	S3	160.01(5)		C6	C5	C4	130.92(11)
C8	Fe1	C9	88.87(7)		C4	C5	S2	119.69(9)
C8	Fe1	C7	102.67(7)		C2	O1	C0aa	110.70(11)
C7	Fe1	Fe1[1]	146.02(4)		O5	C9	Fe1	174.78(13)
C7	Fe1	S3	96.33(4)		C2	C1	S1	111.20(10)
C7	Fe1	S3[1]	102.42(5)		O1	C2	C3	121.92(12)
C5	S2	C5[1]	93.24(8)		C1	C2	C3	112.90(11)
Fe1[1]	S3	Fe1	66.030(14)		C1	C2	O1	125.17(12)
C6	S3	Fe1	100.29(4)		O4	C8	Fe1	176.45(14)
C6	S3	Fe1[1]	100.48(4)		O3	C7	Fe1	174.80(13)
C1	S1	C4	92.75(6)		O2	C1aa	C0aa	112.43(14)
C6[1]	C6	S3	116.22(4)		O1	C0aa	C1aa	112.27(15)
C5	C6	S3	129.77(9)					

[1]1-X,+Y,3/2-Z

Table 2.18. 18 Hydrogen Atom Coordinates (Å×10^4) and Isotropic Displacement Parameters (Å^2×10^3) for 64.

Table 18 Hydrogen Atom Coordinates (Å×10^4) and Isotropic Displacement Parameters (Å^2×10^3) for 64				
Atom	***x***	***y***	***z***	**U(eq)**
H1	3043	5891	4208	25
H4	6019	8838	6075	40
H5	4434	8812	5820	40
H2	5374	8925	4819	44
H3	6182	7897	5057	44

Chapter 3 – [FeFe]-Hydrogenase Mimetic Metallopolymers with Exceptional Catalytic Activity for Hydrogen Production in Water

William P. Brezinski,[a] Metin Karayilan,[a] Kayla E. Clary, Nicholas G. Pavlopoulos,[a] Sipei Li,[b] Liye Fu,[b] Krzysztof Matyjaszewski,[b] Dennis H. Evans, [c] Dennis L. Lichtenberger, [a]* Richard S. Glass [a]* and Jeffrey Pyun [a,d] *

The material in this chapter is from [FeFe]-Hydrogenase Mimetic Metallopolymers with Exceptional Catalytic Activity for Hydrogen Production in Water Angew. Chem. Int. Ed. 10.1002/anie.201804661. Copyright Wiley-VCH Verlag GmbH & Co. KGaA. Reproduced with permission.

Abstract: *Electrocatalytic [FeFe]-hydrogenase mimics for the hydrogen evolution reaction (HER) generally suffer from low activity, high overpotential, aggregation, oxygen sensitivity, and low solubility in water. Using atom transfer radical polymerization (ATRP), we have prepared a new class of [FeFe]-metallopolymers with precise molar mass, composition, and low polydispersity. The synthetic methodology introduced here allows for facile variation of polymer composition to optimize the [FeFe] solubility, activity, and long term chemical and aerobic stability. We find that water soluble functional metallopolymers perform electrocatalytic hydrogen production in neutral water with loadings as low as 2 ppm and operate at rates many orders of magnitude faster than hydrogenases (2.5 x 10^5 s^{-1}) and with low overpotential requirement. Furthermore, unlike the hydrogenases, these systems are insensitive to oxygen during catalysis with turnover numbers on the order of 40,000 under both anaerobic and aerobic conditions.*

The development of clean, sustainable chemical fuels remains an important societal challenge, in particular via the storage of intermittent energy in the form of chemical bonds.[159,160] The strong chemical bond in molecular hydrogen (H_2) offers an energy dense, renewable, carbon-free fuel.[161] Electrochemical water splitting to generate H_2 and O_2 typically uses expensive and rare platinum metal, which has the benefit of one of the highest exchange current densities at zero overpotential for the proton/hydrogen reaction. Inspiration for promising alternative catalysts has been provided by nature: hydrogenase enzymes,[27] produced by anaerobic bacteria, catalyze the reduction of protons to H_2 with high rates (up to *ca.* 10^4 molecules of H_2 per sec per active site[3,27]), low overpotential, and with Earth-abundant and inexpensive metals such as iron and nickel in their active sites. Consequently, [FeFe]-hydrogenases and [NiFe]-hydrogenases have inspired the study of small molecule mimics of these active sites as electrocatalysts for H_2 production.[162–164] Despite impressive advances,[59,63,76,77,89,90,92,93,99,108,109,111,165–179] several important challenges remain in this area: (1) increase the activity and chemical stability of the catalysts, (2) lower their overpotential, (3) use water as the solvent, (4) inhibit aggregation while maintaining rapid electron transfer to the active site, and (5) increase aerobic stability.[180–183] We report here the incorporation of a [2Fe-2S] hydrogenase biomimetic into a polymer that affords advances on all of the outlined challenges and provides a high-performance catalyst for the hydrogen evolution reaction (HER) in neutral water (Scheme 3.1).

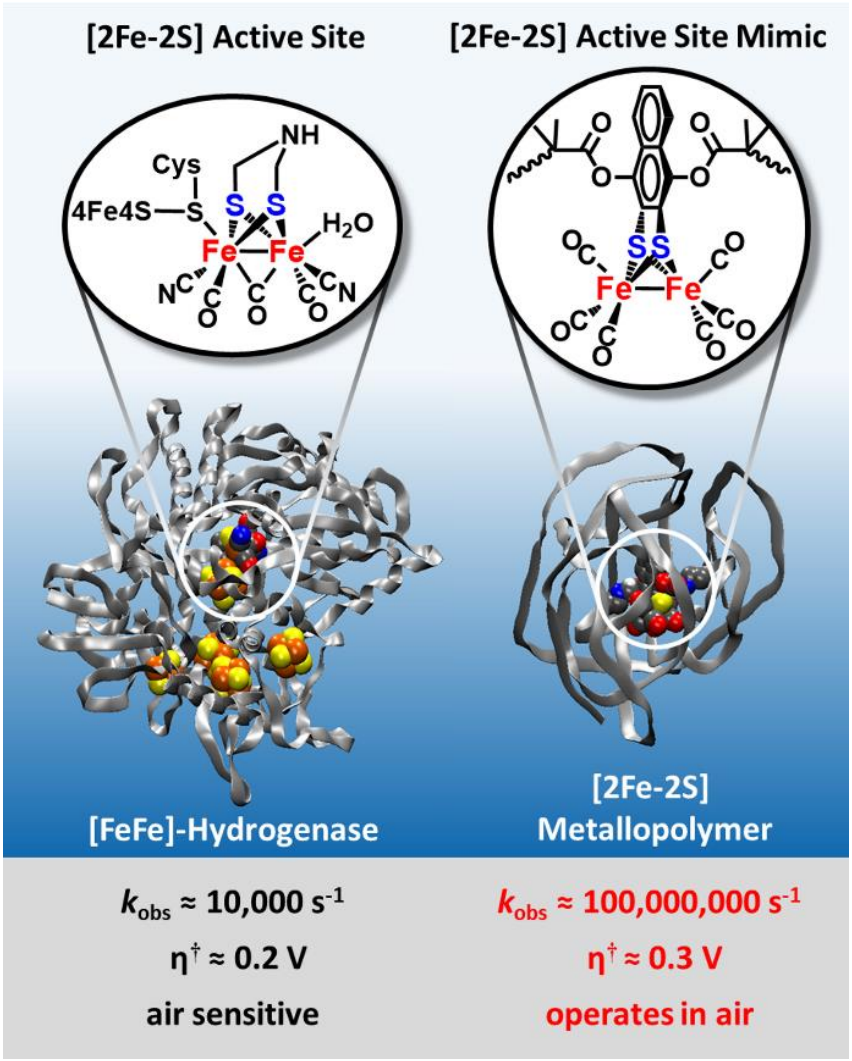

Scheme 3.1. Comparison of a new class of HER [2Fe-2S]-metallopolymer vs. [FeFe]-hydrogenase catalysts. The metallopolymer HER catalyst is remarkably faster than the enzyme and is air stable at neutral pH. In addition, current densities greater than 300 mA cm2 are achieved with 75 μM catalyst loading. $\eta^{\dagger}$ is the overpotential requirement[50] to achieve an operating cell current density of 0.1 mA cm^{-2}. See the appendix B for details. Reproduced with permission from *Angew. Chem. Int. Ed.*[12]

Our approach is the first use of atom transfer radical polymerization (ATRP)[121] methods to prepare a new class of metallopolymers[102] which incorporate electrocatalytically active [2Fe-2S] sites into polymers with controllable molecular weights and low polydispersity. Our synthetic strategy begins with preparation of a [2Fe-2S] complex bearing two ATRP initiator moieties so that polymer growth from both sides of the complex affords steric isolation of the central active site. Studies of small molecule [FeFe]-hydrogenase active site mimetics have found that upon reduction these complexes tend to dimerize and become deactivated for reduction of protons to hydrogen.[140] Of course, the supramolecular protein structures of [FeFe]-hydrogenases isolate the buried active site from dimerization, and other approaches to site isolation have been investigated.[59,63,76,77,89,90,92,93,99,108,109,111,165–174,184–186] Furthermore, we introduce here the ability of ATRP to modulate the solubility and secondary coordination sphere around the [2Fe-2S] catalytic complex by simple variation of commercially available vinyl monomers. In this study, we include flexible alkyl amine (R-NMe_2) groups as side-chains along the polymer backbone to impart water solubility to the metallopolymer. An amine in the dithiolate bridge of [FeFe]-hydrogenases has been found to be crucial the catalytic activity of

the enzyme,[187] and Bullock et. al. have demonstrated flexible amines are crucial to the activity of the fastest reported molecular electrocatalysts.[188–191] Furthermore, most [FeFe]-hydrogenases and [2Fe-2S] biomimetics are deactivated by oxygen, but Darensbourg *et al.* suggested that neighboring amino groups mitigate this deactivation by promoting complete reduction of the partially reduced oxygen species responsible for catalyst deactivation.[183]

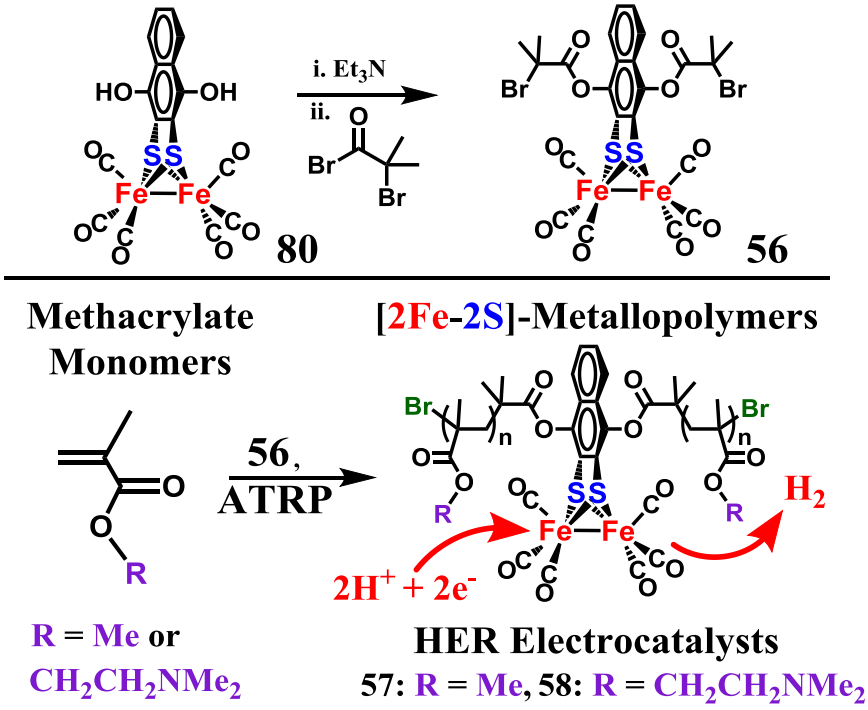

Figure 3.1. Synthetic scheme for metalloinitiator **56** and metallopolymers **PMMA-*g*-[2Fe-2S] 57** and **PDMAEMA-*g*-[2Fe-2S] 58** via ATRP to enable facile modulation of catalyst solubility. Reproduced with permission from *Angew. Chem. Int. Ed.*[12]

Metalloinitiator **56** for ATRP was prepared in one step start-ing with complex **1** from our previous studies.[192] Esterification of **1** with α-bromoisobutyryl bromide (BIBB) afforded metalloinitiator **56** in good isolated yield (>85%) after purification by column chromatography. The structure of metalloinitiator **56** was unequivocally confirmed by single crystal X-ray crystallography (Figure B.1). The use of a functionalized [2Fe-2S] complex as a metalloinitiator for a controlled/living radical polymerization process has not been previously reported and gives a distinctly different metallopolymer construct when compared with previous [2Fe-2S]-metallopolymers which incorporated the [2Fe-2S] moiety as a part of the main chain,[99,167,168] on side chains[90,109,165] or as a chain-end functional group.[166] Furthermore, it improves the scalability of the process as only a small amount of initiator is needed for each batch of polymer, while ensuring covalent inclusion of [2Fe-2S] moieties into the resulting metallopolymers.

The synthesis of metallopolymers is shown in Figure 1. The ATRP of methyl methacrylate (MMA) was investigated first as a model system to confirm the chemical tolerance of the [2Fe-2S] complex to polymerization conditions and to facilitate characterization of metallopolymers using conventional polymer solution characterization methods. Molar masses of *ca.* 10,000 g/mol (i.e., 5,000 g/mol per each initiator site) were targeted to enable sufficient site isolation of the iron complex while still being amenable to size exclusion chromatography (SEC) and

NMR spectroscopy end-group analysis for molecular weight characterization (see Supporting Information and Figures S2-S5 for polymer characterization).

The successful formation of well-defined **PMMA-*g*-[2Fe-2S] 57** metallopolymers ($M_{n,\ SEC}$ = 11,982 g/mol; M_w/M_n = 1.10) was confirmed using a combination of IR spectroscopy revealing the characteristic Fe-CO stretching frequencies along with size exclusion chromatography (SEC) in tetrahydrofuran (THF) coupled with UV-vis detection (at 400 nm) and end-group analysis using ^{1}H NMR spectroscopy.

Upon confirmation that well-defined [2Fe-2S] metallopolymers could be prepared via the ATRP methodology with full retention of the catalytic [2Fe-2S] core, the preparation of water soluble materials was then pursued. These metallopolymers were prepared by the ATRP of 2-(dimethylamino)ethyl methacrylate (DMAEMA) from metalloinitiator **56** to afford the **PDMAEMA-*g*-[2Fe-2S] 58** metallopolymer, as confirmed by IR spectroscopy (Figure B.5f) and SEC in LiBr-DMF mobile phase ($M_{n,SEC}$ = 12,700 M_w/M_n = 1.27; Figure B.2b). PDMAEMA metallopolymers with molar mass in the range of 10,000-15,000 g/mol with low polydispersity were prepared and found to be soluble in water, acetonitrile, and N,N-dimethylformamide. Both **PMMA-g-[2Fe-2S] 57** and **PDMAEMA-g-[2Fe-2S] 58** metallopolymers were found to be electrocatalytically active for HER in acetonitrile in the presence of acetic acid, with **58** producing greater catalytic current at lower overpotential compared to **57** (Figure B.7b).

Electrocatalytic efficiency of water soluble metallopolymers was probed first by cyclic voltammetry (CV). Figure 2 revealed that the **PDMAEMA-*g*-[2Fe-2S] 4** metallopolymer produces hydrogen electrocatalytically at a very high rate in neutral water (the solution is buffered to pH 7 to adjust for the basicity of the PDMAEMA polymer and to minimize the rise in pH during electrolysis). A 100 μM concentration of the catalyst gives a current density with a glassy carbon electrode essentially matching that of a planar platinum electrode and with equivalently quantitative Faradaic yield (see SI and Figure B.14). Also striking, the catalyst operates in neutral water, operates similarly with different electrode materials and so is not dependent on specific electrode surface interactions, and operates in the presence of oxygen (*vide infra*). Surface analysis of carbon electrodes after catalysis by scanning electron microscopy (SEM) and energy-dispersive X-ray spectroscopy (EDX) confirmed that Fe-species were not deposited as a consequence of either metallopolymer immobilization or decomposition (see SI). A study of the dependence on catalyst concentration yielded the striking result that loadings as low as 2 ppm (200 nM by IR) were effective at catalysing the HER reaction with reproducibly high current densities (J = 22 mA cm^{-2}) under our conditions (Figure B.8f). At higher catalyst concentrations the current profile showed evidence of a Langmuir adsorption isotherm with a sharp decrease in slope above about 10 μM metallopolymer concentration indicating near-monolayer coverage in dynamic equilibrium with solution at this concentration (see SI).

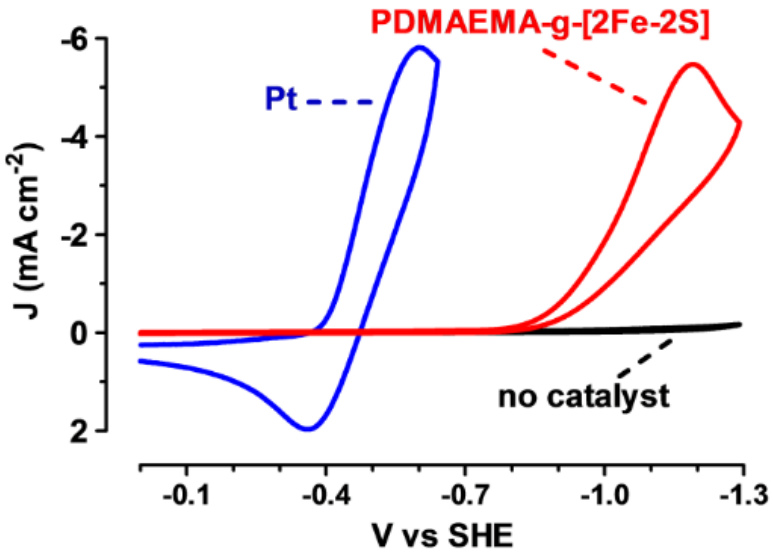

Figure 3.2. CV Comparison of Pt disk electrode and 100 µM metallopolymer 58 in pH 7 sodium phosphate buffer. Cyclic voltammograms (CV) showing HER current density a Pt disk electrode (blue ϕ = 1.6 mm) and a glassy carbon disk electrode with 100 µM metallopolymer **58** (red) in pH 7; 0.1 M sodium phosphate buffer; 0.1 M KCl electrolyte. The black trace is the background current density for the glassy carbon disk electrode (ϕ = 3 mm) in absence of electrocatalyst. Scan rate was 100 mV/s for all experiments, quiet solution condition. Reproduced with permission from *Angew. Chem. Int. Ed.*[12]

Estimation of the observed turnover frequency based on the CV by methods commonly used in the literature[193,194] is highly uncertain in this case because (1) the catalysis is too fast to approach first-order kinetics even with an *extremely* low 0.1 µM concentration of catalyst (see SI) and (2) kinetic analysis of the CV requires uncertain assumptions regarding the mechanism. Digital simulation of the CV curves shows that the current is dependent on the equilibrium concentration of the conjugate acid form of the buffer species (i.e., NaH_2PO_4 in sodium phosphate buffer, ~40% in the protonated state at pH 7). This was confirmed with a switch to tris buffer (2-amino-2-(hydroxymethyl)propane-1,3-diol), which is ~92% protonated at pH 7 and significantly increases the catalytic current and performance (see SI and Figure B.8). This enhancement of the catalytic performance by a protonated buffer is likely to be general for HER catalysts operating in water. Furthermore, the amine groups on the PDMAEMA polymer catalyst are 95% protonated at pH 7[195] (Figure B.5g), meaning that this catalyst also benefits inherently from an environment that is rich in protonated amines at pH 7.

To provide a more direct and practical indication of catalyst performance than surmised from cyclic voltammetry, we report the catalytic HER performance in terms of the Tafel plot[196,197] (log of the current density versus overpotential) relative to a standard HER catalyst operating under the same conditions. The standard of choice for a comparison of HER activity is a planar platinum electrode.[198] The Tafel plot for 75 µM **PDMAEMA-*g*-[2Fe-2S] 4** at a glassy carbon electrode compared to the Tafel plot for a platinum electrode conditioned at the cathodic potentials for electrolysis[198] is shown in Figure 3. The **PDMAEMA-*g*-[2Fe-2S] 4** system shows a similar Tafel slope to platinum and the current density matches that of platinum in the range from about 1 to 200 mA cm^{-2} with less than 0.2 V greater overpotential requirement than platinum. The rate of hydrogen production per molecule of metallopolymer catalyst at 10 µM concentration is 250,000 s^{-1} assuming complete monolayer coverage of closest-packed polymers on the entire electrode surface and a lower bound for the plateau current density (see SI). The Tafel plot results with the glassy carbon electrode are shown here to emphasize the performance with an inexpensive and easily fabricated electrode.

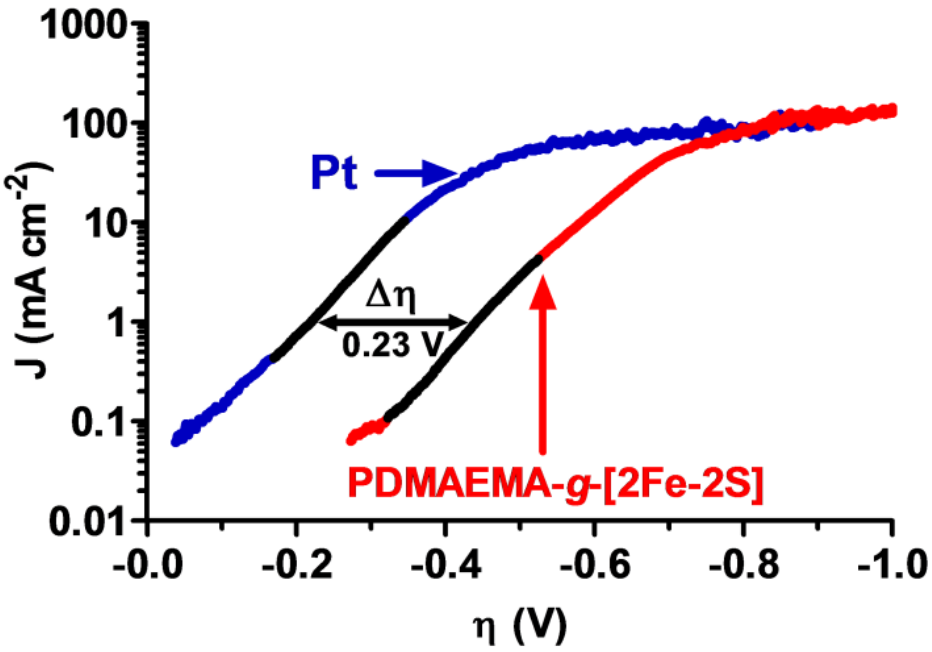

Figure 3.3. Tafel comparison of PDMAEMA-g-[2Fe-2S] (58) wth a cathodically conditioned Pt disk electrode. Pt disk (ϕ = 1.6 mm, blue trace, Tafel slope 124 mV/decade) in 1.0 M tris buffer solution at pH 7 and a glassy carbon disk electrode (ϕ = 3 mm) in the same solution with added 58 (red trace, Tafel slope 123 mV/decade, 100 μM [2Fe-2S] by IR, 1.9 mg/mL mass loading). The black overlay lines show the segments for determination of the Tafel slopes. Scan rate 5 mV/s, solution magenticaly stirred at 1600 rpm. Δη is the difference in overpotential. Reproduced with permission from *Angew. Chem. Int. Ed.*[12]

One of the major challenges in developing robust [2Fe-2S] biomimetic catalysts is the poor oxygen stability of these complexes, a problem which also plagues the [FeFe]-hydrogenase enzymes. The stability of **PDMAEMA-*g*-[2Fe-2S] 4** in the presence of oxygen during the course of catalysis was explored by reproducing the electrochemical experiments above under aerobic rather than anaerobic conditions. The CVs showed the same maximum catalytic peak current in an air-saturated solution as under argon (Figure B.10). Likewise, the linear sweep voltammetry of the catalytic current density versus potential is essentially identical (Figure 4). Faradaic yield of hydrogen taken from the headspace of the cell under aerobic conditions was 99±3% of the yield under anaerobic conditions. The turnover numbers (CPE operated at -0.95 V vs SHE, 0.54 V overpotential for periods up to six days, see SI) are the same in air and in argon ($4\pm2\times10^4$ molecules of hydrogen per catalytic site in solution).

In summary, we have developed a highly scalable new synthetic method to a metallopolymer HER catalyst system which (a) gives essentially quantitative Faradaic yield of hydrogen, (b) is profoundly faster in HER rate than [FeFe]-hydrogenases, (c) achieves current densities in excess of 20 mA cm^{-2} at extremely low (2 ppm) catalyst loadings, (d) yields a turnover number greater than 10^4 molecules of hydrogen per metallopolymer catalyst site and (e) operates either anaerobically or aerobically. The figures of merit for this catalyst from the combined metrics of low overpotential requirement for high current density[193,194] (as demonstrated in the Tafel plots, overpotential 0.23 V relative to platinum in the current density range 0.07 to 30 mA/cm^2, ~100 mA/cm^2 current density at 0.8 V overpotential) substantially exceeds that of any other reported homogeneous catalysts for electrocatalytic HER of which we are aware and approaches the realm of heterogeneous catalysts as exemplified by platinum. Furthermore,

this system offers many opportunities to tune and optimize the catalytic behavior, such as modifications of the polymer chain including utilization of other vinylic monomers, and modification of the active catalyst site for example with substitution of the dithiolate or carbonyl ligands.

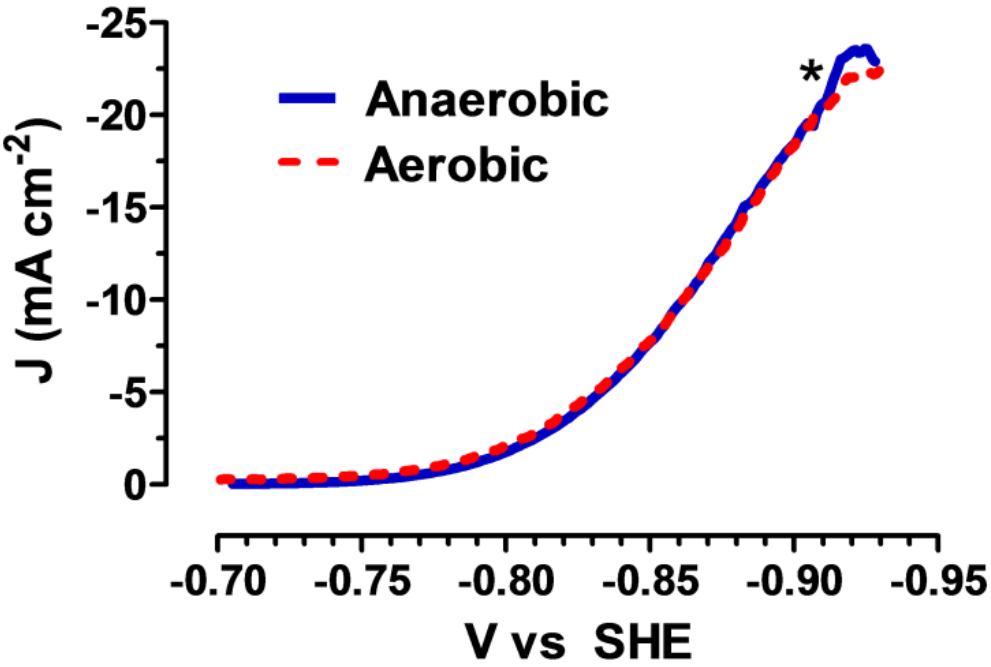

Figure 3.4. Linear sweep voltammetry of 10 μM **PDMAEMA-g-[2Fe-2S] 58** (0.2 mg/mL) using a glassy carbon electrode (ϕ = 3 mm) in 1.0 M pH 7 tris buffer under anaerobic (blue line) and aerobic (red dashed line) conditions. Scan rate 5 mV/s, solution magnetically stirred at 1600 rpm. *Excessive hydrogen bubble formation at potentials negative of -0.9 V. Reproduced with permission from *Angew. Chem. Int. Ed.*[12]

Experimental Section.

See Appendix B.

Acknowledgements.

DLL, RSG and JP gratefully acknowledge support of this work by NSF (CHE-1664745), Dr. Andrei Astachkine for his assistance with the X-ray crystallographic structural analysis, Dr. Michael L. Heien and his group members for electrochemical consultation. KM acknowledges support of this work by NSF (DMR 1501324).

.

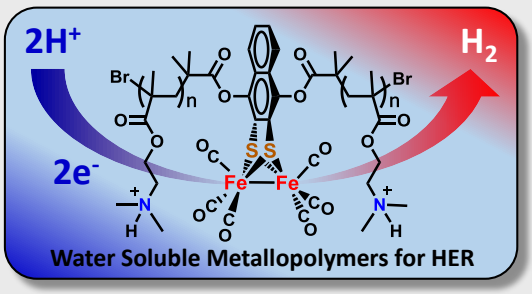

William P. Brezinski,[a] Metin Karayilan,[a] Kayla E. Clary,[a] Nicholas G. Pavlopoulos,[a] Sipei Li,[b] Liye Fu,[b] Krzysztof Matyjaszewski,[b] Dennis H. Evans,[c] Richard S. Glass,[a]* Dennis L. Lichtenberger,[a]* and Jeffrey Pyun [a,d] *

[FeFe]-Hydrogenase Mimetic Metallopolymers with Exceptional Catalytic Activity for Hydrogen Production in Water

TOC Figure. The forgery exceeds the master: An organometallic [2Fe-2S] mimic of the active site of an [FeFe]-hydrogenase enzyme was incorporated into a metallopolymer. The electrocatalytic performance for hydrogen production in water at pH 7 by the [2Fe-2S]-metallopolymer was found to greatly exceed the performance of the enzyme, and approaches the performance of platinum. Unlike the enzyme, the [2Fe-2S]-metallopolymer catalyst operates in air. Reproduced with permission from *Angew. Chem. Int. Ed.*[12]

Chapter 4 Macromolecular Engineering the Outer Coordination Sphere of [2Fe-2S] Metallopolymers to Enhance Catalytic Activity for H_2 Production

William P. Brezinski,[a] Metin Karayilan,[a] Kayla E. Clary,[a] Liye Fu,[b] Krzysztof Matyjaszewski,[b] Dennis H. Evans,[c] Dennis L. Lichtenberger,*[a] Richard S. Glass,*[a] and Jeffrey Pyun*[a,d]

[a] Department of Chemistry and Biochemistry, University of Arizona, 1306 E. University Blvd., Tucson, Arizona 85721, United States

[b] Department of Chemistry, Carnegie Mellon University, 4400 Fifth Avenue, Pittsburgh 151213, United States

[c] Department of Chemistry, Purdue University, 560 Oval Drive, West Lafayette, Indiana 47907, United States

[d] Department of Chemical and Biological Engineering, Program for Chemical Convergence for Energy & Environment & the Center for Intelligent Hybrids, Seoul National University, Seoul 151-744, Korea

Abstract: *Small molecule catalysts inspired by the active sites of [FeFe]-hydrogenase enzymes have long struggled to achieve fast rates of hydrogen evolution, long term stability, water solubility, and oxygen compatibility. We recently reported that* ***PDMAEMA-g-[2Fe-2S] 58****, a metallopolymer with a single [2Fe-2S] active site buried in a polymer chain rich in protonated tertiary amines, achieves electrocatalytic rates of hydrogen evolution on the order of* 10^8 s^{-1} – 10^4 *faster than the fastest rates reported for the [FeFe]-hydrogenase enzymes. Further, it preforms the reaction with a similar overpotential requirement to that of the enzyme, and retains full activity under aerobic conditions. Intrigued by this activity, we chose to investigate the role of incoproating amines on the polymer chain, as they have been suggested to crucial to the activity of the enzyme, and provide a measure of aerobic stability in certain small molecule systems. To that end, we used atom transfer radical polymerization to synthesize three new water soluble metallo(co)polymers with varying amounts of amine containing monomer, 2-(dimethylamino)ethyl methacrylate (DMAEMA). Tuning the macromolecular support in this way was found to have a dramatic effect on catalysis, with all metrics of polymer activity and stability improving with increased feed ratios of DMAEMA, and lower feed ratios of oligo(ethylene glycol) methacrylate (OEGMA).* ***PDMAEMA-g-[2Fe-2S], 58*** *showed complete aerobic stability with catalytic current densities in excess of 20* $mA \cdot cm^{-2}$*, while* ***POEGMA-g-[2Fe-2S], 59*** *fails to reach 1* $mA \cdot cm^{-2}$ *even with the application of high overpotentials (*$\eta > 0.8$ *V) and* ***59*** *loses all activity in the presence of oxygen. Random copolymers* ***60*** *and* ***61*** *of the two monomers polymerized with the same [2Fe-2S] initiator showed intermediate activity in terms of current density, overpotential, and aerobic stability.*.

The increase in renewable generation of electricity, namely via wind and solar, demands efficient methods for storing excess energy to mediate the intermittent nature of these generation methods. The electrochemical generation of molecular hydrogen (H_2) offers a chemical storage method which produces an energy dense, transportable fuel with no carbonaceous emissions.[26] Current electrolysis cells generally use *platinum* as a *heterogeneous catalyst* for the hydrogen evolution reaction (HER). However, due to the high cost and low Earth abundance of noble metals there have been extensive efforts on the development of HER electrocatalyst systems composed of inexpensive, heterogeneous carbon electrodes in conjunction with high activity homogeneous catalysts.[17] [FeFe]-Hydrogenase (H_2ase) enzymes have long been known to

efficiently catalyze the conversion of protons and electrons to H_2 in nature and to be highly active homogeneous HER electrocatalysts.[27,199] The preparation of synthetic organometallic HER catalysts mimicking the [FeFe]-hydrogenase active site based on [2Fe-2S]-complexes have been widely explored as a route to *developing improved homogeneous HER electrocatalysts*.[6] Despite extensive work on small molecule HER electrocatalysts, there remain several *important challenges t*o address namely: *(1) modular modification of the outer coordination sphere to tune activity in water, (2) improving catalyst stability and increasing turnover number, (3) catalyst site isolation against associative deactivation, (4) decreased overpotential and (5) increased air stability.*

The synthesis of functional ligands and [2Fe-2S] complexes has been explored as route to modify the secondary coordinate sphere of these homogeneous HER catalysts and impart water solubility. Structural analysis of the enzyme and seminal small molecule systems by Dubois, Bullock, have demonstrated the crucial role of flexible amines as proton relays in the outer coordination sphere for [FeFe]-hydrogenase enzymes and the fastest small molecule HER catalysts they have inspired.[14,200–205] Metallopolymers have been synthesized which incorporate [2Fe-2S]-complexes along the main chain,[99,167,168] side chain,[109,165,206] or as single chain nanoparticles.[166] Polymeric supports have been particularly effective in photocatalytic systems where Fréchet-type dendrimers, poly(acrylic acid)- and polyethylenimine- (PEI) grafted [2Fe-2S] systems have demonstrated improved turnover numbers (TON, on the order of 2×10^4) and a significant improvement over an analogous water soluble small molecule which was observed to exhibit much lower TON (5×10^2). [46,88,113,207,208] The effect of macromolecular scaffolds on electrocatalytic systems is less well studied, but membrane electrodes fabricated with [2Fe-2S]-metallopolymers have demonstrated reasonable catalytic currents in aqueous media.[98,168] Notably, a pendant carboxylate group was demonstrated to improve the current density of membrane electrodes in water with added acetic acid[168] but so far all functionalized electrode systems suffered from bleaching of the [2Fe-2S] system upon extended electrocatalysis. Schubert and Weigand *et al.* also elegantly demonstrated the use of the reversible addition-fragmentation chain transfer (RAFT) polymerization to incorporate [2Fe-2S] units as side chains into metallopolymers.[111] While all of these systems point to the benefits of conjugation of [2Fe-2S] HER catalysts into metallopolymer systems, there remain important challenges to develop versatile and facile synthetic methods to create HER metallopolymers with improved activity, aerobic stability and extended catalytic lifetime in neutral aqueous media.

We recently demonstrated using atom transfer radical polymerization (ATRP)[119,120] the synthesis of well-defined, water soluble poly(2-dimethylamino)ethyl methacrylate) functional [2Fe-2S] metallopolymers (PDMAEMA-*g*-[2Fe-2S]) with profoundly improved HER electrocatalytic activity in neutral water.[12] This homogeneous metallopolymer electrocatalyst was found to exhibit greatly enhanced aerobic stability in neutral water and extremely fast rates for HER ($2.5 \times 10^5\ s^{-1}$, an order of magnitude faster than Fe-Fe hydrogenases, with current densities comparable to platinum) while operating at 1-2 ppm catalyst loadings. This remarkable improvement of HER catalytic activity in water was attributed to both enhanced chemical stability of the [2Fe-2S] due to site isolation in the metallopolymer and the presence of protonated ammonium groups (from PDMAEMA and the buffer medium). While this initial demonstration pointed to the benefits of this metallopolymer approach to improve catalytic performance, there remain numerous questions on

whether the presence of amine groups is critical to improved H_2 generation. Hence, the preparation of new functional metallopolymers affords the possibility of further improving HER electrocatalytic activity. In particular, the versatility of ATRP allows for a wide range of functional monomers to be incorporated into metallopolymers as either homopolymer, or copolymer segments which for the [2Fe-2S] catalyst for H_2 generation.

Herein, we report on the first comparative HER catalytic study on the effects of homo- and copolymer composition in well-defined [2Fe-2S] metallopolymers derived from ATRP. In this study, a new, non-ionic, water soluble metallopolymer based on poly(oligo(ethylene glycol) methyl ether methacrylate) (POEGMA) was synthesized via ATRP from [2Fe-2S] metalloinitiators and directly compared with the activity of PDMAEMA-*g*-[2Fe-2S] metallopolymers. Furthermore, we prepare for the first time random metallocopolymers of poly(DMAEMA-*r*-POEGMA) to demonstrate tuning of the outer coordination sphere as means to modular HER catalytic activity.

To demonstrate the ability to modulate the HER activity of metallopolymers of the outer coordination sphere and nanoscopic environment, a series of polymethacrylate homopolymers and random copolymers conjugated to [2Fe-2S] active sites were synthesized via ATRP. We previously found the tertiary amine side chains from PDMAEMA-*g*-[2Fe-2S] metallopolymers in neutral water (with various buffers) resided as almost fully protonated ammonium groups, which we proposed created a high concentration of efficient proton donating groups to the catalyst site and resulted in enhanced H_2 generation.

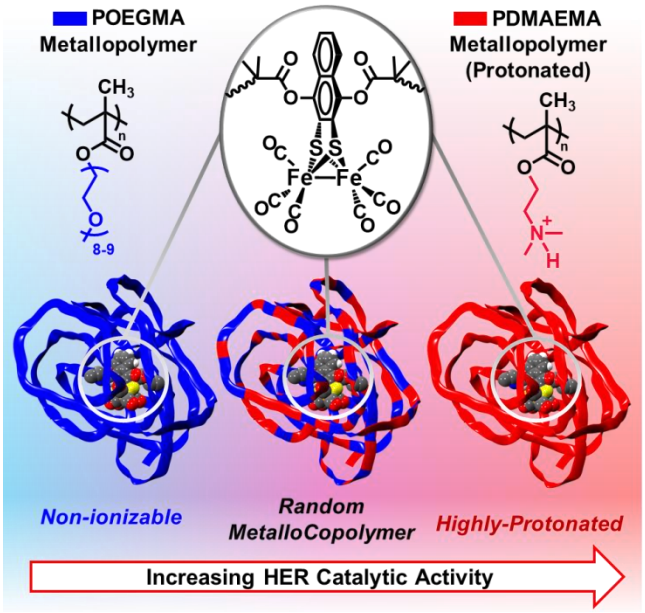

Scheme 4.1. Representation of **PDMAEMA-*g*-[2Fe-2S]** (**58**) and **POEGMA-*g*-[2Fe-2S]** (59) metallopolymers and **P(DMAEMA-*r*-OEGMA)-*g*-[2Fe-2S]** metallocopolymers (**60** and **61**).

In the current study, we interrogate this proposed mechanism by the synthesis, non-ionic PEGylated, water soluble metallopolymers (i.e., **POEGMA-*g*-[2Fe-2S]**, **59**) that do not carry proton donating side chains, as well as random metallopolymers introducing variable amounts of

tertiary amine/quaternary ammonium groups (Scheme 4.1). With access to a range of these model metallopolymer with systematic variation of composition in the outer coordination sphere, we are able to for the first time create structure-activity correlations for these systems for HER overpotential, turnover frequency (rate) and aerobic stability. The general synthetic approach to prepare these homogeneous HER electrocatalysts was the synthesis of a functional [2Fe-2S] metalloinitiator complex, followed by ATRP of various commercially available methacrylate monomers. The key advantage of this approach is the ability to ensure covalent tethering of polymers to a single [2Fe-2S] site per metallopolymer in a single step while also enabling facile modification of metallopolymer composition using controlled radical polymerization methods. For the synthesis of metallo(co)polymers for this study, bromoisobutyrate functionalized metalloinitiator **56** was prepared as previously described for the ATRP of DMAEMA to prepare **PDMAEMA-*g*-[2Fe-2S]** metallopolymer **58** (Scheme 4.2).[12] The ATRP of an oligo(ethylene glycol) methacrylate macromonomer (OEGMA, Mn = 475 g/mol) from metalloinitiator **56** to prepare the desired, non-ionic **POEGMA-*g*-[2Fe-2S]** metallopolymer **59** (Scheme 4.2)**.** Similar ATRP conditions were employed to prepare **poly(DMAEMA-*r*-OEGMA)]-*g*-[2Fe-2S]** metallocopolymers of varying copolymer composition (Scheme 4.2, metallocopolymer **60**, PDMAEMA 72-mol%/POEGMA 28-mol% and **61** PDMAEMA 56-mol%/POEGMA 44-mol% see Appendix C for synthetic details).

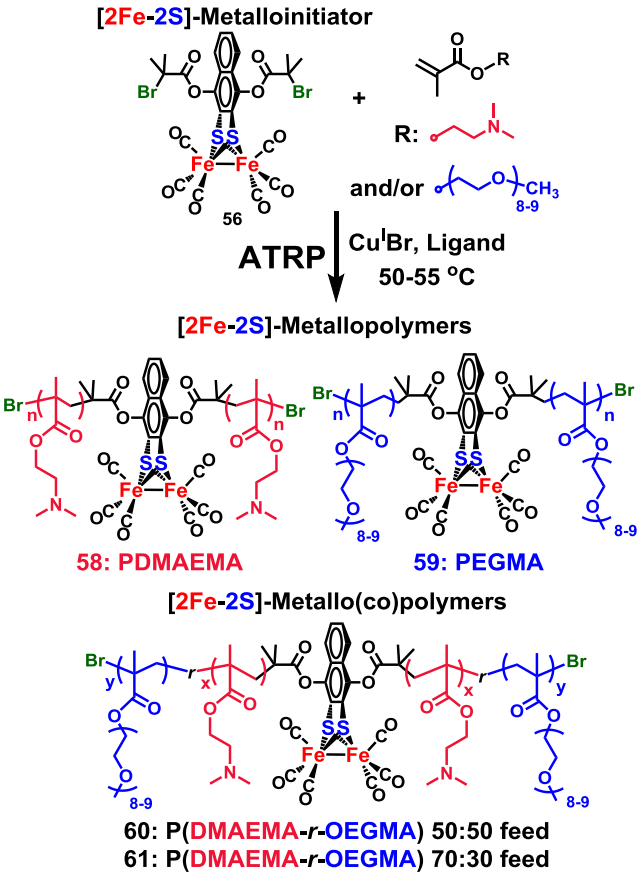

Scheme 4.2. Synthesis of [2Fe-2S]-*grafted* metallo(co)polymers via ATRP of methacrylic monomers initiated with [2Fe-2S]-metalloinitiator **56**

Metallo(co)polymers **58-61** were prepared possessing molar masses in the range of 10,000 - 15,000 g/mol, where structural characterization of the targeted materials was confirmed using a combination of SEC, NMR and IR spectroscopies. The covalent incorporation of the [2Fe-2S] system was confirmed by SEC of **POEGMA-*g*-[2Fe-2S]**, **59** and **PDMAEMA-*g*-[2Fe-2S]**, **58** with UV-Vis detection at a wavelength characteristic of the [2Fe-2S] system. Both **PDMAEMA-*g*-[2Fe-2S]**, **58** and **POEGMA-*g*-[2Fe-2S]**, **59** were found to have *Mn* of approximately 10-15 kg/mol, and Mw/Mn ≤ 1.3 (Figure 4.1). Further, IR spectroscopy confirmed structural retention of Fe-CO stretching frequencies characteristic of the [2Fe-2S] catalytic core (Figure 4.1). Similar findings were confirmed in the synthesis of metallocopolymers **60** and **61** (see Appendix C).

Metallopolymers **58**-**61** were investigated electrochemically to observe the effect on HER catalysis by including proton donating groups into the macromolecular polymer framework. Electrochemical experiments were conducted in water buffered to pH 7 using 0.75 M sodium phosphate as the buffering agent with polymer loadings of 100 μM based on [2Fe-2S] concentration by IR. The initial comparative investigation between the electrocatalytic behavior of metallopolymers **58-61** was done using cyclic voltammetry (CV). The CV data shown in Figure 4.2 indicates the **PDMAEMA-*g*-[2Fe-2S], 58** homopolymer, the **POEGMA-*g*-[2Fe-2S], 59** homopolymer, and two random copolymers, **60** and **61** all exhibit electrocatalytic hydrogen evolution.

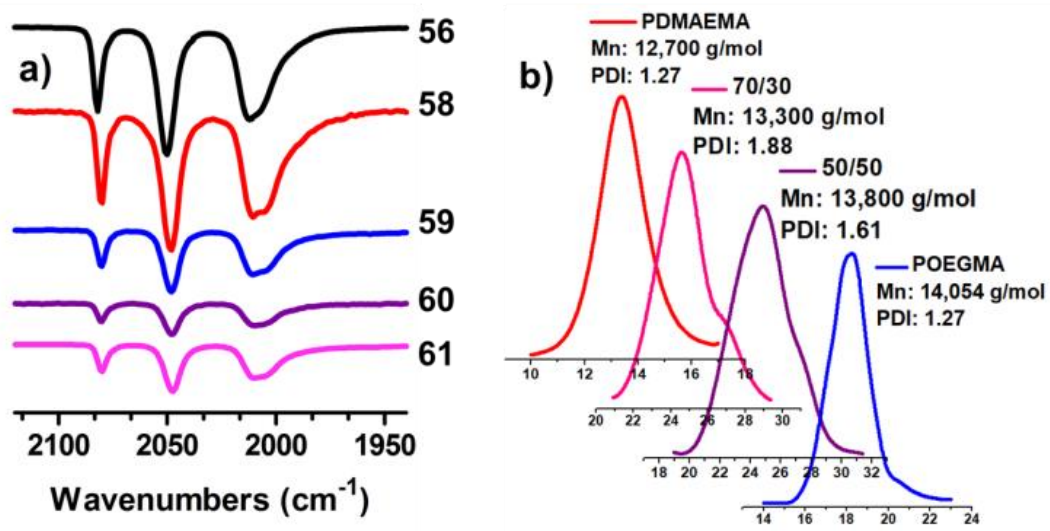

Figure 4.1. IR and GPC characterization of metallo(co)polymers 58-61. a) IR spectra of the Fe-CO region for metalloinitiator **56**, homopolymers **58** and **59** and random copolymers **60** and **61**. **b)** SEC traces for **58**, **59**, **60**, and **61** (y-axis is retention time in minute. See Appendix C for details)

As we postulated, the current-potential responses show a positive correlation between pendant amine inclusion and relative activity towards electrocatalytic hydrogen production. The homopolymer **PDMAEMA-*g*-[2Fe-2S], 58** achieves the highest current density and lowest overpotential, while the **POEGMA-*g*-[2Fe-2S], 59** homopolymer only exhibits weak electrocatalysis. Displaying both the level of tunability and the sensitivity of these metallopolymer

systems to the amount of amine inclusion, the random copolymers **60** and **61** have intermediate responses. Further, we would like to emphasize that the substantial difference in activity seen in the voltammograms between **58** and **59** occurs with no change to the [2Fe-2S] catalytic core.

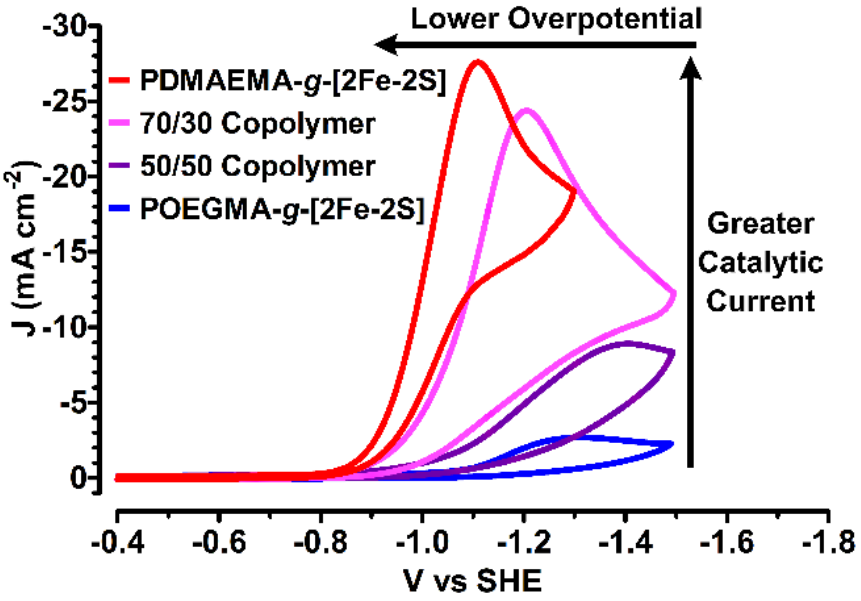

Figure 4.2. CV comparison of 58-61 in pH 7 sodium phosphate buffer. (100 μM based on [2Fe-2S] concentration) in an aqueous solution buffered to pH 7.0 with sodium phosphate (0.75 M). Scans were performed at a sweep rate of 100 mV/s, in quiet solution conditions, and an anaerobic argon sparged solution.

In Figure 4.3, we report the performance of metallopolymer systems **58**-**61** versus a Pt disk electrode as a standard for HER activity using Tafel analysis. Tafel analysis offers a more direct measure of catalytic current density as a function of overpotential requirement than afforded by CV. The zero overpotential for the Tafel plot was based on where the Pt exchange current equals zero for the given solution conditions (Figure C16). As shown in Figure 4.3, the difference of overpotentials between **PDMAEMA-*g*-[2Fe-2S] 58** and Pt surface is approximately 360 mV at a current density of 1 mA/cm^2. Accentuated by plotting the current density on a log scale, the catalytic current onset of **PDMAEMA-*g*-[2Fe-2S] 58**, 70:30 copolymer **61**, and 50:50 copolymer **60** occur at a similar overpotential requirement of approximately 362 mV. Additionally, at current densities below 0.3 mA/cm^2, **58**, **60** and **61** show a comparable Tafel slopes of 55mV/dec, 69 mV/dec, and 58 mV/dec. As the current density increases above 0.3 mA/cm^2, the Tafel slope of the random copolymers decreases with the 50:50 copolymer **60,** diminishing more rapidly than the 70:30 copolymer **61**. The homopolymer **POEGMA-*g*-[2Fe-2S] 59** has a significant overpotential of 722 mV at 0.1 mA/cm^2 and a Tafel slope of 155 mV/dec.

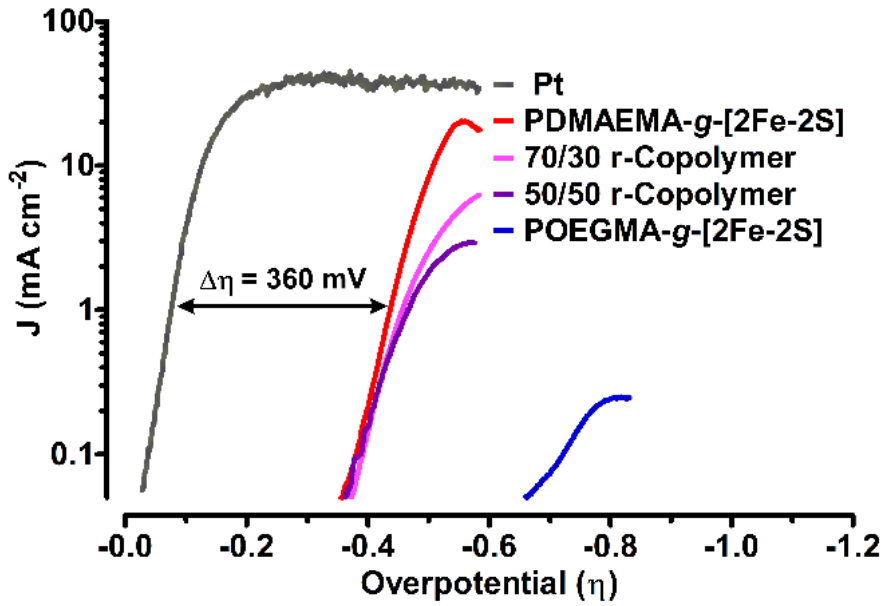

Figure 4.3. Tafel comparison between 58-61 and a Pt disk electrode. Tafel analysis of LSV conducted in an argon purged solution buffered at pH 7 with 0.75 M sodium phosphate using a gold amalgam disk working electrode. The Δη is the difference in overpotential between Pt and **58** at a current density of 1 mA cm^{-2}.

The hydrogenase enzyme and small molecule mimics of the [2Fe-2S] active site suffer from lack of oxygen stability; however, in our previous study, we have demonstrated that **PDMAEMA-*g*-[2Fe-2S] 58** is oxygen stable under catalytic operating conditions.[12] To determine if the presence of protonated amines is necessary to afford oxygen stability, linear sweep voltammetry (LSV) and CV experiments were performed to examine the catalytic current response in the absence and presence of oxygen for metallopolymer systems **58-61**. The CV responses shown in Figure C18 indicate that in ambient air (21% O_2) a notable increase of potential requirement occurs for all systems. However, when evaluating the retention of current density in aerobic conditions, **PDMAEMA-*g*-[2Fe-2S], 58** maintains practically all current response while the homopolymer **POEGMA-*g*-[2Fe-2S] 59** and random copolymers **60** and **61** show significantly diminished current densities compared to scans when the solutions were sparged with argon.

We provide a more quantitative approach to the oxygen stability of metallopolymers **58**-**61** by presenting the LSV data in Figure 4.4. The LSV data mirrors the activity trend of the cyclic voltammograms. **POEGMA-*g*-[2Fe-2S], 59** in an anaerobic environment shows the weakest response and is barely catalytic in the potential window. Under aerobic conditions, **POEGMA-*g*-[2Fe-2S] 59** does not achieve a catalytic current that is above the increased background current the (see inset in Figure 4.4). In contrast, the 50:50 copolymer, **60** retained approximately 60% of its peak catalytic current under aerobic conditions and the 70:30 copolymer, **61** improves to 82% retention of catalytic current under aerobic conditions. **PDMAEMA-*g*-[2Fe-2S], 58** was again found to retain all of its catalytic activity under aerobic conditions, consistent with our previous report. [12] The electrochemical experiments on systems **58**-**61** clearly demonstrate an structure activity relationship showing that increasing the proton donors present in the metallopolymers has three beneficial effects on catalysis; (1) achieving higher current densities, which is correlated to faster rates of hydrogen generation, (2) lower overpotentials, increasing the efficiency of the

catalytic reaction by reducing the energy required to run the reaction and (3) provide aerobic stability to a class of catalysts which are typically irreversibly deactivated by the presence of even small amounts of oxygen.

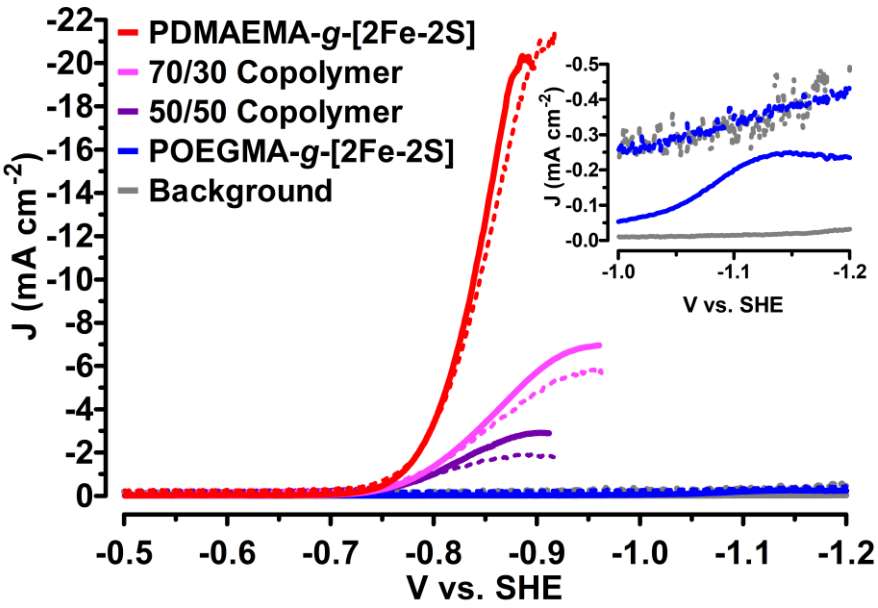

Figure 4.4. LSV comparison of electrocatalytic HER activity of metallopolymers 58-61 under anaerobic and aerobic conditions. Linear sweep voltammetry of the four metallopolymer systems **58-61** under aerobic (dashed lines) and anaerobic (solid lines) conditions in pH 7 sodium phosphate buffer (0.75 M) with rapid stirring and a sweep rate of 5 mV/s. The inset shows a zoomed-in region to show the current response of **POEGMA-g-[2Fe-2S] 59**.

This work demonstrates an exciting new application for controlled radical polymerization techniques in which a functional metalloinitiator provides access to modular synthetic method to generate metallopolymers in which the polymer functions not only as a support to modulate the physical properties of the catalyst (i.e., solubility, processability, etc.), but also tunes catalyst activity by manipulating the macromolecular environment around the active site. We have shown that by varying only the identity and feed ratios of the commercially available (co)monomers used, we can drastically improve the activity and stability of a small molecule organometallic catalyst providing increases to electrocatalytic rates, catalyst stability, oxygen stability, and catalyst efficiency by reducing the overpotential requirement. Achieving hydrogen evolution rates that far exceed that of the fastest [FeFe]-hydrogense and provides oxygen tolerance to systems typically relegated to completely anaerobic conditions demonstrates the power of this methodology for the synthesis of functional metallopolymers and reinforces the importance of the outer coordination sphere in HER electrocatalysts.

Acknowledgements

DLL, RSG, and JP gratefully acknowledge support of this work by NSF (CHE-1664745). KM acknowledges support of this work by NSF (DMR 1501324)

Abbreviations

ATRP, atom transfer radical polymerization; HER, hydrogen evolution reaction; PDMAEMA, poly-dimethylaminoethylamine; PEGMA, poly-oligoethyleneglycolmethacrylate; TON, turnover number; TOF turnover frequency; η, overpotential

Chapter 5 Synthesis and Characterization of Water Sensing PEDOT:Nafion Colloidal Polymers

Richard F. Vreeland[1,2], William P. Brezinski[1,2], Adam R. Meier[1], Sean M. Lambert[1], Nicholas D. Laude[1], Richard S. Glass[1], Michael L. Heien[1,*]

1. Department of Chemistry and Biochemistry, University of Arizona, 1306 East University Boulevard, Tucson, AZ 85721, U.S.A.

2. These authors contributed equally to this work

*To whom correspondence should be addressed

mheien@arizona.edu
FAX: 520-621-8407

Abstract

Oligo-EDOT:Nafion composite colloids are easily prepared via a one pot synthesis in ambient conditions from commercially available reagents. These particles form uniform dispersions in acetonitrile with a diameter of approximately 100 nm, and we characterize them by visible absorption spectroscopy, thermogravimetric analysis, x-ray photoelectron spectroscopy, transmission electron microscopy, and dynamic light scattering. When suspended in acetonitrile, these particles form a stable suspension of low molecular weight PEDOT and Nafion, as the particles have a zeta potential of -49 ± 11 mV. Exposure to water or other polar protic solvents induces chemical and physical changes in the colloids, resulting in a bathochromic shift in the absorption spectrum and a constriction of the nanoparticle geometry from a diameter of 111 ± 8 nm to 71 ± 6 nm. Here, we adapt this supramolecular behavior to inexpensively (<2 USD) and rapidly (a few seconds) detect the water content of acetonitrile with UV-VIS absorption spectroscopy. The limit-of-detection of water in acetonitrile is 125 ppm, and the linear dynamic range extends up to 2500 ppm.

Introduction

Nanoparticles are an important class of functional materials with potential to impact a variety of problems of interest. The field of colloidal polymers is rapidly growing, with applications of colloidal polymer dispersions seen in imaging,[209,210] drug delivery systems and medicine,[211–213] biosensors,[214–216] separations[217] and electronic materials.[218] While the colloidal polymer synthesis field is fairly mature, there is still a need for new functional polymer colloids. Polythiophenes such as poly(3,4-ethylenedioxythiophene) (PEDOT) or poly(3,4-propylenedioxythiophene) (ProDOT) are of particular interest because of their conductivity and ubiquity in electronic devices,[219–221] electrochromic devices,[222] supercapacitors,[223,224] medical coatings,[225] and biosensors.[226,227] The ethylene (EDOT) or propylene (ProDOT) bridge provides a site to incorporate modifiers and linkers making polythiophenes an excellent scaffold upon which to incorporate biotherapeutics or electronic interface modifiers.[228]

When polymerized, PEDOT is a blue solid; intractable in all solvents regardless of small molecule doping. As a result, PEDOT is most commonly used as a polymeric blend with a polystyrenesulfonate (PSS) counterion.[229] The deprotonated sulfonate groups on PSS interact with positively charged polarons on PEDOT chains through a coulombic attraction, establishing a strong intermolecular interaction in which PSS chains entangle PEDOT.[230,231] With this interaction, PEDOT and PSS form a stable and soluble dispersion, which is easily processed by spin coating, spray coating, doctor blading, or dip coating.[229]

Here, we draw inspiration from polystyrenesulfonate and form a stable colloidal dispersion of oligo-EDOT by oligomerizing EDOT in the presence of an aqueous dispersion of perfluorinated sulfonated polymer (Nafion). The solubility of the PEDOT is greatly enhanced, and the fluorinated backbone of the Nafion gives rise to unique solution-dispersed behavior. After the addition of polar protic solvents such as water or methanol, these nanoparticle dispersions undergo a chemical change, and irreversibly change conformation to minimize free energy in the new solvation environment. We exploit this behavior to use these colloidal dispersions as quantitative detectors of water content in acetonitrile.

A promising application of solvation environment-sensitive colloidal polymers is to use them to detect impurities in solvents. Anhydrous conditions are required for a many industrial syntheses and device fabrication techniques. Drying solvents is expensive - molecular sieves require activation by extended heating at high temperatures (>200 ^{o}C) and rely on slow diffusion of water into 3 – 4 Å pores, industrial scale distillation requires enormous amounts of energy and can pose serious safety concerns, and liquid-liquid extraction generates large amounts of waste.[232,233] Due to the high economic and environmental cost of purifying solvents the Karl-Fischer titration is routinely used to quantify the water content of solvents used in industrial applications.[234] These titrations are accurate from the parts per million up to the parts per hundred range, but require an expensive ($5000 USD) instrument that must be operated by an expert and is only useful for the task of Karl-Fischer titrations. Other quantitative methods exist, such as ^{19}F NMR spectroscopy or gas chromatography, but these methods require internal standards and access to expensive instruments.[235,236] A clear niche exists for a simple, rapid, inexpensive, and accurate method to quantify the water content of organic solvents.

Here, we present the synthesis and characterization of a PEDOT:Nafion colloidal polymer system which provides an inexpensive ($2 USD per calibration and measurement), simple, rapid, and quantitative assay for water in acetonitrile. In addition to this practical application, these nanoparticles may have further utility in serving as a scaffold for drug delivery, electronic device interface modifiers, or sensors for other types of molecules.

Experimental

Chemicals and Synthesis. Polymer colloids were prepared by solvent evaporation oligomerization in borosilicate glass 20 mL scintillation vials. Unless otherwise specified, 150 µL of 3,4-ethylenedioxythiophene (EDOT) (Sigma Aldrich, St. Louis, MO, USA) and 150 µL of Nafion (LQ-1105, 5% w/w in solution of lower aliphatic alcohols and water) (Ion Power, New Castle, DE, USA) was added to 10 mL of HPLC grade acetonitrile (EMD Millipore, Darmstadt, Germany) and the vial was left uncapped in a laboratory fume hood for 18 hours. A purple solid formed at the bottom of the vials which turned red upon the addition of 20 mL acetonitrile.

UV/Visible Absorbance Measurements. This solution was split evenly into separate glass vials, and spiked with 10-100 µL of a nanopure water/acetonitrile stock solution to bring the concentration of added water to between 125 ppm (parts per million) and 16 ppt (parts per thousand). Vials were capped and mixed for 5 seconds, and then UV/Vis absorbance measurements were made in a capped quartz 1 cm path length cuvette. Measurements were made using an Agilent 8453 diode array UV/Visible spectrophotometer (Agilent Technologies, Santa Clara, CA, USA) was used for all UV/Vis measurements.

Thermogravometric Analysis Measurements. A Tecnai Spirit transmission electron microscope (FEI, Hillsboro, OR, USA) operated at 100 kV was used for all electron microscopy. Samples were spotted 5-10 times onto a 300 mesh carbon-coated copper TEM grid (Electron Microscopy Sciences, Hatfield, PA, USA) and dried in air.

X-ray Photoelectron Spectroscopy. All x-ray photoelectron spectra were acquired with a KratosAxis Ultra 165 DLD Spectrometer equipped with magnetic immersion electron lens using 300 W monochromatic Al(kα) radiation in constant analyzer energy mode. The sample analysis area used was 700 µm x 300 µm. Survey spectra were collected using a pass energy of 160 eV and specific elemental regions were collected using 20 eV pass energy and averaged over multiple scans. The analysis chamber was maintained at a pressure $\leq 5 \times 10^{-9}$ torr. Samples were prepared by drop casting 1 mL of a 10 mg/mL solution of dispersed polymer colloids onto a 1 cm^2 glass substrate and dying in ambient conditions.

Trace Metal Analysis. ICP-MS was performed using a Perkin Elmer ELAN DRC II (Perkin Elmer, Waltham, MA, USA). All reagents were trace metal grade, and quantitation was done relative to an indium internal standard.

Dynamic Light Scattering and Zeta Potential Measurements. Dynamic light scattering (DLS) was performed on a Zetasizer ZS (Malvern Instruments, Worcestershire, United Kingdom). 3 mL of aliquots of the particles were analyzed in borosilicate glass cuvettes at 25°C using the automatic mode (n = 3 batches of particles). The z-average radius ($z_{average}$) and polydispersity index (PDI) were calculated from the correlation function using the Malvern Zetasizer Software

version 7.03 (Malvern Instruments, Worcestershire, United Kingdom). The zeta potential of the particles was measured in ethanol because our zeta potential cell was not compatible with acetonitrile.

Results and Discussion

Synthesis and Thermogravimetric Analysis of PEDOT:Nafion Colloidal Polymers. The solvent evaporation polymerization of PEDOT:Nafion colloids is depicted in Scheme 5.1. A dilute solution of EDOT and Nafion in acetonitrile is added to a scintillation vial, which is left exposed to atmosphere and evaporated in a fume hood for 18-24 hours (a). After evaporation, a solid mass of particles is formed on the container (b), which is readily solubilized by the addition of acetonitrile (c). Varying the EDOT and Nafion concentrations yields differently colored solids, ranging from brown to red to purple to blue, with higher concentrations of EDOT and Nafion resulting in dark brown colored material. After exposure to ambient humidity for hours to days (depending on airflow and humidity), nanoparticle suspensions that start brown, red, or purple will shift in color to blue. After preparation, the nanoparticles will remain suspended in acetonitrile for several months with a maximum dispersable mass loading of approximately 5-10 mg/mL.

In order to probe the reagents for adventitious metals which might catalyze the reaction by oxidation, the acetonitrile, Nafion, and EDOT were quantitatively analyzed for the elements Be, Al, Ti, V, Cr, Mn, Fe, Co, Ni, Cu, Zn, As, Se, Mo, Ag, Cd, Sn, Sb, Ba, and Pb by ICP-MS by evaporating 1 mL of each sample and re-suspending them in 10 mL of 0.1 M nitric acid, followed by filtration through a 0.45 um nylon syringe filter. No metals were found at concentrations above 10 ppb in any of the reagents. Three freeze-pump-thaw cycles were performed on a solution of EDOT and Nafion in an oxygen-free glovebox, where the synthesis was repeated successfully, indicating that oxygen is not required for oligomerization, and confirming that the formation of oligo-EDOT is likely not proceeding through the standard oxidative route. The Nafion in some manner acts as an oligomermerizing agent for EDOT, though sulfonate groups are not known to be oxidizing. When the synthesis is repeated with a lithiated (instead of protonated) Nafion analog (LITHion, Ion Power, New Castle, DE, USA) in place of Nafion, no particles or colored solids form, suggesting that a low pH is needed for this polymerization.

Thermogravimetric Analysis and X-ray Photoelectron Spectroscopy Measurements of Polymer Content in the Colloidal Particles. To determine the amount of oligo-EDOT and Nafion in the resulting colloids, two different approaches were taken. First, thermogravimetric analysis of nanoparticles (Figure 5.1a) shows a large decrease in mass (~80 %) of the particles at an onset temperature of approximately 420 °C corresponding to the thermal degradation of the CF_2 portion of Nafion. Further, the next largest feature in the thermogram is a loss in the range of 350 to 380 °C which corresponds to the loss of the sulfonate groups from Nafion. Lastly, the evaporation of excess EDOT and low order EDOT oligomer is expected in the range of 200 to 250 °C. The remaining mass is lost in this region indicating only a small fraction of EDOT and oligomer are present.

To edify the TGA results XPS analysis was performed on the particles. A thin film of the particles was made by drop casting and drying was analyzed by XPS. The results of this analysis showed the primary elemental content of the particles includes F, C, O, and S (Figure 1B). This is expected based on the structure of both Nafion and EDOT (refer back to Scheme 5.1). To quantify the content of particles we used the S2p region of the spectrum as this region contains a reporter peak for both Nafion and EDOT (Figure C1). The dominant sulfur feature is due to the sulfonate from the Nafion (Binding energy = 168.5 eV) whereas the spectral feature from alkyl sulfur (Binding energy = 164 - 165 eV), is owed to sulfur in the oligo-EDOT chains. Comparison of the integrals of these peaks revealed that the particles are made up of 89 ± 3 % Nafion and 11 ± 3 % oligo-EDOT (± SEM, n = 3). This confirms the TGA analysis which suggested that the particles were mostly Nafion in content. Taken together these data indicate that only a small amount of oligo-EDOT is needed to form the colloidal polymer.

UV-visible Absorbance Spectroscopy Measurements. The synthesis of the particles was optimized by modifying the concentration of the starting reagents. UV-Vis absorption spectra of a panel of synthesis conditions are shown in Figure 5.2. Colloidal particles were synthesized by varying the EDOT concentration from 665 ppm to 66500 ppm with Nafion held at a constant 310 ppm, or by varying the Nafion concentration from 5 ppm to 3125 ppm with EDOT held constant at 16625 ppm. The particles were synthesized as described in Scheme 5.1, and suspended in 20 mL acetonitrile prior to measurement. Absorption below 300 nm corresponds to EDOT, while protonated EDOT oligomers are present between approximately 325 nm and 450 nm. The dimer absorbs at maxima of 325 nm and 334 nm, the trimer at 353 nm, 382 nm, and 408 nm, and the tetramer at 400 nm, 426 nm, and 447 nm. In synthesis conditions with higher EDOT or Nafion concentrations (above 310 ppm Nafion and 6650 ppm EDOT), colloidal particles approximately 100 nm in size become measurable by dynamic light scattering (DLS), and absorbance maxima at both 491 nm and 589 nm are visible.

To examine the effect of various solvents on the particle's absorption maximum wavelength, two separate batches of nanoparticles were prepared with 125 µL Nafion, 125 µL EDOT, and 10 mL acetonitrile. These particles were re-solvated in 20 mL of acetonitrile and combined into a 50 mL beaker. From this beaker, nine 3 mL aliquots of dispersed particles in acetonitrile were removed and added to quartz cuvettes. To each of these cuvettes, between 2 and 10 drops of solvent were added. The solvents varied in polarity hydrogen bonding capacity (as measured by the solvatochromic pyridinium N-phenolate betaine dye),[237] and proticity, and including diethyl ether, dichloromethane, 1-butanol, ethyl acetate, acetone, acetronitrile (control), methanol, ethanol, and water. The results are summarized in Table 1. A large volume of solvent (10 drops) was added to vials that did not appear to change color upon the addition, and a small amount (2 drops) was added to cuvettes where a large shift in absorption occurred. In general, aprotic solvents do not shift the absorption maximum of the particles when compared to the control. Protic solvents shift the absorption maximum by between 13 nm (butanol) and 46 nm (water). Additionally, the absorption maximum shift upon the addition of water is greater than the shift observed with less polar protic solvents.

Transmission Electron Microscopy Measurements. Transmission electron microscopy (TEM) was used to visualize the structure of the dispersed particles and to examine the effects of

hydration on particle structure. A batch of OEDOT:Nafion particles were prepared with 125 µL Nafion, 125 µL EDOT, and 10 mL acetonitrile. These particles were re-suspended in 20 mL acetonitrile, and appeared red in color. The particles were split into two 10 mL aliquots, and to one solution, 2500 ppm water was added. After the addition of water, the color of this solution changed from red to blue. Both aliquots were then filtered with 0.2 µm nylon syringe filters and spotted onto carbon TEM grids within 10 minutes of re-suspension.

Representative transmission electron micrographs are shown in Figure 5.3, with (A) depicting a colloidal particle prepared at [EDOT] = 1.12 mM in an unhydrated solution of acetonitrile, (B) depicting a colloidal particle prepared at [EDOT] = 1.12 mM in a hydrated (2500 ppm H_2O) solution of acetonitrile. Both A and B show a similar microstructure, with nodules 10-30 nm in diameter connected in a twisted chain configuration. In the absence of water, the colloidal particles exhibit an open configuration while the hydrated colloids typically exhibit a closed configuration, perhaps to minimize surface energy. No particles were identified by TEM when Nafion or EDOT alone was dispersed in acetonitrile or ethanol and drop cast onto carbon grids.

Dynamic Light Scattering In the interest of understanding the synthetic mechanism and painting a clearer picture of solution-phase particle dynamics, the size of the colloidal particles was evaluated by dynamic light scattering (DLS). A batch of particles was prepared with 125 µL Nafion, 125 µL EDOT, and 10 mL acetonitrile. These particles were brought up in 20 mL acetonitrile, and appeared red in color. The particles were filtered with a 0.2 µm nylon syringe filter, split into equal volumes, and stored in separate containers. To one container, 3 drops of water were added, and the hydrated particles changed color from red to blue in a few seconds. To the other container, 3 drops of acetonitrile were added. The hydrodynamic diameter (size) of both the hydrated and unhydrated solutions was measured by dynamic light scattering (DLS). Unhydrated nanoparticles had an average diameter of 111 ± 8 nm (± represents SEM, n = 3 batches of particles) with a polydispersity index (PDI) of 0.31 ± 0.09, and hydrated particles had an average diameter of 71 ± 6 nm with a PDI of 0.26 ± 0.05 (Figure 5.3c). The difference between average diameter is statistically significant (Student's t test, $p < 0.01$), while the difference in PDI is not. The average hydrodynamic diameter of the particles decreased by 36% upon the addition of water to the dispersed solution in acetonitrile. A reasonable explanation for this behavior is a solvent-induced minimization of surface energy that manifests in a conformational change.

Oligo-EDOT:Nafion Colloidal Polymers for the Quantitative Qetection of Trace Water in Acetonitrile. With the addition of water or other solvents to red dispersions of particles suspended in acetonitrile, a bathochromic shift in the absorption maximum wavelength of the solution is observed over the course of 1-2 seconds when gently shaken or stirred. This bathochromic shift is not reversible when particle dispersions used for water quantitation are dried with molecular sieves. These colloidal particles undergo structural (as observed by TEM) and chemical (as observed by spectroscopy) changes upon the addition of polar protic solvents. Here, we exploit these changes to employ the particles as a sensor for water in acetonitrile. Solutions with a red color upon suspension in acetonitrile were chosen for water detection as they displayed the largest bathochromic shift in absorption maximum upon the addition of water, and therefore had the highest sensitivity. Figure 5.4a shows the absorption spectra of a single pot

synthesis of particles (prepared with 125 µL Nafion, 125 µL EDOT, and 10 mL acetonitrile), separated into six vials (3 mL per vial). A volume of 10-100 µL of a water/acetonitrile mixture was spiked into the vials, and they were quickly mixed for 5 seconds then measured on the spectrophotometer. Figure 5.4b shows the UV/visible absorption spectra maximum in the visible range plotted against the water concentration, where error bars are standard error of the mean, with replicate measurements coming from a new solution of dispersed particles with new water spikes. The limit of detection is probably dictated by the 1 nm resolution of our spectrophotometer at a concentration of 125 ppm H_2O. The linear dynamic range extends up to 2500 ppm H_2O, though quantitation is possible via non-linear fits up to 10000 ppm H_2O.

The spectrum contains three peaks, one at ~380 nm, one at ~410 nm, and one at ~510 nm. The first two peaks correspond to the protonated EDOT trimer, and the latter peak corresponds to low order oligo-EDOT (>5 monomer units).[229] Upon the addition of water, the peak at 380 nm grows in intensity, and the peak at 510 nm shifts bathochromically while decreasing in magnitude. This shift suggests that the important absorbance transition is a $p \rightarrow p^*$ transition as increased polarization forces lower the energy difference between ground and excited states. Whereas a hypsochromic shift would result in a blue shift in absorbance max resulting from $n \rightarrow p^*$ transitions which arise from increased solvation of non-bonded electron pairs which lowers ground state energy of the n orbital. Bathochromic shifts are typically smaller than hypsochromic shifts which is also consistent with the observed magnitude of the shift which is 60 – 70 nm at maximum.

When a 20 mL vial containing 4 mL of dispersed particles in acetonitrile is left capped after the quantitative addition of water, the absorbance of the dispersed particles changes slowly with time. Figure 5.5 illustrates this time-dependent absorption of water by monitoring the wavelength of maximum absorbance for solutions of water-spiked acetonitrile over the course of 12 hours. After solutions were spectroscopically measured, they were stored under dry argon. The acetonitrile blank's absorbance wavelength maxima increases by ~3 nanometers per hour. Additionally, in solutions left to equilibrate for an extended period of time, the absorbance maxima increases more rapidly at water concentrations under 5000 ppm, and rises to a slightly higher plateau. This effect has practical consequences for utilizing these nanoparticles as quantitative sensors. Measurements must be performed within the first 5-10 minutes of particle-solvent interaction to achieve maximum sensitivity as defined by $\lambda_{max,\ sample} - \lambda_{max,\ blank}$, otherwise changes in λ_{max} may be incorrectly interpreted as arising from changes in water concentration.

Conductivity and Zeta Potential Measurements. For many applications, PEDOT is used because of its conductivity. We wanted to determine if these particles were also conductive. To determine if the particles were conductive from all tested synthesis conditions were not conductive when drop-cast onto glass slides and rinsed with water. This could be a product of the low-order EDOT oligomers having a high charge hopping barrier, or perhaps due to the synthesis conditions favoring oligomers with an interrupted pi-conjugation system. To determine the possible polymerization mechanisms and level of conjugation in the polymer we performed a synthesis using triflic acid, the monomeric homologue of Nafion. Analysis of the resultant oligo-EDOT by MALDI-MS showed that short oligomers (2 – 6 monomer units) were formed. A mass

difference of 142 a.m.u. indicated that the PEDOT formed by this reaction still has hydrogen present at the bonded carbons and is therefore not conjugated (Figure D3).

We also measured the zeta potential of particles synthesized with 125 µL Nafion, 125 µL EDOT, and 10 mL acetonitrile and re-dispersed in 10 mL ethanol was measured to be -49 ± 11 mV (n = 3 batches of particles) (Figure 5.6). This zeta potential is consistent with the observation that these particles do not settle in solution, as a highly charged surface will resist aggregation. No particles were observed by DLS and no zeta potential measurements could be made when EDOT or Nafion alone was dispersed in acetonitrile or ethanol, respectively. This also supports the conclusion that the particles themselves are not useful as conductors because they would not be in close proximity to one another.

Lastly, the ability to create oligo-EDOT without an oxidant or applied potential is of great broad interest as a potential new synthetic method for PEDOT. A solution of nanoparticles (prepared with 9 µM EDOT, 200 µL Nafion in 10 mL ACN) left capped in a hood for 60 days to ensure any and all reactions that would promote polymerization went to completion. This produced some nanoparticles with very interesting morphologies (Figure 5.7) consistent with our assertion that the particles are a colloidal polymer system. Phase or crystal boundaries on the order of 5 nm are readily apparent in the micrograph, indicating that there are areas of differing electron density in the branches, possibly from longer EDOT oligomers (or PEDOT). This is promising evidence for a new synthesis of PEDOT in the absence of oxidant. Efforts toward elucidating the mechanism of this oligomerization are detailed in Appendix D.

Conclusions

Herein, we have characterized a novel synthesis of OEDOT:Nafion colloidal polymers. These nanoparticles are easily synthesized from two inexpensive, commercially available materials in a one-step room temperature procedure requiring no special equipment. The oligomerization proceeds even under strict anaerobic conditions, indicating oxygen is not required for particle genesis. Given the absence of other possible oxidizing species, this would seem to indicate a non-oxidative mechanism is at play. This oligomerization mechanism is of great general synthetic interest, as to our knowledge; there are no outstanding examples of non-oxidative oligomerization of non-halogenated polythiophenes.[238] By manipulating synthetic conditions to increase the length of the oligomer chains, this methodology could potentially provide a new route to polythiophenes. A non-oxidative polymerization of thiophenes could potentially provide a more homogeneous conductive material than what is prepared by oxidative polymerization with a Lewis acid such as $FeCl_3$ due to the complete exclusion of any trace metal impurities. The mechanism of the oligomerization may be of high general synthetic interest and is under investigation.

The colloidal particles have a tunable starting color, and because of both chemical and physical changes, their absorbance and morphology change predictably upon encountering protic polar solvents while suspended in acetonitrile. We have exploited this interesting supramolecular behavior to employ these colloidal polymer particles as a quantitative water sensor in acetonitrile using a UV/Visible spectrophotometer. The linear dynamic range of water detection extends from 125 ppm up to 2500 ppm, which is a concentration range of interest for trace water analysis.

Appendix D Description

Zeta potential measurements, mass spectra, a discussion of and studies towards the elucidation of the mechanism by which Nafion-OEDOT particles form was well as additional quantitative calibration data are available in Appendix D.

Acknowledgements

This work was supported by University of Arizona startup funds. The authors thank Dr. Lawrence Hill, Dr. Jared Griebel, Dr. Philip Dirlam, and Dr. Nick Pavlopoulos for fruitful polymer discussions. The authors also thank Dr. Katrina Miranda for use of the UV/Visible spectrophotomer, Dr. Craig Aspinwall for use of the Malvern Zetasizer, and Mary Kay Amistadi for performing the trace metals analysis. The authors thank Paul Lee for technical expertise and XPS experiments.

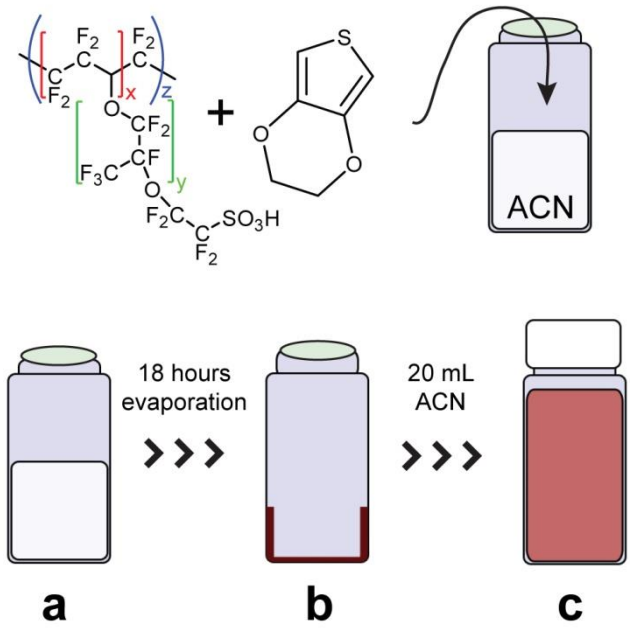

Scheme 5.1. Synthesis of oligo-EDOT:Nafion nanoparticles by solvent evaporation. X, Y, and Z represent polymer subunits. On average, there are 18 CF2 units between each sulfonate for the particular MW dispersion of Nafion used. **a)** A mixture of EDOT and an aqueous dispersion of Nafion are dispersed in acetonitrile. This solution is mixed and left uncapped in a fume hood for 18 hours. **b)** Red and purple particles are formed on the bottom and sides of the vial. **c)** Upon re-suspension in acetonitrile, a uniform dispersion of oligo-EDOT:Nafion nanoparticles appear red in color.

Table 5.1. Shifts in absorbance caused by the addition of solvents to the nanoparticle dispersion in acetonitrile. (± SEM, n = 3). ET(30) is an indicator of polarity and hydrogen bonding capacity adapted from C. Reichardt.[237]

Solvent	$E_T(30)$ (kcal·mol^{-1})	Max. Abs. λ (nm)	Protic	Drops added
Acetonitrile (control)	46	531 ± 4	no	10
diethyl ether	34.5	535 ± 3	no	10
ethyl acetate	38	535 ± 4	no	10
dichloromethane	41	533 ± 3	no	10
acetone	42	531 ± 2	no	10
1-butanol	50	544 ± 5	yes	2
ethanol	52	570 ± 2	yes	2
methanol	55	557 ± 6	yes	2
water	63	577 ± 4	yes	2

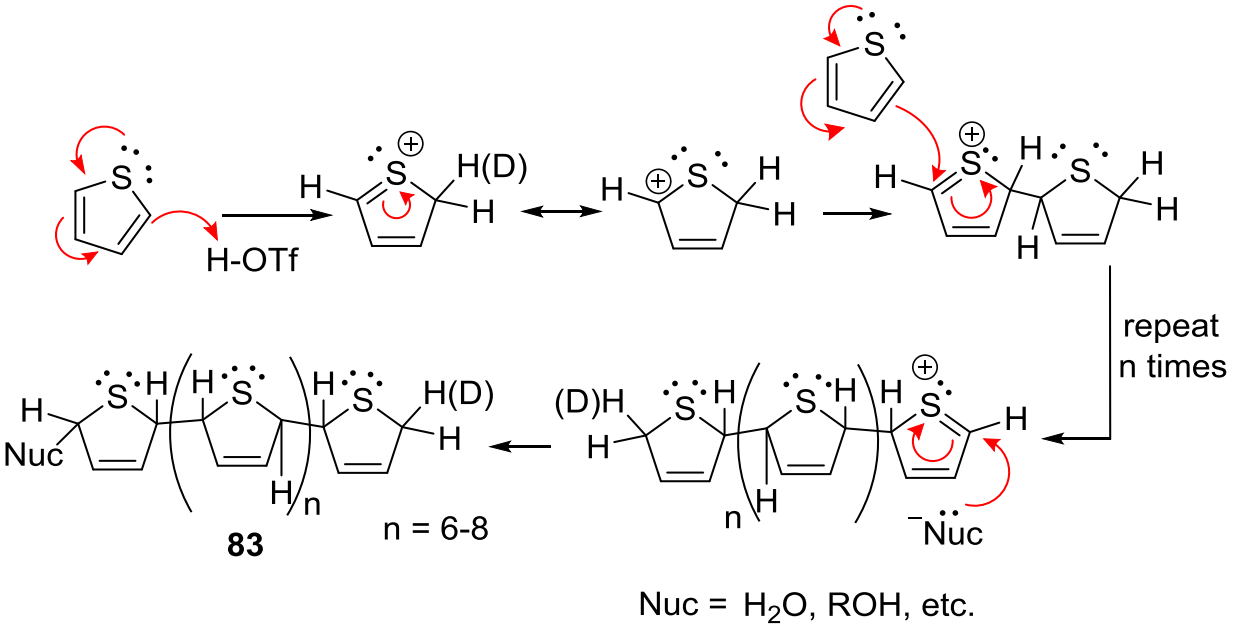

Scheme 5.2 Proposed cationic oligomerization of EDOT to dihydro-OEDOT (83) catalyzed by Nafion.

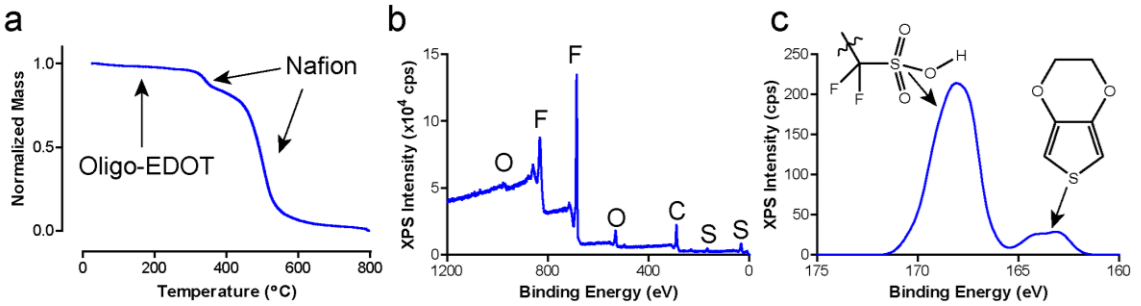

Figure 5.1. Characterization of the chemical composition of the colloidal particles. a) Thermogram obtained from 2.2 mg of nanoparticles. Range = 25 – 800 °C, rate = 10 °C/minute, stabilized at 25 °C for 10 minutes prior to run. EDOT monomer, dimer, trimer, and oligomers are evaporated at 50 – 250 °C, while Nafion degrades at temperatures in the range of 350 – 550 °C. **b)** X-ray photoelectron spectrum of a film of nanoparticles prepared by drop-casting 1.0 mL of a 10 mg/mL solution of nanoparticles onto a 1 cm2 glass substrate and dying in ambient conditions. This spectrum shows that the primary chemical composition of the particles is C, O, S, and F. **c)** Zoom-in of the sulfur-2p region of the XPS spectrum. As both of the polymers contain sulfur in different chemical bonding environments, this region can be used to approximate the relative abundance of thiophene and sulfonate in the particles

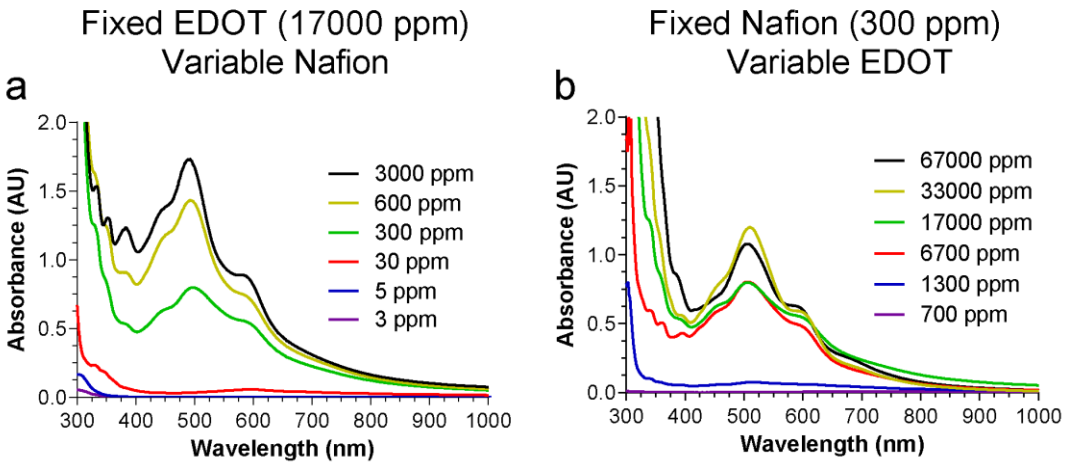

Figure 5.2. UV-Visible absorption spectra of nanoparticles prepared in different synthesis conditions. a) At a fixed EDOT concentration, with variable Nafion concentrations. **b)** At a fixed Nafion concentration, with variable EDOT concentrations.

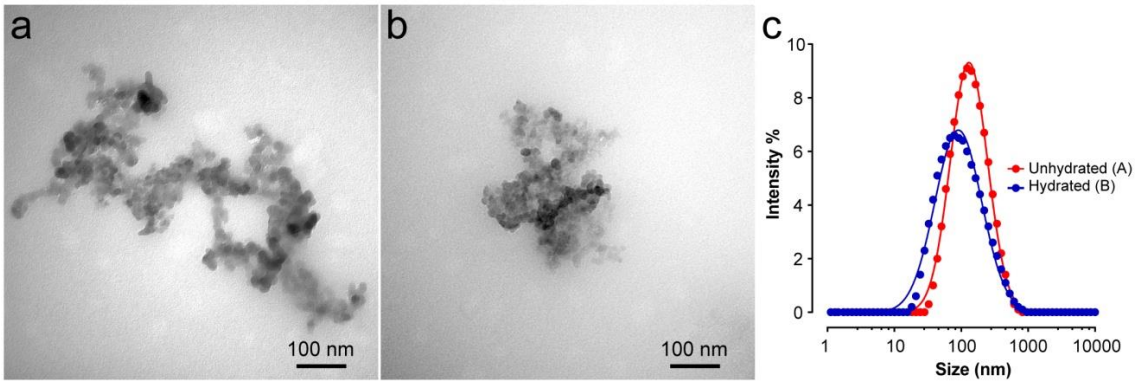

Figure 5.3. Two representative nanoparticles prepared from the same pot of solution. a) Half of the particles were drop-cast onto a TEM grid within 10 minutes of re-suspension. These particles exhibit an open conformation. **b)** The other half of the particles were exposed to 2500 ppm H2O prior to being drop-cast. The particle exhibits a surface-energy minimizing conformation, wrapping itself into a spherical shape. **c)** This size change was confirmed with dynamic light scattering measurements, which show a statistically significant decrease (111 ± 8 nm vs. 71 ± 6 nm, a 36 % decrease, ± represents SEM, n = 3 batches of nanoparticles, $p < 0.01$) in particle size upon hydration.

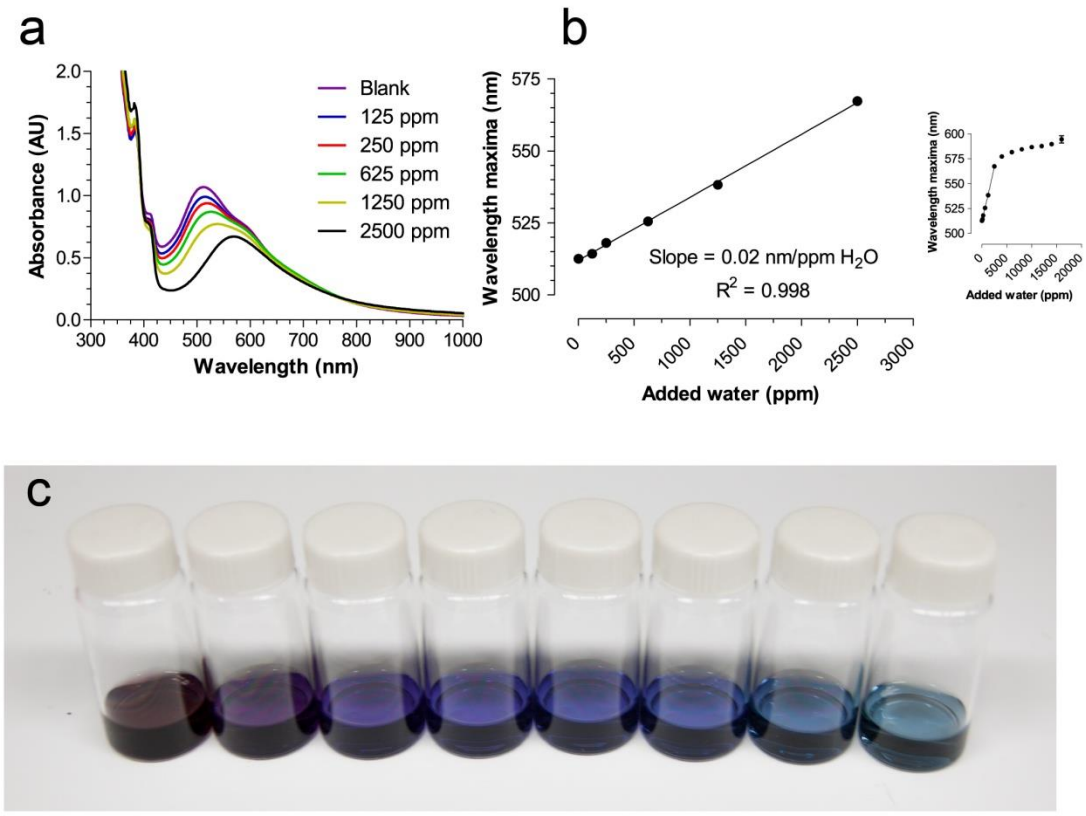

Figure 5.4. Oligo-EDOT:Nafion nanoparticles as a quantitative water sensor. a) UV/Visible absorption spectra of acetonitrile-dispersed nanoparticles with different concentrations of water in solution. **b)** Linear region of the calibration plot of water concentration vs. wavelength maxima of visible absorbance. (n = 3, error bars are standard error of the mean) Inset: Entire range of tested water concentrations shows a roll-off in linearity after 2500 ppm H2O. **c)** Solutions of nanoparticles dispersed into 4.0 mL aliquots of acetonitrile. L to R – increasing concentrations of water added, 0 ppm, 1000 ppm, 2000 ppm, 3000 ppm, 4000 ppm, 5000 ppm, 6000 ppm, 7000 ppm.

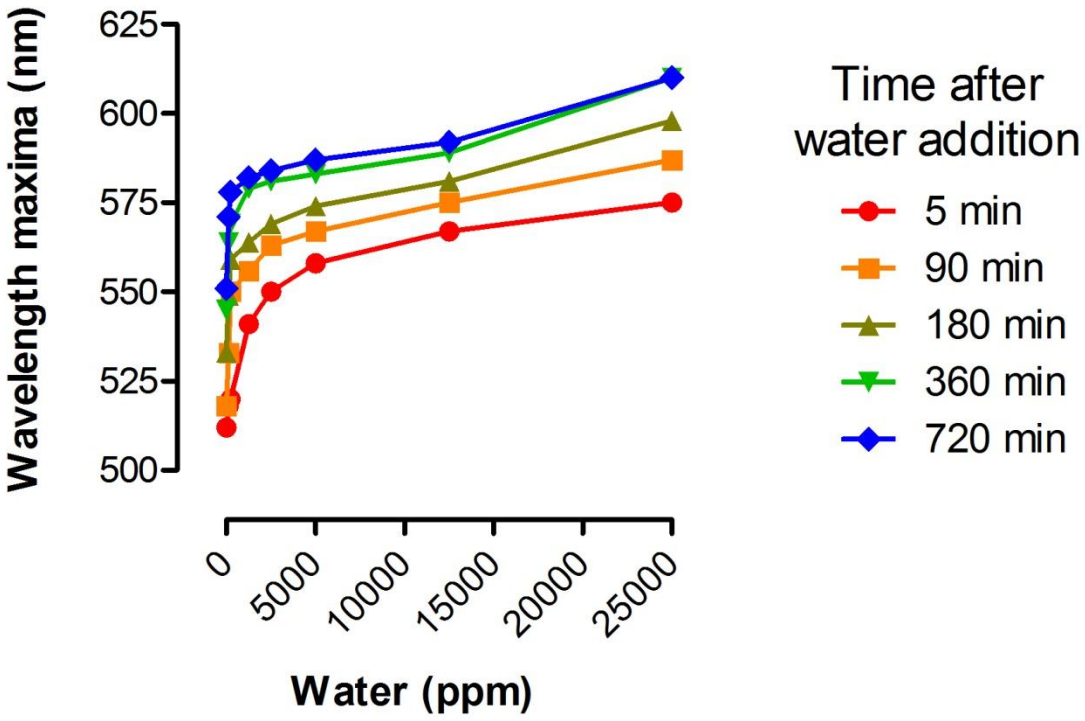

Figure 5.5. Time-dependent wavelength of maximum absorbance for nanoparticle dispersions with varying concentrations of added water. Nanoparticle dispersions were stored under dry argon between measurements to minimize the effect of atmospheric water.

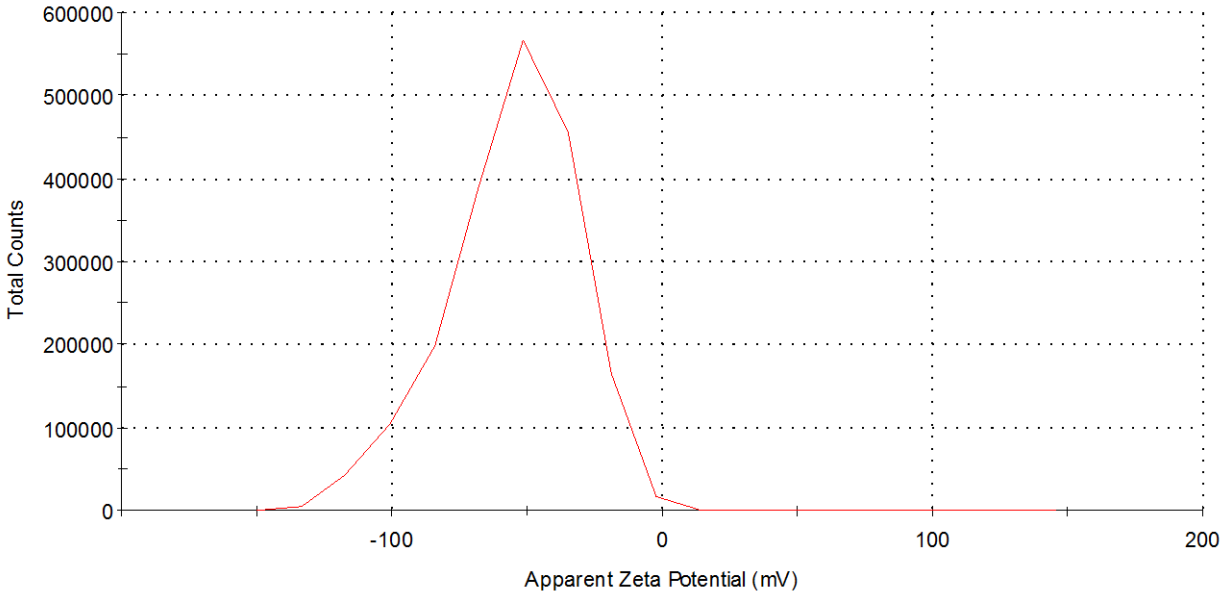

Figure 5.6. Zeta potential measurement of colloidal particles. Particles synthesized with 125 µL Nafion, 125 µL EDOT, and 10 mL acetonitrile. Particles were suspended in 10 mL ethanol for measurements. The measured zeta potential was to be -49 ± 11 mV (n = 3 batches of particles). There was no measureable zeta potential for solutions containing only Nafion or EDOT.

.

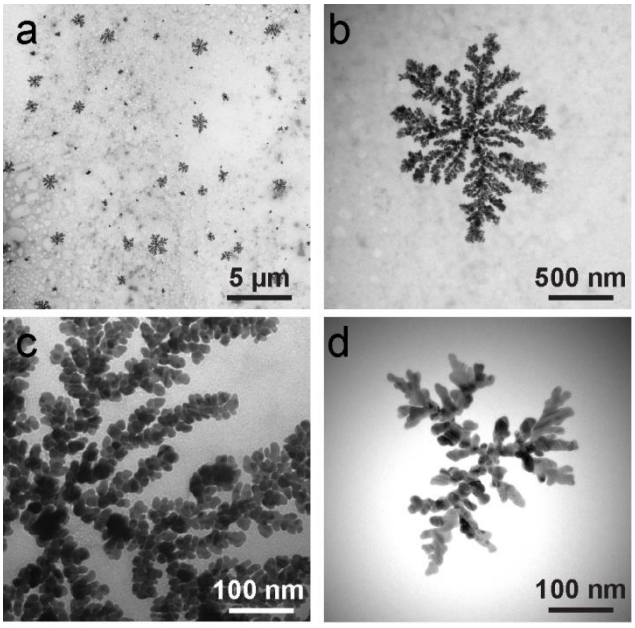

Figure 5.7. Transmission electron micrographs of oligo-EDOT:Nafion colloidal polymers. Colloidal particles prepared with [EDOT] = 9 µM, 200 µL Nafion in 10 mL ACN, left capped in a hood for 60 days, and filtered with a 0.45 µm syringe filter prior to spotting on a TEM grid. The solution was light blue in color.

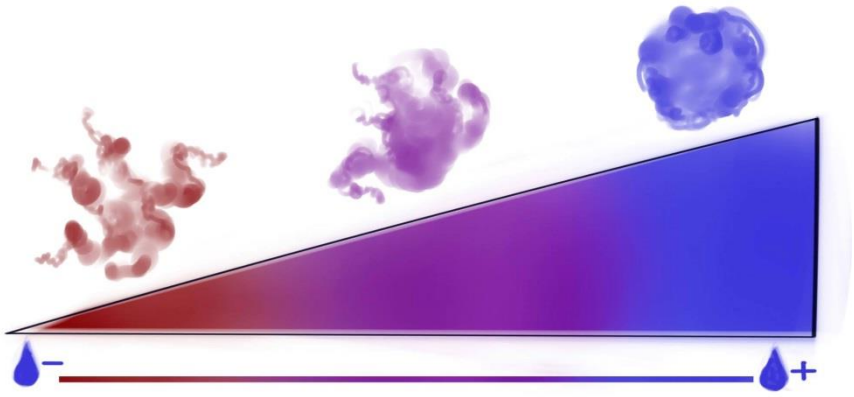

Figure 5.8. TOC Figure

Appendix A - Attempts Towards Characterizing the Photochemical Hydrogen Evolution Catalytic Activity of Small Molecule [2Fe-2S] Catalysts

Preliminary photochemical experiments were conducted in a 10 mL Erlyenmeyer flask sealed with a 14/20 septum with GC analysis of the headspace done using a Shimadzu GC-8A with TCD detector setup by Mark Yanagihashi. Catalysts **80** and **64** were investigated as 1 mM solutions in DCM with thiophenol (PhSH) added as both an acid and electron donor. The results, though qualitative in nature, seem to indicate that the naphthohydroquinone catalyst is a more potent photo-HER catalyst than the EDOT catalyst, with a 2.5 fold increase in H_2 area in the two runs in which hydrogen was able to be detected by GC, as well as the observation of a buildup of significant pressure in the flask when NHQcat was used, despite a less volatile solvent being used, and a water bath employed to try to keep the temperature under control (see the methods section for a complete write up of experimental details). One possible explanation for this is the well documented photo-acid effect of hydroquinones, where the excited state has a much lower pKa than that of the ground state. In 1,4-hydroquinone, this effect has been shown to lower the pKa from 10.0 in the ground state to 3.1 in the excited state.[239] To test this hypothesis, compounds **81** and **82** could be synthesized by deprotonation of **80** with triethylamine (TEA) followed by quenching the resulting anion(s) with methyl iodide. This would give a structure with only one photo-acid site (**81**) or no photo-acid sites (**82**), but otherwise comparable structures and electronics (in terms of the electron richness of the naphthyl system). Comparison of the photocatalytic activity of **80** with **81** and **82** should reveal whether or not the photo-acid effect is contributing to the activity of **1**. If it is indeed assisting in catalysis, then the activity should follow the trend **80** > **81** > **82**.

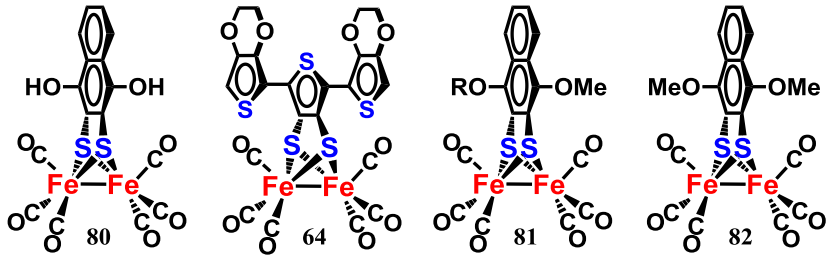

Figure A.1. Structures of small molecule [2Fe-2S] photocatalysts used in these studies (**80** and **64**) and proposed catalysts] structures **81** and **82.**

After the preliminary photocatalytic experiments, a refined setup was designed based on methods described by Li and Yang et al.[207] A 10 mL microwave reaction vial sealed with a crimped septum cap was used as the reaction vessel, and the light was oriented vertically rather than horizontally as in the preliminary setup. Additionally, the filter was changed from a 495 nm long pass filter to a 450 nm long pass filter, to better take advantage of the absorption profile of [2Fe-2S] catalysts. Toluene was chosen as the solvent for its high boiling point, good photostability, and compatibility with the septa being used in the microwave vials. A 1 mM solution of **64** with 1 M thiophenol as both proton source and electron donor demonstrated and increase in H_2/CH_4 ratio over 18 hours. Determination of the TON for this system is uncertain due to a faulty GC which has since been replaced. The faulty instrument was used for both collection of the

experimental data and generation of a calibration curve. Despite being done just one day apart, this calibration curve is likely not trustworthy, and the TON calculated from this data (10 mol H_2 mol^{-1} cat) should be treated as highly uncertain.

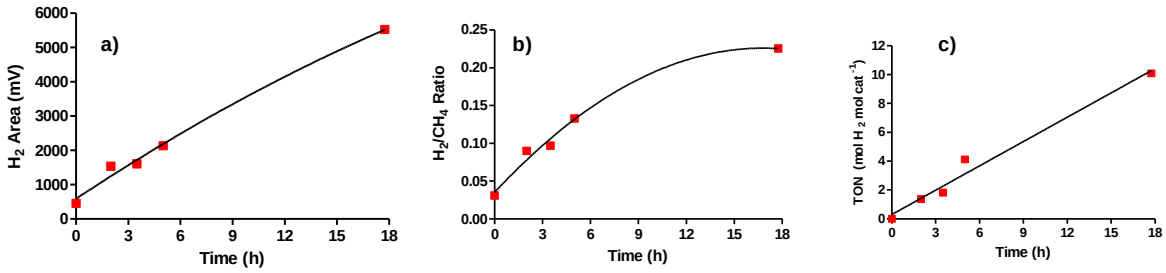

Figure A.2. GC data from photocatalysis of 64. 64 (3.6 mg, 1 mM), PhSH (0.51 mL, 1 M) in toluene (5 mL) and an internal standard of 100 uL CH_4 were irradiated with a Xenon lamp equipped with a 450 nm long pass filter. The solution was magnetically stirred throughout the course of the reaction.

The final photo-HER system examined was [(μ-bdt)$Fe_2(CO)_6$] **21** with regio-regular poly-3-hexylthiophene (rr-P3HT, **83**) as a photosensitizer. We were interested in using end-group functionalization to attach a [2Fe-2S] moiety to a rr-P3HT chain. P3HT is one of the most common electron donor materials in organic photovoltaics. Using a regio-regular polymer, the hexyl chain enforce planarity of the thiophene rings, increasing the effective pi-conjugation length which stabilizes the polaron formed upon one electron donation to an electron acceptor – the [2Fe-2S] system in our case. Band energy analysis of benzcat using HOMO and LUMO energies determined by UPS and cyclic voltammetry respectively and published band energies for rr-P3HT showed the bands were aligned such that the desired electron transfer even could theoretically take place (see **Fig A3** below).[240–242] To confirm that electron transfer was possible between P3HT and benzcat, we attempted photo-HER with benzcat (1 mM) and thiophenol (1 M) with and without P3HT. The inclusion of just 3 mg of rr-P3HT resulted in an increase in H_2 peak area of over 300 fold (see **Fig A4** below). A control experiment preformed without benzcat did not produce detectable amounts of hydrogen.

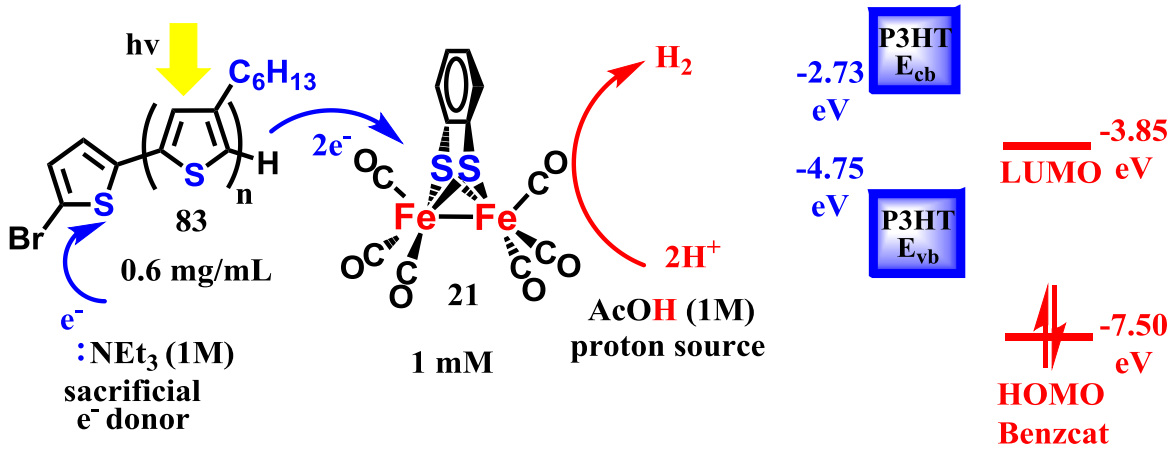

Figure A.3. Structure of [2Fe-2S] catalyst **21**, rr-P3HT photosensitizer **83** and proposed photo-HER sceheme as well as a band energy diagram showing the band alignment for **21** and **83**

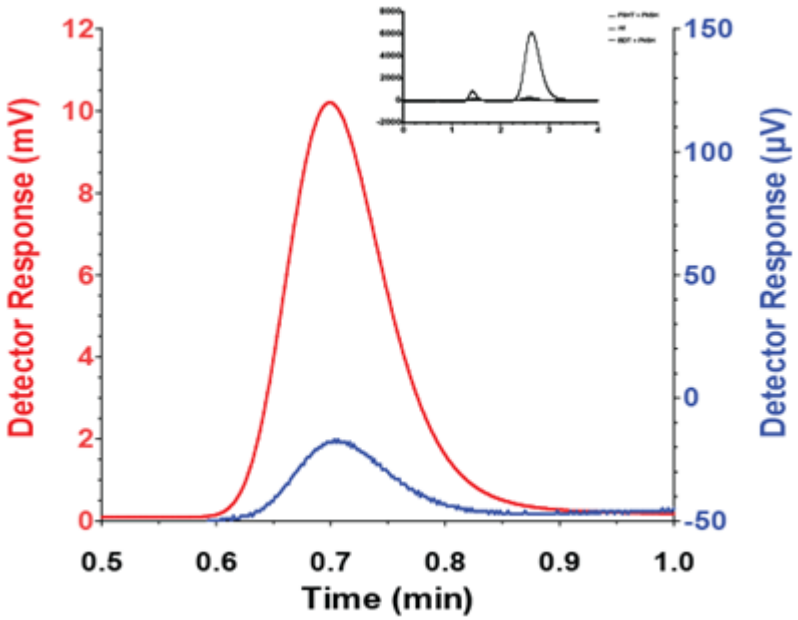

Figure A.4. GC data from photocatalysis of 21. 21 (2.1 mg, 1 mM), PhSH (0.51 mL, 1 M) in toluene (5 mL) and an internal standard of 100 uL CH4 (blue trace, right y-axis) were irradiated with a Xenon lamp equipped with a 450 nm long pass filter. The same solution was subjected to the same irradiation conditions with the addition of a 0.6 mg/mL loading of **83** (red trace, left y-xis). A Xenon lamp with 450 nm long pass filter was used to illuminate the solution which was magnetically stirred throughout the course of the reaction.

After successful photosensitization of **5** using P3HT, an attempt was made to end-group functionalize a rr-P3HT chain with a [2Fe-2S] moiety. As shown in **Figure A3**, rr-P3HT made using Grignard initiated metathesis (GRIM) has a terminal bromine group. Our initial synthetic strategy was to use a lithium halogen exchange to create a reactive anion at that site, then add $Fe_2S_2(CO)_6$, which is susceptible to nucleophilic attack by strong anion such as Grignard reagents and organolithium species. Nucleophilic attack on one of the sulfur atoms opens the S-S bond and generates a thiolate species which is then quenched with a good electrophile, methyl iodide

in our case, to quench the dithiolate and give metallopolymer **84**. This synthetic scheme is shown in **Scheme A1**.

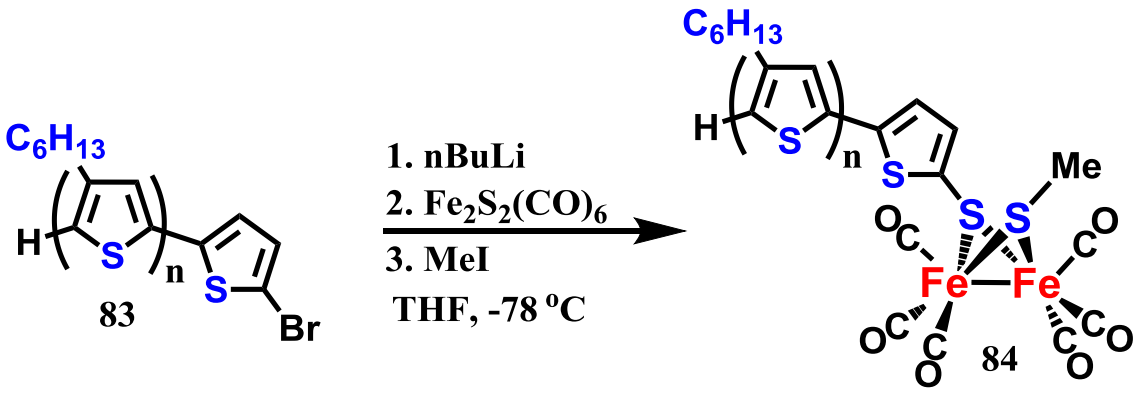

Scheme A.1. Synthetic scheme for chain-end functionalization of rr-P3HT with a [2Fe-2S] moiety **84**.

IR of a hexane soluble portion of the resulting material showed broad bands in the Fe-CO region at 2075 cm^{-1}, 2038 cm^{-1}, and 2005 cm^{-1}. For comparison, a 20:1 mixture of unmodified **83** and $Fe_2S_2(CO)_6$ was examined on IR and found to have sharp peaks at 2083 cm^{-2}, 2042 cm^{-2}, 2005 cm^{-2} (see **Fig A5** for IR data). Both the shift in Fe-CO stretching frequency and the broadening of the peaks are consistent with a change in the diiron system and provide positive evidence of formation of **84**. This route was soon abandoned however after the rejection of the NSF proposal which was intended to fund the work.

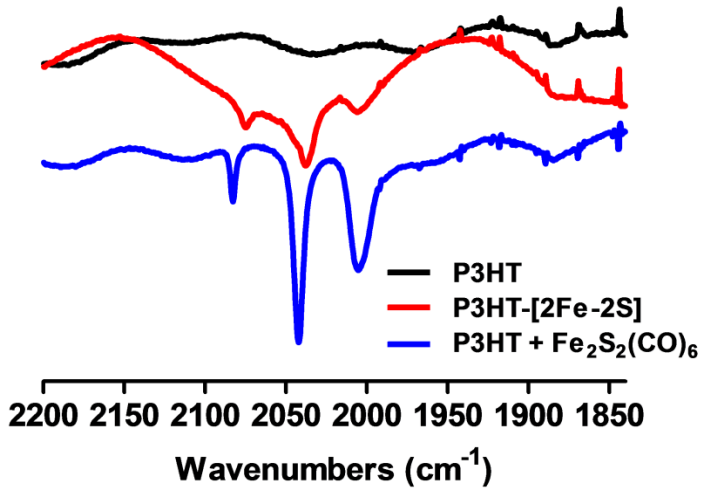

Figure A.5. IR spectrum of the Fe-CO stretching region for P3HT **83** (black), a 20:1 mixture of P3HT **83** and $Fe_2S_2(CO)_6$ (blue) and a hexane soluble fraction from the reaction depicted in **Scheme A1** (red) thought to be **84**

Experimental

General Methods:

A Nicolet Avatar 360 FT-IR with EZ-OMNIC software for H_2O and CO_2 correction. Resolution set to 0.964 cm^{-1} for all IR spectra. A Fisher Scientific FT-30 30specRFL500700*L IRSEC cell with 0.5 mm Teflon spacer (total path length = 1 mm) and CaF_2 window (Alfa-Aesar) was used for quantitative IR measurements. Qualitative IR was performed using solutions in $CHCl_3$ in thin films between NaCl plates (Fisher Scientific). Spectral processing and graphing were performed using Microsoft Excel, Origin Pro 8.0, and Prism Graph Pad 5.0. A Shimadzu GC-8A equipped with a 5 Å molecular sieves column and a thermal conductivity detector operating at 70 mA was used for H_2 detection. Argon was used as a carrier gas at a flow rate of 25 mL/min to maximize the difference in thermal conductivity between H_2 and the carrier gas.

Preliminary Photo-H_2 Experiments

80 1st run

A solution of 10 mg **80** was dissolved in 5 mL dichloromethane to give a 4mM solution. The vial was wrapped in foil (to prevent premature light exposure) and 0.03 mL AcOH and 0.05 mL thiophenol (PhSH) added and the solution was freeze-pump-thawed (FPT) to degass (3 cycles). After being carried to Koffler, it was transferred via de-oxygentated syringe to a 10 mL Erlenmeyer flask stoppered with a 14/20 septum one the flask has been purged with N_2 at a fast flow rate for at least 5 minutes. The flask was suspended in a water bath *ca.* 2 inches above the lens of our xenon lamp equipped with the 495 nm cutoff filter. Headspace measurements at 15 and 30 minutes showed no hydrogen, only a negative solvent peak. After 24 hours irradiation, the solution had changed from homogenous red to mostly clear solvent with dark brown/black ppt floating in it. The GC revealed two peaks, one assigned to H_2 at 1.014 minutes with an area of 6135 arbitrary units (48.65%) , and a second unknown peak at 1.783 minutes with an area of 6475 a.u. (51.35%). A small negative solvent peak is observed just before the second peak elutes. The volume of gas injected into the GC was 150 µL. Irradiation setup shown below in **Figure A6**.

80 2nd run

In order to ascertain whether thiophenol could function as the proton source rather than acetic acid, the following preliminary experiment was preformed. Solution prepared as before but with 2.5 mg **80** (1 mM), 0.51 mL PhSH (1 M) in 5 mL DCM, acetic acid omitted. No chromatograms were obtained to verify H_2 generation, but after 24 hours illumination the septum was being visible forced out of the flask (which requires a good bit of force). Upon unclamping the flask, the septum lost its last support and popped out. I tried to put it back on as quickly as possible but the follow up GC had no H_2, presumably because it was all lost to the atmosphere.

64 1st run

To a very dilute solution (282 µM in CH_3CN) of **64** made for UV-Vis, 0.38 mL trifluoroacetic acid and 0.51 mL PhSH are added, solution FPT 3x, and transported to Koffler under Al foil.

Illumination was done on the same setup, but changing the filter to 400 nm and removing the water bath. Even after 15 minutes, it looked like the solution was photobleaching, and after an hour it certainly had (dark red → yellow) No H_2 was detected.

64 2nd run

For the second run, the solvent was changed to THF (anhydrous, dried refluxing over Na, Benzophenone then stored on activated 4 Å MS for 24 hours) 3.9 mg **64** was dissolved in 5 mL THF (1.1 mM) in a light shielded, flame dried vial and 0.51 mL PhSH added. Solution FPT 3x, and handled as others. The 495 nm cutoff filter was employed this time to avoid photobleaching, and the water bath reestablished (due to THF's low b.p.) as in first experiment with **80**. After 17 hours of illumination, a hydrogen peak is present at 0.988 minutes with area 1809. A sample injected at 21 hours found an area of 2435, a 33% increase. Extending the illumination time to 40 hours did not increase the hydrogen peak further.

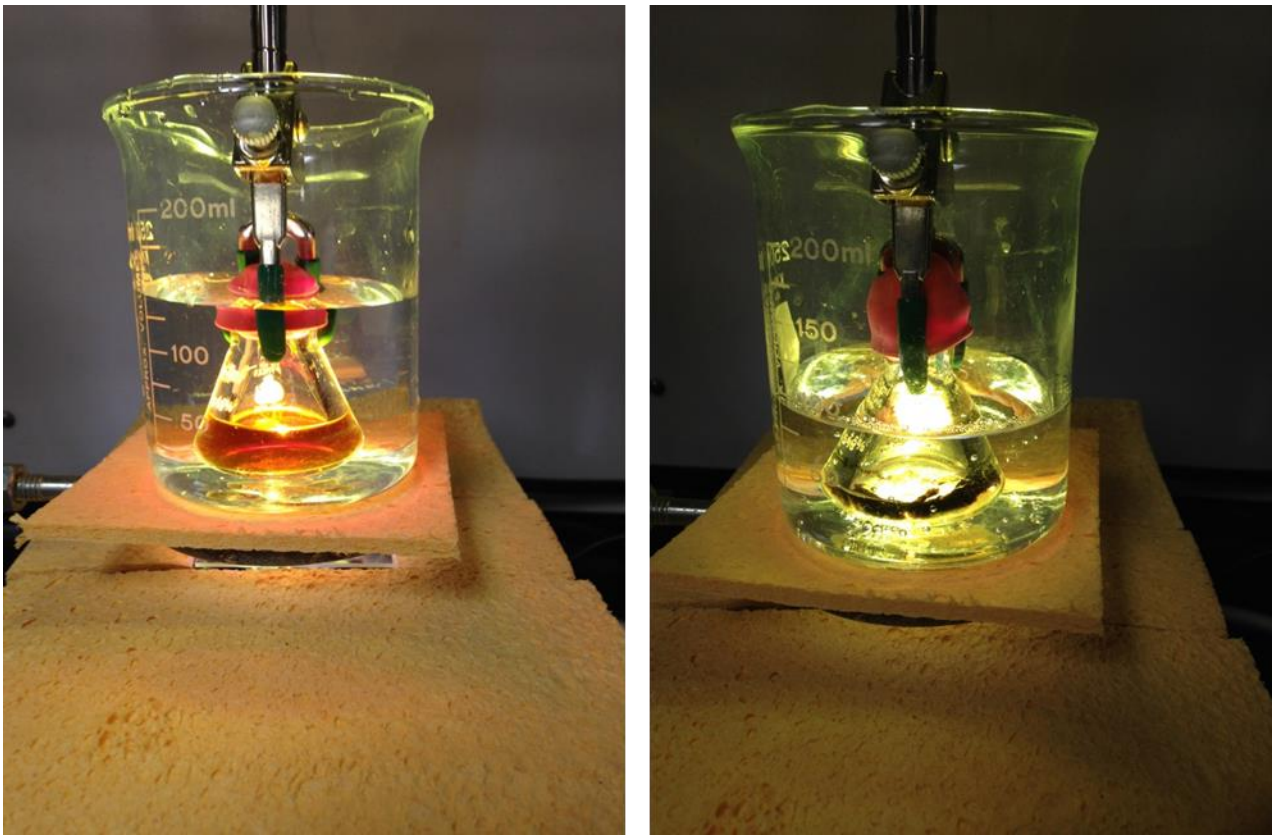

Figure A.6. Preliminary photochemical H2 setup with **80** (2.5 mg, 1mM) + PhSH (0.51 mL, 1M) in CH2Cl2 (5 mL) solvent using a Xenon lamp and 495 nm long pass filter. In the photo on the right, the solvent is still present, but is now clear with black particulate in the bottom of the flask.

Revised Photocatalytic Method

General procedure: The catalyst (0.005 mol) and any other solid reagents (photosensitizer if used) are weighed into a 10 mL microwave reaction vial (Fisher Scientific). A small Teflon coated magnetic stir bar is added and the vial is capped by crimping on a new septum cap. Anhydrous toluene is added (5 mL, EMD Millipore) followed by a quantity of acid and electron donor

sufficient to reach 1M concentration (0.51 mL for PhSH, which served both roles). The solution was then freeze-pump-thawed three times (0.001 torr vacuum) before 100 μL of methane (99.9%, Matheson gas) is added through the septum cap. The flask is allowed to equilibrate to room temperature in the dark, then is irradiated with a Xenon lamp, using a high pass filter to filter out wavelengths below 450 nm. An aliquot of headspace is taken at regular intervals using a gas tight syringe (250 μL, Hamilton Scientific) equipped with a stopcock. Small diameter needles (28-32 gauge) are preferred to gas effusion from the cell. The headspace sample is immediately injected into a the GC. H_2 peak elutes at approximately 0.7 minutes, followed by any trace O_2 (1.4 min) and N_2 (2.5 min). CO (from catalyst decomposition) can be detected around 8.3 minutes.

Synthesis

Regioregular poly-3-hexylthiophene (rr-P3HT, 83) via GRIM

Anhydrous LiCl (42 mg, 1.0 mmol) is weighed into a 10 mL Schlenk flask which is evacuated and filled with dry argon (2x) then vacuum is pulled and held while the flask is heated with a heat gun (~ 20 minutes) to drive off any water. The flask is allowed to cool, and refilled with argon, then taken to the balance. A syringe loaded with 2-bromo-3-hexyl-4-iodothiophene is inserted through the septum and the monomer is weighed into the flask (212.6 mg, 0.57 mmol) the *exact* mass is recorded and used to calculate the amount of Grignard and nickel catalyst needed. Anhydrous THF (5 mL, degassed via argon sparge) is added to the monomer/LiCl mixture and the solution is stirred to dissolve the LiCl. Once the solid is dissolved, the solution is cooled in an ice bath to 0 °C. tBuMgCl (0.79 mL, 0.72 M, 0.57 mmol, *exact amount calculated from mass of monomer* recently titrated with Te_2Ph_2 at room temp), is added dropwise over 5 minutes and the solution is stirred for 1 hour. Toward the end of the hour (~50 min in) the ice bath is removed and solution allowed to attain room temp. The argon flow is then turned up very high as the flask is briefly uncapped and the nickel catalyst $Ni(dppp)Cl_2$ (21.6 mg, 0.04mmol, 0.07 eq, *exact amount calculated from exact mass of monomer determined earlier*) is added as a solid in one portion. The solution should take on a red color almost immediately and become somewhat more viscous. Stirred 1.75 hours at room temp then 2 mL of HCl (5 M) is added through septum to quench. The solution is stirred for five minutes then pipetted dropwise into 250 mL of vigorously stirred MeOH to precipitate. Stir an additional 20-30 minutes to allow complete precipitation, then gravity filter over a tightly packed glass wool plug, eluting with MeOH then acetone until no color is visible in the rinse solution (this may take several hours as the polymer tends to clog the filter and make it run very slowly). Once no color remains in the acetone rinse, the glass wool can be rinsed with $CHCl_3$ into a round bottom flask to obtain polymer. The solution is concentrated until just barely solvated, then precipitated again into MeOH. A granular solid (29.5 mg) should form if enough $CHCl_3$ was removed. This solution is allowed to settle and most of the solvent decanted to another flask before gravity filtering the solid onto filter paper for collection. Vacuum filtration is avoided because it tends to suck the polymer into the paper and makes recovery difficult or impossible. On a larger scale, Soxhlet extraction may be attempted to circumvent the tedious gravity filter washes. ^{1}H NMR (500 MHz, 298 K) δ 6.97 (s, 1H, broad) 2.80 (s, 2H, broad), 1.64 (s, 2H, broad), 1.44 (s, 2H, broad), 1.34 (s, 2H, broad), 0.91 (s, 3H, broad).

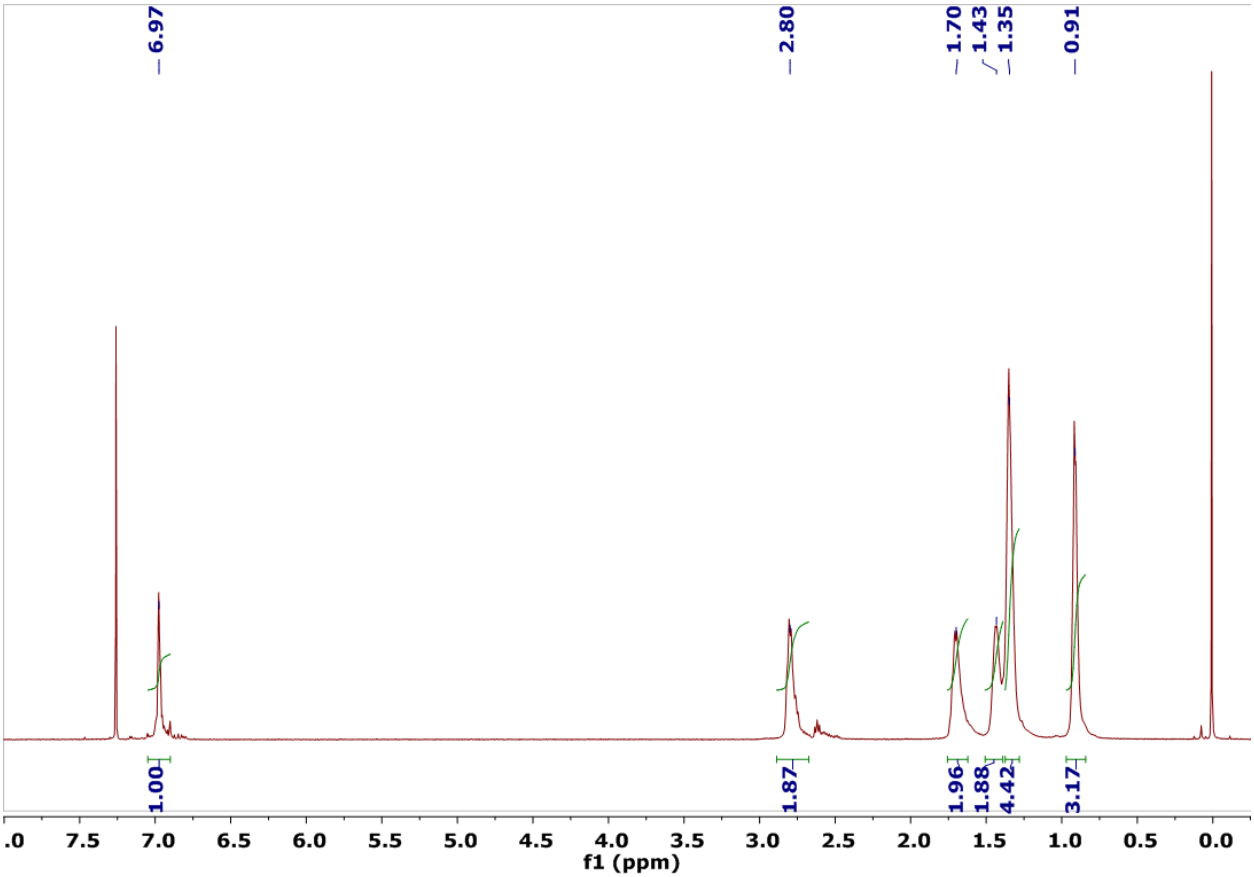

Figure A.7. ^{1}H NMR spectrum of rr-P3HT **83.**

[2Fe-2S]-regioregular poly-3-hexylthiophene (84)

A solution of **83** (29.5 mg, ~9.5 x 10^{-3} mmol $M_{n,SEC=}$ = 3100, DP = 19)was dissolved in anhydrous THF under argon, then cooled in a dry ice-acetone bath. The polymer would precipitate if left in the bath and allowed to cool completely, so a target temperature of 20 °C was maintained by intermittently adding dry-ice and monitoring the temperature with a low temp thermometer. A solution of n-butyllithium in THF (10 uL, 0.19 mmol, 1.90 M by Te_2Ph_2 titration) is added and stirred for 45 minutes. In a separate flask $Fe_2S_2(CO)_6$ (13.1 mg, 0.038 mmol) is dissolved in anhydrous THF (0.5 mL) under argon. At the end of the 45 minute period, the diiron solution is added dropwise to the polymer solution. Once addition is complete, the mixture is stirred for 45 minutes at -20 °C then MeI (10 uL, 0.16 mmol) is added and the cold bath is removed. The solution is allowed to stir for a total of 30 minutes after the addition, then the whole solution was added to rapidly stirred MeOH. When a precipitate failed to form, the solvent was removed using a rotary evaporator, then the crude red solid was re-dissolved in 0.5 mL $CHCl_3$ and pipetted dropwise into rapidly stirred methanol. After stirring for several hours a precipitate formed which was filtered over a glass wool plug and washed with methaol, hexanes, and acetone sequentially. The rinse solutions were saved and concentrated. A significant portion of the solid came through with the hexanes wash, and this portion was examined via IR and found to contain Fe-CO peaks at 2075 cm^{-1}, 2038 cm^{-1}, and 2005 cm^{-1} (**Fig A5** above). ^{1}H NMR closely matched the starting material with the addition of a sharp peak at 1.26 ppm which may be due to hexanes

contamination, or belong to the methyl group expected in **84** ^{1}H NMR (500 MHz, 298 K) δ 6.97 (s, 1H, broad) 2.80 (s, 2H, broad), 1.71 (s, 2H, broad), 1.43 (s, 2H, broad), 1.34 (s, broad), 1.26 (s, broad), 0.89 (s, broad).

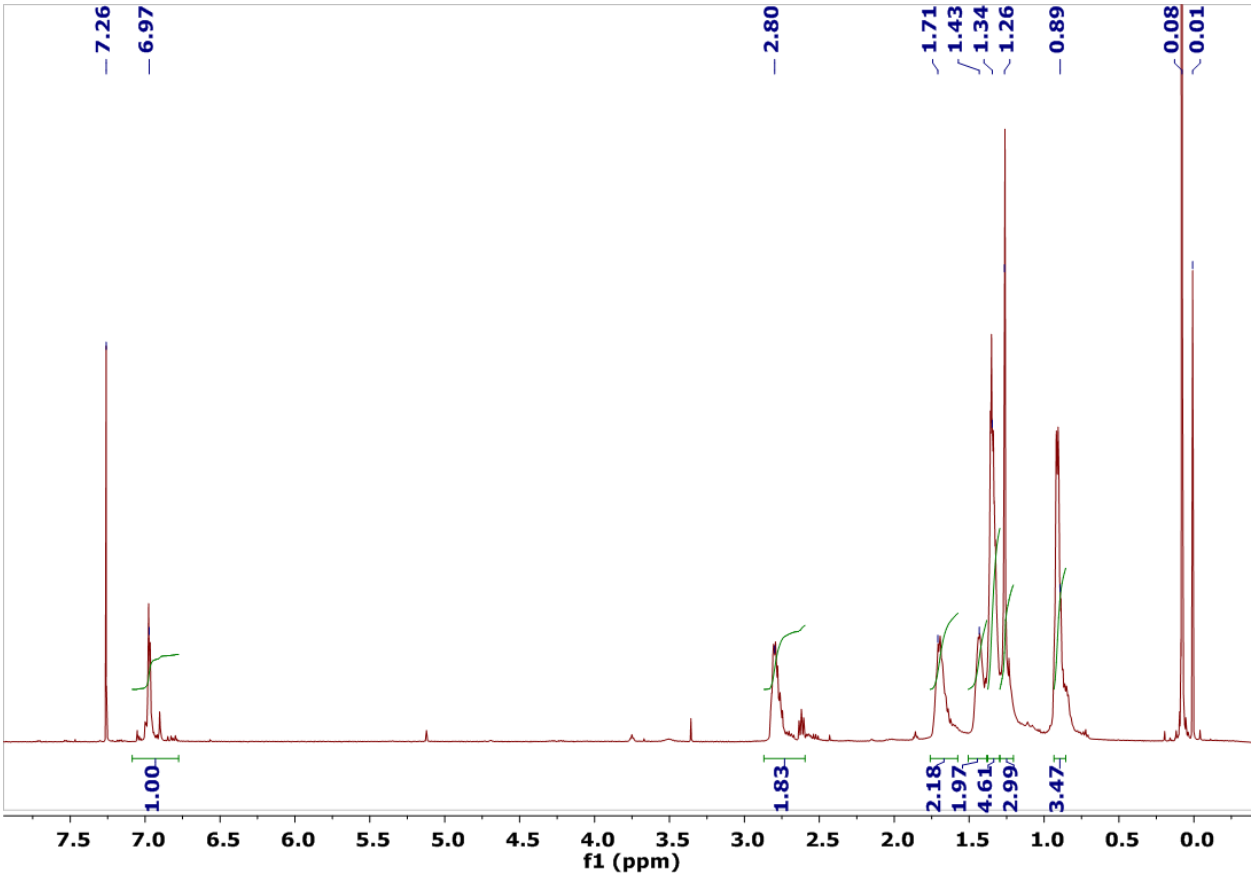

Figure A.8. ^{1}H NMR spectrum of hexane soluble portion of reaction described in **scheme A1**, believed to be **84**.

Appendix B - Supporting Information for [FeFe]-Hydrogenase Mimetic Metallopolymers with Exceptional Catalytic Activity for Hydrogen Production in Water

William P. Brezinski[1], Metin Karayilan[1], Kayla E. Clary[1], Nicholas G. Pavlopolous[1], Sipei Li[2], Liye Fu[2], Krzysztof Matyjaszewski[2], Dennis H. Evans[3], Dennis L. Lichtenberger[1*], Richard S. Glass[1*] and Jeffrey Pyun[1,4*]

[1]Department of Chemistry and Biochemistry, The University of Arizona, 1306 E. University Blvd., Tucson, AZ 85721, USA [2]Department of Chemistry, Carnegie Mellon University, 4400 Fifth Avenue, Pittsburgh, PA 15213, USA [3]Department of Chemistry, Purdue University, 560 Oval Drive, West Lafayette, Indiana 47907-2084, USA [4]Program for Chemical Convergence of Energy & Environment, School of Chemical & Biological Engineering, Seoul National University, Seoul, Korea

The material below is from [FeFe]-Hydrogenase Mimetic Metallopolymers with Exceptional Catalytic Activity for Hydrogen Production in Water Angew. Chem. Int. Ed. 10.1002/anie.201804661 Copyright Wiley-VCH Verlag GmbH & Co. KGaA. Reproduced with permission.

*Correspondence and requests for materials should be addressed to J.P., D.L.L. or R.S.G.

Materials. Unless otherwise noted, solvents were received from Fischer Scientific as ACS grade and used without further purification. $Fe_2S_2(CO)_6$ was prepared according to literature procedures[1] and sublimed before use. $Fe(CO)_5$ (99.5 %,Alfa-Aesar), NaOH (EMD, ACS grade), NH_4Cl (EMD, ACS grade), S_8 (Mallinckrodt, sublimed), Na_2SO_4 (EMD, ACS grade), $NaCNBH_3$ (Sigma-Aldrich, 95%), $Me_3NO{\bullet}2H_2O$ (Sigma-Aldrich), PPh_3 (Sigma-Aldrich, 99%), Tris-base (99%, Sigma-Aldrich), $NaH_2PO_4{\bullet}H_2O$ (VWR analytical grade), Na_2HPO_4 (VWR analytical grade), Celite 545(VWR), and Silica Gel (SiliaFlash F60, 230-400 mesh, Silicycle) were used as received without further purification. 1,4-naphthoquinone (Alfa-Aesar, 97%, up to 5% H_2O) was passed through a silica gel column with diethyl ether before use. Triethylamine (EMD, 99.5%) was distilled from KOH then stored on activated 3Å linde-type molecular sieves under argon. α-Bromoisobutyryl bromide (BIBB, Sigma-Aldrich, 98%) was initially used as received but found to decompose over time, requiring vacuum distillation (10 torr, 55^{o}C) once it had taken on a yellow color. KCl (EMD, ACS grade) was recrystallized twice from hot 0.1 M HCl before use. Methyl methacrylate (MMA) (Aldrich, 99%), and 2-(Dimethylamino)ethyl methacrylate (DMAEMA) (Aldrich, 98%) were purified by passing through a short column of neutral alumina to remove inhibitors. Copper(I) bromide (Cu(I)Br) (Aldrich, 98%) was purified by stirring overnight in glacial acetic acid, filtering, washing with ethanol and diethyl ether, and drying under vacuum before use. Alternatively, Cu(I)Br was purified by precipitation from 48% HBr followed by washing with de-ionized water, ethanol, and diethyl ether sequentially then drying under vacuum, as described in e-Eros Reagents for Organic Chemistry.[2] 4,4'-Di-n-nonyl-2,2'-bipyridine (dNbpy) (Alfa Aesar, 97%), N,N,N',N'',N''-Pentamethyldiethylenetriamine (PMDETA) (Aldrich, 99%), 1,1,4,7,10,10-Hexamethyltriethylenetetramine (HMTETA) (Aldrich, 97%), Dowex 50WX8-200 ion exchange resin (Aldrich), Alumina (Al_2O_3, activated, neutral, 50-200 μm, 60 Å, Acros Organics), Tetrahydrofuran (THF) (EMD, GC grade), Dichloromethane (DCM) (ACS grade), Methanol (ACS grade, EMD), Hexanes (ACS grade, EMD), and Toluene (ACS grade, EMD) were used as received. For the synthesis of **56**, triethylamine (NEt_3) (EMD, ACS reagent grade) was distilled at atmospheric pressure under argon. For metallopolymer syntheses, THF (DriSolv, Anhydrous, EMD, GC grade) and Toluene (DriSolv, Anhydrous, EMD, GC grade) stored over 3Å molecular sieves were used. 3Å molecular sieves (Sigma Aldrich) were activated by drying in an oven at 300 ˚C for a minimum of 16 hours.

Instrumentation. ^{1}H and ^{13}C nuclear magnetic resonance (NMR) spectra were obtained using a Bruker DRX 500 MHz or a Bruker Avance III 400 MHz spectrometer. Chemical shifts were referenced to $Si(Me)_4$ (δ 0.00 ppm) for ^{1}H NMR and the $CDCl_3$ solvent peak (δ 77.0 ppm) for ^{13}C NMR. MestReNova 10.0 software was used for spectral processing. IR spectra were obtained on a Nicolet Avatar 360 FT-IR with EZ-OMNIC software for H_2O and CO_2 correction. Resolution set to 0.964 cm^{-1} for all IR spectra. During quantification of molar absorptivity (ε) for Fe-CO stretches in **56** and resulting metallopolymers 128 scans were used. A Fisher Scientific FT-30 30specRFL500700*L IRSEC cell with 0.5 mm Teflon spacer (total path length = 1 mm) and CaF_2 window (Alfa-Aesar) was used for quantitative IR measurements. Determination of ε for Fe-CO's was performed by preparing 10 mL of *ca.* 1.0 mM **56** in $CHCl_3$ using volumetric glassware. This stock was diluted to *ca.* 0.1 mM, 0.2 mM, 0.4 mM, and 0.6 mM in four separate 5 mL volumetric flasks using a 1 mL syringe to transfer the stock solution, then diluting to volume. The measurement was performed in triplicate and R^2 values for each linear regression were 0.98 or

better. Qualitative IR was performed using solutions in $CHCl_3$ in thin films between NaCl plates (Fisher Scientific). Spectral processing and graphing were performed using Microsoft Excel, Origin Pro 8.0, and Prism Graph Pad 5.0. Scanning electron microscopy (SEM) and energy dispersive X-ray spectroscopy (EDX) were conducted using a FEI Helios 660 NanoLab Dual Beam SEM/FIB for imaging for carbon electrodes before and after electrolysis experiments.

MW Determinations. Molecular weight (M_n) and molecular weight distribution (M_w/M_n) were determined by gel permeation chromatography (GPC). Samples for GPC analysis were prepared by dissolving 1-2 mg of the purified polymer in 1.0 mL of THF (with 0.1 V% toluene as a reference) and passing the resulting solution through 0.2 µm PTFE filter. The GPC analysis for **PMMA-*g*-[2Fe-2S] 57** was performed in a THF mobile phase with a Waters 1515 isocratic pump running three 5-µm PLgel columns (Polymer Labs, pore size 10^4, 10^3 and 10^2 Å) at a flow rate of 1.0 mL/min at 35 ^oC with a Waters 2414 differential refractometer and a Waters 2487 dual-wavelength UV-vis spectrometer. Molar masses were calculated using the Waters Empower software, calibrated against low polydispersity linear PMMA and polystyrene (PS) standards. pH measurements made using a VWR symphony SB70P pH meter or a Fischer Scientific Accumet AE150 pH meter calibrated with pH 4.01, 7.0, and 10.01 standards (Sigma-Aldrich). Molecular weight and molecular weight distribution data for **PDMAEMA-*g*-[2Fe-2S] 58** metallopolymer were collected by using a GPC with a Waters 515 HPLC pump, Wyatt Optilab refractive index detector, and PSS GRAM columns containing polyester copolymer networks with 50 mM LiBr DMF solution as eluent phase at a flow rate of 1mL/min at 50 °C and a GPC system with a Waters 1515 isocratic pump running one PSS GRAM column containing polyester copolymer networks with 50 mM LiBr DMF solution as eluent phase at a flow rate of 0.8 mL/min at 50 ^oC with a Waters 2414 differential refractometer and a Waters 2487 dual-wavelength UV-vis spectrometer at 254 nm or 400 nm.

B. X-ray Crystallography of Metalloinitiator (56)

X-ray Diffraction Analysis. Data was collected at the University of Arizona X-ray Diffraction Facility. Crystals were mounted onto a *MiTeGen* micromount under a protective film of Paratone® oil and diffraction data for all crystals were measured using a Bruker Kappa APEX II DUO diffractometer, with graphite-monochromated Mo-Kα radiation (λ = 0.71073 Å) generated by a sealed tube, and an APEX II CCD area detector. The diffractometer was fitted with an Oxford Cryostream low-temperature device and data sets were collected using the *APEX2* software package (Bruker AXS Inc., Madison, WI, 2007). The data were corrected for absorption effects using a multi-scan method in *SADABS* (Sheldrick, G. M. University of Göttingen, Germany 1997). CCDC 1577155 contains the supplementary crystallographic data for this paper. These data are provided free of charge by The Cambridge Crystallographic Data Centre. All structures were solved by direct methods (*SHELXS-97*), and developed by full least-squares refinement based upon F^2 (*SHELXL*)[3] interfaced *via X-Seed*[4] and *OLEX2*[5] Crystallographic figures were prepared using *Mercury* (Version 3.9).

C. Electrochemistry

General Instrumentation. A Gamry Interface 1000 and a Gamry Reference 3000 were used for all data collections with Gamry Framework 6 software. The glassy carbon (GC) working electrode with a diameter of 0.3 cm (calculated area = 0.071 cm^2), platinum-disk (Pt) working electrode (diameter 0.2 cm, calculated area = 0.031 cm^2), and gold (for the gold amalgam) electrode (diameter 0.3 cm, calculated area = 0.071 cm^2) were obtained from BASi. The Pt Wire counter electrode was from Sigma-Aldrich (99.9%). The edge plane graphite rod (diameter 3 mm, 10 cm length was from BASi. Acid experiments were performed with acetic acid (Alfa-Aesar, 99.998%) degassed via three cycles of freeze-pump-thaw using 10 µL or 100 µL Eppendorf auto pipettes.

Materials for Experiments in Acetonitrile. Acetonitrile (anhydrous, 99.8%, Sigma-Aldrich) and tetrabutylammonium hexafluorophosphate (n-Bu_4NPF_6, Fluka, puriss electrochemical grade) were used to prepare acetonitrile solutions. Silver wire (99.999% Alfa Aesar), $AgNO_3$ (99.9%, Sigma-Aldrich, ACS reagent) and Vycor frits were used to fabricate reference electrodes to fit the cell. The reference electrodes used were double junction with the inner compartment containing 1 mM $AgNO_3$ and 0.1 M n-Bu_4NPF_6 solution and outer compartment filled with 0.1 M n-Bu_4NPF_6 solution each separated by a Vycor frit. Once fabricated, a reference electrode was stored for up to 7 days before being remade. Acetonitrile was degassed by sparging with argon for 30 minutes prior to preparation of solutions. The cell was assembled and flushed with argon deoxygenated solution was added through a 14/20 rubber septum via deoxygenated syringe. An initial scan is taken to ensure no oxygen ($E^o \approx$ -1.0 V vs ref) is present. If O_2 is detected, the solution is bubbled with argon in five minute increments until O_2 reduction is no longer detected.

Materials for Experiments in Water. Aqueous solutions were prepared using 18 MΩ water purified using a Millipure water filtration system. 0.1 M KCl (99%, Alfa-Aesar, recrystallized twice from 0.1 M HCl) was used as a supporting electrolyte in the 0.1 M sodium phosphate buffer. Phosphate buffers were made with NaH_2PO_4/Na_2HPO_4 (VWR, ACS grade) according to literature preparations found in *Ruzin, 1999 Plant Microtechnique and Microscopy* accessed at (http://microscopy.berkeley.edu/-Resources/instruction/buffers.html) and adjusted to exact pH using 1.0 M HCl or NaOH. 1.0 M phosphate buffers were used without added KCl. Tris buffers were prepared by dissolving tris-base (12.114 g, 0.1 mol) in 18 MΩ water (*ca*. 60 mL) and 36% HCl was added to adjust the pH to 7.00 then the solution was diluted with 18 MΩ water to a final volume of 100 mL in a volumetric flask. The reference electrode was a double junction design consisting of a chloridized silver wire in a solution of 3 M KCl in the inner cell and the bulk solution (*i.e.,* 1 M Tris, 1 M sodium phosphate buffer or 0.1 M sodium phosphate buffer with 0.1 M KCl) in the outer chamber. Vycor frits separated the chambers. The Ag/AgCl wire was fabricated by soaking Ag wire (99.999% Alfa Aesar) in a commercial bleach solution (Clorox) for 16 hours. The wire was then rinsed thoroughly with 18 MΩ water and stored in 3M KCl for up to 1 week. Aqueous solutions were prepared in air and deoxygenated in the cell by bubbling the stirred solution with argon for 30 minutes.

Gas Chromatography for Faradaic Yield. For determination of the Faradaic yield, the headspace of the electrochemical cell was sampled using a Hamilton gas-tight syringe (250 µL)

fitted with a stopcock to inject 250 µL of headspace into a Shimadzu GC-8A equipped with a thermal conductivity detector operating at 70 mA, using Argon as a carrier gas at a flow rate of 25 mL/min.

Materials for Controlled Potential Electrolysis. For controlled potential electrolysis (CPE), the long running time of these experiments required the gold amalgam electrode and the frit-separated carbon electrode. The electrolysis cell included a mercury-gold amalgam foil electrode prepared with gold foil (99.99%, Sigma-Aldrich, 0.1 mm thick, 7 mm wide) with a NiChrome wire spot welded to one end for attachment of leads. The foil was cleaned with hexanes, acetone, and methanol followed by soaking in 15% H_2SO_4 for 2 minutes and rinsing with de-ionized water. The foil was then dried and soaked in distilled mercury (Mallinckrodt) for 5 minutes, polishing on filter paper for 30 seconds per side then dipping again in mercury for 2-3 minutes and mechanically removing excess mercury. The foil was immersed approximately 8-10 mm into the electrolysis solution to give an area of *ca.*1.5 cm^2. The 3 mm diameter gold amalgam disk electrode was integrated in the cell to allow for CV and LSV interrogation of the solution before, after, and at intermediate times in the electrolysis experiment.

II. Methods

All syntheses and anaerobic electrochemical experiments were carried out under argon using standard Schlenk and inert atmosphere techniques.

A. Syntheses and Characterizations

Synthesis and Characterization of Metallo-initiator [µ-2,3-(naphthalene-1,4-diylbis(2-bromo-2-methylpropanoate)-dithiolato]bistricarbonyliron 56. Compound 80 is known to oxidize in air to the corresponding quinone complex[6,7] so before starting the reaction, it was analyzed via ^{1}H NMR to determine what mol % had been oxidized to the quinone product and one molar equivalent of sodium cyanoborohydride is used to convert the quinone complex into the desired hydroquinone 80 in situ. $NaCNBH_3$ (2.26 mg, 0.036 mmol) and 80 (45 mg, 0.090 mmol) were added to a flask with THF (2 mL) and the solution was stirred at room temperature in the dark for 2 hours. Triethylamine (TEA) (75 µL, 0.54 mmol) was then added and the solution was stirred for 20 minutes. Finally BIBB (30 µL, 0.22 mmol) was added and the solution was stirred at room temperature for 2.25 hours. The reaction was filtered to remove precipitate and solvent removed by rotary evaporation (23 ^{o}C, *ca.* 200 torr) to yield a red/orange solid. Purification via column chromatography (SiGel, 30% dichloromethane in hexane) gave 63 mg (0.079 mmol, 87%) of 56 as a powdery orange solid upon removal of solvent. This solid was recrystallized via layering of toluene/MeOH to obtain crystals for electrochemical experiments and polymer synthesis. The structure was confirmed by X-ray crystallography (see Figure B.1). The crystallographic information is provided free of charge by The Cambridge Crystallographic Data Centre under refcode 1577155. ^{1}H NMR: ($CDCl_3$, 500 MHz, 298 K) δ (ppm) 7.81 (2H, dd *J* = 6.5, 3.4 Hz) 7.49 (2H, dd *J* = 6.5, 3.4 Hz), 2.19 (12H, s) ^{13}C: ($CDCl_3$, 125 MHz, 298 K) δ (ppm) 206.8 (OC-Fe), 168.3 (C=O), 143.0 (C1,4-O), 134.8 (C,2,3-S), 129.1 (C6,7-H), 128.1 (C9,10), 121.9 (C5,8-H), 54.8 (CH-Br), 31.0 (CH_3) IR ($CHCl_3$, thin film on NaCl): 3688 cm^{-1} (w), 3619 cm^{-1} (w, Csp^2-H), 3154 cm^{-1} (w, Csp^2-H), 3019 cm^{-1} (vs, Csp^2-H), 2976 cm^{-1} (w, Csp^3-H), 2082 cm^{-1} (Fe-

CO, s), 2050 cm^{-1} (Fe-CO, s), 2012 cm^{-1} (Fe-CO, s) 1760 cm^{-1} (C=O ester, w), 1522 cm^{-1} (C=C, w), 1423 cm^{-1} (C-H, w), 1210 cm^{-1} (C-O, vs).

Synthesis and Characterization of PMMA-g-[2Fe-2S] 57.

(M)o : (I)o : (CuI)o : (L)o = 200 : 1 : 1 : 2. Atom transfer radical polymerization (ATRP) of MMA was adapted from the literature and modified for the synthesis of PMMA metallopolymers.[8,9] A typical ATRP was conducted as follows: A 10 mL Schlenk flask was loaded with Cu(I)Br (3.35 mg, 0.0234 mmol) and dNbpy (19.1 mg, 0.0467 mmol). Deoxygenated toluene (0.25 mL) was added and the resulting mixture was stirred at room temperature for 10 minutes to allow for the formation of the Cu-ligand complex, yielding a dark red solution. To a separate 10 mL Schlenk flask, **56** (18.7 mg, 0.0234 mmol) was added followed by MMA (0.468 g, 4.67 mmol) and the resulting mixture was stirred at room temperature until **56** was completely dissolved. The flask was then heated in an oil bath thermostated at 55 ^{o}C until desired conversion was achieved (100 min, 53% monomer conversion by ^{1}H NMR of the crude reaction mixture). The reaction was quenched by exposure to air and addition of 2.0 mL of dichloromethane. The copper catalyst was removed by passing the reaction mixture through a short neutral alumina column. The polymer solution was concentrated via rotary evaporator and the polymer was isolated via precipitation from 200 mL of rapidly stirred methanol, followed by filtration to yield a yellow/orange powder (135 mg isolated yield).

Molecular weight (M_n) and molecular weight distribution (M_w/M_n) were determined by gel permeation chromatography (GPC). Samples for GPC analysis were prepared by dissolving 1-2 mg of the purified polymer in 1.0 mL of THF (with 0.1 V% toluene as a reference) and passing the resulting solution through 0.2 µm PTFE filter. Molar masses were calibrated against low polydispersity linear PMMA and polystyrene (PS) standards. ^{1}H NMR (CD_2Cl_2, 400 MHz, 298 K) δ (ppm) 7.55-7.38 (broad, aromatic, end group), 3.70-3.40 (3H, broad, -$COOCH_3$), 1.98-1.66 (2H, broad, aliphatic main chain), 1.54-1.31 (broad, methyl, end group), 0.96-0.65 (3H, broad, -CH_3, main chain). IR ($CHCl_3$, thin film on NaCl): 3020 cm^{-1} (-CH_2-, strong, sharp), 2951 cm^{-1} (-CH_3, medium), 2081 cm^{-1} (Fe-CO, sharp), 2049 cm^{-1} (Fe-CO, strong, sharp), 2011 cm^{-1} (Fe-CO, sharp), 1728 cm^{-1} (C=O, strong, sharp), 1449 cm^{-1} (-OCH_3. strong, sharp), 1243 cm^{-1} (-CH_2-, sharp), 1215 cm^{-1} (C-O, strong, sharp), 1153 cm^{-1} (C-O, strong, sharp). THF GPC: $M_{n,\ SEC}$ = 11,982 g/mol, $M_{w,\ SEC}$ = 13,229 g/mol, M_w/M_n = 1.10.

Synthesis and Characterization of PDMAEMA-g-[2Fe-2S] 58.

(M)o : (I)o : (CuI)o : (L)o = 100 : 1 : 1 : 1.5. ATRP of DMAEMA was adapted from the literature and modified for the synthesis of PDMAEMA metallopolymers.[10–12] A 10 mL Schlenk flask was loaded with Cu(I)Br (2.55 mg, 0.0178 mmol) and 0.20 mL of deoxygenated, anhydrous THF was added to the flask followed by the addition of deoxygenated HMTETA (7.3 µL, 0.0267 mmol). The resulting mixture was stirred for 10 minutes to allow for the formation of the Cu-ligand complex. To a second 10 mL Schlenk flask **56** (14.24 mg, 0.0178 mmol) was added. Then 0.30 mL of deoxygenated, anhydrous THF was added. The solution was stirred until homogeneous then the resulting mixture was transferred to the reaction flask. Finally, purified and deoxygenated DMAEMA (0.30 mL, 1.78 mmol) was added to the reaction flask and the flask was submerged in an oil bath preheated to 50^{o} C and the reaction was stirred at 50° C. After 90 minutes, the

reaction flask was placed in an ice bath and 2.0 mL of deoxygenated THF was added and the solution was stirred for 10 minutes in the cold bath to quench the polymerization. The reaction mixture was then transferred to the deoxygenated solution of Dowex resin in MeOH (700 mg in 20 mL MeOH) and stirred for 1.5 hours to remove the copper catalyst. The red-orange solution was then filtered to remove Dowex resin and the methanol was removed on a rotary evaporator (200 torr, 23 ^{o}C). The crude, sticky solid was redissolved in a minimum amount of dichloromethane and precipitated in a rapidly stirred solution of hexanes (200 mL). The hexanes was decanted and precipitated reddish-brown polymer was rinsed with hexanes. The precipitation was repeated and the final solid was transferred to a vial as a solution in DCM, then solvent was removed on a rotary evaporator and dried overnight under vacuum (*ca.* 0.5 torr at room temperature). (66% conversion; 171 mg isolated yield). ^{1}H NMR (CD_2Cl_2, 400 MHz, 298 K) δ (ppm) 7.63-7.43 (broad, aromatic, end group), 3.94 (2H, broad, -O**CH_2**$CH_2N(CH_3)_2$), 2.45 (2H, broad, -OCH_2**CH_2**$N(CH_3)_2$), 2.17 (6H, s, -OCH_2CH_2**$N(CH_3)_2$**), 2.05-1.60 (2H, broad, aliphatic main chain), 1.44-1.28 (broad, methyl, end group) 1.07-0.68 (3H, broad, -CH_3, main chain). IR ($CHCl_3$, thin film on NaCl): 2950 cm^{-1} (C-H stretching, strong), 2827 cm^{-1} (C-H stretching of $N(CH_3)_2$, sharp), 2779 cm^{-1} (C-H stretching of $N(CH_3)_2$, sharp), 2080 cm^{-1} (Fe-CO, sharp), 2048 cm^{1} (Fe-CO, sharp), 2011 cm^{-1} (Fe-CO, sharp), 1725 (C=O stretching, strong, sharp), 1459 cm^{1} (-CH_2- bending, sharp), 1271 cm^{1} (C-O, sharp), and 1153 cm^{-1} (C-N stretching, strong, sharp). DMF GPC: $M_{n,\ SEC}$ = 12,700 g/mol, M_w/M_n = 1.27

Synthesis of PDMAEMA-*g*-[2Fe-2S] 58 with Low Copper Catalyst Concentration. $[M]_o : [I]_o : [Cu^{I}]_o : [L]_o$ = 100 : 1 : 0.2 : 0.2.

Synthesis via ATRP was conducted with a low copper catalyst concentration as well. A 10 mL Schlenk flask was loaded with **56** (11.84 mg, 0.0148 mmol) followed by DMAEMA (0.25 mL, 1.48 mmol) and 0.25 mL of 12 mM Cu(I)Br/PMDETA solution in THF. The flask was heated in an oil bath at 50 ^{o}C for 3 hours. The reaction was then quenched by removing the heat and addition of 5 mL of THF and was rapidly passed through a short alumina column to remove the copper catalyst. The solvent was removed on a rotary evaporator and the polymer was purified by precipitation in 200 mL of hexanes. (67% conversion; 85 mg isolated yield). ^{1}H NMR (CD_2Cl_2, 400 MHz, 298 K) δ (ppm) 7.63-7.43 (broad, aromatic, end group), 3.94 (2H, broad -O**CH_2**$CH_2N(CH_3)_2$), 2.45 (2H, broad -OCH_2**CH_2**$N(CH_3)_2$), 2.17 (6H, s, -OCH_2CH_2**$N(CH_3)_2$**), 2.05-1.60 (2H, broad, aliphatic main chain), 1.44-1.28 (broad, methyl, end group) 1.07-0.68 (3H, broad, -CH_3, main chain). IR ($CHCl_3$, thin film on NaCl): 2950 cm^{-1} (C-H stretching, strong), 2827 cm^{-1} (C-H stretching of $N(CH_3)_2$, sharp), 2779 cm^{-1} (C-H stretching of $N(CH_3)_2$, sharp), 2080 cm^{-1} (Fe-CO, sharp), 2048 cm^{1} (Fe-CO, sharp), 2011 cm^{-1} (Fe-CO, sharp), 1725 (C=O stretching, strong, sharp), 1459 cm^{1} (-CH_2- bending, sharp), 1271 cm^{1} (C-O, sharp), and 1153 cm^{-1} (C-N stretching, strong, sharp).$M_{n,\ SEC}$ = 9,500 g/mol, M_w/M_n = 1.33

In all syntheses of **PDMAEMA-*g*-[2Fe-2S] 58** it was imperative to remove Cu species from the crude polymer as it was found to facilitate oxidative decomposition of the [2Fe-2S] core. Copper species are competently removed from **PMMA-*g*-[2Fe-2S] 57** via alumina column, however PDMAEMA is known[13] to complex Cu, so additional care had to be taken to ensure removal of all

Cu species from crude **PDMAEMA-*g*-[2Fe-2S] 58**. After the reaction, stirring the crude polymer solution without exposing to air in degassed MeOH with Dowex-50 resin was found to be the preferred method of copper removal. Also, replacing PMDETA with HMTETA ligand and decreasing the amount of copper catalyst in ATRP reaction helped removing residual copper from the final polymer.

Synthesis and Characterization of ATRP Initiator Naphthalene-1,4-diyl bis(2-bromo-2-methylpropanoate) 86.

1,4-naphtalenediol (160 mg, 1.0 mmol) was dissolved in anhydrous THF (10 mL). Triethylamine (TEA) (0.84 mL, 6.0 mmol) was added and the solution was stirred for 1.5 hours. BIBB (0.33 mL, 2.7 mmol) was added and the solution was stirred at room temperature for 4 hours. The reaction was filtered through a 5 cm silica gel plug (eluted with DCM) to remove an off white precipitate which had formed, and solvent removed by rotary evaporation (35 ^{o}C, *ca.* 200 torr) to yield an off-white solid. Purification via column chromatography (SiGel, 30% dichloromethane in hexane) gave 384 mg (0.84 mmol, 84%) of **86** as a powdery white solid upon removal of solvent. This solid was recrystallized from diethyl ether to obtain chunky transparent crystals for polymer synthesis. ^{1}H NMR: ($CDCl_3$, 500 MHz, 298 K) δ (ppm) 8.07 (2H, dd *J* = 6.5, 3.3 Hz) 7.60 (2H, dd *J* = 6.5, 3.3 Hz), 7.30 (2H, s) 2.19 (12H, s) ^{13}C NMR (101 MHz, $CDCl_3$) δ 170.06 (C=O), 144.37 (C_q-O, $C_{1.4}$), 127.7 (C_q, $C_{4a,8a}$), 127.3 (CH, $C_{6,7}$) 121.5 (CH, $C_{5,8}$), 117.07 (CH, $C_{2,3}$), 55.24 (C_q, C-(Me_2)Br, 30.83 (CH_3).

Synthesis and Characterization of [2Fe-2S]-Free PDMAEMA Homopolymer 87 $(M)_o : (I)_o : (Cu^I)_o : (L)_o = 100 : 1 : 1 : 1.5$.

A 10 mL Schlenk flask was loaded with Cu(I)Br (6.26 mg, 0.0437 mmol) and vacuumed and backfilled with argon three times. Then, 0.20 mL of deoxygenated, anhydrous THF was added to the flask followed by the addition of deoxygenated HMTETA (17.83 µL, 0.066 mmol). The resulting mixture was stirred for 10 minutes to allow for the formation of the Cu-ligand complex. Then, purified and deoxygenated DMAEMA (0.735 mL, 4.37 mmol) was added to the reaction flask. To a second 10 mL Schlenk flask, difunctional naphthyl ATRP initiator 6 (20 mg, 0.0437 mmol) was added and the flask was vacuumed and backfilled with argon three times. Then, 0.30 mL of deoxygenated, anhydrous THF was added to the flask and the solution was stirred until homogeneous then the resulting mixture was transferred to the reaction flask. Finally, the flask was submerged in an oil bath preheated to 50^{o} C and the reaction was stirred at 50° C for 2 hours. After 2 hours, the solution was opened to air and 2.0 mL of THF was added to quench the polymerization. The crude mixture was passed through a short neutral alumina column to remove Cu catalyst and then all solvent was removed. The sticky solid polymer was dissolved in a minimum amount of dichloromethane and precipitated in a rapidly stirred solution of hexanes (200 mL). The hexanes was decanted and the precipitated white polymer was rinsed with hexanes. The final solid was transferred to a vial as a solution in DCM then solvent was removed on a rotary evaporator and dried overnight under vacuum at room temperature. (80% conversion; 470 mg of isolated yield). ^{1}H NMR (CD_2Cl_2, 400 MHz, 298 K) δ (ppm) 7.86-7.78 (2H, broad, aromatic, end group), 7.53-7.46 (2H, broad, aromatic, end group), 7.16-7.11 (2H, broad, aromatic, end group), 3.95 (2H, broad, -O**CH_2**$CH_2N(CH_3)_2$), 2.46 (2H, broad , -OCH_2**CH_2**$N(CH_3)_2$), 2.17 (6H, s, -

$OCH_2CH_2\mathbf{N(CH_3)_2}$), 1.97-1.63 (2H, broad, aliphatic main chain), 1.03-0.70 (3H, broad, $-CH_3$, main chain). $M_{n,\ theo}$ = 13,100 g/mol and $M_{n,\ NMR}$ = 15, 500 g/mol.

Titration Curve for PDMAEMA-g-[2Fe-2S] 58. The titration curve for **PDMAEMA-*g*-[2Fe-2S] 58** in 0.2 M KCl is shown in Figure B.5g. This titration agrees well with a published titration in 0.15 M NaCl.[14] The same paper gives a titration curve for PDMAEMA in 1.0 M NaCl, which is almost identical to the monomer, DMAEMA (pKa 8.4). This far away from the pH of the solution, there is only about a 1% difference in protonated species between pK_a 8.3 and 8.4. Based on this curve ~95% of the amines in **PDMAEMA-*g*-[2Fe-2S] 58** are protonated at pH 7.

B. Electrochemistry

General Electrochemical Procedures and Materials.

All electrochemical experiments utilized a standard three-electrode system with a working electrode, a counter electrode, and a reference electrode. Solution resistance was compensated at 90% of measured cell resistance. To determine that catalysis did not rely on electrode materials, two different working electrodes were employed: a glassy carbon disk electrode and a gold amalgam disk electrode. A platinum (Pt) disk electrode was used as a standard for comparison of electrocatalysis in the electrolyte/buffer solution in the absence of metallopolymer. The physically measured areas of the electrode surfaces were confirmed electrochemically by means of the current of the oxidation peak of ferrocene in acetonitrile. To reduce the effect of minor surface variations, the GC and Pt working electrodes were polished between scans in a figure eight pattern on a Buehler microcloth polishing cloth with 1.0 then 0.05 micron alumina micropolish (1 minute per grade) suspended in de-ionized water. Two different counter electrodes were employed also. In controlled potential electrolysis experiments, the counter electrode was an edge plane graphite rod (diameter 3 mm, 10 cm length) placed in a glass chamber separated from the rest of the cell by a 4 Å molecular sieve frit. Control experiments with this graphite rod counter electrode confirmed that a Pt wire counter electrode was suitable for cyclic voltammetry and linear sweep voltammetry but not for long-term electrolysis due to eventual crossover of Pt from the Pt wire counter electrode to the cathode, as also shown in the literature.[243] Potentials in water are referenced to SHE using the standard conversion of +0.210 V from the potential of the Ag/AgCl/3M KCl reference electrode.[244] For the CV experiments a scan rate of 100 mV/s was used unless otherwise noted.

In order to estimate the concentration of [2Fe-2S] sites per mass unit of polymer, a calibration curve was constructed for the characteristic Fe-CO stretching frequencies. The calibration was performed in triplicate and R^2 values for each linear regression were 0.98 or better. Each batch of polymer was inspected via IR and a mmol mg^{-1} value for the concentration of [2Fe-2S] was established using this calibration curve.

Effects of Buffer on Catalysis.

Electrochemical simulations indicated a relationship between the catalytic current density and the concentration of the conjugate acid of the buffer (i.e., NaH_2PO_4 in sodium phosphate buffer, ~40% in the protonated state at pH 7). This was subsequently confirmed by the observation of increased current density at increased buffer concentration (see Figure B.9). To further increase

the concentration of the conjugate acid species, 2-amino-2-(hydroxymethyl)propane-1,3-diol buffer (tris) was used as it has a higher solubility and higher proportion of conjugate acid species at pH 7 (~92% protonated at pH 7). This simple change in buffer significantly increased current density without changing the reduction potential required to initiate catalysis. It should be noted that in principle the buffer is not consumed in the overall water splitting reaction, because protons consumed in the hydrogen reduction half-reaction are generated at the water oxidation half-reaction. In this sense, the buffer is a co-catalyst that has no activity on its own but increases the rate of the water splitting reaction without being consumed. The pH 7 tris at 1 M concentration serves the triple purpose of (1) the electrolyte for the electrochemistry, (2) the buffer for the pH, and (3) a co-catalyst for the hydrogen production.

This effect of the tris buffer is also interesting in relation to the critical role of the covalently bound amine in the active site of [FeFe]-hydrogenases. While the amine of the tris buffer is not covalently bound to the [2Fe-2S] active site of the metallopolymer, at this pH 7 the tris buffer provides a protonated-amine rich environment for the catalyst and significantly increases the rate of hydrogen production. Regardless of the precise mechanism, this shows that the nature of the buffer can be tuned to optimize hydrogen-evolving reactions.

Determination of Faradaic Yield.

Faradaic yield was established by preparing a 25 μM solution (10 mL) of **PDMAEMA-*g*-[2Fe-2S] 58** in 1.0 M pH 7 tris buffer in an airtight electrochemical cell. Controlled potential electrolysis was performed by holding the glassy carbon working electrode at -1.39 V vs SHE until 2.025 C had been passed, which corresponds to 250 μL H_2 assuming 100% Faradaic yield. Note that this potential is over 440 mV negative of the holding potential used for later bulk electrolysis experiments which assessed to TON of the catalyst. This was done to increase the rate of hydrogen production at the relatively small area disk electrode and demonstrates that a high Faradaic yield is achieved even at very high overpotentials where side reactions would be more likely. At the end of this period, the headspace was sampled using a Hamilton gas-tight syringe to inject 250 μL of headspace into a Shimadzu GC-8A equipped with a thermal conductivity detector operating at 70 mA, using Argon as a carrier gas at a flow rate of 25 mL/min. The signal was calibrated against the signal from a 250 μL aliquot of H_2 that was manually added to the head space of the argon-purged cell and allowed to sit for 8 minutes to replicate the time required to generate the same volume of H_2 in the controlled potential experiment. This process was repeated three times to obtain an average value and standard deviation for the Faradaic yield. A Faradaic yield of 93±2% was determined by comparison of the average peak area of the standard injections relative to the H_2 area from the headspace after electrolysis (see Figure B.14). The same procedure was repeated with a platinum electrode to test the accuracy of the procedure. This also provides some cancelation of errors introduced by the gas transfer processes, gas dissolution, micro-bubbles adhering to the surfaces, leakage from the cell, and the GC analysis. The platinum electrode gave a Faradaic yield of 96±2%. Thus the Faradaic yield of the **PDMAEMA-*g*-[2Fe-2S] 58** is 97±3% of the Faradaic yield of platinum for hydrogen production.

In addition, the Faradaic yield was determined by the shift to higher pH caused by reduction of protons in solution in the controlled potential electrolysis experiments. The pH after controlled potential electrolysis was compared to the initial pH of 7.00 using the Henderson-Hasselbach

equation and the number of protons consumed was calculated and compared with the number of electrons passed over the course of electrolysis. This method gave a Faradaic yield of 103±3%. In conclusion the Faradaic yield is quantitative within the certainty of these measurements.

Tafel Analysis.

Tafel analysis is a preferred measure of catalytic performance over cyclic voltammetry because it gives a direct measure of the catalytic current density response as a function of the overpotential in steady-state flow conditions. The current density as a function of voltage was measured for several concentrations of **PDMAEMA-*g*-[2Fe-2S] 58** catalyst and different arrangements of electrodes (glassy carbon working electrode with platinum wire counter electrode and gold amalgam electrode with frit-separated carbon counter electrode) with similar results. These plots were compared with similar measurements for a planar platinum disk electrode that was cathodically conditioned for several minutes at -1 V vs. the reference electrode until the electrode current stabilized for reproducible HER.[122] In each case the current was measured by linear sweep voltammetry at a rate of 5 mV/s and with 1600 rpm magnetic stirring, and the solution contained 1 M tris buffer adjusted to pH 7.

Controlled Potential Electrolysis and Turnover Number (TON).

Controlled potential electrolysis (CPE) was used to determine the turnover number (TON) and lifetime of the catalyst under catalytic conditions, as well as the total Faradaic yield over the many hours run time of electrolysis. Because of the long running time of these experiments they were limited to the gold amalgam electrode and the frit-separated carbon electrode in order to (1) avoid unacceptable background current from direct reduction with the glassy carbon electrode, (2) avoid possible crossover of platinum from a platinum counter electrode to the working electrode,[243] and (3) avoid decomposition of the catalyst by oxidation at the counter electrode. The electrolysis cell included a gold amalgam foil electrode immersed approximately 8-10 mm into the electrolysis solution to give an area of ~1.5 cm^2. The potential for electrolysis was chosen as –0.95 V vs. SHE (overpotential η of ~0.54 V) where the Tafel plot indicates reasonable current density without excessive voltage. The background current in these conditions in the absence of catalyst yielded only 0.4 coulombs anaerobically and 26 coulombs aerobically over 18 hours. The 3 mm diameter gold amalgam disk electrode was integrated in the cell to allow for CV and LSV interrogation of the solution before, after, and at intermediate times in the electrolysis experiment. The high current density and excessive formation of bubbles at the working and counter electrodes, as well as the sensitivity to placement and collection of bubbles at the reference electrode which occurred throughout the electrolysis, created challenges for obtaining a steady current response in electrolysis experiments that ran for periods up to six days in our apparatus. Determination of the amount of hydrogen evolved by headspace analysis posed serious experimental difficulties due to significant effusion of hydrogen past the seals of the cell over these long periods of these electrolyses. Instead, we have measured the pH of the solutions after electrolysis and calculated the Faradaic yield based on proton consumption. As mentioned in the section on Faradaic yield determination, the pH measurement indicated a yield of 103±3%. Consequently, the measured coulombs are good indication of the hydrogen produced.

Figure B.15 shows representative examples of the measured coulombs vs. time and current vs. time for the CPE experiments and the corresponding turnover numbers. We have used an

exponential decay function to model catalyst decay using the method of Costentin, Passard, and Savéant.[245] This decay function has been overlaid with our data in Figure B.15a to show that the catalysis is operating as a solution-phase catalyst (albeit in equilibrium with surface adsorption as discussed below) in a steady-state condition from the beginning of operation and throughout the catalysis.[246] The current vs. time plot shown in Figure B.15a' displays some fluctuations in the current which were due to restarting the potentiostat and from oxygen evolution at the counter electrode. The counter electrode used in bulk electrolysis was separated with a frit from the working CPE solution and suspended in a glass tube filled with buffered solution containing no catalyst. During electrolysis, the evolution of oxygen at the counter electrode caused build-ups of O_2 in the glass tube such that a counter electrode was cut-off from the frit connecting the counter electrode to the working solution causing the current to decrease. When the oxygen bubbles were dislodged, the amount of current being passed increased back to approximately the same level before the bubble formed. Figures S15b and S15c give a closer look at the early stage of electrolysis. Figure B.15a indicates a "stability factor of merit" as defined by Costentin, Passard and Savéant[24] of 6.5×10^4. In comparison, Figure B.16 shows metalloinitiator **56** and **PMMA-g-[2Fe2S] 57** (anaerobic) lose all of their catalytic activity in about 30 minutes and have stability factors of merit of less than 10 that are profoundly inferior to the 6.5×10^4 factor of **58**. The electrochemistry of **21** was studied previously. The CPE of **21** was not reported but the CPE and stability factor of merit of the closely related complex (benzenedithiolato)$Fe_2(CO)_6$ is similar to that of **56** and **57**.[21] Figures S15b and S15c appear to indicate that aerobic stability is greater than anaerobic stability but we do not feel this difference is significant due to variability in the cathode area and hydrogen bubble behavior in different cell assemblies. The measured coulombs in all experiments, both anaerobic and aerobic, gave turnover numbers in the range of $2\text{-}6\times10^4$ molecules of hydrogen per catalyst site.

With regard to the O_2 tolerance, we have performed the electrolysis of pH 7.0 tris buffer solution (pH 7.0) operating in air without catalyst. The total charge passed was 26 C which is *ca.* 5% of the nearly 500 C passed with catalyst present. However, this represents the worst-case scenario in which ambient oxygen is able to continuously re-dissolve in the solution to maintain a high steady state concentration. In contrast, during the bulk electrolysis experiments with catalyst present, continuous hydrogen formation is expected to sparge the solution, displacing some oxygen and lowering the steady state O_2 concentration. Thus we believe the charge contribution from oxygen reduction is less than the uncertainty we report for the Faradaic yield from headspace GC measurements (± 3%). This also falls well within the uncertainty of the turnover number, which we report as $4\pm2\times10^4$.

SEM/EDX Imaging of Carbon Electrodes After Electrolysis.

To confirm the absence of irreversibly adsorbed or deposited metal particulate or decomposed species from **PDMAEMA-*g*-[2Fe2S] 58** metallopolymers, a series of SEM/EDX measurements were conducted on planar carbon electrodes subjected to CPE HER experiments. SEM of bare carbon electrodes before use revealed that surfaces were featureless and free of any adsorbed contaminants that would complicate morphological and spectroscopic interpretation (Figure B.18). SEM secondary electron imaging (Figure B.18B) revealed a featureless, planar surface for the bare carbon electrode, along with featureless images for EDX elemental mapping of C K_α (Figure B.18C), Cl K_α (Figure B.18D) and Fe K_α (Figure B.18E). CPE using **PDMAEMA-*g*-[2Fe-2S] 58**

(10 μM [2Fe-2S] by IR, 0.2 mg/mL in 1 M tris buffer (pH 7)) of this same planar carbon electrode was then conductedusing conditions previously described above for a reaction time of one-hour to ensure sufficient exposure of the electrode to the solution-phase metallopolymer during electrolysis (Figure B.19). SEM/EDX imaging of this same planar carbon electrode was conducted where the electrode remained *unrinsed* from the electrolyte salts from the electrolysis medium. SEM secondary electron imaging of this sample revealed the presence of large-micron sized deposits, of irregular morphology, in addition to bare exposed regions of the electrode surface. These larger deposits were attributed to electrolyte/buffer salts from the reaction medium, which was confirmed by identical spatial positioning of EDX C K_α (Figure B.20C), Cl K_α (Figure B.20D) elemental mapping. However, EDX elemental mapping of Fe K_α (Figure B.20E) was completely featureless, which confirmed that adsorbed, or deposited species from the metallopolymer catalyst were absent from the electrode surface after electrolysis. Finally, SEM/EDX analysis of this same electrode after rinsing revealed a featureless electrode surface, further confirming the absence of any irreversibly deposited species from the metallopolymer catalyst (Figure B.21). Quantitative analysis of the EDX spectra taken from this series of experiments (Figure B.18A, 20A, 21A) are summarized in Table S1, also confirming the absence of adsorbed/deposited Fe-containing species during electrolysis.

Transient Adsorption of PDMAEMA-g-[2Fe-2S] 58.

A key question that needed to be resolved to enable meaningful mechanistic and kinetic insights into the rates of H_2 generation was the homogeneous vs. heterogeneous nature of the metallopolymer during electrocatalysis. The imaging experiments of both unrinsed and rinsed electrodes via SEM-EDX confirmed that irreversibly deposited species were not formed during electrocatalysis. So the resulting mechanistic possibilities were whether the metallopolymer catalyst **58** remained homogeneous during electrocatalysis, or was adsorbed in a reversible, transient fashion to the electrode due to electrostatic interactions (i.e., electrosorption) between the positively charged protonated ammonium side chain groups from the metallopolymer and the negatively polarized charged surface of the electrode under bias. Literature studies of other charged polymers (i.e., polyelectrolytes) indicate that adsorption is likely.[247–249] In the next sections we provide evidence of adsorption from experiments in which we investigate the dependence of CV peak currents on catalyst **58** concentration, the dependence of CV peak currents on doping the catalyst **58** solution with Fe-free PDMAEMA polymer, and the dependence of LSV plateau currents on catalyst 4 concentration. The currents are modeled accurately by a Langmuir adsorption-based model.

The first evidence for reversible adsorption of the metallopolymer on the surface was provided by a simple rinse test. After establishing catalysis at the GC electrode with the catalyst in solution, the electrode was removed, rinsed, and placed in a cell with buffer solution without catalyst. Cyclic voltammetry scans through the potential of catalysis showed a weak current on the first scan that disappeared on subsequent scans. A report has noted that the rinse test should be carefully interpreted regarding adsorption at the electrode surface in case the species might re-dissolve.[246] In this case, the cyclic voltammetry indicates that the intact metallopolymer has a weak attractive interaction with the GC electrode, but the metallopolymer leaves the surface under the reducing conditions of catalysis, indicating a dynamic equilibrium for adsorption dependent on the solution concentration.

Catalyst Concentration Dependence and Langmuir Adsorption Analysis.
With such high peak current densities in the CV (>70 mA/cm^2 at 10 μM catalyst concentration and 100 mV/s scan rate), we were inspired to attempt lower catalyst concentrations and found that loadings of 100 nM metallopolymer (2 μg/mL, 2 ppm) still gave appreciable catalytic peak current density in cyclic voltammetry (18 mA/cm^2, see Figure B.8f). The CV peak current densities from 0.1 μM **PDMAEMA-*g*-[2Fe2S] 58** catalyst concentration to 100 μM catalyst concentration are shown in Figure B.8f. The current density vs. concentration profile is characteristic of an adsorption isotherm, as shown by the fit of the blue line based on a Langmuir-type adsorption model.

To be specific, in the Langmuir adsorption model the fraction of adsorption sites to which a solute molecule has become attached, is given by:

$$\theta = \frac{K_{\text{ads}}[\text{A}]}{1 + K_{\text{ads}}[\text{A}]} \qquad \text{Equation 1}$$

where K_{ads} is the equilibrium constant for the reaction:

$$\text{A} + \text{S} \rightleftharpoons \text{AS} \qquad \text{Equation 2}$$

S is an empty surface site and AS is a surface site occupied by A. The equilibrium constant expression is then:

$$K_{\text{ads}} = \frac{[\text{AS}]}{[\text{A}][\text{S}]} \qquad \text{Equation 3}$$

The units for K_{ads} are not critical as long as they are consistent. For example, the units for [AS] and [S] represent the concentration of surface sites per unit surface area and might be mol cm^{-2}, but this unit cancels in the equilibrium constant. The units for [A] are concentration per unit volume and to be consistent with most electrochemical equations can be mol cm^{-3}, giving a unit for K_{ads} of cm^3 mol^{-1}. However, this unit cancels in the calculation of the fraction of occupied surface sites θ to give a unitless fraction.

The peak current due to adsorbed catalyst in the CV of the **PDMAEMA-*g*-[2Fe-2S] 58** solution in equilibrium with the electrode surface is the fraction of surface sites that are occupied times the maximum current when all sites are occupied, $i_{\text{ads}}^{\max}$:

$$i_{\text{p}} = \theta \times i_{\text{ads}}^{\max} = \frac{K_{\text{ads}}[\text{A}]}{1 + K_{\text{ads}}[\text{A}]} \times i_{\text{ads}}^{\max} \qquad \text{Equation 4}$$

When $K_{\text{ads}}[\text{A}]$ << 1 the current increases nearly linearly with the concentration [A], as in the region below 1 μM catalyst concentration in Figure B.8f. When $K_{\text{ads}}[\text{A}]$ >> 1 the current becomes nearly constant at $i_{\text{ads}}^{\max}$ from the full monolayer of adsorbed catalyst. The transition from the high slope of the current/concentration profile at low concentration to the low slope at higher concentration is the region of monolayer formation, shown from 1 μM to 10 μM catalyst concentration in Figure B.8f.

The gradually increasing current as the catalyst concentration increases above 10 μM is generally indicative of growth of a second layer which contributes to the current. This builds on the first monolayer and is proportional to the catalyst solution concentration, and in the early stages of growth can be modeled by the following equation:

$$i = \theta * i_{\text{ads}}^{\max} \times (1 + [\text{A}]\text{x}) \qquad \text{Equation 5}$$

where x is the proportionality of the current increase with the increase in the solution catalyst concentration and has units of current/M. The blue line in Figure B.8f is obtained with Equation 5 and K_{ads} = 5×10^9 cm^3 M^{-1}, $i_{\text{ads}}^{\max}$ corresponding to a current density of 45 mA cm^{-2} for monolayer adsorption, and x = 9×10^{-3} mA μM^{-1}.

Addition of Analogous but Catalytically Inactive Polymer.

Additional insight into the dynamic nature of the solution catalyst in equilibrium with surface adsorbed species is gained from a competition experiment in which a polymer similar to **PDMAEMA-*g*-[2Fe-2S] 58** but without the catalytically active [2Fe-2S] site (referred to as "Fe-free PDMAEMA") is added to the solution. For these experiments, Fe-free PDMAEMA **7** with similar molecular weight was prepared via ATRP of DMAEMA from a difunctional α-haloester naphthyl initiator (see Figure 6). **7** is a polymer identical to **PDMAEMA-*g*-[2Fe-2S] 58** but the naphthalene-based initiator is lacking the $S_2Fe_2(CO)_6$ functional group. Addition of Fe-free PDMAEMA **7** will compete equally with **PDMAEMA-*g*-[2Fe-2S] 58** for the surface sites, and in the region of monolayer adsorption the current due to adsorbed species will fall proportional to the decrease in the mole fraction of the catalyst polymer to total polymer on the surface (see Figure B.22).

The results of these experiments are collected in Figure B.12. The experiments start with a 10 micromolar (0.2 mg/mL) loading of **PDMAEMA-*g*-[2Fe-2S] 58**, where the Langmuir models described above indicate formation of the monolayer is 98% complete. A 0.2 mg/mL loading of Fe-free PDMAEMA **7** gives a comparable concentration. The small contribution to the current from **7** is due to direct reduction of the ammonium groups on the polymer chains at the electrode. The CV of **7** with the gold amalgam electrode shows that this reduction shifts to more negative potential as expected with this electrode while the **PDMAEMA-*g*-[2Fe-2S] 58** catalysis peak does not shift appreciably, and thus the **PDMAEMA-*g*-[2Fe-2S] 58** peak current on the gold amalgam electrode does not have appreciable contribution from direct reduction of the ammonium groups.

The addition of increasing equivalents of Fe-free PDMAEMA **7** to the 10 μM **PDMAEMA-*g*-[2Fe-2S] 58** solution results in decreasing catalytic peak currents, showing that competition is taking place for surface sites (Figure B.12a). Addition of one equivalent of Fe-free PDMAEMA **7** decreases the peak current by 25%. However, this 1:1 ratio is a 50% reduction in the mole fraction of active polymer and, given equal competition for a similar number of surface sites, should reduce the peak current by 50% if the surface is completely covered by adsorbed molecules. The reduction in peak current by 25% means that ~50% of the current is due to adsorbed molecules and the other 50% of the peak current does not depend on the mole fraction of polymer but instead depends on the solution concentration of the catalyst in the electroactive region.

These observations suggest a Langmuir-based adsorption model adapted for the mole fraction of catalytically active polymer molecules on the surface plus a contribution to the current dependent on the solution concentration of the catalyst. Figure B.12b shows excellent correlation between the model described below and the experimental reduction in peak current with added equivalents of free-PDMAEMA.

When *m* equivalents of Fe-free PDMAEMA **7** are added to the 10 μM solution of **PDMAEMA-*g*-[2Fe-2S] 58** the total polymer concentration increases by a factor of (1 + *m*) and the fractional surface coverage with *m* equivalents increases to:

$$\theta_m = \frac{K_{\text{ads}}[\text{A}](1+m)}{1+K_{\text{ads}}[\text{A}](1+m)} \qquad \text{Equation 6}$$

In addition, the fraction of these sites occupied by catalytically active molecules is reduced to $1/(1+m)$. The current due to adsorbed species for addition of *m* equivalents of **7** is then the first term in the following equation:

$$i_{\text{p}}^{m} = \frac{1}{(1+m)} \times \theta_m \times i_{\text{ads}}^{\max} + (1-\theta_m) \times i_{\text{C}}^{\max} \qquad \text{Equation 7}$$

The second term accounts for the catalytic current that is proportional to the concentration of catalyst in solution (not the mole fraction) given by the limiting current $i_{\text{C}}^{\max}$ for the 10 μM catalyst concentration. This term is weighted by the fraction of the surface that is not blocked by adsorbed polymer, although this fraction should not be viewed as a static model due to the dynamics of the on/off adsorption equilibrium. This is the equation that fit the data in Figure B.12b with variables K_{ads} 61 cm^3 μM^{-1}, $i_{\text{ads}}^{\max}$ corresponds to a current density of 83 mA cm^{-2}, and $i_{\text{C}}^{\max}$ corresponds to a current density of 70 mA cm^{-2}. The R^2 goodness of fit value is 0.999. The proportion of the limiting contributions to the peak current from $i_{\text{ads}}^{\max}$ and $i_{\text{C}}^{\max}$ is not accurately known from the fit, but the similarity of their values indicates similar kinetics for catalysis by these processes even though the statistics for competition with the catalytically inactive polymer **7** differ.

While this analysis shows the dynamic equilibria taking place at the electrode surface during catalysis, these CV peak currents could not be used to estimate the observed rate of hydrogen production per catalyst molecule because plateau currents could not be obtained even at very low catalyst loadings (0.1 μM) and high scan rates. Instead we report the estimated observed rate based on steady-state electrochemical experiments as follows.

Linear Sweep Voltammetry and Langmuir Adsorption Analysis.

Figure B.13a shows the collective Tafel plots for **PDMAEMA-*g*-[2Fe-2S] 58** at concentrations from 0.2 μM (2 μg/mL) to 150 μM (1.5 mg/mL) using a glassy carbon electrode. Higher concentrations showed little further change. The currents stabilized near their maximum at -1.6 V overpotential. The plateau currents (taken at -1.45 V as the average current from -1.35 V to the limit of the scan at -1.55 V to reduce the noise from bubble formation) as a function of concentration are shown in Figure B.13b, along with the simulation based on the Brunauer-Emmett-Teller (BET) adsorption isotherm model, which applies to systems of multilayer adsorption. The blue dotted line is the fit to the data. After the nearly complete monolayer

coverage is reached the current increases in a straight line with concentrations from 20 μM to 80 μM, indicating the early stages of formation of a second monolayer. The low and constant slope indicates the second layer of adsorption is weak. According to the BET model the fit value of the C parameter of 600 indicates that the difference in enthalpy between formation of the first layer and formation of the second layer is about 4 kcal/mol, meaning that there is little formation of the second layer, although it does contribute to the catalytic current. This high value of C also indicates that the assumptions in the Langmuir adsorption model are reasonably valid for this system.

Figure B.13c shows the modeling of the current/concentration curve according to the Langmuir-type model for the adsorption isotherm. With inclusion of current from the second monolayer as in Equation 5 and allowing for a solution concentration dependent current as indicated from the competition experiment (as in Equation 7), the observed current vs. concentration can be modeled as in the following equation.

$$i = \theta \times i_{\text{ads}}^{\max} \times (1 + [\text{A}]\text{x}) + (1 - \theta)[\text{A}]R \qquad \text{Equation 8}$$

The parameter *R* is the rate of change of the catalytic current that is concentration-dependent and has units of current divided by concentration (amps μM^{-1}). This concentration-dependent term is included primarily because it is indicated by the competition experiment presented above, but the confidence level of its relative contribution is low. In Figure B.13c, the blue dashed line is the contribution from the first term (adsorbed catalyst) and the red dashed line is the contribution to catalysis from the second term (concentration dependent). The purple line is the fit sum. The parameters are K_{ads} = 2×10^{9} cm^3 M^{-1}, $i_{\text{het}}^{\max}$ corresponds to a current density of 144 mA cm^{-2}, x = 8×10^{-3} amp μM^{-1}, and *R* = 1×10^{-2} amp μM^{-1}.

A similar analysis was carried out with the gold amalgam electrode with the same conclusions. The analysis differed in analyzing the currents at lower overpotential (0.6 V) and lower currents due to more complex current behavior at higher potentials. The equilibrium constant for adsorption was about 1/3 of that on the glassy carbon electrode and consequently the monolayer coverage occurred at a higher concentration of about 10 μM.

Turnover Frequency (TOF) per Catalyst Molecule.

The operational measure of catalyst speed is the amount of hydrogen produced per second per quantity of catalyst as a function of potential. These are all easily measured macroscopic values. It is common to report a value derived from these measures for the rate of hydrogen produced per catalyst molecule in the electroactive region. The rate of hydrogen produced is easily determined from the plateau current density = i_{plateau}/A where *A* is the electrode area. For the 10 μM **PDMAEMA-*g*-[2Fe-2S] 58** concentration (95% monolayer coverage by the fit of Equation 8), i_{plateau} = 15.7 mA and the current density *J* is 222 mA cm^{-2}. The rate of hydrogen production per second per cm^2 electrode surface area is (given 100% Faradaic efficiency):

$$\frac{J}{\text{nF}} = \frac{0.222 \text{ coulombs s}^{-1} \text{ cm}^{-2}}{2 \times 96485 \text{ coulombs mol}^{-1}} = 1.2 \times 10^{-6} \text{ moles}_{\text{H2}} \text{ s}^{-1} \text{ cm}^{-2} \qquad \text{Equation 9}$$

Dividing this number by the number of catalyst molecules in the electroactive region yields the turnover frequency for hydrogen production per catalyst molecule. Unfortunately, determination of the number of catalyst molecules in the electroactive region generally requires assumptions and approximations of the catalyst behavior in this region. We will use assumptions that lead to a lower bound for k_{obs}, the turnover frequency.

For surface adsorbed catalysts the current is proportional to the surface coverage Γ^0 and the rate k_{obs}, (TOF).

$$i_{\text{plateau}} = \text{nF}Ak_{\text{obs}}\Gamma^{\text{o}} \qquad \text{Equation 10}$$

Where
$i_{plateau}$ is the plateau current in coulombs s^{-1}
n = 2 for two electrons per hydrogen molecule to relate the current to the rate of production of H_2.
F = 96485 coulombs mol^{-1} Faraday constant
A is the area of the electrode = 0.071 cm^2 in these experiments
Γ^o is the catalyst surface coverage in mol cm^{-2}
k_{obs} is the observed overall rate constant in s^{-1}.

Complete surface coverage by the monolayer of catalyst is assumed. The number of molecules in this maximum surface coverage is estimated by the closest-packed approach verified by Long and Chang for their system.[116] It is assumed that each metallopolymer molecule sits on a tile on the surface that is ~60 Angstroms square. This dimension is based on the hydrodynamic radius of 28 Angstroms obtained from a diffusion ordered spectroscopy (DOSY) NMR experiment run for **PDMAEMA-*g*-[2Fe-2S] 58** under the conditions of these electrolysis experiments (100 μM, 0.8 mg/mL **58** in D_2O with 1 molar tris buffer adjusted to pH 7 using DCl). Using the self-diffusion of water in D_2O as internal reference yielded a value for the diffusion coefficient of $5.05\pm0.07\times10^{-7}$ cm^2 s^{-1}. A 28 Angstrom hydrodynamic radius was determined using the Stokes-Einstein equation taking into consideration the change in viscosity by performing control DOSY experiments with 1 M tris adjusted to pH 7. This dimension is also consistent with the radius of the molecular model of the roughly spherical coiled polymer shown in Scheme 1 in the manuscript. This gives a tile surface area of 3600 A^2 per molecule. This area per molecule is then converted to moles/cm^2 for Γ^o.

3600 A^2 molecule^{-1} = 3.6×10^{-13} cm^2 molecule^{-1}

Inverting gives 2.8×10^{12} molecules cm^{-2} on the surface for a closest-packed monolayer.

2.8×10^{12} molecules cm^{-2} = 4.6×10^{-12} mol cm^{-2} = $\Gamma^{\text{monolayer}}$

From the fit of Figure B.13c, monolayer coverage is 95% achieved at a catalyst concentration of 10 μM, where the current is near plateau at 15.7 mA. Using this current gives:

$$k_{\text{ads}} = \frac{i_{\text{plateau}}^{\text{monolayer}}}{\text{nF}A\Gamma^{\text{monolayer}}} = 2.5\times10^5\ \text{s}^{-1} \qquad \text{Equation 11}$$

This rate is likely a lower bound for several reasons:

- Full closest-packed coverage is assumed. If the catalyst molecules are competing with other species in solution for surface sites (e.g. electrolyte, buffer, and solvent) then the number of catalyst molecules on the surface will be smaller and k_{obs} per molecule will be larger.
- The catalyst hydrodynamic radius is assumed to correspond to a near spherical polymer as shown in the molecular model, but if the polymer flattens and spreads on the surface (as expected) the concentration of polymer per surface area in a closest packed array deceases.
- Electroactivity is assumed for all surface sites for the full area of the electrode.
- All catalyst molecules on the surface are assumed to be oriented correctly for both electron transfer from the electrode and for reduction of protons from the solution.
- The true plateau current has not been reached. The dependence on the nature and concentration of the buffer shows that the rate is somewhat limited by the buffer substrate. Increasing the tris buffer concentration from 1 M to 3 M increases the CV peak current by only about 30%, so the true plateau current is expected to increase k_{obs} but not by an order of magnitude.

Consequently the inherent catalyst rate is likely faster than shown by Equation 11.

III. Figures

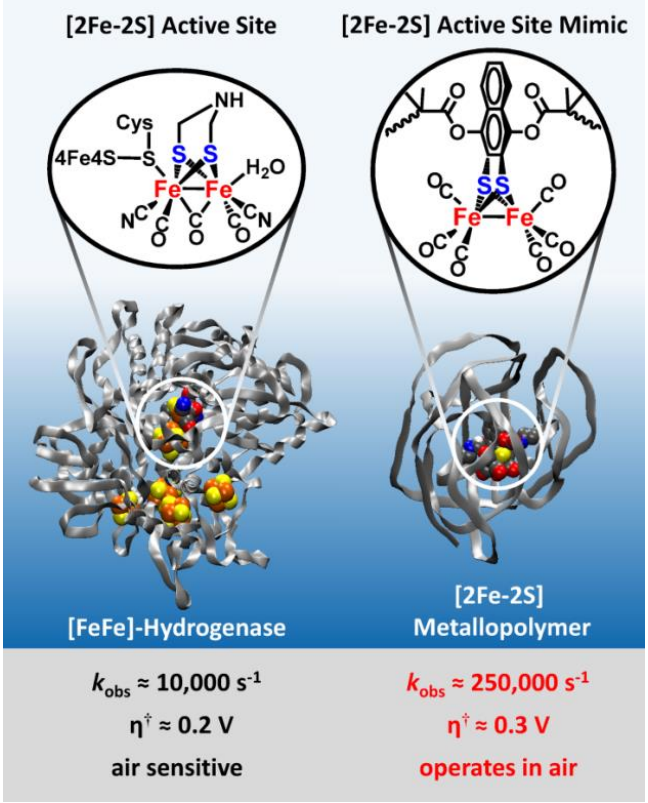

Reproduced with permission from *Angew. Chem. Int. Ed.*[12]

Scheme 3.1 Extended Caption.

Scheme 3.1: Comparison of a new class of HER homogeneous [2Fe-2S]-metallopolymer catalyst vs. [FeFe]-hydrogenase at the same scale, where the metallopolymer HER catalyst is remarkably faster than the enzyme AND is air stable at neutral pH. In addition, current densities greater than 300 mA cm^{-2} are achieved with 75 μM catalyst loading. $\eta^{\dagger}$ is the overpotential requirement to achieve an operating cell current density of 0.1 mA cm^{-2}.

The [FeFe]-hydrogenase structure is taken from the deposit PDB ID 5LA3 in the Protein Data Bank (http://www.rcsb.org/).[35]

The molecular images were created with the Virtual Molecular Dynamics program [250] (http://www.ks.uiuc.edu/Research/vmd/) version 1.9.3.

The k_{obs} for [FeFe]-hydrogenase in the scheme is a representative value for the high range of hydrogenases (including [NiFe]-hydrogenases) adsorbed on pyrolytic graphite edge (PGE) rotating disk working electrodes from the review by Vincent, Parkin and Armstrong.[251] These conditions are similar to the steady-state conditions of the present study. This review talks about distinguishing "between the *inherent* activity of the active site and the *overall* activity of the enzyme-modified electrode" along with issues of mass transport of the substrate and electrode coverage for determining the rate. Taking these issues into account indicates the k_{obs} of 250,000 s^{-1} is a lower bound for the inherent rate of the active site. Moore, et al. have extrapolated a TOF of ~21,000 s^{-1} with a relatively high uncertainty of ±12,000 s^{-1} for single [FeFe]-hydrogenases in direct contact with bare gold.[3] This is still an order of magnitude slower than the lower bound for the [2Fe-2S] metallopolymer.

For comparison of the operating cell potential for catalysis we use the characteristic of "overpotential requirement" presented by Armstrong and Hirst.[50] The overpotential requirement for the [FeFe]-hydrogenase is taken from Figure 2 of the paper that reported the direct electrochemistry of an [FeFe]-hydrogenase on a TiO_2 electrode.[2] The current density measured at a slow sweep rate in water at pH 7 compares with the experiments in this work, and a common current density of 0.1 mA cm^{-2} is selected for comparison of the overpotentials, even though

much higher current densities are achieved for the polymer catalyst at slightly higher overpotential requirements.

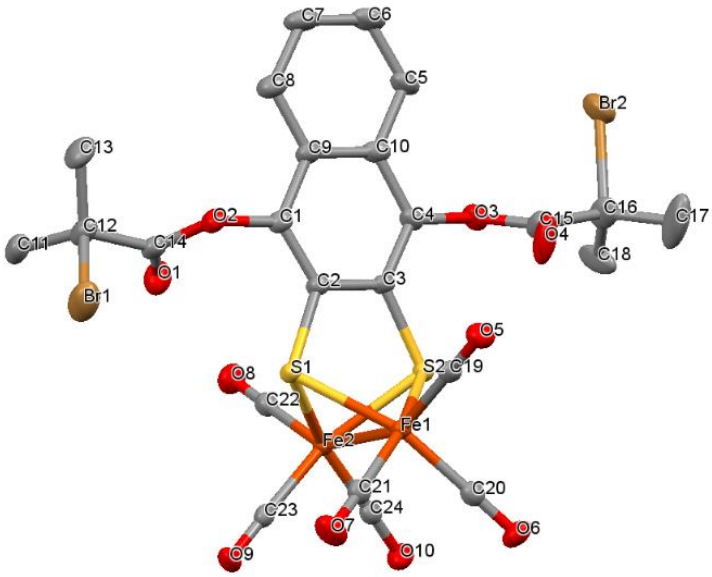

Figure B.1. Oak Ridge thermal ellipsoid plot (ORTEP) diagram of **56** with hydrogen atoms omitted and thermal ellipsoids shown at 50% probability level. CCDC 1577155 contains the supplementary crystallographic data for this paper. These data are provided free of charge by The Cambridge Crystallographic Data Centre. Reproduced with permission from *Angew. Chem. Int. Ed.*[12]

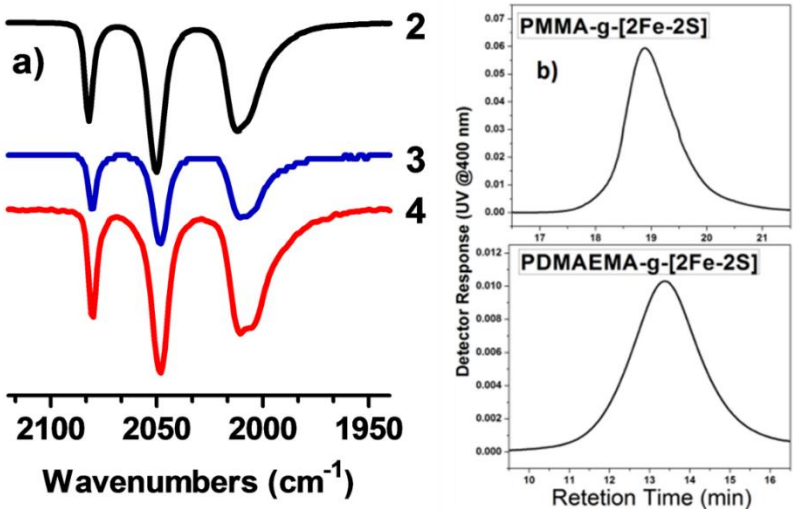

Figure B.2. Confirmation of covalent incorporation of small molecule metalloinitiator 56 in metallopolymers. **a)** IR overlay **56** (black), **57** (blue), and **58** (red) showing retention of characteristic Fe-CO stretching frequencies. **b)** GPC data for **57** (PMMA-*g*-[2Fe-2S], $M_{n,\,SEC}$ = 11,982 g/mol; M_w/M_n = 1.10) and **58** (PDMAEMA-*g*-[2Fe-2S], M_n = 9,500 g/mol, M_w/M_n = 1.33) with a UV-vis detector operating at 400 nm which is characteristic of **56**, but not for PMMA or PDMAEMA homopolymers. Reproduced with permission from *Angew. Chem. Int. Ed.*[12]

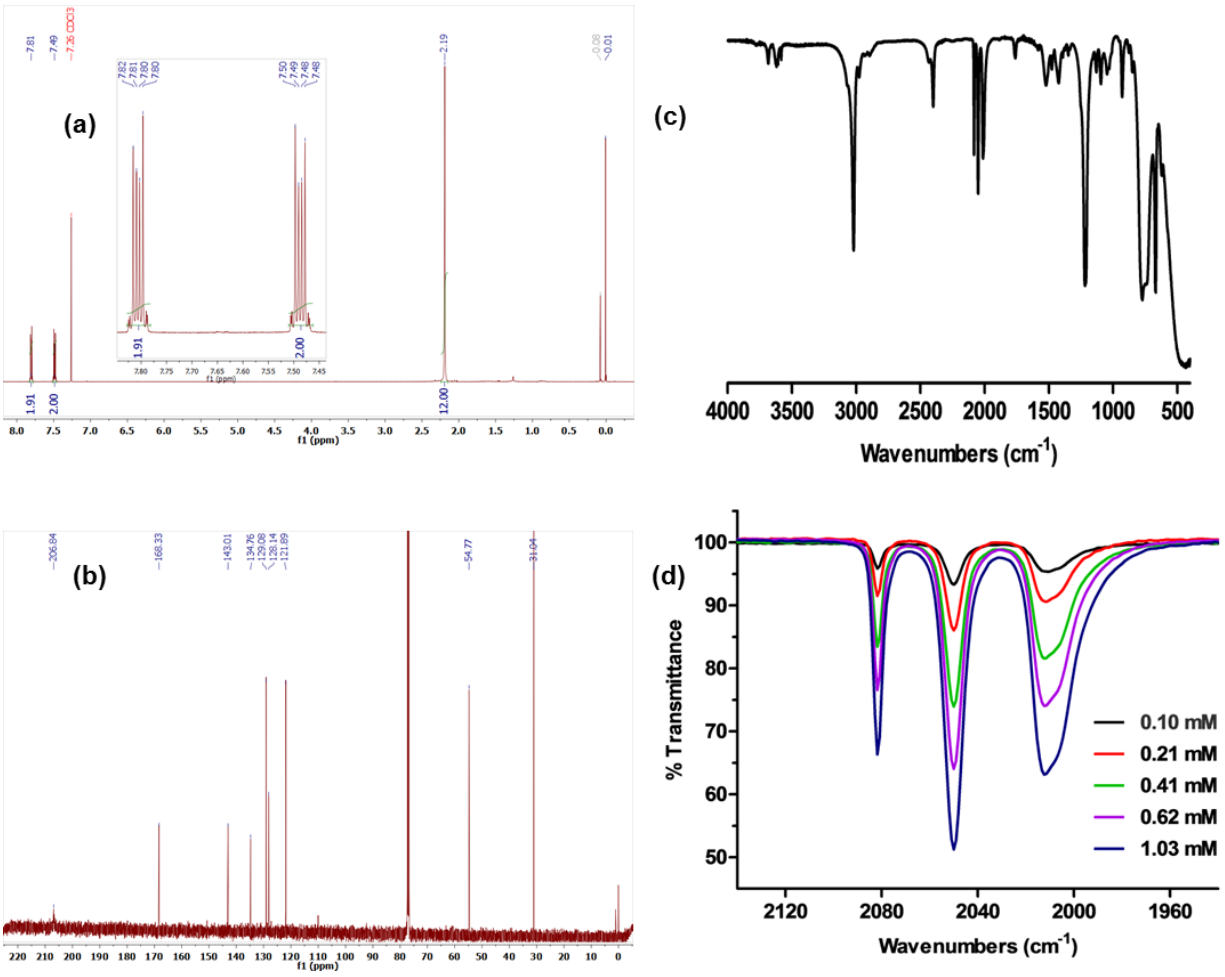

Figure B.3. Spectroscopic Characterization of Metallo-initiator [μ-2,3-(naphthalene-1,4-diylbis(2-bromo-2-methylpropanoate)-dithiolato]bistricarbonyliron 56. **a)** ^{1}H NMR spectrum of **56**, **b)** ^{13}C NMR spectrum of **56**, **c)** full IR spectrum of **56** (solution in $CHCl_3$, thin film on NaCl plates), **d)** Overlay of IR spectra of Fe-CO stretching region for **56** for concentrations 0.1 mM to 1.0 mM. Baselines have been normalized to 100% transmittance Calculated ε values are 173.62 ± 1.92 M^{-1} mm^{-1} (2082 cm^{-1}) ; 280.75 ± 1.11M^{-1} mm^{-1} (2050 cm^{-1}); 186.4 ± 9.9 M^{-1} mm^{-1} (2012 cm^{-1}). Reproduced with permission from *Angew. Chem. Int. Ed.*[12]

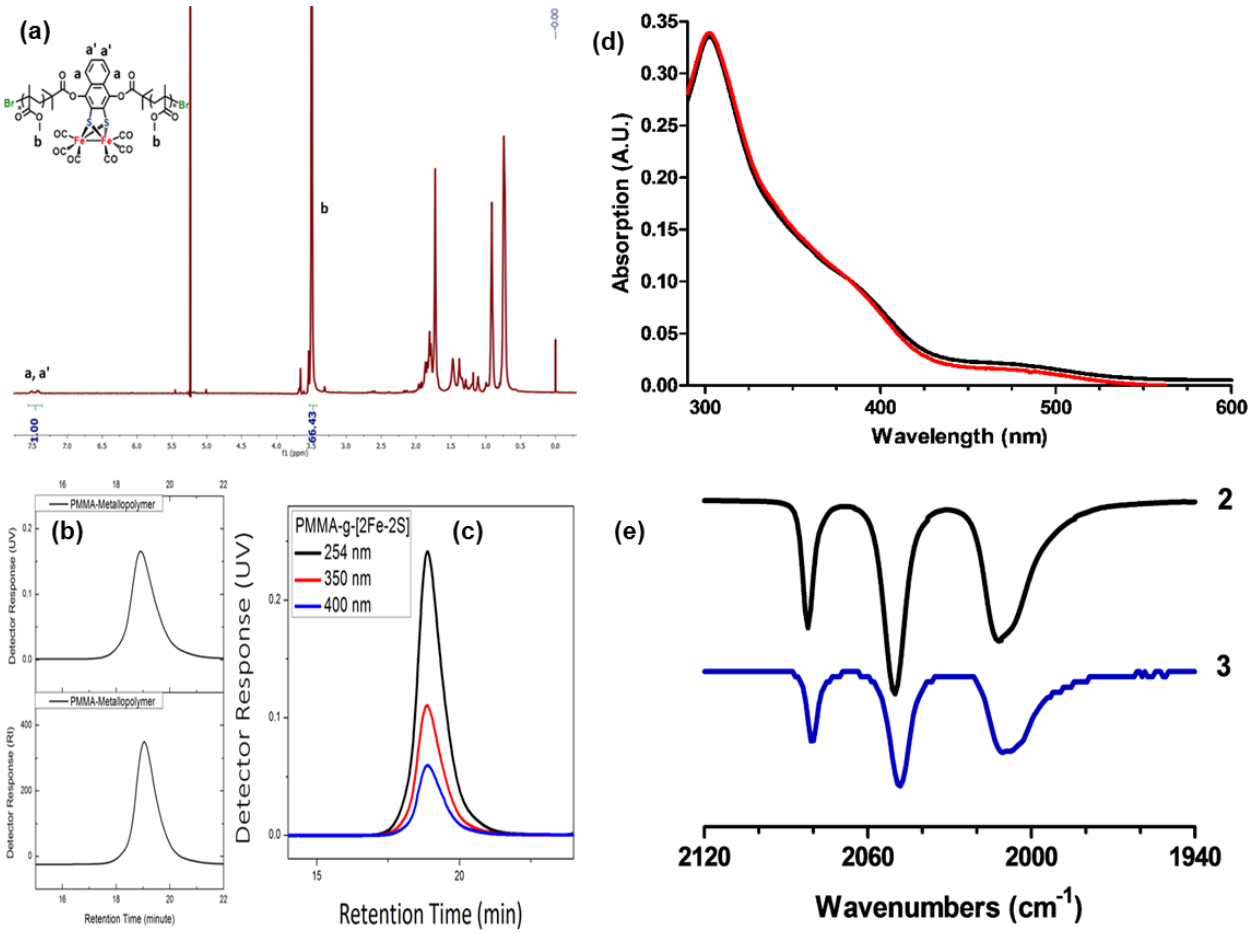

Figure B.4. Spectroscopic Characterization of PMMA-g-[2Fe-2S] 57. **(a)** ^{1}H NMR of **57** in CD_2Cl_2 ($[MMA]_o/[\mathbf{56}]_o/[Cu^{I}Br]_o/[dNbpy]_o$: 200:1:1:2, $M_{n,\ SEC}$ = 11,982 g/mol, $M_{w,\ SEC}$ = 13,229 g/mol, M_w/M_n = 1.10, $M_{n,theo}$ = $[M]_o/[I]_o$*(% monomer conversion)*(MW of the monomer) + (MW of the initiator) = 11,413 g/mol, $M_{n,\ NMR}$ = 9,668 g/mol via end-group analysis), **(b)** THF GPC of 57 with different detection methods (UV vs. refractive index) and with **(c)** UV detector at different wavelengths, **(d)** UV-vis spectra of metalloinitiator **56** (11.2 µM, black trace) and PMMA-*g*-[2Fe-2S] **57** (120 µg/mL) in toluene were found to be identical (PMMA does not absorb at 400 nm, which confirms the selectivity of the SEC UV-vis detection to detect the covalent incorporation of the [2Fe-2S] moiety into metallopolymers), **(e)** Overlay of Fe-CO region of IR spectrum for metalloinitiator **56** (black) and PMMA-*g*-[2Fe-2S] **57** (blue) in $CHCl_3$ (The characteristic Fe-CO vibrational stretching modes in metalloinitiator **56** were observed at 2082 cm^{-1}, 2050 cm^{-1}, and 2012 cm^{-1} and were similarly retained for the PMMA-*g*-[2Fe-2S] **57** metallopolymer with a very slight shift in these peaks to 2080 cm^{-1}, 2050 cm^{-1} and 2011 cm^{-1}, along with a slight broadening of the third peak that allowed for resolution of new peaks at 2007 cm^{-1}). Reproduced with permission from *Angew. Chem. Int. Ed.*[12]

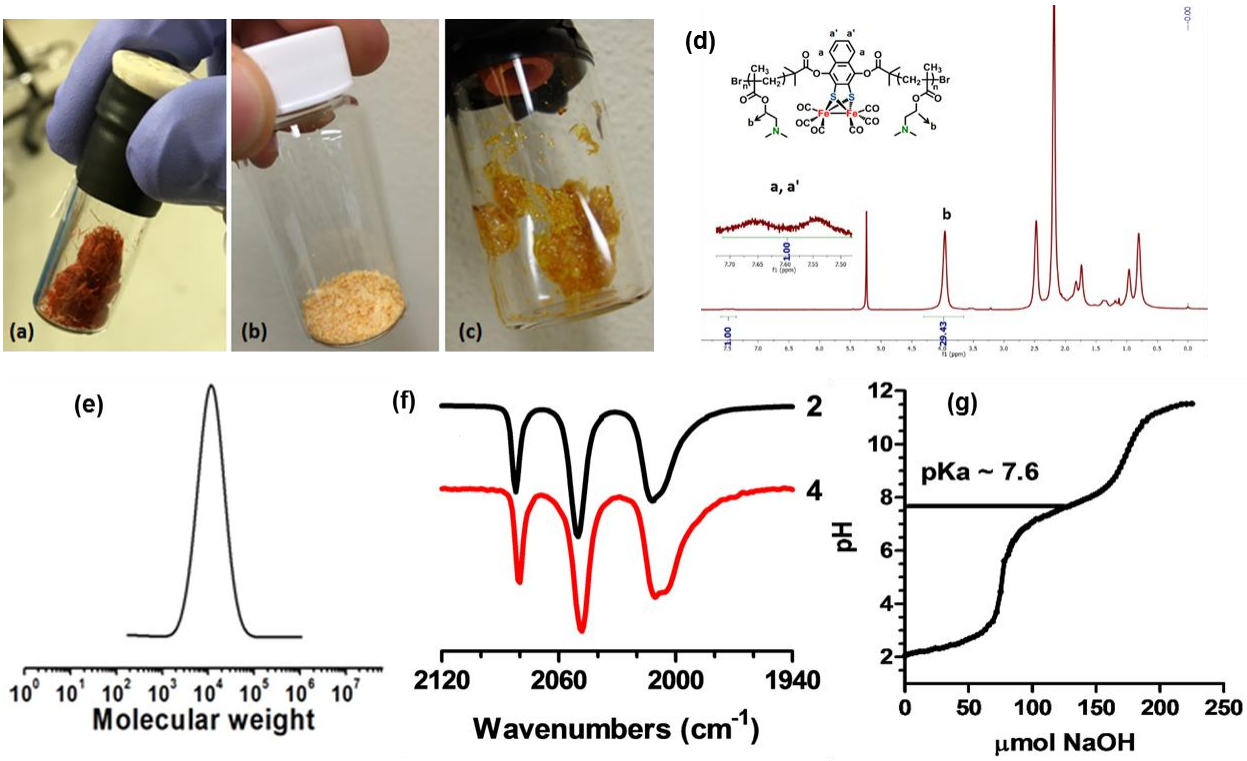

Figure B.5. Characterization of PDMAEMA-g-[2Fe-2S] 58. Appearance of **(a)** metalloinitiator 56**, (b)** PMMA-*g*-[2Fe-2S] **57**, **(c)** PDMAEMA-*g*-[2Fe-2S] **58**. **(d)** ^{1}H NMR of **58** in CD_2Cl_2 ($[DMAEMA]_o/[\mathbf{56}]_o/[Cu^{I}Br]_o/[HMTETA]_o$: 100:1:1:1.5, $M_{n,\ SEC}$ = 12,700, M_w/M_n = 1.27, $M_{n,theo}$ = $[M]_o/[I]_o$*(% monomer conversion)*(MW of the monomer) + (MW of the initiator) = 11,097 g/mol, $M_{n,\ NMR}$ = 10,053 g/mol via end-group analysis), **(e)** DMF GPC of 58 ($[DMAEMA]_o/[\mathbf{56}]_o/[CuBr]_o/[PMDETA]_o$: 100:1:1:1, $M_{n,\ SEC}$ = 9,500 g/mol, M_w/M_n = 1.34, $M_{n,theo}$ = 11,300 g/mol), **(f)** overlay of IR spectra of Fe-CO stretching region for 56 vs. PDMAEMA-*g*-[2Fe-2S] 58, **(g)** titration curve for PDMAEMA-*g*-[2Fe-2S] **58** in 0.2 M KCl. Reproduced with permission from *Angew. Chem. Int. Ed.*[12]

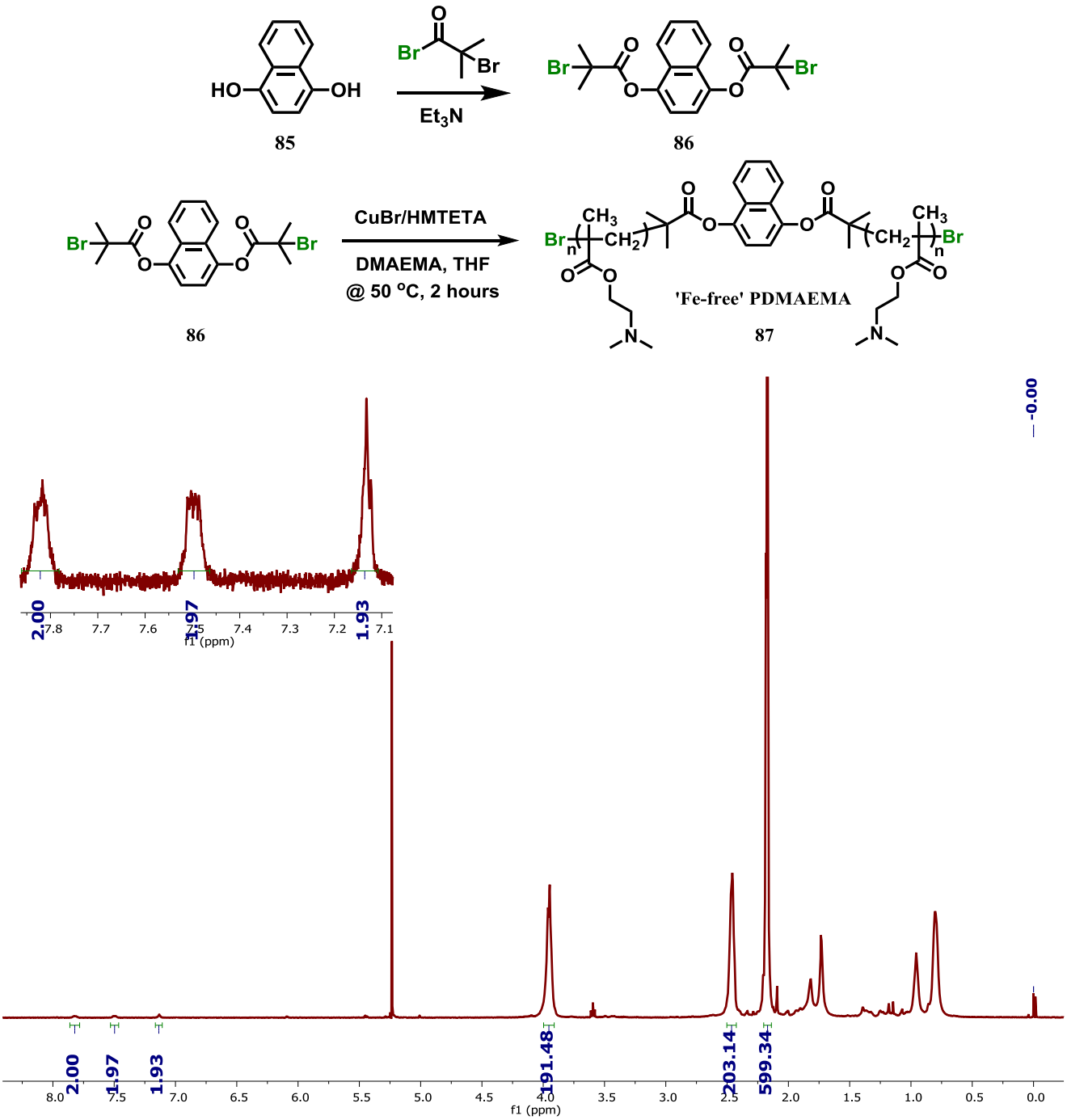

Figure B.6 Synthesis and characterization of Fe-free PDMAEMA 87. Synthetic scheme and ^{1}H NMR spectrum for Fe-free PDMAEMA **87** in CD_2Cl_2. $M_{n,theo}$ = 13,100 g/mol ($M_{n,\ theo}$= %conversion*(M/I)*(MW of DMAEMA) + MW of initiator), $M_{n,\ NMR}$ = 15,500 g/mol (via end group analysis). Reproduced with permission from *Angew. Chem. Int. Ed.*[12]

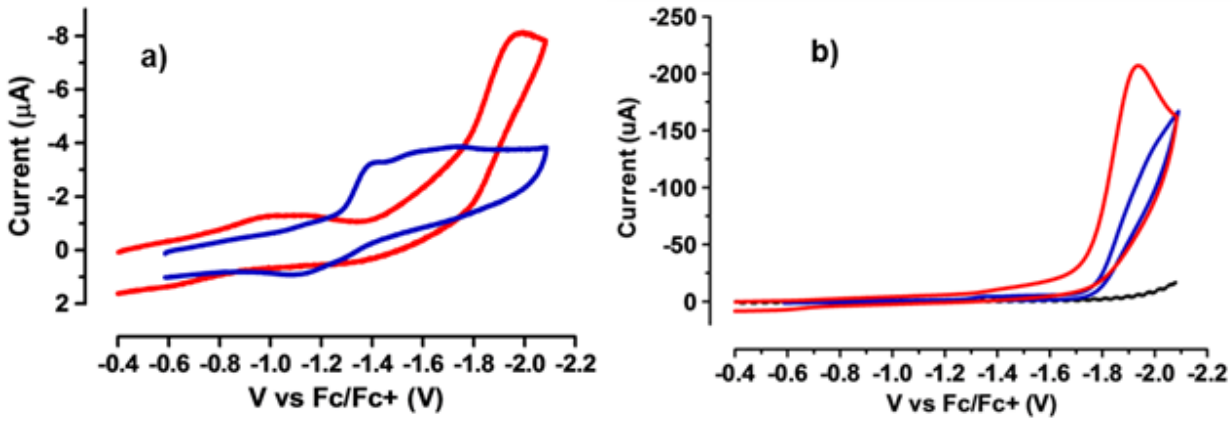

Figure B.7. Cyclic voltammetry of PMMA-*g*-[2Fe-2S] 57, and PDMAEMA-*g*-[2Fe-2S] 58 in acetonitrile. (a) Cyclic voltammetry of **PMMA-*g*-[2Fe-2S] 57** (blue, 2 mg/mL, 100 μM by IR) and **PDMAEMA-*g*-[2Fe-2S] 58** (red, 2.5 mg/mL, 100 μM [2Fe-2S] by IR) in 0.1 M n-Bu_4NPF_6 acetonitrile solution. **(b)** Cyclic voltammetry of PMMA-*g*-[2Fe-2S] **57** (blue, 2 mg/mL, 100 μM by IR), **PDMAEMA-*g*-[2Fe-2S] 58** (red, 2.5 mg/mL, 100 μM [2Fe-2S] by IR), and direct reduction on glassy carbon electrode (A = 0.071 cm^2, black dotted line) in 0.1 M n-Bu_4NPF_6 acetonitrile solution with 50 mM acetic acid. Quiet solution conditions were employed in all experiments. Scan rate 100mV/s, glassy carbon working electrode, platinum wire counter electrode, $Ag/AgNO_3$ reference electrode as described in electrochemical methods. Potentials referenced to an internal Fc/Fc^+ standard. Reproduced with permission from *Angew. Chem. Int. Ed.*[12]

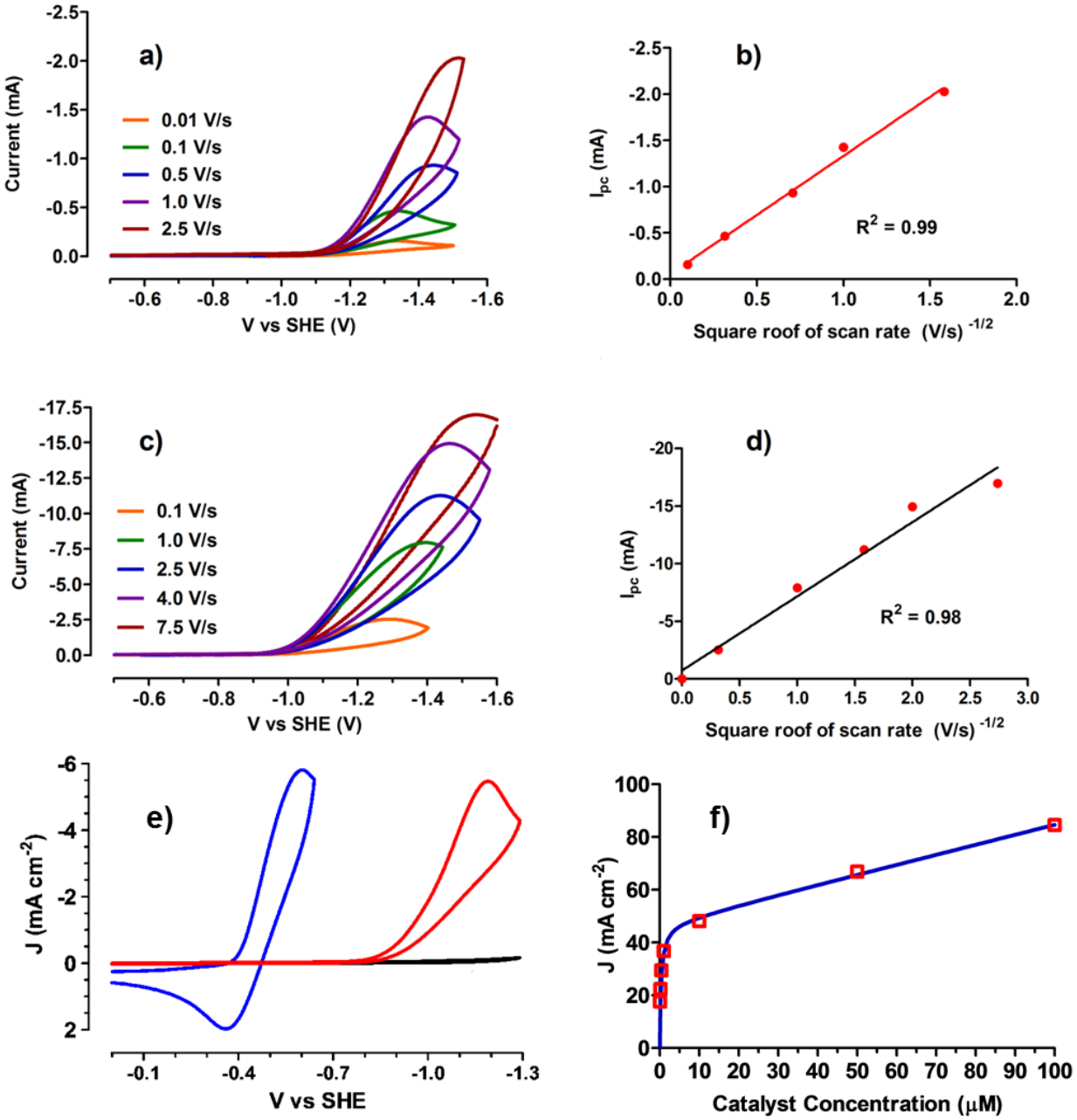

Figure B.8. Representative cyclic voltammetry data in buffered water. (a) Cyclic voltammetry of PDMAEMA-*g*-[2Fe-2S] **58** in 0.1 M pH 7.0 sodium phosphate buffer with added 0.1 M KCl compared at various scan rates. **(b)** Maximum cathodic current (I_{pc}) obtained in data shown in **(a)** plotted vs. square root of scan rate showing the linear dependence of the relationship. I_{pc} was reached at -1.33 V vs SHE for 0.01 and 0.1 V/s, -1.44 V vs SHE for 0.5 V/s, and -1.51 V vs SHE for 1.0 and 2.5 V/s. **(c)** Cyclic voltammetry of 1 μM (0.02 mg/mL) PDMAEMA-*g*-[2Fe-2S] **58** in 1.0 M pH 7.0 tris buffer compared at various scan rates compared with background current (black) for a glassy carbon electrode (ϕ = 3 mm) at 0.1 V/s. **(b)** Maximum cathodic current (I_{pc}) obtained in data shown in **(c)** plotted vs. square root of scan rate showing the linear dependence of the relationship. I_{pc} was reached at -1.24 V vs SHE for 0.1 V/s, -1.37 V vs SHE for 1.0 V/s, -1.42 V vs SHE for 2.5 V/s, -1.45 V vs SHE for 4.0 V/s, and -1.52 V vs SHE for 7.5 V/s. **(e)** Cyclic voltammetry of a Pt disk electrode (ϕ = 1.6 mm, blue line) and a glassy carbon disk electrode (ϕ = 3 mm) in 0.1 M sodium phosphate buffer (pH 7.0) with 0.1 M KCl added. The black trace is the glassy carbon electrode in the absence of catalyst, the red trace is 100 μM (2.0 mg/mL) PDMAEMA-*g*-[2Fe-2S] **58** in the

same solution. **(f)** Peak current density values obtained from cyclic voltammetry of various concentrations of PDMAEMA-*g*-[2Fe-2S] **58** in 1 M tris buffer (pH 7.0) using a glassy carbon electrode (ϕ = 3 mm) at a scan rate of 100 mV/s. The blue dotted line is the fit with a Langmuir-type adsorption isotherm (see text). A platinum wire counter electrode, Ag/AgCl/3M KCl reference electrode we used in all experiments as described in electrochemical methods. Reproduced with permission from *Angew. Chem. Int. Ed.*[12]

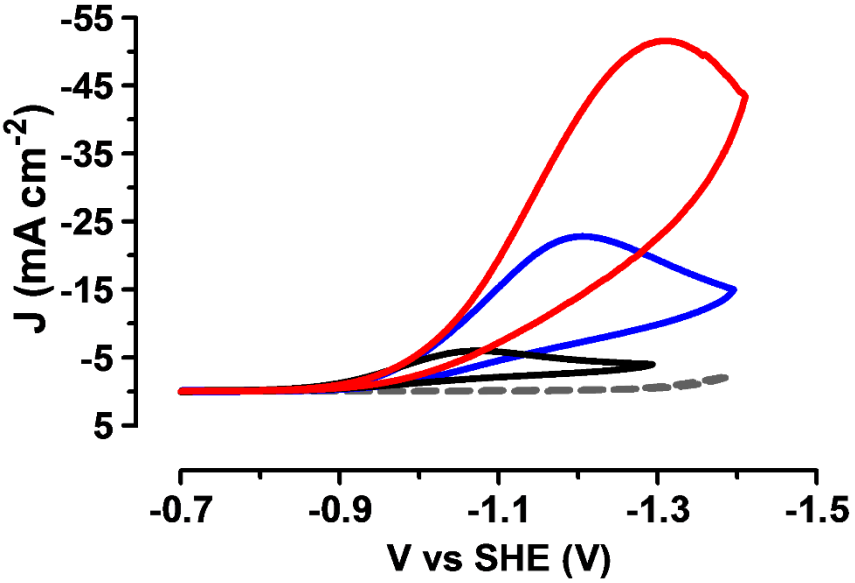

Figure B.9. Cyclic voltammetry comparing HER of 10 μM PDMAEMA-*g*-[2Fe-2S] 4 in different buffer systems at pH 7. Cyclic voltammogram comparing HER current density at a glassy carbon (GC) electrode in pH 7.0 aqueous tris buffer (1.0 M) and a scan rate of 0.1 V/s without catalyst (dashed grey line), in the presence of 10 μM PDMAEMA-g-[2Fe-2S] **58** (red line) in the same solution and using **58** in 1.0 M sodium phosphate buffer (blue line) and 0.1 M sodium phosphate buffer (black line). Metallopolymer mass loading was 0.2 mg/mL when present. Quiet solution conditions were employed. A platinum wire counter electrode, Ag/AgCl/3M KCl reference electrode was used in all experiments as described in electrochemical methods. Reproduced with permission from *Angew. Chem. Int. Ed.*[12]

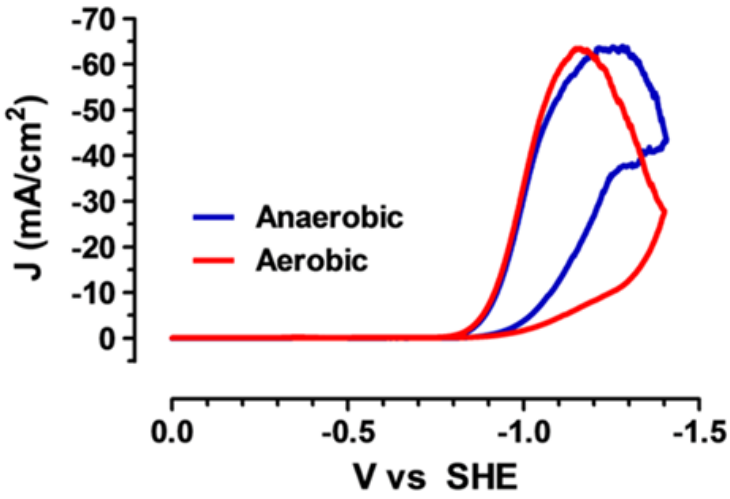

Figure B.10. Comparison of PDMAEMA-*g*-[2Fe-2S] 58 in 1 M Tris Buffer Under Aerobic and Anaerobic Conditions. Cyclic voltammetry of 10 μM (0.2 mg/mL) PDMAEMA-*g*-[2Fe-2S] **58** in 1 M tris buffer (pH 7.0) using a mercury gold amalgam working electrode (ϕ = 3 mm). The red trace shows the current-potential response for the solution saturated with air (21% O_2) and the blue trace was obtained for the oxygen free solution under argon atmosphere. The difference in peak shape shows the effect of the difference in atmosphere, but the same peak current maximum is obtained in both cases. Quiet solution conditions were employed. A glassy carbon counter electrode, Ag/AgCl/3M KCl reference electrode were used. Reproduced with permission from *Angew. Chem. Int. Ed.*[12]

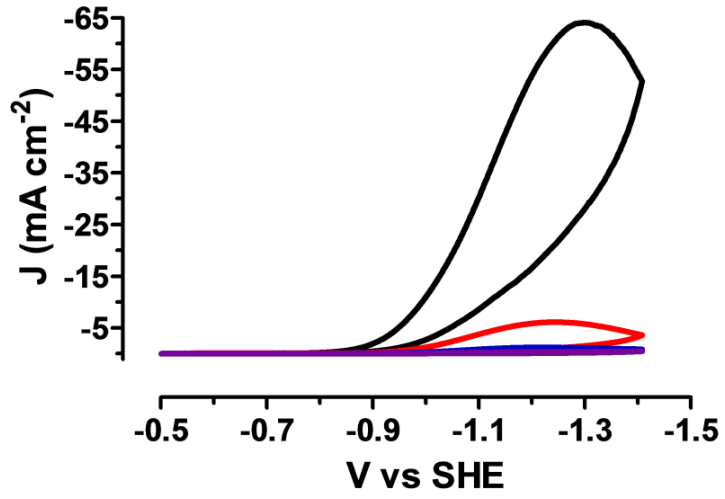

Figure B.11. PDMAEMA-*g*-[2Fe-2S] 58 rinse test. Cyclic voltammetry of 10 μM (0.2 mg/mL) PDMAEMA-*g*-[2Fe-2S] **58** in 1 M tris buffer (pH 7.0, black). The glassy carbon working electrode (ϕ = 3 mm) was removed from the cell, rinsed with de-ionized water and placed in a solution of 1 M tris (pH 7.0) without catalyst. The first scan (red) shows approximately 10% of the peak current seen in catalyst solution. A second scan retains only 20% of the current seen in the first scan, and by the third scan all catalytic activity has been bleached out of the electrode. Quiet solution conditions were employed in all experiments. A glassy carbon counter electrode, Ag/AgCl/3M KCl reference electrode we used. Reproduced with permission from *Angew. Chem. Int. Ed.*[12]

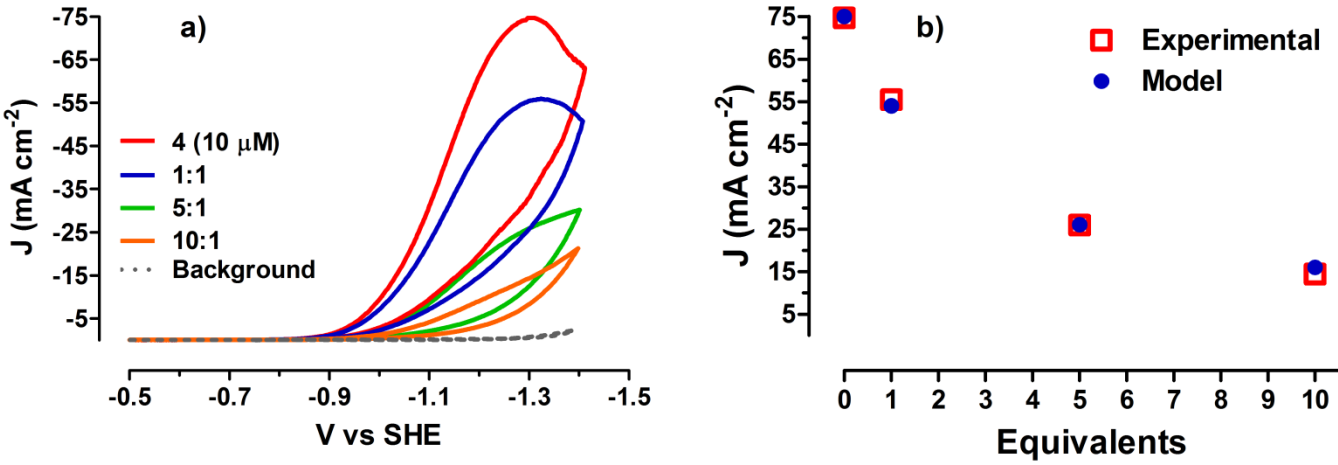

Figure B.12 PDMAEMA-*g*-[2Fe-2S] 58/Fe-free PDMAEMA 7 Competition Experiment. Cyclic voltammetry scans of PDMAEMA-g-[2Fe-2S] 58 (10 μM, 0.2 mg/mL) in pH 7.0 tris buffer (1 M) using a stationary glassy carbon working electrode (ϕ = 3 mm) in an unstirred (quiet) solution under anaerobic conditions (argon atmosphere). The red trace is the catalyst solution (10 mL) without any additional Fe-free PDMAEMA **87**. The blue trace has one equivalent (by mass, 2 mg) of Fe-free PDMAEMA **87** added. The green trace has five equivalents (10 mg total) of Fe-free PDMAEMA added and the purple trace has ten equivalents (20 mg total) of Fe-free PDMAEMA **87** added. The dotted grey line is background current in pH 7.0 tris buffer (1 M) in the potential window of interest in the absence of catalyst. A glassy carbon counter electrode and Ag/AgCl/3M KCl reference electrode were used. b) Catalytic currents obtained in a) (taken at the potential -1.3 V corresponding to the peak maximum of the 10 μM solution of **58**) (red squares) and fit with the Langmuir-based model (blue circles, R2 = 0.999, see text). Reproduced with permission from *Angew. Chem. Int. Ed.*[12]

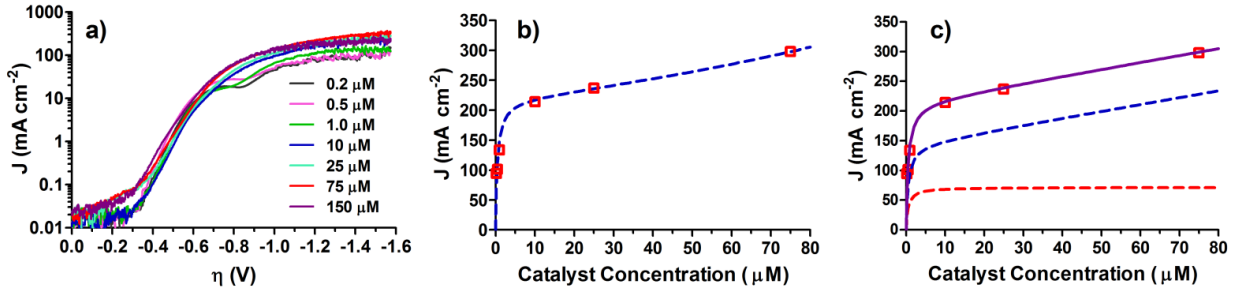

Figure B.13 LSV current density and adsorption isotherms. a) Tafel analysis of linear sweep voltammetry scans of **PDMAEMA-*g*-[2Fe-2S] 58** (various concentrations from 0.2 μM (2 μg/mL mass loading) to 150 μM (1.5 mg/mL mass loading) in pH 7.0 tris buffer (1 M) using a stationary glassy carbon working electrode (ϕ = 3 mm) in a magnetically stirred (1600 rpm) solution under anaerobic conditions (argon atmosphere). A glassy carbon counter electrode and Ag/AgCl/3M KCl reference electrode were used. **b)** Plateau catalytic currents from Tafel plots presented in a) (red squares, taken at -1.45 V as the average current from -1.35 V to the limit of the scan at -1.55 V to reduce the noise from bubble formation). The blue dotted line is the Brunauer-Emmett-Teller (BET) adsorption isotherm model fit to the data. **c)** Plateau catalytic currents (red squares, taken as in **b)**). The blue dashed line is the contribution from the first term (adsorbed catalyst) in the Langmuir adsorption isotherm modeled with equation 8. The red dashed line is the contribution to catalysis from the second term (concentration dependent). The purple line is the fit sum. The parameters are $\boldsymbol{K}_{\mathbf{ads}}$ = 2×10^{9} cm^{3} M^{-1}, $\boldsymbol{i}_{\mathbf{het}}^{\mathbf{max}}$ corresponds to a current density of 144 mA cm^{-2}, x = 8×10^{-3} amp μM^{-1}, and *R* = 1×10^{-2} amp μM^{-1}. Reproduced with permission from *Angew. Chem. Int. Ed.*[12]

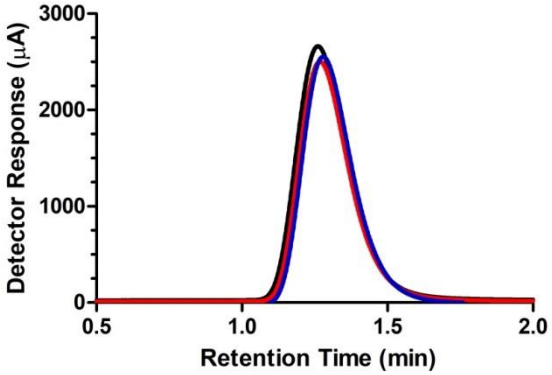

Figure B.14. Faradaic yield comparison. GC chromatogram of median trace for three 250 μL measures of hydrogen manually introduced to the head space of the cell (black), sample from headspace after electrolysis of **PDMAEMA-*g*-[2Fe-2S] 58 (**100 μM, 2 mg/mL) in pH 7.0 tris buffer (1 M) reached a number of coulombs (2.025 C) to produce 250 μL of hydrogen assuming 100% yield (red) using a glassy carbon disk electrode (ϕ = 3 mm), and the same experiment except with electrolysis by a Pt disk electrode (ϕ = 1.6 mm) in pH 7.0 tris buffer (1 M) (ϕ = 1.6 mm, blue). Reproduced with permission from *Angew. Chem. Int. Ed.*[12]

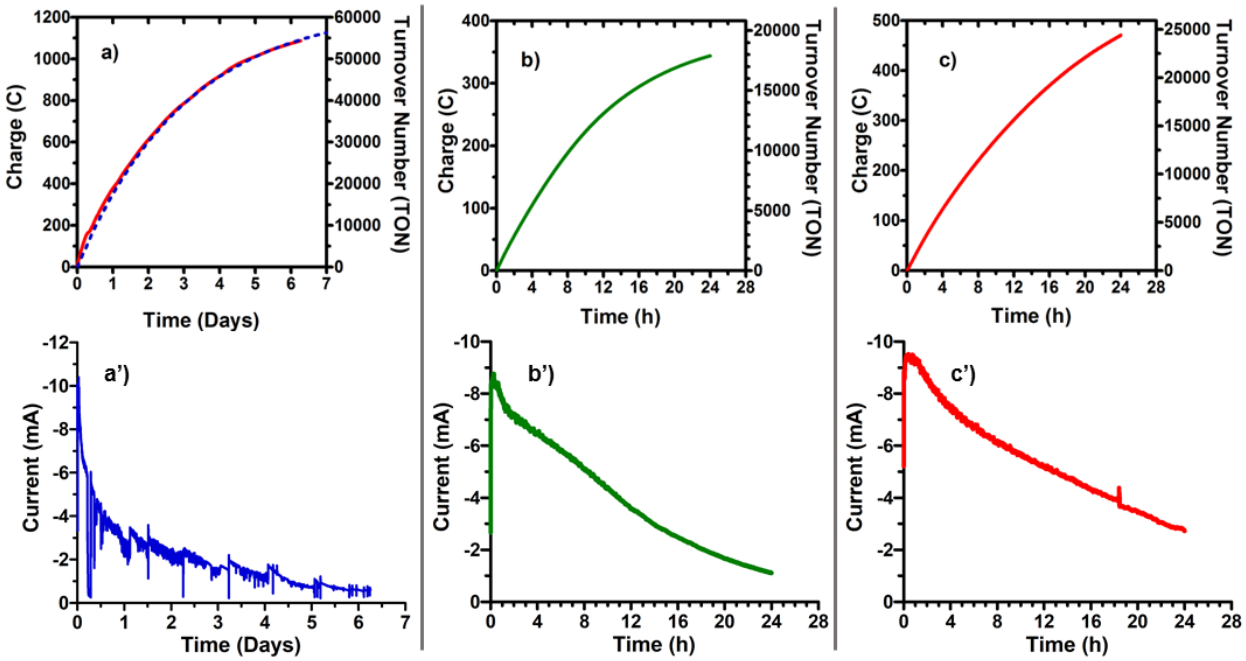

Figure B.15. Controlled Potential Electrolysis Experiments for PDMAEMA-*g*-[2Fe-2S] 58 in Aqueous Media. Charge vs time (**a**)-**c**))and current vs time (**a'**)-**c'**)) data obtained from controlled potential electrolysis of 10 μM PDMAEMA-*g*-[2Fe-2S] **58** in 1 M tris buffer (pH 7) under anaerobic conditions **(a)** and **b)**) and aerobic conditions **c)**. The right y-axis on the charge vs time plots display the charge collected converted to TON based on two electrons used per molecue of hydrogen produced, and 100% Faradaic yield. The glitches in the current response shown in the current vs time graph for **a')** was due to the rapid formation of bubbles on the counter electrode and from restarting the experiment. At times, the formation of oxygen at the counter electrode caused a visible bubble that acted as a barrier between the counter electrode and working CPE solution causing dips in the current. See above section for details of CPE experiments. Reproduced with permission from *Angew. Chem. Int. Ed.*[12]

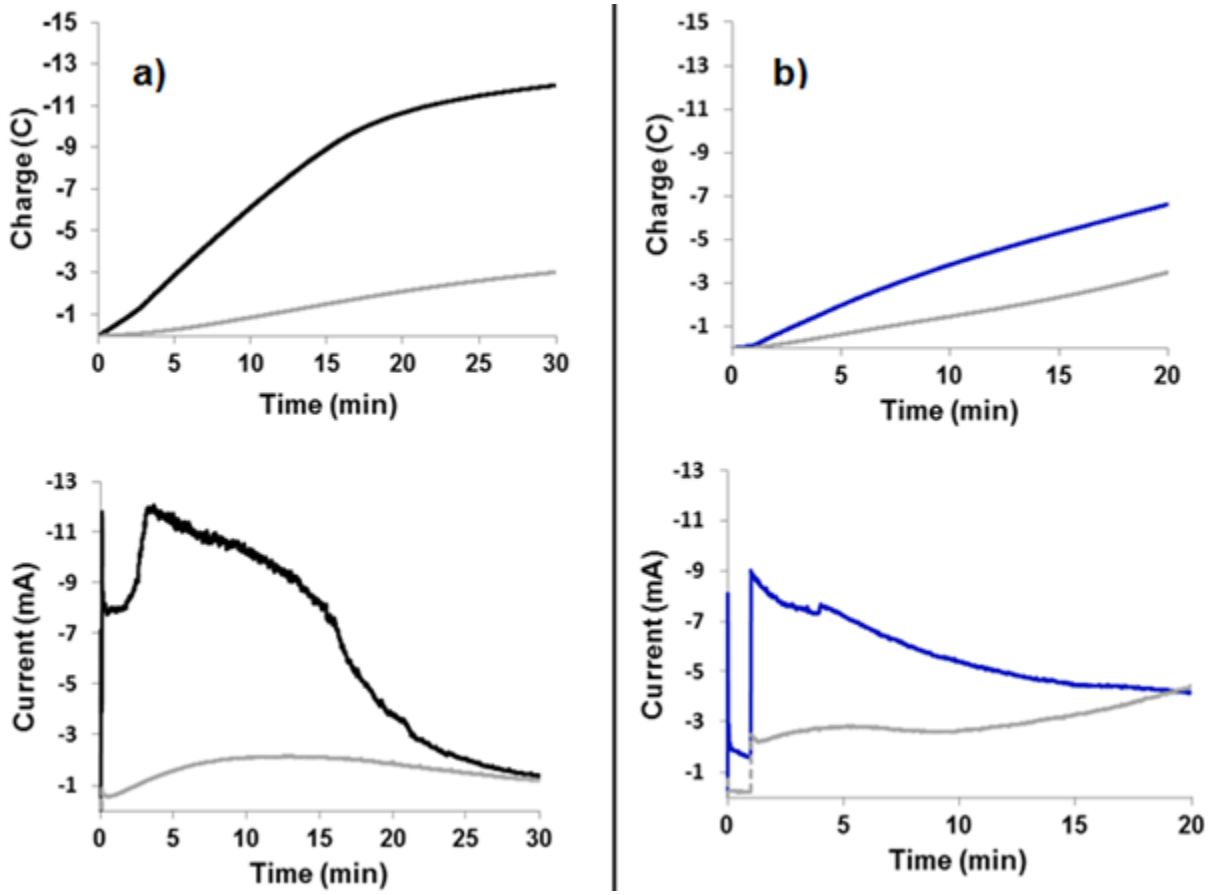

Figure B.16. Controlled Potential Electrolysis Experiments for Metalloinitiator 56 and PMMA-g-[2Fe-2S] in Acetonitrile. Controlled potential electrolysis of metalloinitiator **56** (1 mM) and PMMA-g-[2Fe-2S] **57** (100 μM, 0.2 mg/mL), a) Charge vs. time and current vs. time plots for controlled potential electrolysis of 56 in acetonitrile with 50 mM acetic acid and 0.1 M TBAPF6. The holding potential was -1.72 V vs Fc/Fc+. The black trace is with 100 μM catalyst, the grey trace is background current in the absence of catalyst. b) Charge vs. time and current vs. time plots for controlled potential electrolysis of **57**, in acetonitrile with 50 mM acetic acid and 0.1 M TBAPF6. An initial step of -1.3 V vs Fc/Fc+ was held for 60 seconds before stepping to the final holding voltage of -1.72 V vs Fc/Fc+. The blue trace is with 100 μM catalyst, the grey traces is background current in the absence of catalyst. In both experiments a three chamber cell was employed with medium porosity glass frits separating the three chambers. A 20 ppi vitreous carbon foam working electrode was used in the central chamber. A 100 ppi vitreous carbon foam working electrode was used as the counter electrode in one outer chamber, and a Ag|AgNO3 reference electrode (described on page 9 in our general electrochemical methods section) was in the third chamber. The solution was magnetically stirred at approximately 1600 rpm, and all solutions were degassed via argon sparge (15 minutes) and handled using Schlenk techniques. Reproduced with permission from *Angew. Chem. Int. Ed.*[12]

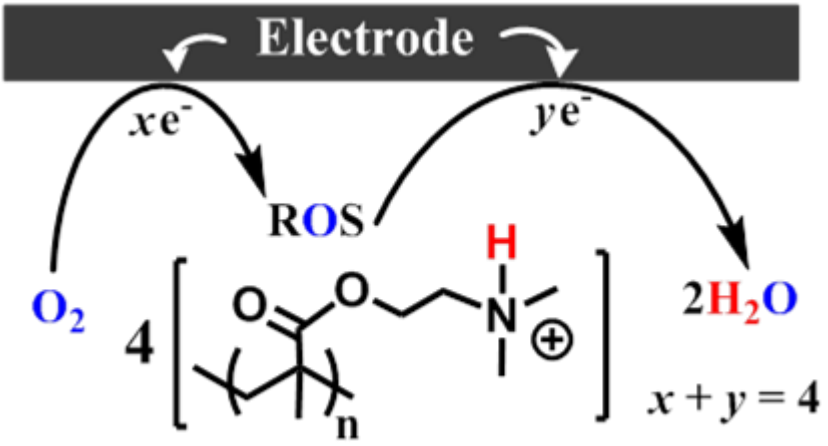

Figure B.17. Possible Mechanism for O2 Protection in PDMAEMA-*g*-[2Fe-2S] 4 System. Reduction of oxygen generates reactive oxygen species (ROS) (which may or may not be protonated before further reduction). These species may decompose the active site. However, this system uniquely favors rapid and complete reduction of O_2 to H_2O because all four electrons can be rapidly supplied by the electrode directly or via the [2Fe-2S] site and protons are available intramolecularly from the manifold protonated amine groups on the PDMAEMA chain thus complete reduction of O_2 occurs before the intermediary ROS can decompose the catalytic site. Adapted for our system from a mechanism proposed in work by Darensbourg and Dey. [14] Reproduced with permission from *Angew. Chem. Int. Ed.*[12]

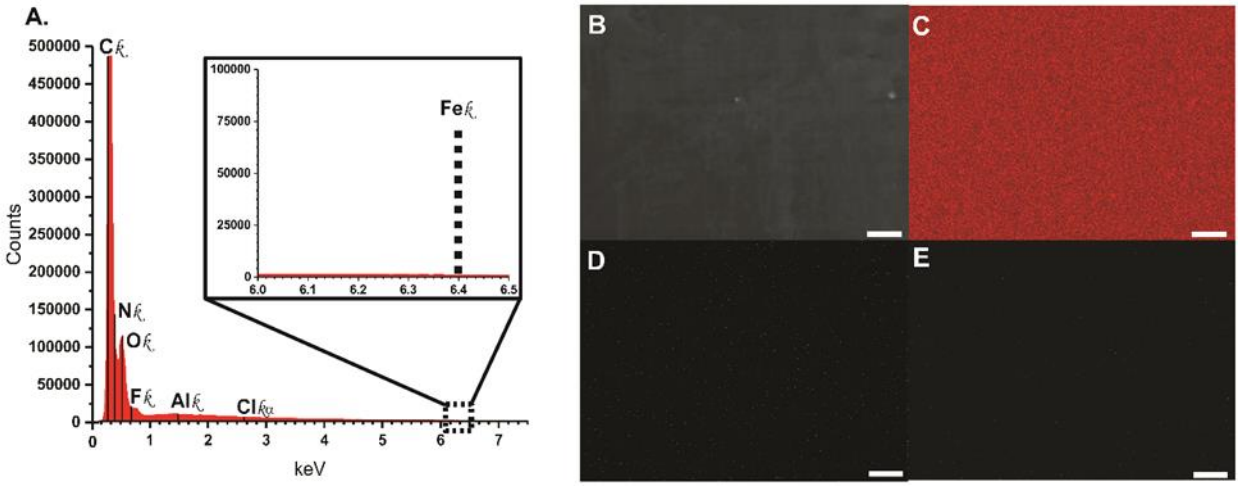

Figure B.18. A) EDX spectrum of pristine glassy carbon electrode. **B)** SEM image of glassy carbon electrode. **C)** EDX mapping of the C Kα line over the imaged region. **D)** EDX mapping of the Cl Kα line over the imaged region. **E)** EDX mapping of the Fe Kα line over the imaged region. All scale bars are 10 microns. Reproduced with permission from *Angew. Chem. Int. Ed.*[12]

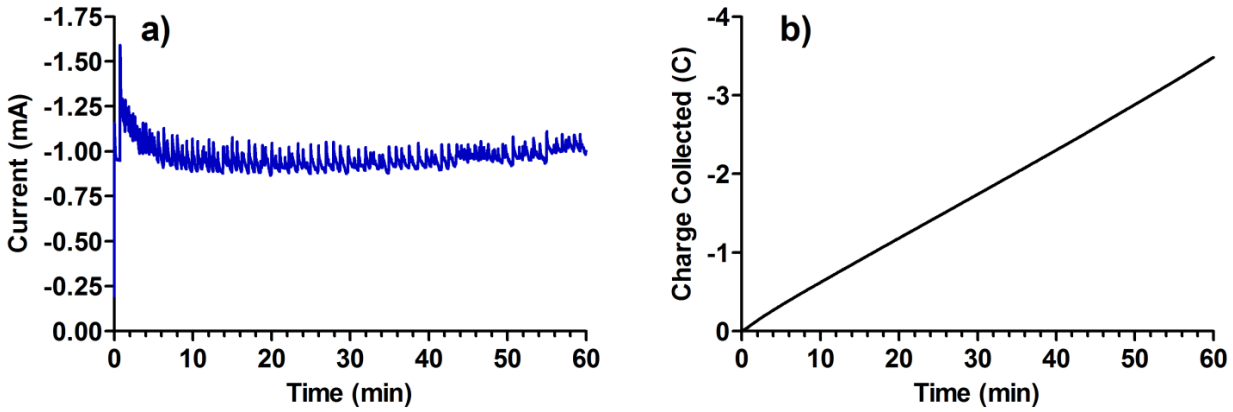

Figure B.19. a) Current vs. time plot and **b)** Charge vs. time plot for 1 hour controlled potential electrolysis (holding potential -0.95 V vs SHE) 1 M Tris buffer (pH 7.0) using a glassy carbon plate electrode under anaerobic conditions before surface analysis of the plate via SEM and EDX. The fluctuating current response in a) is due to bubble formation on the surface of the electrode. Reproduced with permission from *Angew. Chem. Int. Ed.*[12]

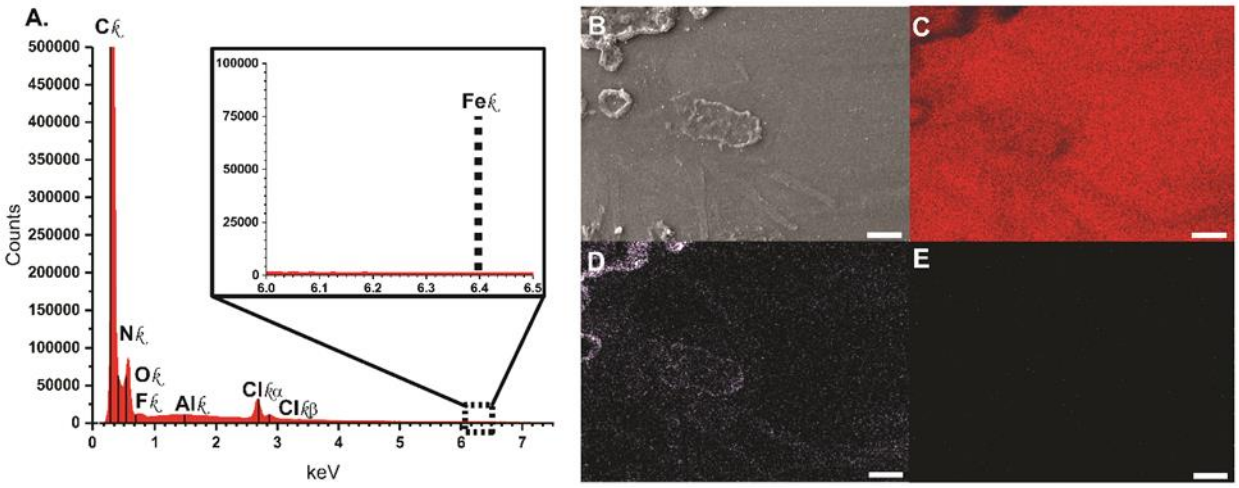

Figure B.20. A) EDX spectrum of glassy carbon electrode post CPE treatment, and prior to rinsing. **B)** SEM image of the electrode. **C)** EDX mapping of the C K_α line over the imaged region. **D)** EDX mapping of the Cl K_α line over the imaged region. **E)** EDX mapping of the Fe K_α line over the imaged region. All scale bars are 10 microns. Reproduced with permission from *Angew. Chem. Int. Ed.*[12]

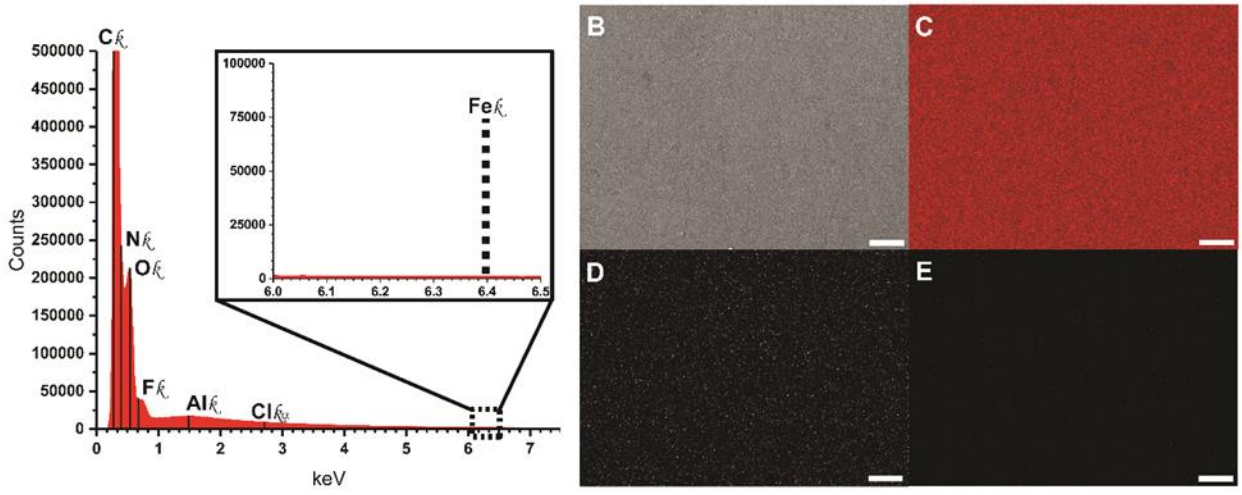

Figure B.21. A) EDX spectrum of glassy carbon electrode post CPE treatment, and post rinsing with DI water. **B)** SEM image of the eletrode. **C)** EDX mapping of the carbon K_α line over the imaged region. D) EDX mapping of the Cl K_α line over the imaged region. **E)** EDX mapping of the Fe K_α line over the imaged region. All scale bars are 10 microns. Reproduced with permission from *Angew. Chem. Int. Ed.*[12]

Element	**Pristine Electrode**		**Post CPE Electrode (No Rinse)**		**Post CPE Electrode (Rinsed)**	
	Weight %	**Atomic %**	**Weight %**	**Atomic %**	**Weight %**	**Atomic %**
C K_α	52.08	57.09	40.94	45.96	41.03	46.04
Cl K_α	0.03	0.01	1.68	1.17	0.03	0.01
Fe K_α	0.04	0.01	0.01	0.00	0.03	0.01

Table B.1. . Summarized EDAX eZAF Smart Quant data for elements highlighted in **Figures B18, B20, and B21.** Weight % and Atomic % determined from a 100 micron x 100 micron section of the electrode surface at an accelerating voltage of 15.0 kV and beam current 13.0 nA. Reproduced with permission from *Angew. Chem. Int. Ed.*[12]

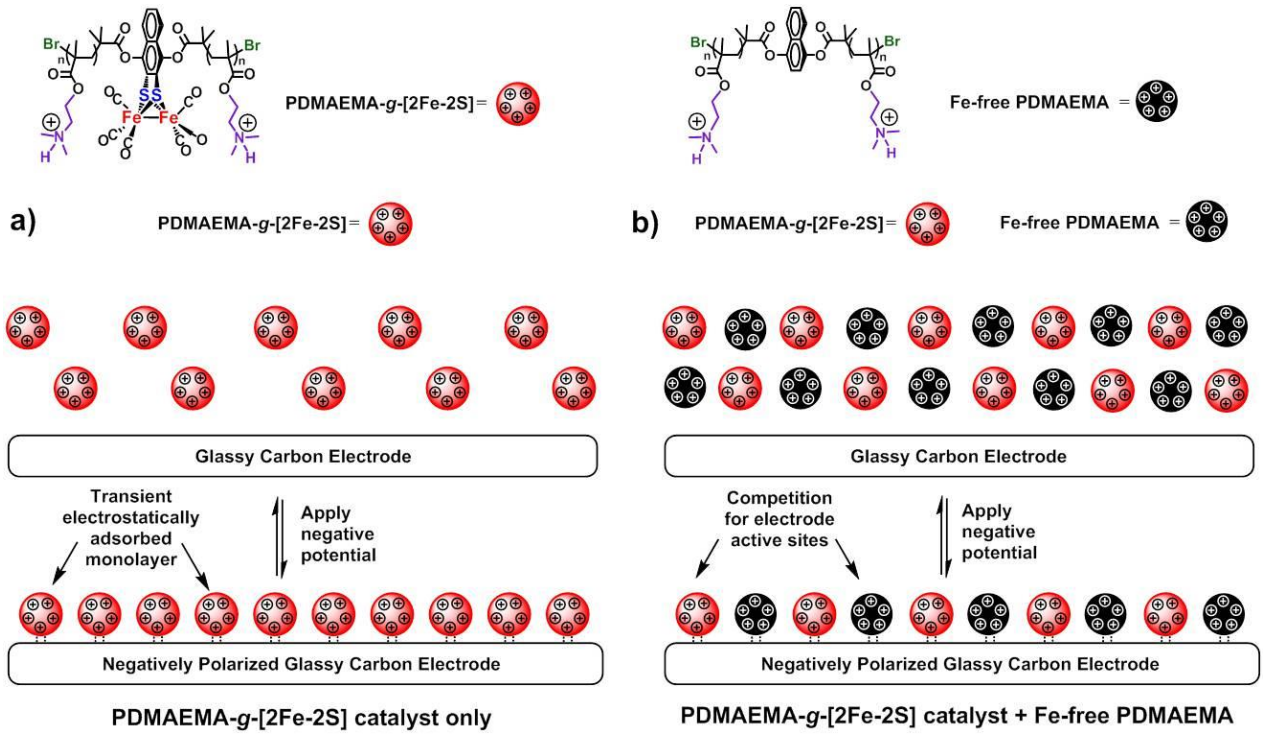

Figure B.22 Conceptual Scheme of Transient Electrostatically Adsorbed Monolayer Species. A spherical globule conformation of **PDMAEMA-*g*-[2Fe-2S] 58** is used to minimize polymer size and maximize polymer concentration on the surface in order to estimate a lower bound of k_{obs}. As shown in the literature, the background electrolyte screens the charges on the polymer chain and decreases the inter- and intrachain repulsion, such that a more compact conformation and adsorbed layer can be formed on the oppositely charged surface in high salt concentration.[249,252] Panel **a)** shows the electrostatic adsorption effect with only **PDMAEMA-*g*-[2Fe-2S] 58** in tris solution (1 M, pH 7.0) and panel **b)** shows the competition experiment where Fe-free PDMAEMA **87** is added to the same concentration of **PDMAEMA-*g*-[2Fe-2S] 58** as in **a)** to compete for active sites on the electrode surface. Reproduced with permission from *Angew. Chem. Int. Ed.*[12]

Appendix C - Supporting Information for Macromolecular Engineering the Outer Coordination Sphere of [2Fe-2S] Metallopolymers to Enhance Catalytic Activity for H_2 Production

William P. Brezinski,[a] Metin Karayilan,[a] Kayla E. Clary,[a] Liye Fu,[b] Krzysztof Matyjaszewski,[b] Dennis H. Evans,[c] Dennis L. Lichtenberger,*[a] Richard S. Glass,*[a] and Jeffrey Pyun*[a,d]

[a] Department of Chemistry and Biochemistry, University of Arizona, 1306 E. University Blvd., Tucson, Arizona 85721, United States

[b] Department of Chemistry, Carnegie Mellon University, 4400 Fifth Avenue, Pittsburgh 151213, United States

[c] Department of Chemistry, Purdue University, 560 Oval Drive, West Lafayette, Indiana 47907, United States

[d] Department of Chemical and Biological Engineering, Program for Chemical Convergence for Energy & Environment & the Center for Intelligent Hybrids, Seoul National University, Seoul 151-744, Korea

1. Experimental

a. Materials and Characterization

Unless otherwise noted, solvents were used as received from Fischer Scientific as ACS grade and used without further purification. $Fe_2S_2(CO)_6$ was prepared according to literature procedures[149] and sublimed before use. $Fe(CO)_5$ (99.5 %,Alfa-Aesar), NaOH (EMD, ACS grade), NH_4Cl (EMD, ACS grade), S_8 (Mallinckrodt, sublimed), Na_2SO_4 (EMD, ACS grade), $NaCNBH_3$ (Sigma-Aldrich, 95%), $Me_3NO{\bullet}2H_2O$ (Sigma-Aldrich), Celite 545(VWR), and Silica Gel (SiliaFlash F60, 230-400 mesh, Silicycle) were used as received without further purification. 1,4-naphthoquinone (Alfa-Aesar, 97%, up to 5% H_2O) was passed through a silica gel column with diethyl ether before use. Triethylamine (EMD, 99.5%) was distilled from KOH then stored on activated 3Å linde-type molecular sieves under argon. α-Bromoisobutyryl bromide (BIBB, Sigma-Aldrich, 98%) was initially used as received but found to decompose over time, requiring vacuum distillation (10 torr, 55^{o}C) once it had taken on a yellow color. KCl (EMD, ACS grade) was recrystallized twice from hot 0.1 M HCl before use. Oligo(ethyleneglycol) methyl ether methacrylate (OEGMA, Mn: 475 g/mol) (Aldrich) and 2-(Dimethylamino)ethyl methacrylate (DMAEMA) (Aldrich, 98%) were purified by passing through a short column of neutral alumina to remove inhibitors. Copper(I) bromide (Cu(I)Br) (Aldrich, 98%) was purified by stirring overnight in glacial acetic acid, filtering, washing with ethanol and ethyl ether, and drying under vacuum before use. Alternatively, Cu(I)Br was purified by precipitation from 48% HBr followed by washing with de-ionized water, ethanol, and diethyl ether sequentially then drying under vacuum, as described in *e-Eros Reagents for Organic Chemistry.*[152] *N,N,N',N'',N''*-Pentamethyldiethylenetriamine (PMDETA) (Aldrich, 99%), 1,1,4,7,10,10-Hexamethyltriethylenetetramine (HMTETA) (Aldrich, 97%), Dowex 50WX8-200 ion exchange resin (Aldrich), alumina (Al_2O_3, activated, neutral, 50-200 μm, 60 Å, Acros Organics), tetrahydrofuran (THF) (EMD, GC grade), dichloromethane (DCM) (ACS grade), methanol (ACS grade, EMD), hexanes (ACS grade, EMD), and toluene (ACS grade, EMD) were used as received. For the synthesis of **56** α-Bromoisobutyryl bromide (BIBB) (Aldrich, 98%) was distilled under reduced pressure, and triethylamine (NEt_3) (EMD, ACS reagent grade) was distilled at atmospheric pressure under argon. ^1H and ^{13}C nuclear magnetic resonance (NMR) spectra were obtained using a Bruker DRX 500 MHz or a Bruker Avance III 400 MHz spectrometer. Chemical shifts were referenced to $Si(Me)_4$ (δ 0.00 ppm) for ^1H NMR and the $CDCl_3$ solvent peak (δ 77.0 ppm) for ^{13}C NMR. MestReNova 10.0 software was used for spectral processing. IR spectra were obtained on a Nicolet Avatar 360 FT-IR with EZ-OMNIC software for H_2O and CO_2 correction. Resolution set to 0.964 cm^{-1} for all IR spectra. During quantification of molar absorptivity (ε) for Fe-CO stretches in **56** and resulting metallopolymers 128 scans were used. A Fisher Scientific FT-30 30specRFL500700*L IRSEC cell with 0.5 mm Teflon spacer (total path length = 1 mm) and CaF_2 window (Alfa-Aesar) was used for quantitative IR measurements. Determination of ε for Fe-CO's was performed by preparing 10 mL of *ca.* 1.0 mM **56** in $CHCl_3$ using volumetric glassware. This stock was diluted to *ca.* 0.1 mM, 0.2 mM, 0.4 mM, and 0.6 mM in four separate 5 mL volumetric flasks using a 1 mL syringe to transfer the stock solution, then diluting to volume. The measurement was performed in triplicate and R^2 values for each linear regression were 0.98 or better. Qualitative IR was performed using solutions in $CHCl_3$ in thin films between NaCl plates (Fisher Scientific). Spectral processing and graphing were performed using Microsoft Excel,

Origin Pro 8.0, and Prism Graph Pad 5.0. Molecular weight (M_n) and molecular weight distribution (M_w/M_n) of metallopolymers were determined by gel permeation chromatography (GPC). Molecular weight and molecular weight distribution data for PDMAEMA metallopolymers and PDMAEMA-*random*-PEGMA metallocopolymers were collected by using GPC with a Waters 515 HPLC pump, Wyatt Optilab refractive index detector, and PSS GRAM columns containing polyester copolymer networks with 50 mM LiBr DMF solution as eluent phase at a flow rate of 1mL/min at 50 °C. The GPC analyses for PEGMA metallopolymers were performed in a THF mobile phase with a Waters 1515 isocratic pump running three 5-µm PLgel columns (Polymer Labs, pore size 10^4, 10^3 and 10^2 Å) at a flow rate of 1.0 mL/min at 35 ^oC with a Waters 2414 differential refractometer and a Waters 2487 dual-wavelength UV-vis spectrometer. Molar masses were calculated using the Waters Empower software, calibrated against low polydispersity linear PMMA and polystyrene (PS) standards. pH measurements made using Fischer Scientific Accumet AE150 pH meter calibrated with pH 4.01, 7.00, and 10.01 standards (Sigma-Aldrich).

b. Synthesis of [2Fe-2S]-Initiator [µ-2,3-(naphthalene-1,4-diylbis(2-bromo-2-methylpropanoate)dithiolato]bistricarbonyliron (56)

i. Synthetic Procedure. The starting material was synthesized as previously reported[192] was analyzed via ^{1}H NMR to determine what mol % had been oxidized to the quinone product by comparing the integral values for the protons at the C_5 and C_6 positions in both compounds. The sample was found to contain 40% quinone catalyst, so 0.4 equivalents of reducing agent were used. $NaCNBH_3$ (2.26 mg, 0.036 mmol) was weighed on a micro balance and added to a dry, argon filled Schlenk flask. **56** (45 mg, 0.090 mmol) was added to the flask. The flask was then evacuated and filled with argon twice. Anhydrous, deoxygenated THF (2 mL) was added to the flask. The solution was stirred at room temperature in the dark for 2 hours. NEt_3 (75 µL, 0.54 mmol) was then added via micro syringe and the solution was stirred for 20 minutes. BIBB (30 µL, 0.22 mmol) was added via micro syringe and the solution was stirred at room temperature. TLC indicated complete consumption of the starting material 2.25 hours after the addition of BIBB. The solution was filtered through a short silica plug in a Pasteur pipette to remove precipitate. 5 mL of DCM was used to rinse the column until no red color was visible in the eluent. The combined organics were concentrated on rotary evaporator (23 ^oC, *ca.* 200 torr) to a red/orange solid. The solid was redissolved in minimal DCM and purified via column chromatography (SiGel, pack with 15% DCM in hexane, elute with 25-30% DCM in hexane). The pure compound was obtained as a red band which yielded 63 mg (0.079 mmol, 87%) powdery orange solid upon removal of solvent. Subsequent syntheses produced isolated yields between 85-90% providing the BIBB reagent had not decomposed. Crystals suitable for electrochemical studies and synthesis of metallopolymers were obtained by dissolving **56** in toluene (157 mg in 1.57 mL) in a narrow Schlenk tube. This solution was layered freeze, pump, thawed three times to degas, then the cold solution was layered with Ar sparged methanol (12 mL). The solution was allowed to sit undisturbed for 72 hours, the supernatant liquid was removed via syringe and the crystals were transferred to an M porosity fritted glass funnel. Subsequent washing with ice cold methanol (3 x 0.5 mL) and drying on the funnel gave 67 mg (43% recovery) of dark red needles. ^{1}H NMR: $CDCl_3$, 500 MHz, 298 K δ (ppm) 7.81 (2H, dd J = 6.5, 3.4 Hz) 7.49 (2H, dd J = 6.5, 3.4

Hz), 2.19 (12H, s). ^{13}C NMR: $CDCl_3$, 125 MHz, 298 K δ (ppm) 206.8 (OC-Fe), 168.3 (C=O), 143.0 (C1,4-O), 134.8 (C,2,3-S), 129.1 (C6,7-H), 128.1 (C9,10), 121.9 (C5,8-H), 54.8 (CH-Br), 31.0 (CH_3). IR ($CHCl_3$, thin film on NaCl): 3688 cm^{-1} (w), 3619 cm^{-1} (w, Csp^2-H), 3154 cm^{-1} (w, Csp^2-H), 3019 cm^{-1} (vs, Csp^2-H), 2976 cm^{-1} (w, Csp^3-H), 2082 cm^{-1} (Fe-CO, s), 2050 cm^{-1} (Fe-CO, s), 2012 cm^{-1} (Fe-CO, s) 1760 cm^{-1} (C=O ester, w), 1522 cm^{-1} (C=C, w), 1423 cm^{-1} (C-H, w), 1210 cm^{-1} (C-O, vs)

ii. ^1H NMR and ^{13}C NMR Spectra of Metalloinitiator (56)

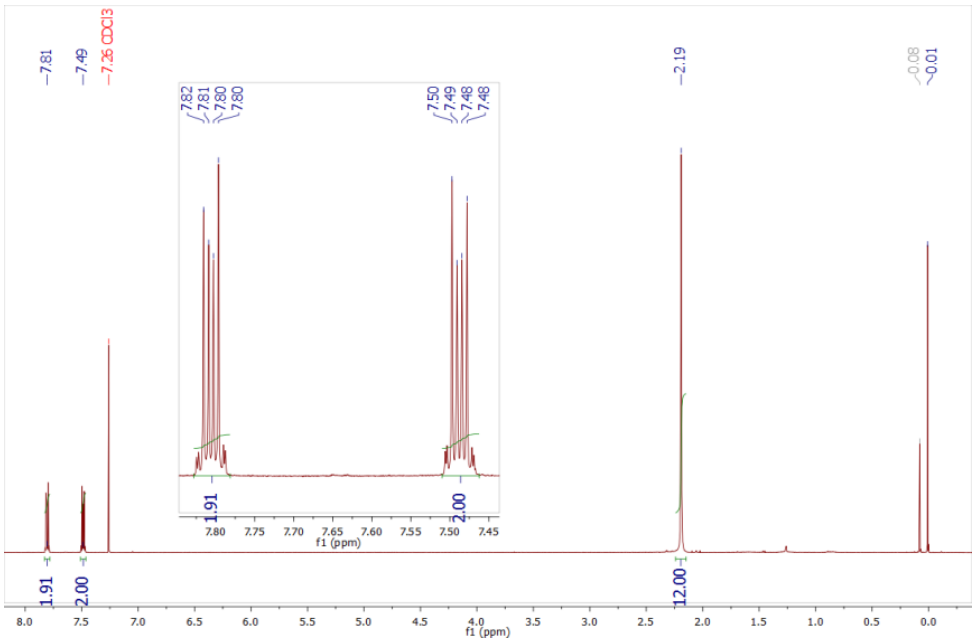

Figure C.1. ^1H NMR spectrum of **56**

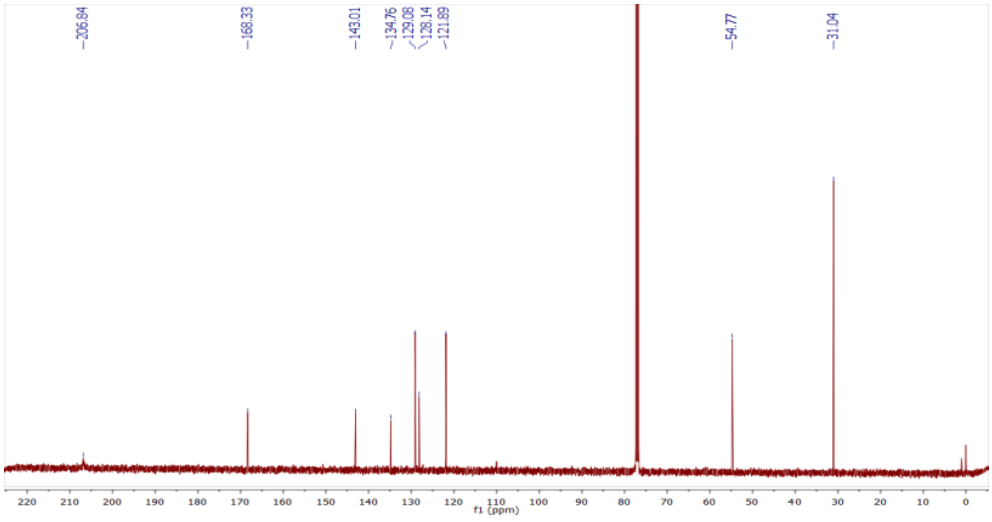

Figure C.2. ^{13}C NMR spectrum of **56.**

iii. IR Spectra of (56)

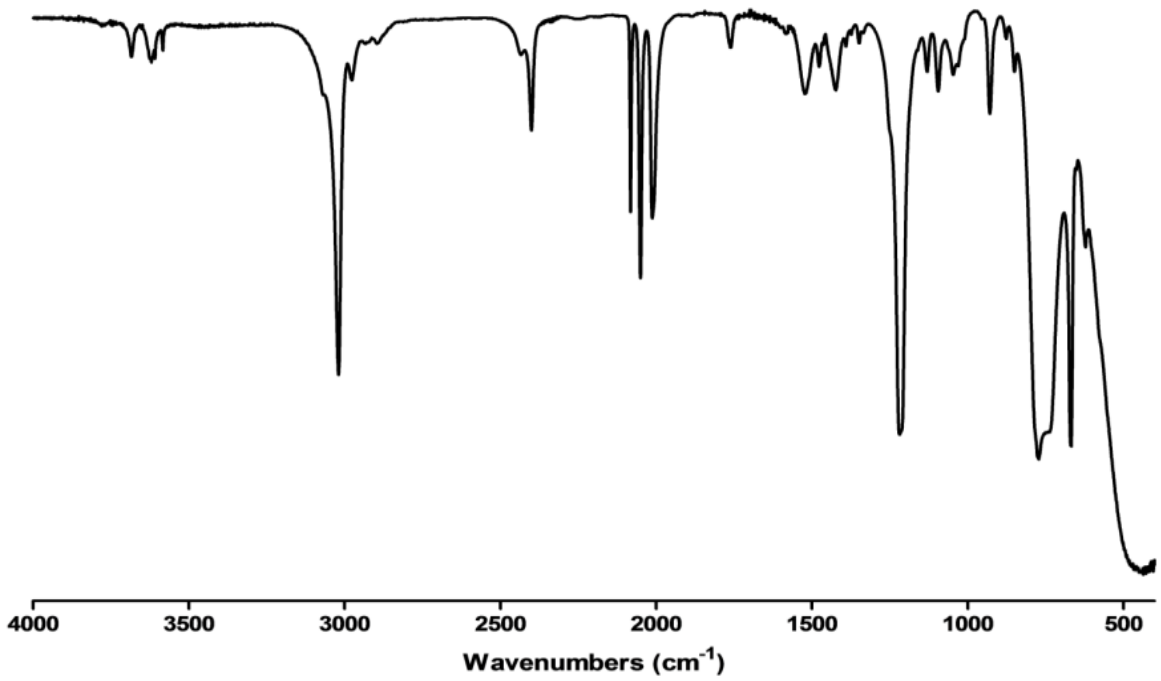

Figure C.3. Full IR spectrum of **56** (solution in $CHCl_3$, thin film between NaCl plates)

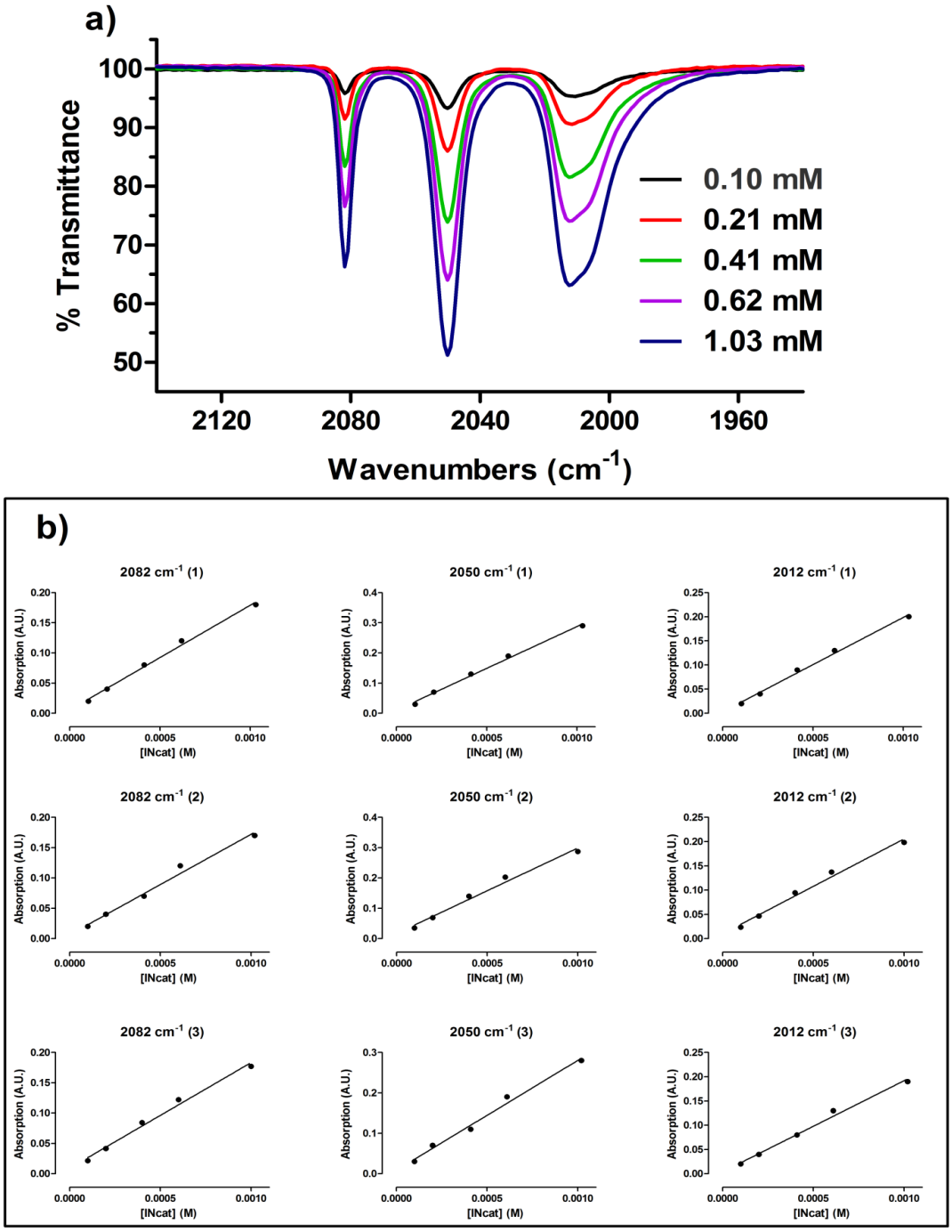

Figure C.4. a) Overlay of IR spectra of Fe-CO stretching region for 56 for concentrations 0.1 mM to 1.0 mM. Baselines have been normalized to 100% transmittance. **b)** Linear regression plots for each Fe-CO peak in 56 generated from above spectra. Calculated ε values are 173.62 ± 1.92 M-1 mm-1 (2082 cm-1); 280.75 ± 1.11M-1 mm-1 (2050 cm-1); 186.4 ± 9.9 M-1 mm-1 (2012 cm-1).

iv. X-ray Crystallography of Metalloinitiator 56

X-ray Diffraction Analysis: Data was collected at the University of Arizona X-ray Diffraction Facility. Crystals were mounted onto a *MiTeGen* micromount under a protective film of Paratone® oil and diffraction data for all crystals were measured using a Bruker Kappa APEX II DUO diffractometer, with graphite-monochromated Mo-Kα radiation (λ = 0.71073 Å) generated by a sealed tube, and an APEX II CCD area detector. The diffractometer was fitted with an Oxford Cryostream low-temperature device and data sets were collected using the *APEX2* software package (Bruker AXS Inc., Madison, WI, 2007). The data were corrected for absorption effects using a multi-scan method in *SADABS* (Sheldrick, G. M. University of Göttingen, Germany 1997). CCDC 1577155 contains the supplementary crystallographic data for this paper. These data are provided free of charge by The Cambridge Crystallographic Data Centre. All structures were solved by direct methods (*SHELXS-97*), and developed by full least squares refinement based upon F^2 (*SHELXL*)[253] interfaced *via X-Seed*[254] and *OLEX2*[158] Crystallographic figures were prepared using *Mercury* (Version 3.9).

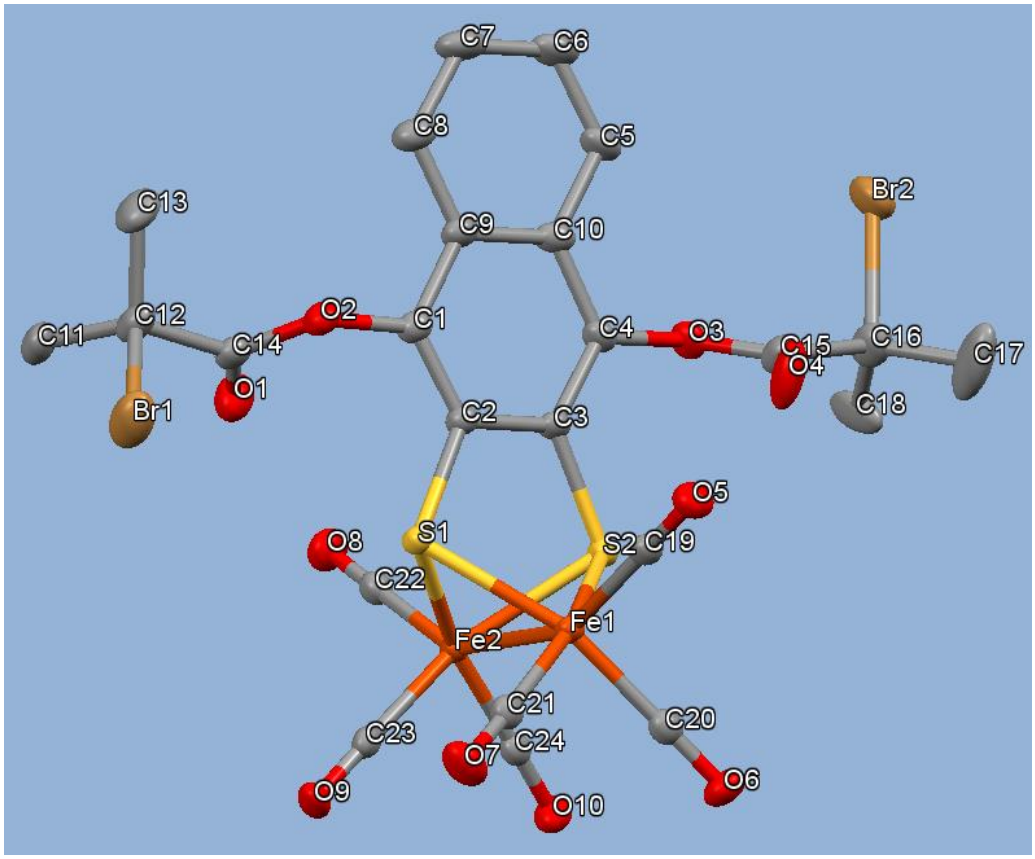

Figure C.5. Oak Ridge thermal ellipsoid plot (ORTEP) diagram of **56** with hydrogen atoms omitted and thermal ellipsoids shown at 50% probability level. CCDC 1577155 contains the supplementary crystallographic data for this paper. These data are provided free of charge by The Cambridge Crystallographic Data Centre

v. Discussion of Spectroscopic Characterization of Metallopolymers

To confirm structural integrity of the [2Fe-2S] core after polymerization, IR spectroscopy of metalloinitiator **56** and metallopolymers **58-61** were conducted. The characteristic Fe-CO vibrational stretching modes in metalloinitiator **56** were observed at 2082, 2050, and 2012 cm^{-1} and were similarly retained for the metallopolymers **58-61** with a very slight shift in of these peaks to 2080, 2050 and 2011 cm^{-1}, along with a slight broadening of the third peak that allowed for resolution of new peaks at 2007 cm^{-1}. These peaks, along with SEC UV-vis absorption confirmed that the [2Fe-2S] core survived ATRP conditions. In order to estimate the concentration of [2Fe-2S] sites per mass unit of polymer, a calibration curve was constructed for the characteristic Fe-CO stretching frequencies (see **Figure C4**). Each batch of polymer was inspected via IR and a mmol mg^{-1} value was established using this calibration curve. This value was used to normalize metallopolymer concentrations for comparison where appropriate.

c. Synthesis and Characterization of PDMAEMA-*g*-[2Fe-2S] (58)

i. Synthesis of PDMAEMA-*g*-[2Fe-2S] (58)

$(M)_o : (I)_o : (Cu^I)_o : (L)_o = 100 : 1 : 1 : 1$

ATRP of DMAEMA was adapted from the literature and modified for the synthesis of PDMAEMA metallopolymers.[255–257] A 10 mL Schlenk flask was loaded with Cu(I)Br (2.55 mg, 0.0178 mmol) and 0.20 mL of deoxygenated, anhydrous THF was added to the flask followed by the addition of deoxygenated HMTETA (7.3 µL, 0.0267 mmol). The resulting mixture was stirred for 10 minutes to allow for the formation of the Cu-ligand complex. To a second 10 mL Schlenk flask **56** (14.24 mg, 0.0178 mmol) was added. Then 0.30 mL of deoxygenated, anhydrous THF was added. The solution was stirred until homogeneous then the resulting mixture was transferred to the reaction flask. Finally, purified and deoxygenated DMAEMA (0.30 mL, 1.78 mmol) was added to the reaction flask and the flask was submerged in an oil bath preheated to 50^o C and the reaction was stirred at 50° C. After 90 minutes, the reaction flask was placed in an ice bath and 2.0 mL of deoxygenated THF was added and the solution was stirred for 10 minutes in the cold bath to quench the polymerization. The reaction mixture was then transferred to the deoxygenated solution of Dowex resin in MeOH (700 mg in 20 mL MeOH) and stirred for 1.5 hours to remove the copper catalyst. The red-orange solution was then filtered to remove Dowex resin and the methanol was removed on a rotary evaporator (200 torr, 23 ^{o}C). The crude, sticky solid was redissolved in a minimum amount of dichloromethane and precipitated in a rapidly stirred solution of hexanes (200 mL). The hexanes was decanted and precipitated reddish-brown polymer was rinsed with hexanes. The precipitation was repeated and the final solid was transferred to a vial as a solution in DCM, then solvent was removed on a rotary evaporator and dried overnight under vacuum (*ca.* 0.5 torr at room temperature). (66% conversion; 171 mg isolated yield). $M_{n,\ SEC}$ = 12,700 g/mol, M_w/M_n = 1.27

In all syntheses of PDMAEMA-*g*-[2Fe-2S] **58** it was imperative to remove Cu species from the crude polymer as it was found to facilitate oxidative decomposition of the [2Fe-2S] core. Copper species are competently removed from PEGMA-*g*-[2Fe-2S] via alumina column, however PDMAEMA is known[258] to complex Cu, so additional care had to be taken to ensure removal of

all Cu species. After the reaction, stirring the crude polymer solution without exposing to air in degassed MeOH with Dowex-50 resin was found to be the preferred method of copper removal.

ii. ^{1}H NMR Spectrum of PDMAEMA-*g*-[2Fe-2S] (58)

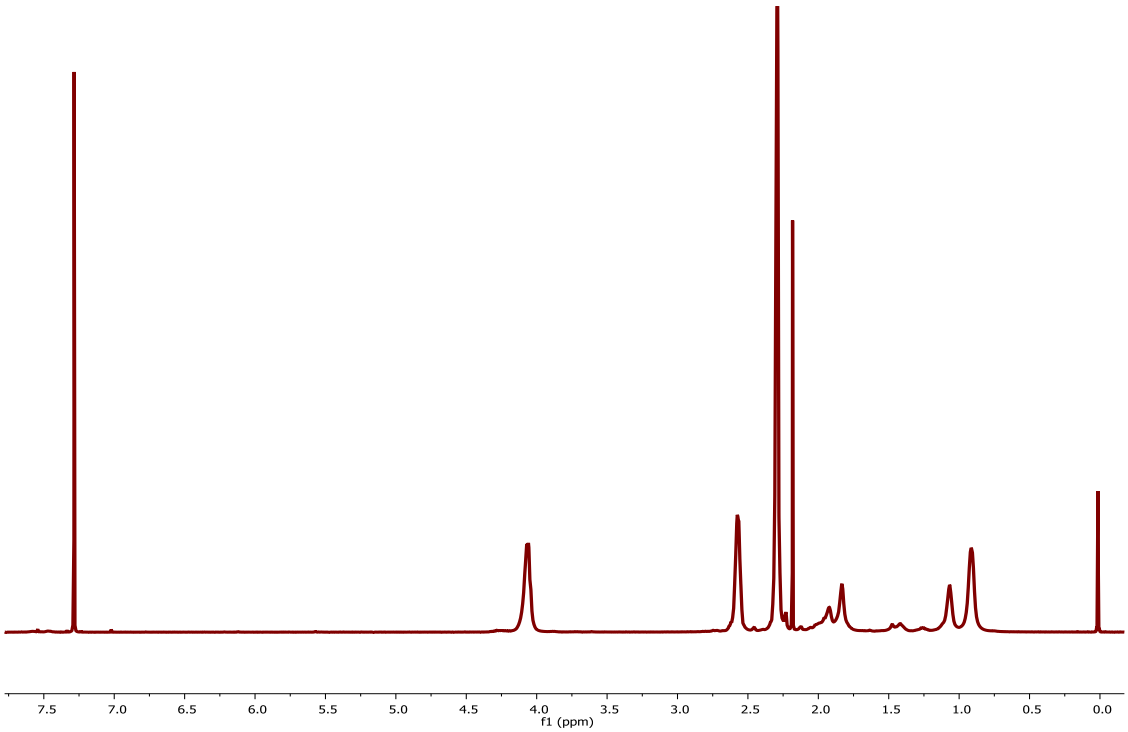

Figure C.6. ^{1}H NMR of **56** in $CDCl_3$

iii. GPC Analysis and IR Spectrum of PDMAEMA-*g*-[2Fe-2S] (56)

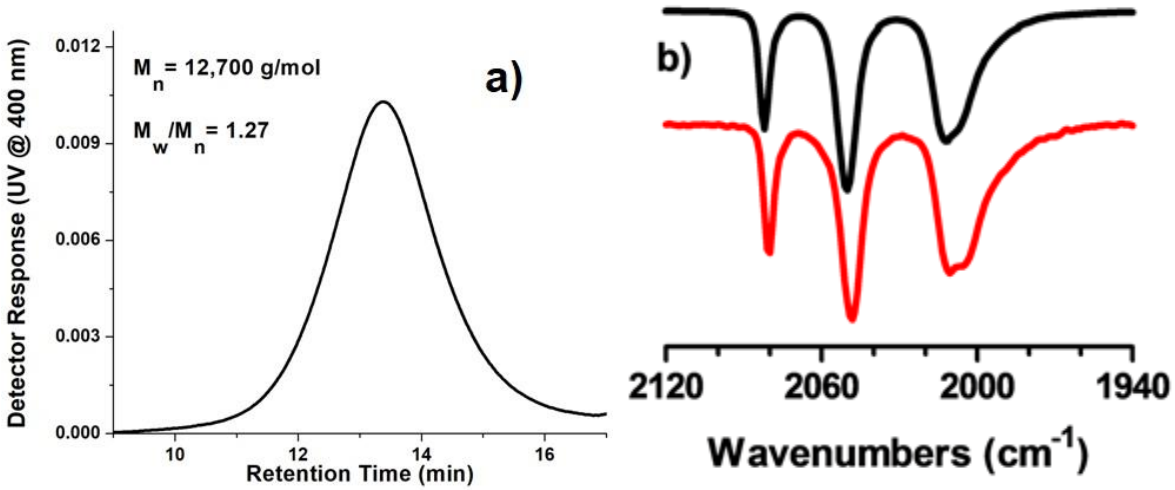

Figure C.7. (a) DMF GPC of **58** ($[DMAEMA]_o/[\mathbf{56}]_o/[CuBr]_o/[HMTETA]_o$: 100:1:1:1, $M_{n,theo}$= 11,176 g/mol, $M_{n,\,SEC}$ = 12,700 g/mol, M_w/M_n = 1.27) (**b)** overlay of IR spectra of Fe-CO stretching region for **56** (black) vs. PDMAEMA-*g*-[2Fe-2S] **58** (red).

d. Synthesis and Characterization of PEGMA-*g*-[2Fe-2S] (59)

i. Synthesis of PEGMA-*g*-[2Fe-2S] (59)
$(M)_o : (I)_o : (Cu^I)_o : (L)_o = 25 : 1 : 2 : 2$

ATRP of oligo(ethylene glycol) methyl ether methacrylate (OEGMA, Mn: 475 g/mol) was adapted from the literature and modified for the synthesis of PEGMA metallopolymers.[259–262] A 10 mL Schlenk flask equipped with a magnetic stir bar was loaded with Cu(I)Br (5.29 mg, 0.0364 mmol), sealed with a rubber septum, evacuated and backfilled with Ar three times. 0.1 mL of deoxygenated THF via Ar purged syringe was added to the flask followed by addition of deoxygenated PMDETA (7.60 µL, 0.0364 mmol). The resulting mixture was stirred for 10 minutes to allow for the formation of the light green Cu-ligand complex. Then, purified deoxygenated oligo(ethylene glycol) methyl ether methacrylate (Mn: 475 g/mol, 0.2 mL, 0.455 mmol) was added to the flask via Ar purged syringe. To a second 10 mL Schlenk flask equipped with a magnetic stir bar, **56** (14.6 mg, 0.0182 mmol) was loaded and the flask was sealed with a rubber septum. The flask was evacuated and backfilled with Argon three times, then 0.3 mL of deoxygenated and anhydrous THF was added via purged syringe. The solution was stirred until homogeneous then the resulting mixture was sparged with Argon for 1 min. The **56/**THF mixture was transferred to the reaction flask via purged syringe and the flask was submerged in an oil bath preheated to 50 ^oC. The reaction was stirred for 6 hours under Ar. After 6 hours, the resulting polymer mixture was diluted with 2.0 mL of DCM and passed through a short column of neutral alumina twice to remove the copper catalyst. The solvent was removed on a rotary evaporator and a red, viscous liquid polymer was obtained. The polymer was washed with 20 mL of hexanes twice and the hexanes was decanted. The polymer was dried overnight under vacuum at room temperature. (Full conversion; 120 mg isolated yield). $M_{n,\ SEC}$ = 14,054 g/mol, M_w/M_n = 1.27

ii. ^{1}H NMR Spectrum of PEGMA-*g*-[2Fe-2S] (59)

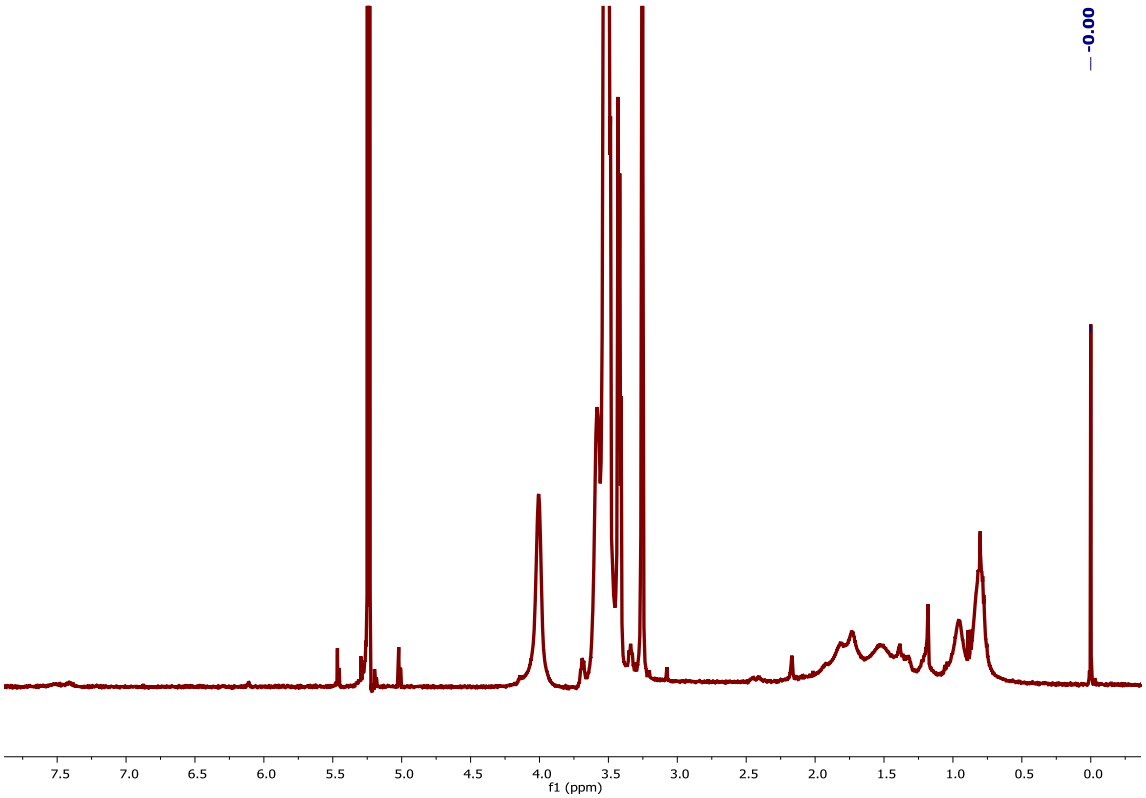

Figure C.8. ^{1}H NMR Spectrum of **59** in CD_2Cl_2

iii. GPC Analysis and IR Spectrum of PEGMA-*g*-[2Fe-2S] (59)

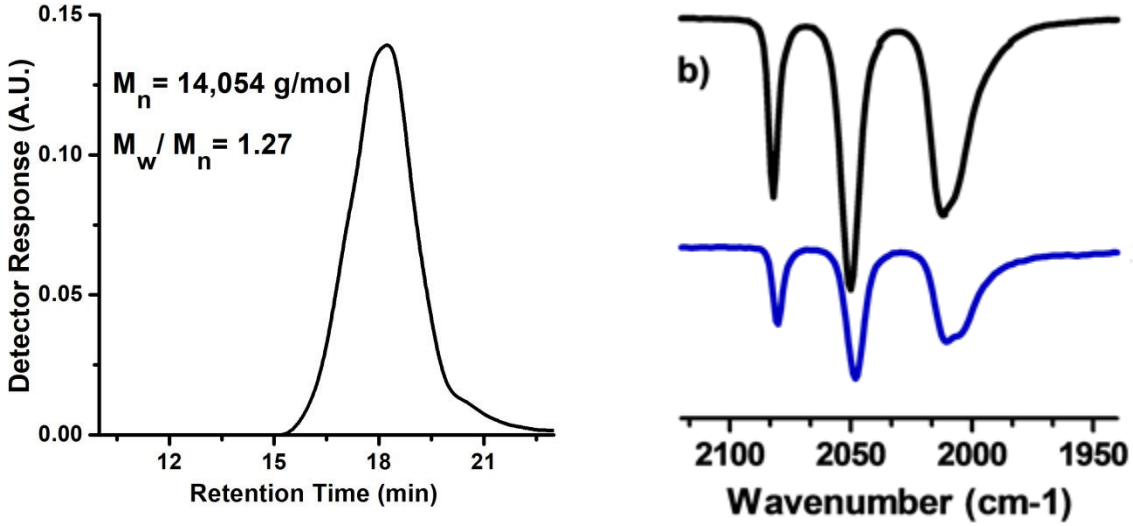

Figure C.9. (a) THF GPC of **59** ($[OEGMA]_o/[\mathbf{56}]_o/[CuBr]_o/[PMDETA]_o$: 25:1:2:2, $M_{n,theo}$ = 12,675 g/mol, $M_{n,SEC}$ = 14,054 g/mol, M_w/M_n = 1.27) b) overlay of IR spectra of Fe-CO stretching region for **56** (black) vs. PEGMA-*g*-[2Fe-2S] (**59**) (blue)

e. Synthesis and Characterization of P(DMAEMA-*r*-OEGMA)-*g*-[2Fe-2S] (60 & 61)

i. Synthesis of P(DMAEMA-*r*-OEGMA)-*g*-[2Fe-2S] (60 & 61)

$(DMAEMA)_o : (OEGMA)_o : (I)_o : (Cu^I)_o : (L)_o$ = 15 : 15 : 1 : 2 : 2 - 50:50 Feed Ratio (60)

A 25 mL Schlenk flask equipped with a magnetic stir bar was loaded with Cu(I)Br (5.84 mg, 0.0396 mmol), sealed with a rubber septum and evacuated and backfilled with Argon three times. 0.2 mL of deoxygenated THF and HMTETA (10.76 µL, 0.0396 mmol) were added to the flask, respectively. The resulting mixture was stirred for 5-10 min to let the catalyst complex form. Monomers were purified by passing through a short column of neutral alumina. Then, OEGMA (Mn: 475 g/mol, 0.130 mL, 0.297 mmol) and DMAEMA (0.05 mL, 0.297 mmol) were added to the flask using purged syringes, respectively. To a separate 10 mL Schlenk flask equipped with a magnetic stir bar, **56** (15.82 mg, 0.0198 mmol) was added. The flask was then sealed with a rubber septum and vacuumed/backfilled with Argon three times. **1** was completely dissolved in 0.2 mL of deoxygenated THF and the resulting mixture was sparged with Argon for 1 minute. Finally, **56**/THF mixture was added to the flask via purged syringe. The resulting solution was stirred in an oil bath at 50 ^oC for 6 hours. After the reaction, the polymer mixture was diluted with 2.0 mL of deoxygenated THF and the resulting mixture without exposing to air was transferred to a deoxygenated 20 mL of Dowex/MeOH solution (*ca.* 0.1g/mL) and stirred for two hours. Then, the resulting solution was passed through a short column of neutral alumina. The solvent was removed in a rotary evaporator and the resulting red viscous liquid polymer was washed with 20 mL of hexanes twice. The hexanes was decanted and the polymer solution was dried under vacuum overnight at room temperature prior to use. (Full conversion; *ca.* 180 mg isolated yield). $M_{n,\ SEC}$ = 22.0 kg/mol, M_w/M_n = 2.72

$(DMAEMA)_o : (OEGMA)_o : (I)_o : (Cu^I)_o : (L)_o$ = 35 : 15 : 1 : 1 : 1.5 - 70:30 Feed Ratio (61)

A 25 mL Schlenk flask equipped with a magnetic stir bar was loaded with Cu(I)Br (2.43 mg, 0.017 mmol), sealed with a rubber septum and evacuated and backfilled with Argon three times. Monomers were purified by passing through a short column of neutral alumina. 0.2 mL of deoxygenated THF and HMTETA (6.92 µL, 0.025 mmol) were added to the flask, respectively. The resulting mixture was stirred for 5-10 min to let the catalyst complex form. Then, the monomers were added to the flask using purged syringes. To a separate 25 mL Schlenk flask equipped with a magnetic stir bar, **56** (13.57 mg, 0.017 mmol) was added. The flask was then sealed with a rubber septum and vacuumed/backfilled with Argon three times. **56** was completely dissolved in 0.3 mL of deoxygenated THF and the resulting mixture was sparged with Ar for 1 minute. Finally, **56**/THF mixture was added to the flask via purged syringe. The resulting solution was stirred in an oil bath at 50 ^oC for 6 hours. After the reaction, the polymer mixture was diluted with 2.0 mL of deoxygenated THF and the resulting mixture without exposing to air was transferred to a deoxygenated 20 mL of Dowex/MeOH solution (*ca.* 0.1g/mL) and stirred for two hours. Then, the resulting solution was passed through a short column of neutral alumina. The solvent was removed in a rotary evaporator and the resulting red viscous liquid polymer was washed with 20 mL of hexanes twice. The hexanes was decanted and the polymer solution was dried under vacuum overnight at room temperature prior to use. (Full conversion; 120 mg isolated yield). $M_{n,\ SEC}$ = 13,800 g/mol, M_w/M_n = 1.61

ii. ^{1}H NMR Spectra of P(DMAEMA-*r*-OEGMA)-*g*-[2Fe-2S] (60 and 61)

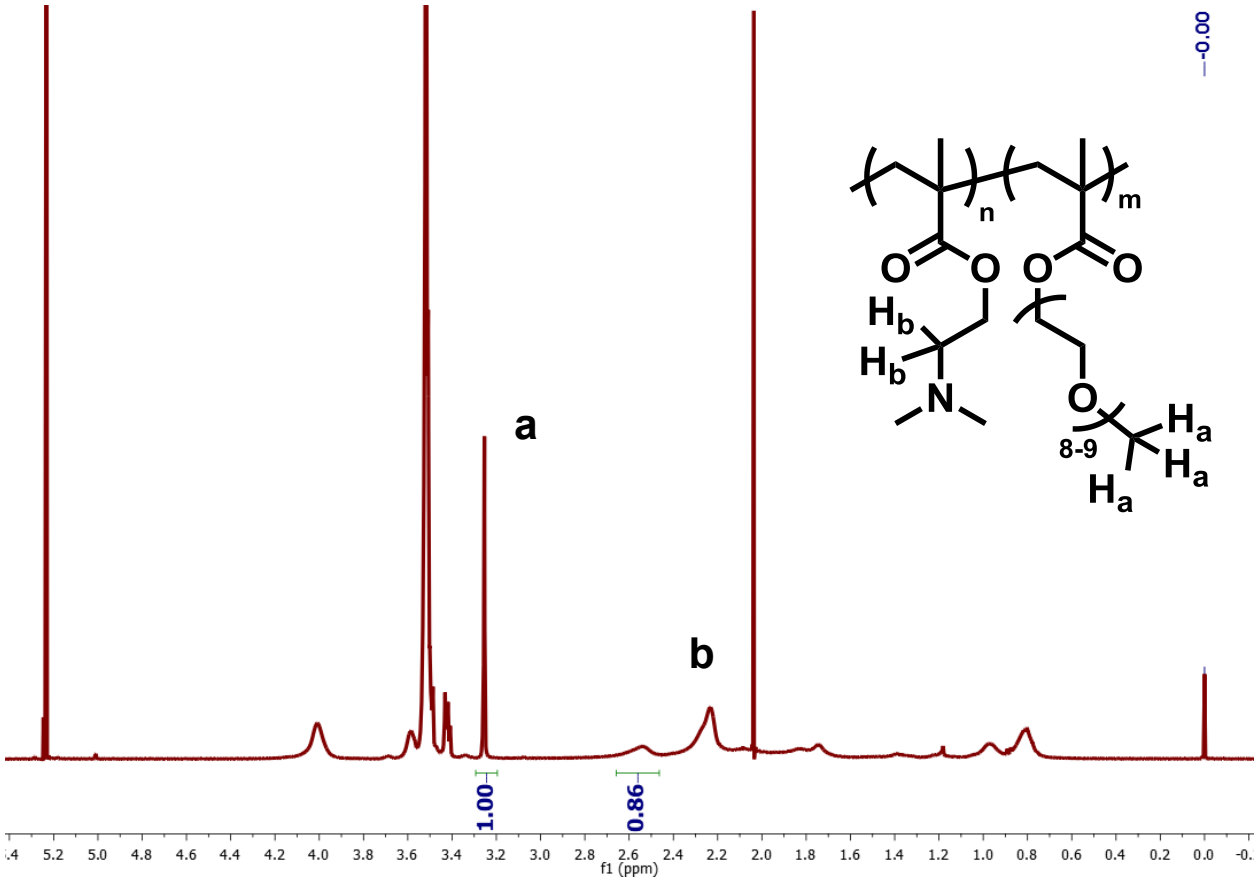

Figure C.10. ^{1}H NMR Spectrum of **60** in CD_2Cl_2 (mol % PEGMA = 44, mol % PDMAEMA = 56)[263]

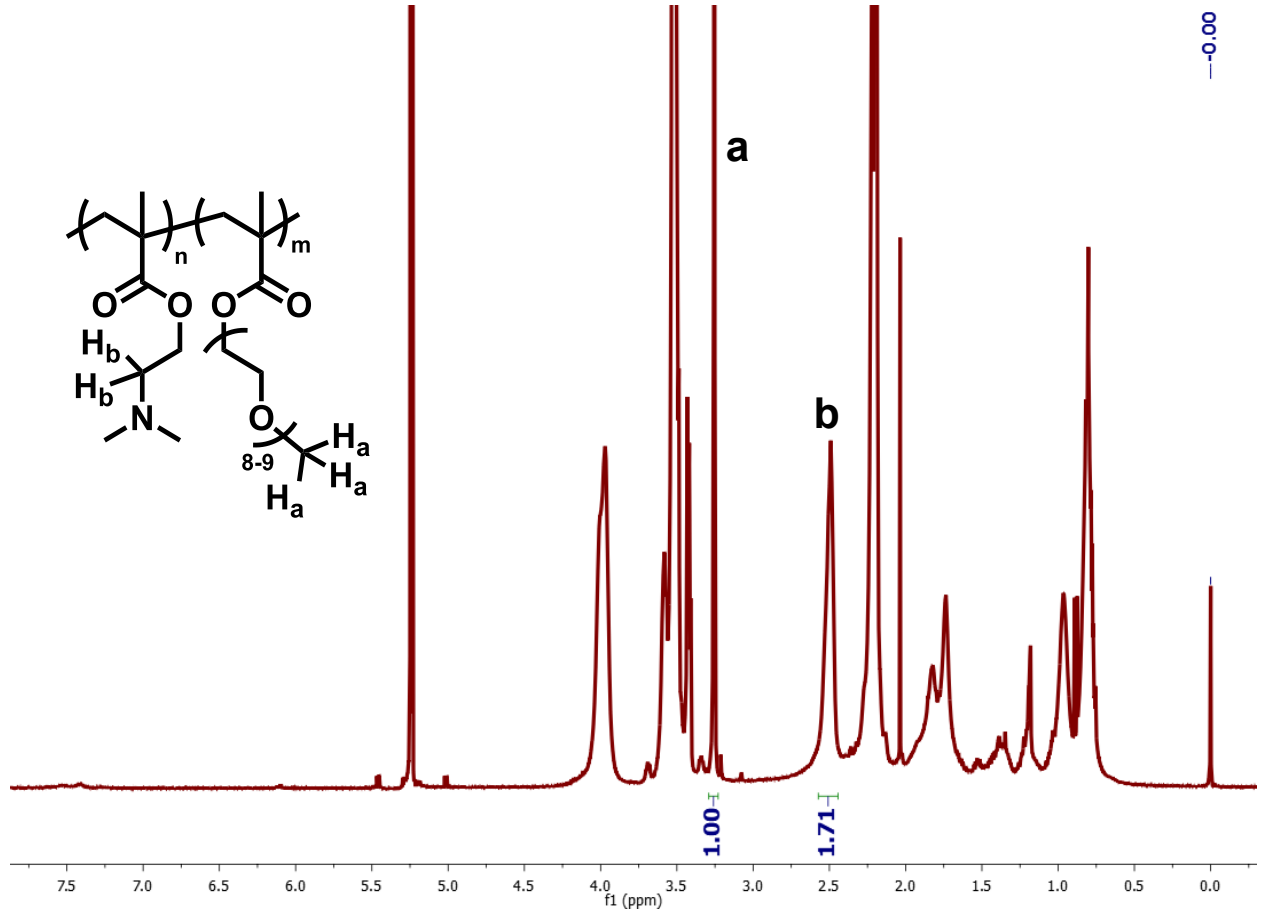

Figure C.11. ^{1}H NMR spectrum of **61** in CD_2Cl_2 (mol % PEGMA = 28, mol % PDMAEMA = 72)

iii. GPC Analysis and IR Spectrum of P(DMAEMA-*r*-OEGMA)-*g*-[2Fe-2S] (60 and 61)

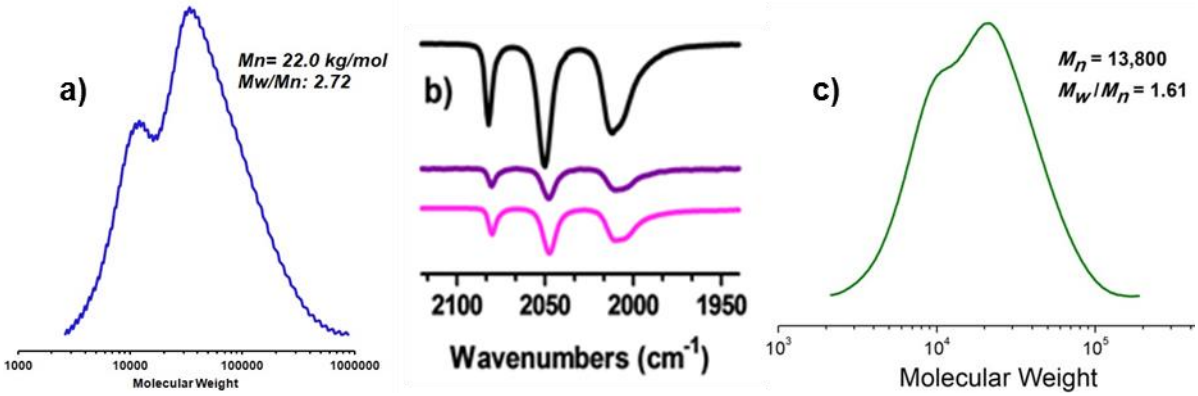

Figure C.12. IR spectra and GPC chromatograms of metallo(co)plymers 60 and 61. a) DMF GPC of **60** (on the left, blue line) ([DMAEMA]o/[OEGMA]o/[**56**]o/[CuBr]o/[HMTETA]o=15:15:1:2:2, Mn,theo = 10,283 g/mol, Mn, SEC = 22.0 kg/mol, Mw/Mn = 2.72) b) overlay of IR spectra of Fe-CO stretching region for **56** vs. P(DMAEMA-r-OEGMA)-g-[2Fe-2S] (**60** and **61**) c) DMF GPC of **61** (on the right, green line) ([DMAEMA]o/[OEGMA]o/[**56**]o/[CuBr]o/[HMTETA]o= 35:15:1:2:2, Mn,theo = 13.427 g/mol, Mn, SEC = 13,800 g/mol, Mw/Mn = 1.61)

f. Electrochemical

i. Procedures and Materials

A Gamry Interface 1000 and a Gamry Reference 3000 were used for all data collection with Gamry Framework 6 software. A custom airtight cell was designed and fabricated in house and is pictured below (**Figure C13**). Potentials in water were referenced to SHE using the standard conversion of +0.210 V vs. Ag/AgCl/3M KCl. A scan rate of 100mV/s was used unless otherwise noted. Solution resistance was measured and compensated at 90% of measured cell resistance. A glassy carbon working electrode with a diameter of 0.3 cm (A = 0.071 cm^2) and an edge plane graphite rod counter electrode (diameter 5 mm) were obtained from BASi. The working electrode was polished between scans in a figure eight pattern on a Buehler microcloth polishing cloth with 1.0 micron alumina mircopolish for 1minute then 30 seconds using 0.05 micron alumina mircopolish followed by 10 seconds of sonication in DI water. Silver wire (99.999% Alfa Aesar), KCl (99%, Alfa-Aesar, recrystallized twice from 0.1 M HCl), and Vycor frits were used to fabricate a double junction reference electrode to fit the cell. Once fabricated, a reference electrode was stored for up to 7 days before being remade. Aqueous solutions were prepared using 18 MΩ water purified using a Millipure water filtration system. Buffered solutions were made with NaH_2PO_4/Na_2HPO_4 (VWR, ACS grade) according to literature preparations found in *Ruzin, 1999 Plant Microtechnique and Microscopy* accessed at (http://microscopy.berkeley.edu/Resources/instruction/buffers.html) and adjusted to exact pH using 1.0 M HCl or NaOH. A Ag/AgCl/3M KCl pseudo-reference electrode was fabricated by soaking Ag wire (99.999% Alfa Aesar) in a commercial bleach solution (Clorox) for 16 hours. The wire was then rinsed thoroughly with 18 MΩ water and stored in 3M KCl for up to 1 week. A 1 mm diameter Pt disk electrode was used to provide comparison with HER at a Pt surface. Aqueous solutions were prepared in air and deoxygenated in the cell by bubbling the stirred solution with argon for 30 minutes. Aerobic experiment conditions were achieved by not bubbling the solution with argon.

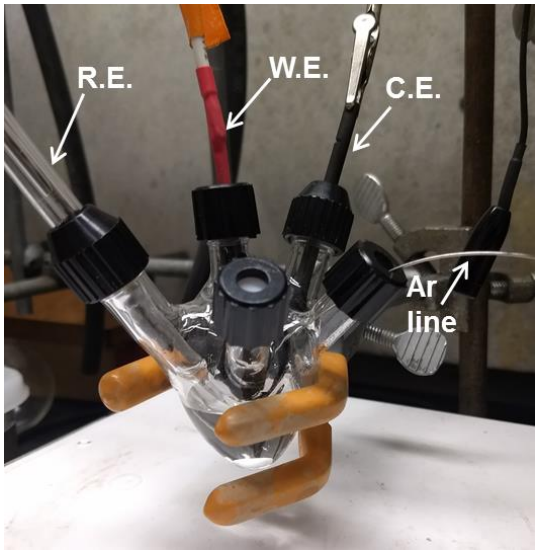

Figure C.13. Cyclic voltammetry cell used for data collection. Working electrode (W.E.), reference electrode (R.E.), and counter electrode (C.E.) are all labeled, as well as the argon line into the cell.

ii. Linear Sweep Voltammetry of 58-61 Comparing Aerobic and Anaerobic Conditions

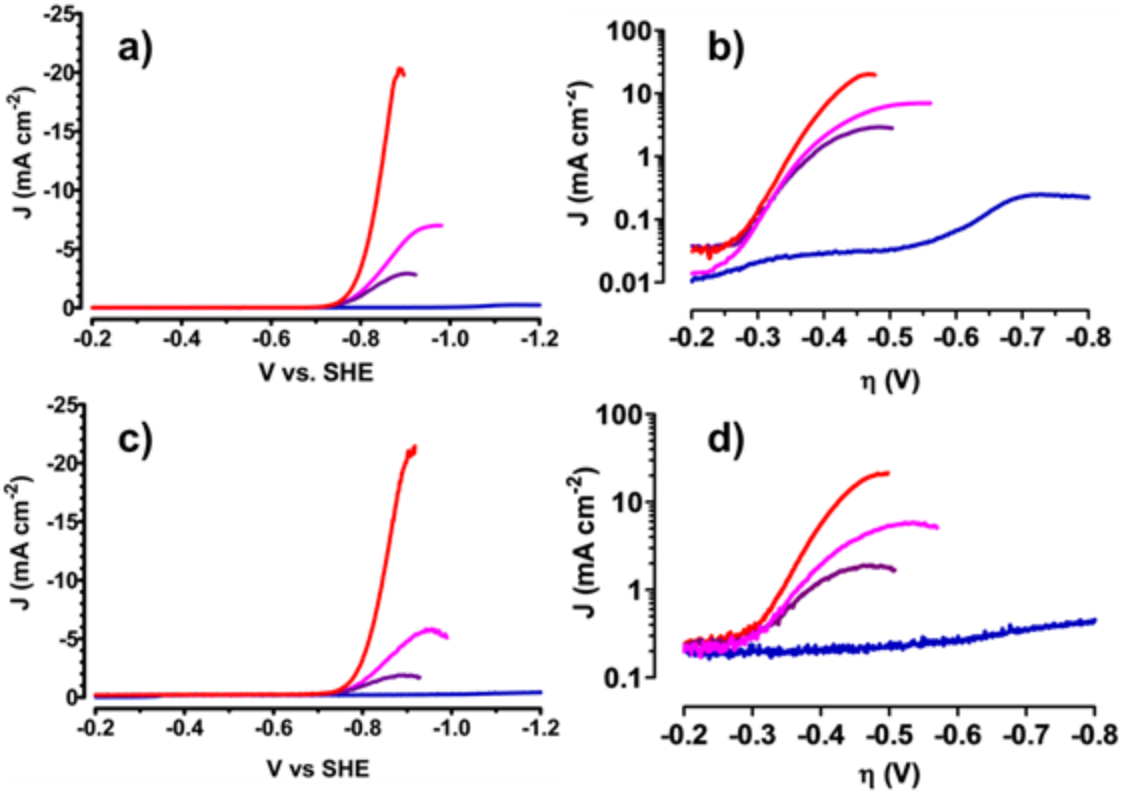

Figure C.14. a) LSV comparison of PEGMA-*g*-[2Fe-2S], **59** (blue), PDMAEMA-*g*-[2Fe-2S], **58** (red), and copolymers (70/30 PDMAEMA/PEGMA, **61** = purple, 50/50, 60 = pink) in pH 7.0 sodium phosphate buffer (0.75 M) and polymer concentration of 0.2-0.3 wt% (0.1 mM [2Fe-2S] by IR. Data collected at a scan rate of 5 mV/s and stir rate of 1600 rpm. **b)** Tafel analysis of LSV data. **c)** LSV comparison of **59** (blue), **58** (red), and copolymers (70/30 PDMAEMA/PEGMA = purple **61**, 50/50 **60** = pink) under aerobic conditions in pH 7.0 sodium phosphate buffer (0.75 M) and polymer concentration of 0.2-0.3 wt% (0.1 mM [2Fe-2S] by IR. data collected at a scan rate of 5 mV/s and stir rate of 1600 rpm. **d)** Tafel analysis of LSV data.

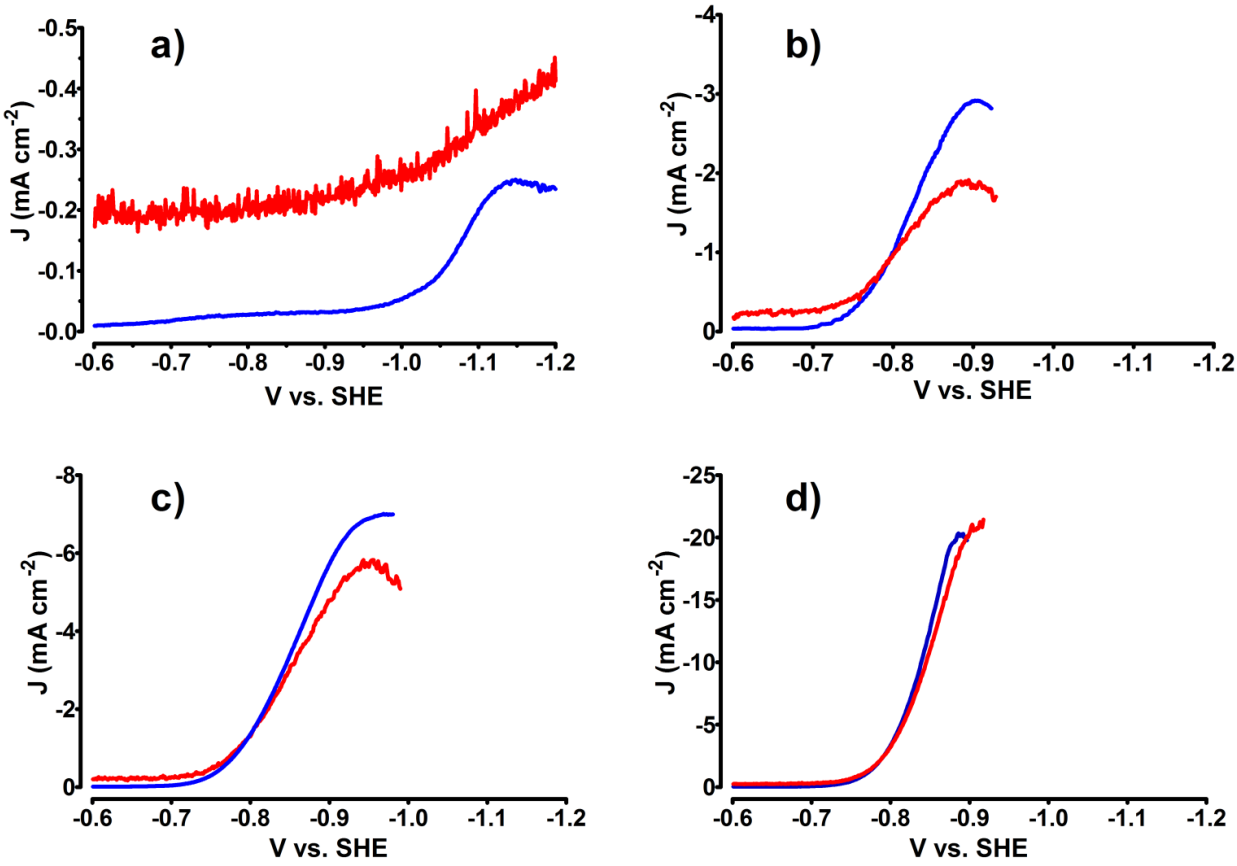

Figure C.15. Linear sweep voltammetry of the four metallopolymer systems **a)** PEGMA-*g*-[2Fe-2s] **59 b)** 50/50 *r*-copolymer **60 c)** 70/30 *r*-copolymer **61 d)** PDMAEMA-*g*-[2Fe-2S] **58** under aerobic (blue) and anaerobic (red) conditions in pH 7 sodium phosphate buffer (0.75 M) using a glassy carbon working electrode (ϕ = 3 mm).

iii. Determination of Zero-Exchange Current Density for a Planar Platinum Electrode

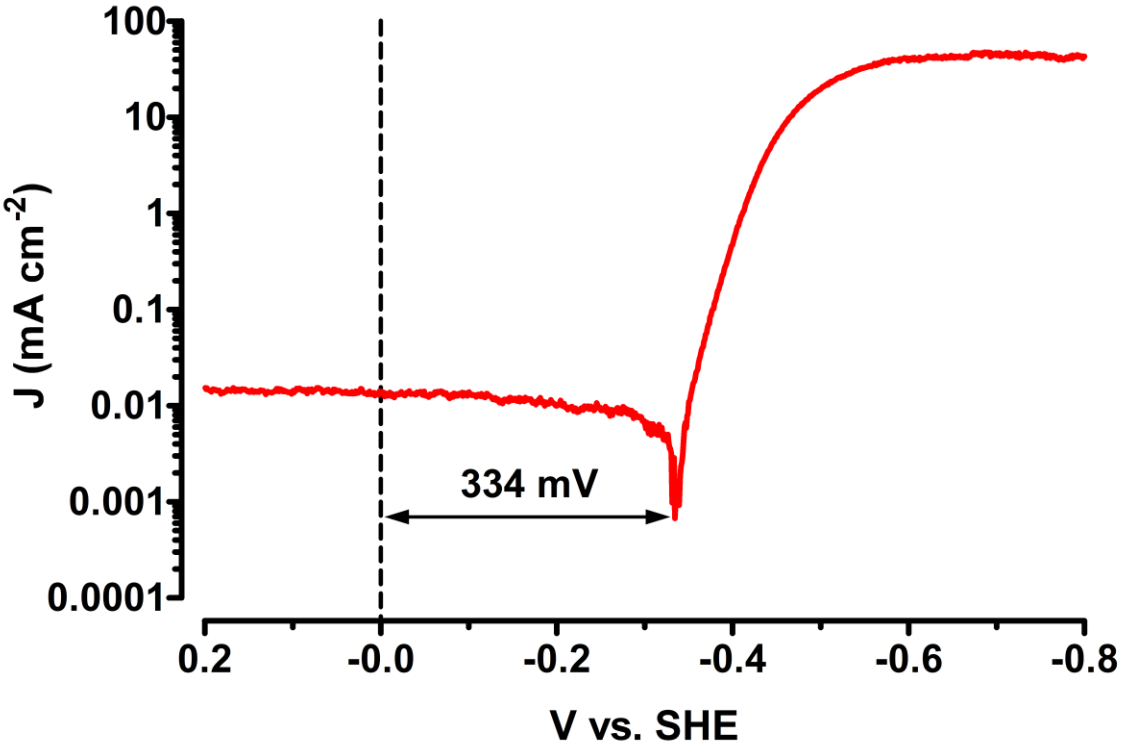

Figure C.16. Linear sweep voltammetry of a planar platinum electrode (ϕ = 1 mm) in pH 7 sodium phosphate buffer showing the potential at which the exchange current density approaches zero (-0.334 V vs SHE). Scan rate 5 mV/s, stir rate 1600 rpm, buffer concentration 0.75 M.

iv. Cyclic Voltammetry Scan Rate Study of Metallopolymers 58-61.

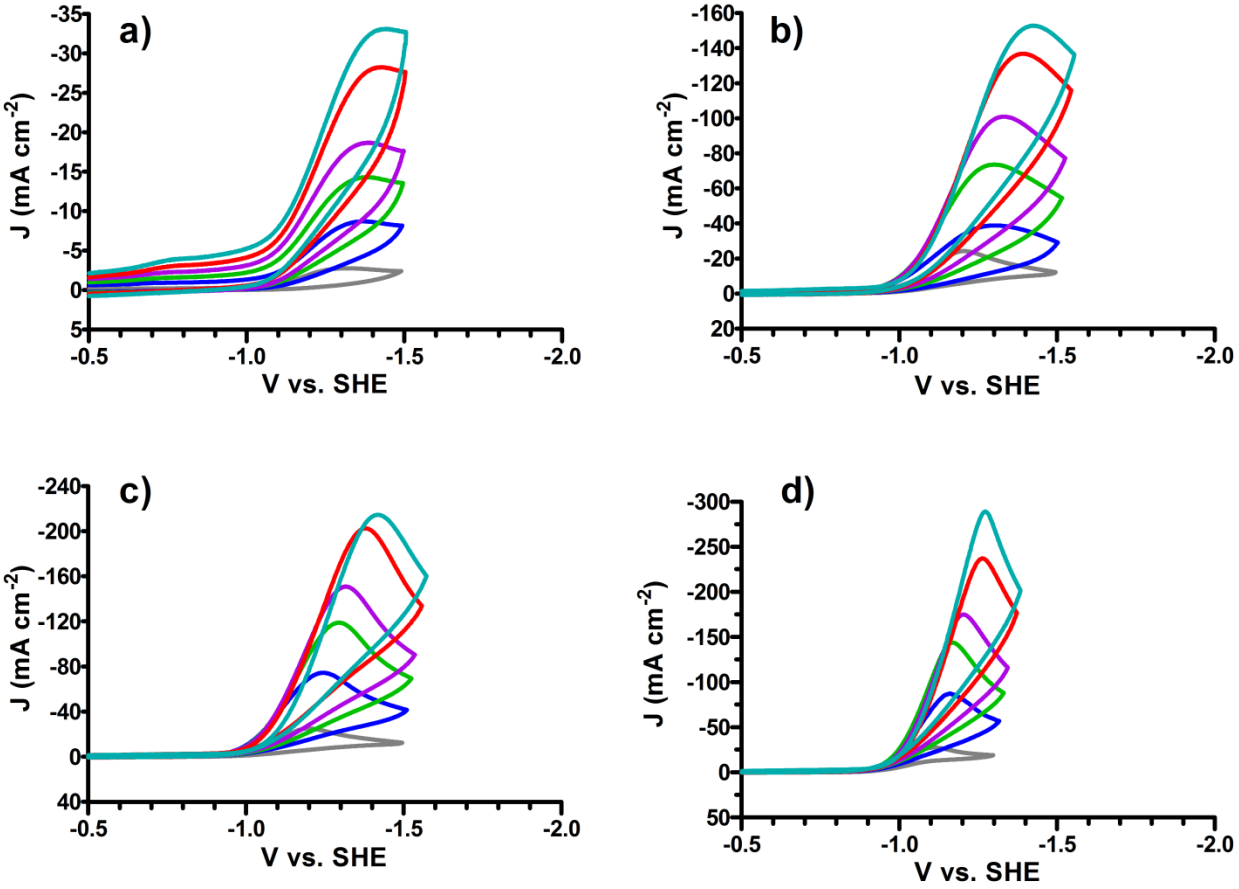

Figure C.17. Cyclic voltammetry of [2Fe-2S]-metallopolymers **a)** PEGMA-g-[2Fe-2S], **59 b)** 50/50-r-copolymer-g-[2Fe-2S], **60 c)** 70/30-r- copolymer-g-[2Fe-2S], **61 d)** PDMAEMA-g-[2Fe-2S], **58**. in pH 7 sodium phosphate buffer (0.75 M) with increasing scan rate from 0.1 V/s to 10.0 V/s. Scan rate = 0.1 V/s (grey), 1.0 V/s (blue), 2.5 V/s (green), 4.0 V/s (purple), 7.5 V/s (red), and 10.0 V/s (teal) (blue). Glassy carbon working electrode (ϕ = 3 mm).

v. Cyclic Voltammetry of Comparison of Metallopolymers 58-61 Aerobic and Anaerobic Conditions

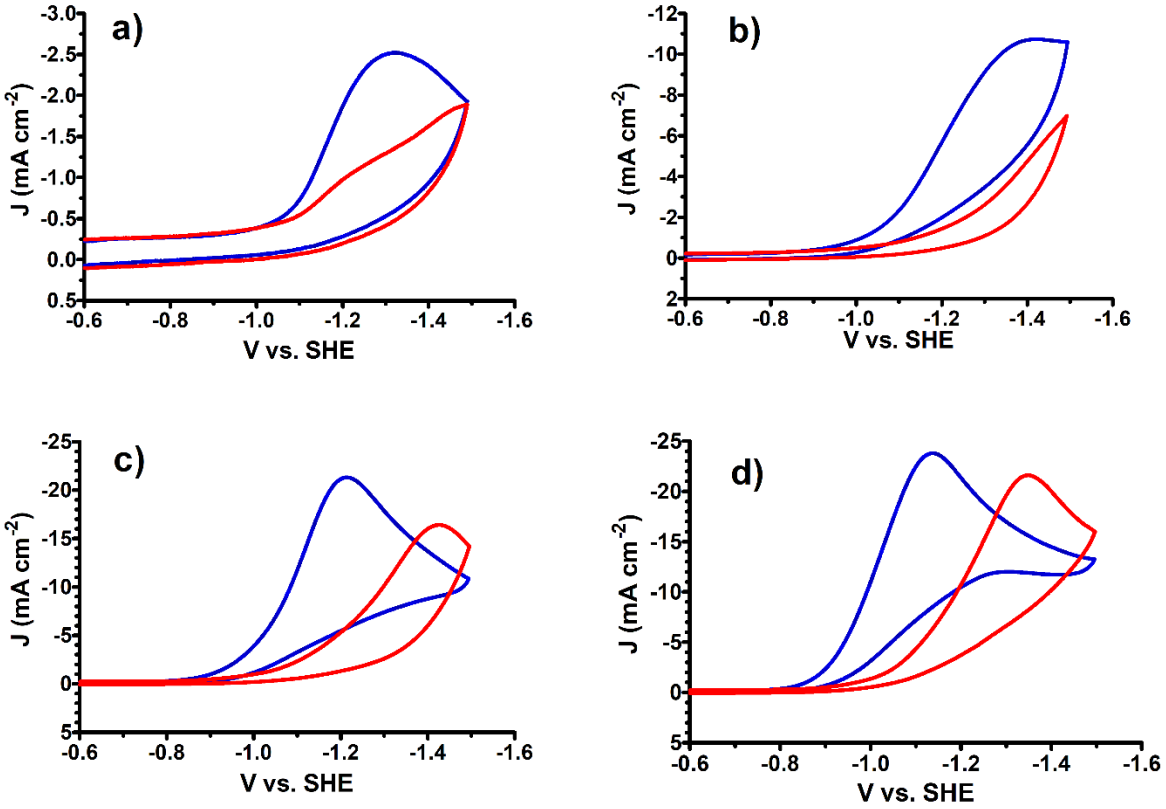

Figure C.18. Cyclic voltammetry of [2Fe-2S]-metallopolymers **a)** PEGMA-*g*-[2Fe-2S], **59 b)** 50/50-r-copolymer-*g*-[2Fe-2S], **60 c)** 70/30-r- copolymer-*g*-[2Fe-2S], **61 d**) PDMAEMA-*g*-[2Fe-2S], **58**. in pH 7 sodium phosphate buffer (0.75 M) under anaerobic (blue) and aerobic (red) conditions. Scan rate 100 mV/s, glassy carbon working electrode (ϕ = 3 mm).

Appendix D - Investigation into the Mechanism of Oligo-EDOT:Nafion Colloidal Polymer Formation

A likely mechanism for the formation of these nanoparticles is a cationic polymerization of EDOT to low order oligo-EDOT catalyzed by the sulfonic acid moieties on PSS. The Nafion would then be free to entangle the oligo-EDOT chain just as in PEDOT:PSS dispersions. This is consistent with zeta potential measurements done by the Heien lab indicating the surface is highly charged, indicating the perfluorinated Nafion is on the exterior. The highly charged surface also explains why the particles resist solution aggregation, even upon standing for long periods of time. To investigate this possibilty, a catalytic amount of TfOH was added to 1 mL of anhydrous, neat EDOT and 3-hexyl thiophene (3-HT). Both solutions underwent and immediate color change. The EDOT solution turned dark blue – a color characteristic of PEDOT films, while 3-HT solution turned a deep red color – a color characteristic of poly-3-hexylthiophene (P3HT) (see **Fig D.1a** below). In addition to the color changes, both solutions became very viscous. The solutions were both quenched with pyridine, then diluted with DCM for UV-Vis Spectra (**Fig D.1b**) which contained local maxima at 440 nm (3-HT solution) and 600 nm (EDOT solution) as well as absorbance peaks below 400 nm which correspond to dimeric and trimeric species. Interestingly, quenching the solution with a weak aqueous base (saturated sodium bicarbonate) resulted in a complete loss of color in the solution, indicating the oligomers formed in the presence of strong acid were de-oligomerized in the presence of aqueous base, but stable to an organic base with a similar pKa. Additionally, when the experiment was repeated with more TfOH, only very small changes were noted in the UV-Vis spectra, indicating the role of TfOH is indeed catalytic in nature.

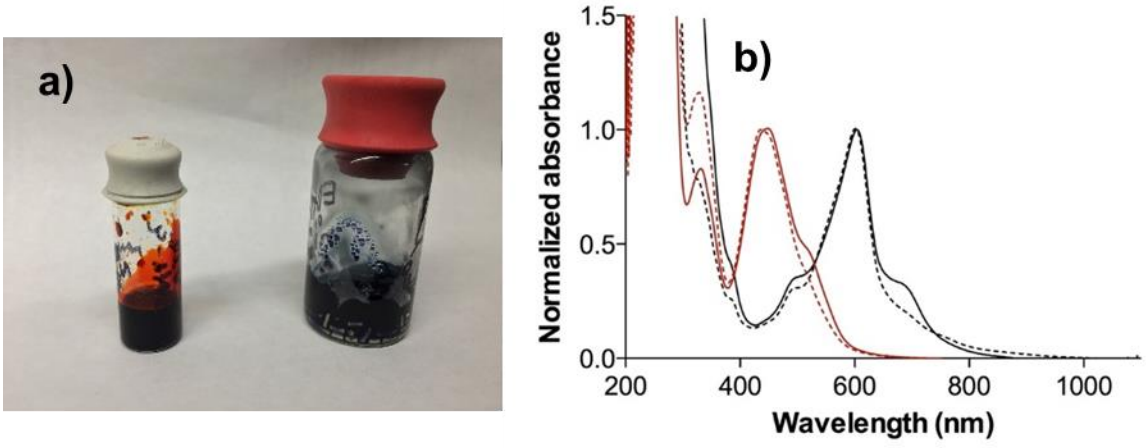

Figure D.1. a) Crude solutions of 3-hexylthiophene (left) and EDOT (right) after the addition of TfOH **b)** UV-Vis spectra of thiophene monomers with triflic acid. Red lines correspond to 3-hexyl thiophene with approximately 30 µL (dashed line) and 90 µL (solid line). The black lines correspond to EDOT with approximately 30 µL (dashed line) and 90 µL (solid line).

An arrow pushing mechanism (**Schemes D.1** and **D.2**) for the cationic oligomerization of thiophenes was developed and ^{1}H and DEPT-135 NMR (**Figure D.2**) as well as MALDI-MS

spectra (**Figure D.3**) were taken of TfOH-EDOT oligomers. ^{1}H NMR revealed a broad singlet at 5.5 ppm which we believed could belong to vinylic protons, and the DEPT 135 spectrum showed two CH peaks around 100 ppm. The mass spectrum contained repeat units separated 142 mass units apart. Taken together, these pieces of information pointed to the formation of a short oligomers (8-9mers) of dihydroEDOT (**83**), which was consistent with our arrow pushing mechanism. To further test this hypothesis, the reaction oligomerization of EDOT was repeated and after 3.5 hour a solution of trityl cation was added as a hydride acceptor. If our mechanism was correct, the addition of a hydride acceptor should allow the EDOT monomer to re-aromatize. Subsequent MS studies (**Figure D.4**) showed the repeat unit had changed from 142 amu to 140 – consistent with cleavage of re-aromatized EDOT monomers. Again, the oligomers seemed to be on the order of 8-10 units based on the highest M/Z peak observed in the MALDI-MS.

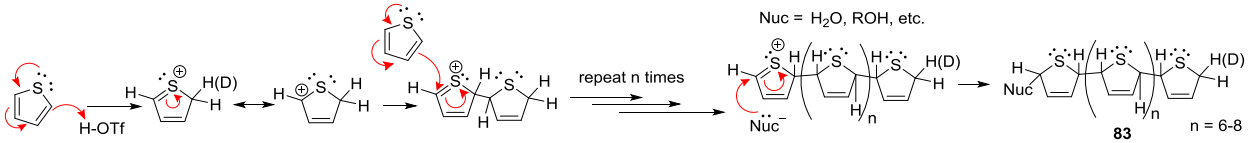

Scheme D.1. Proposed mechanism for the cationic oligomerization dihydroEDOT **83.**

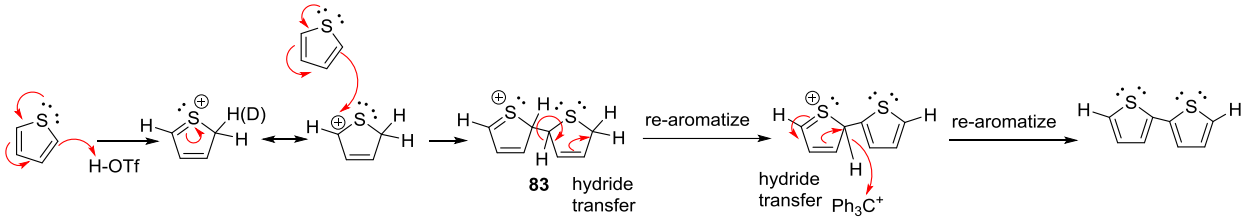

Scheme D.2. Proposed mechanism for re-aromatization of **83** upon addition of a hydride acceptor such as trityl cation. A dimer is shown to simplify the figure, but in principle this mechanism works on higher order oligomers of **83** as well.

a)

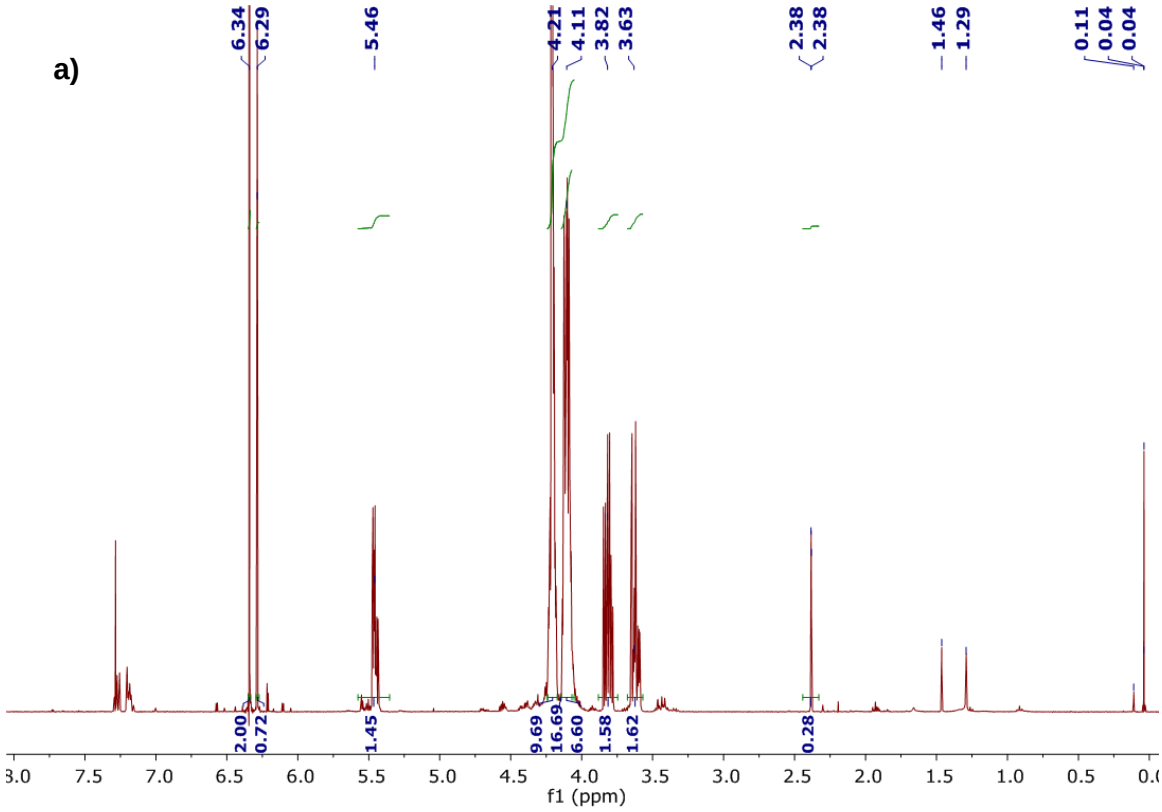
6.34
6.29
5.46
4.21
4.11
3.82
3.63
2.38
2.38
1.46
1.29
0.11
0.04
0.04
2.00
0.72
1.45
9.69
16.69
6.60
1.58
1.62
0.28
f1 (ppm)

b)

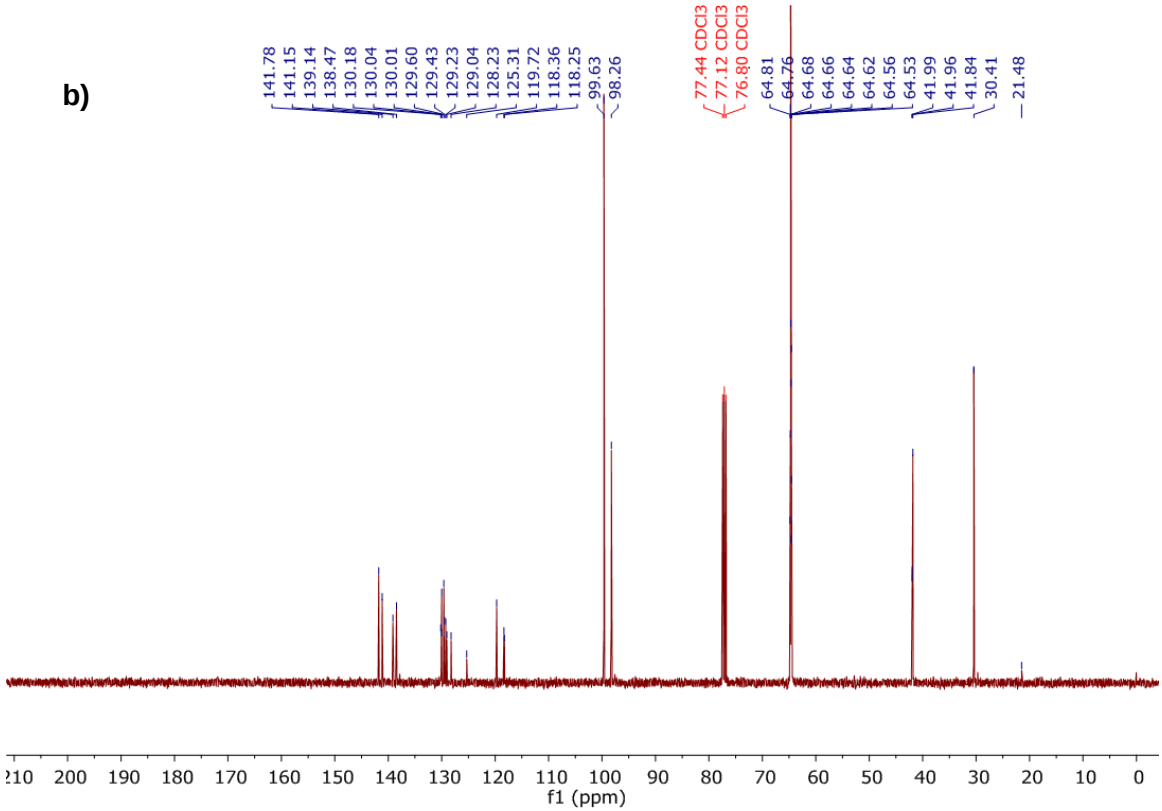
141.78
141.15
139.14
138.47
130.18
130.04
130.01
129.60
129.43
129.23
129.04
128.23
125.31
119.72
118.36
118.25
99.63
98.26
77.44 CDCl3
77.12 CDCl3
76.80 CDCl3
64.81
64.76
64.68
64.66
64.64
64.62
64.56
64.53
41.99
41.96
41.84
30.41
21.48
f1 (ppm)

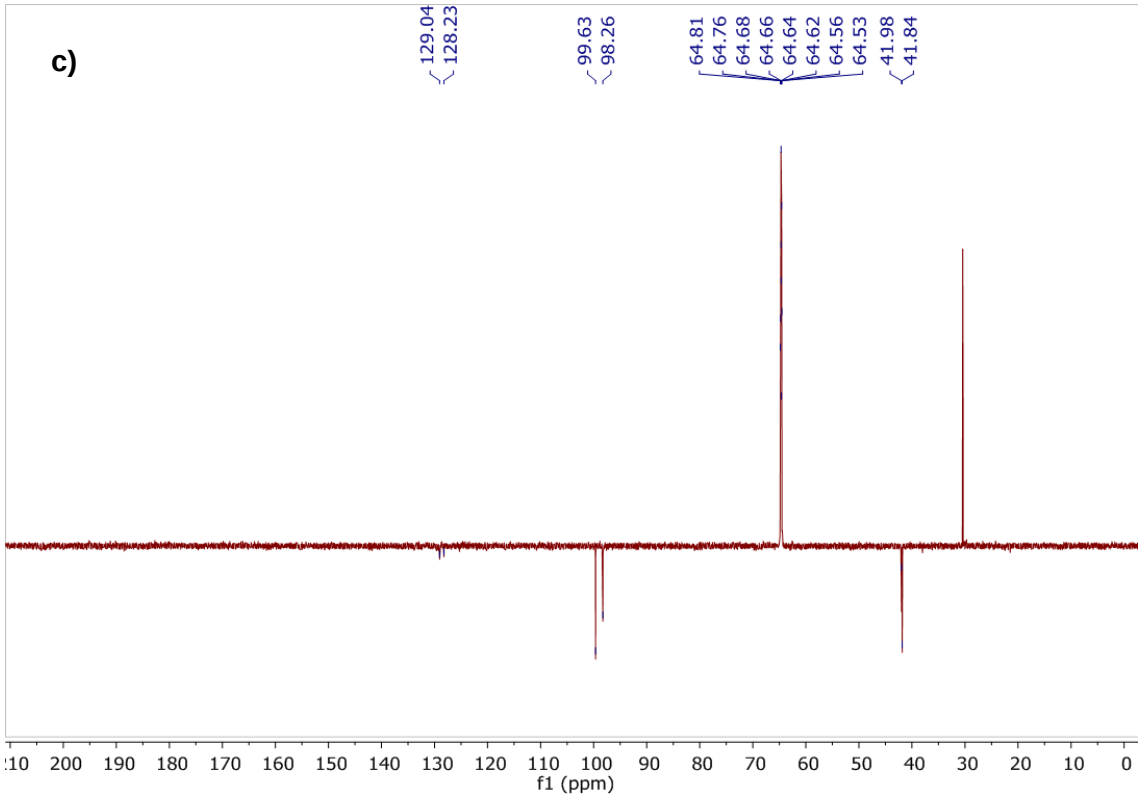

Figure D.2. NMR spectra of reaction mixture of EDOT and 30 µL TfOH. a) ^{1}H NMR b) ^{13}C NMR c) ^{13}C DEPT-135 NMR.

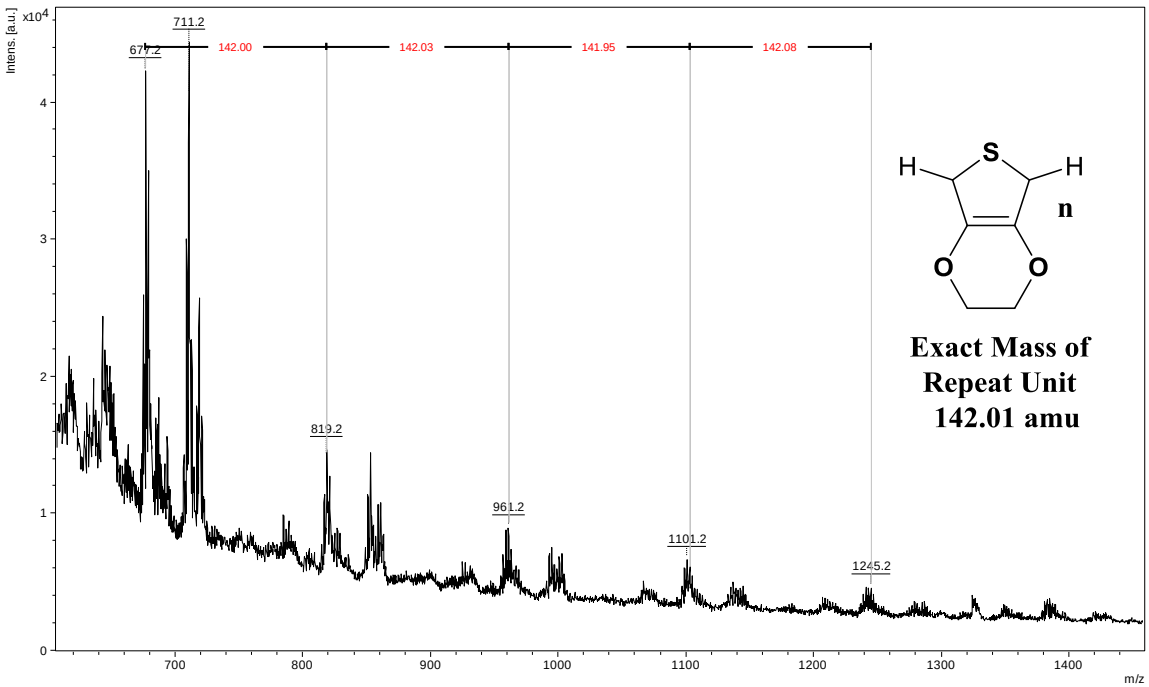

Figure D.3. MALDI-MS of reaction mixture of EDOT and 30 µL TfOH. Repeat units are 142 amu apart, as would be expected for dihydro EDOT.

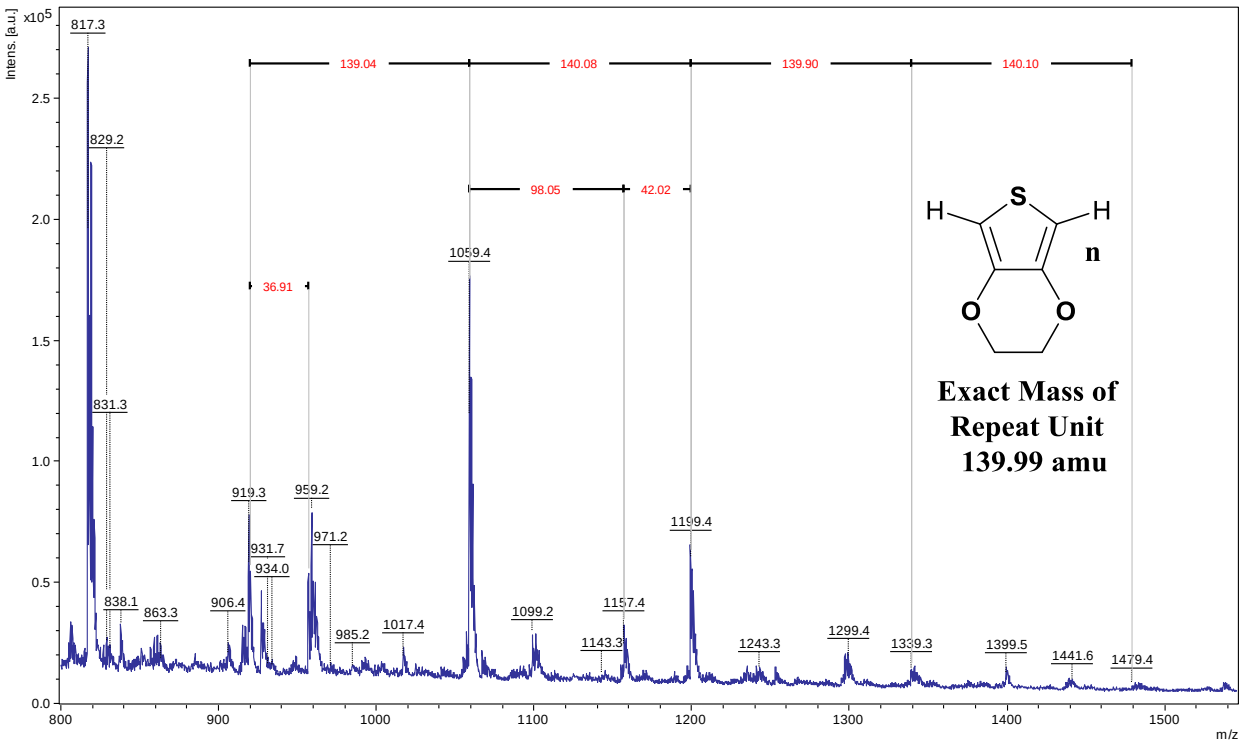

Figure D.4. MALDI-MS of reaction mixture of EDOT and 30 µL TfOH which was allowed to react for 3.5 hours then quenched with trityl cation. Repeat units are 140 amu apart, as would be expected for OEDOT. The highest mass peak observed consistent with a 10-mer.

Appendix E . Suggested Future Directions

Oligothiophenes

62-**64** have a surprisingly large shift in oxidation potentials for the Fe system, which points to a high degree of electronic coupling between the thiophene ligands and the diiron system. This would be an interesting set of molecules to model with DFT calculations to interrogate the orbital interactions that dominate this electron coupling. UPS photoelectron spectra of **62** and **63** have been taken, but **64** should be investigated via UPS as well once the instrument can be brought back online. UPS data in addition to DFT calculations and the electrochemistry already preformed could make a nice publication which needs minimal experimental work to complete. Preliminary results have shown it is possible for **64** to photo-produce detectable amounts of H_2 using thiophenol as both an acid and electron donor without the need for an external photosensitizer. While it may not be as active as the hydroquinone catalysts, [2Fe-2S] systems that serve as photocatalysts with organic photosensitizers are rare, and the author is not aware of any that do so in an intermolecular fashion. This is an interesting photosystem, but its activity may not warrant investigation unless the researcher is also committed to investigating the photoacid effect (described below) due to the significant experimental difficulties involved in developing a reliable and reproducible method for quantitative headspace H_2 measurements.

Investigating the Photo-Acid Effect.

Some phenolic compounds exhibit a photoacid effect, where the excited state has a much lower pKa than that of the ground state. In 1,4-hydroquinone, this effect has been shown to lower the pKa from 10.0 in the ground state to 3.1 in the excited state.[239] To test whether this photoacid effect can be leveraged to improve the photocatalytic capability of a [2Fe-2S] complex, compounds **81** and **82** could be synthesized by deprotonation of **80** with triethylamine (TEA) followed by quenching the resulting anion(s) with methyl iodide (Scheme E.1 below) . This would result in compounds with only one photo-acid site (**81**) or no photo-acid sites (**82**), but otherwise comparable structures and electronics (in terms of the electron richness of the naphthyl system). Comparison of the photocatalytic activity of **80** with **81** and **82** should reveal whether or not the photo-acid effect is contributing to the activity of **1**. If it is indeed assisting in catalysis, then the activity should follow the trend **80** > **81** > **82**.

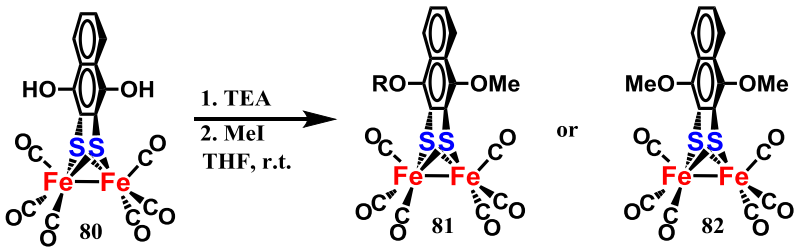

Scheme E.1. Suggested synthetic pathway to **81** and **82**.

Unlike the thiophene systems discussed above, **80**-**82** will likely require an external photosensitizer. The classic choices are ruthenium and iridium species with bpy and ppy ligands, though rhenium complexes have been used as well. Relatively few organic dyes have been used

to photosensitize a [2Fe-2S] catalyst, and to the authors knowledge there are no reports of using a polymer as a photosensitizer for such a photocatalytic system. Band energy comparisons and preliminary experiments have demonstrated that regio-regular poly(3-hexylthiophene) (rr-P3HT, **83**) is an effective photosensitizer for [(μ-bdt)$Fe_2(CO)_6$] (**21**) (see Appendix A, Figs A3 and A4). Use of a new type of completely organic photosensitizer would likely help to elevate the work, and would eliminate the use of expensive and rare transition metal photosensitizers in a system that is ostensibly working towards replacing platinum due to its high cost and scarcity.

Some consideration should be given to the sacrificial donor used in a photocatalytic system with **80**. Ascorbic acid is one of the most popular choices due to its ability to function both as an acid and an electron donor, and may be an excellent choice in this system in particular. **80** is easily oxidized to its quinone form, an undesirable reaction if the goal is to study the photoacid effect in **80** as this will effectively drop the active concentration of **80** by some unknown amount, complicating the experiment. Ascorbic acid is well known for it's anti-oxidant properties, and a high concentration relative to the catalyst concentration (which is desirable anyway for its role as an electron donor) may help prevent or reduce the oxidation of **80**. Due to the distinct NMR peak shift visible when **80** is oxidized, it may be able to study whether or not ascorbic acid has a protecting effect via ^{1}H NMR over a period of time, by watching for the loss of the peaks for **80** and the appearance of the quinone peaks.

Experimentally, getting good headspace H_2 quantitation is most challenging aspect of this proposed work. An internal standard of CH_4 recommended to help account for the high effusion rate of H_2, but GC conditions may need optimization to prevent CH_4 from eluting too slow and tailing excessively. Standards curves should be established by using a fixed volume of methane and varying the amount of H_2 injected into the cell. Each H_2/CH_4 concentration should be run in triplicate, and the cell should be set up and handle in an identical manner to that of the photocatalytic experiments, except without catalyst present, to accurately account for gas dissolution. If possible, a photostable solvent should be used that has similar solubilities for hydrogen and methane, but if not a carful internal standards curve should still account for the solubility difference. The TCD using Ar carrier gas with which our Shimadzu GC-8 is equipped is more responsive to H_2 than CH_4 so a large internal standard may be worth considering, with relatively small headspace samples taken. Another consideration is that in theory, the H_2 is continually produced in a catalytic system, while the CH_4 is all introduced at the beginning, so repetitive headspace samples will deplete the CH_4 volume and change the expected H_2/CH_4 response ratio. In light of the significant technical difficulties in obtaining reliable quantitation of headspace H_2, it may be best to find a collaborator who is already equipped for the measurements, or willing to teach a student from a colleague's lab how to overcome these problems to obtain trustworthy data.

[2Fe-2S]-Metallopolymers

With the incredible results achieved with the **PDMAEMA-*g*-[2Fe-2S]** (**58**) system many promising research avenues have opened up. The transient adsorption effect observed with **58** is very interesting and will require careful thought. It also may be one of the most important areas to explore because now that the effect has been demonstrated with **58**, any future publications on polymer systems which function as polyelectrolytes (such as PDMAEMA or poly(acrylic acid)) or

even systems which may be able to form close interactions with ions present in buffer solution such as the P(OEGMA) which may be able to complex cations in the same way as crown ethers with its long, flexible oligoethylene glycol chains. Zeta potential measurements will likely be useful in confirming the formation of a polyelectrolyte monolayer on the surface of a polarized electrode. Another possibility would be to tether some spectroscopic reporter group to the polymer chain to allow imaging of the monolayer via waveguide spectroscopy.

The formation of the adsorbed layer significantly complicates evaluation of the catalytic activity of the **58** when considering it in the classic small molecule manner (*i.e.* evaluation of TOF and TON on a per molecule basis), but in some ways simplifies the system for comparison with heterogeneous catalysts, which rely more heavily on Tafel plots and amperometric methods though these comparisons may not be overly favorable to our system, as the field of heterogeneous catalysis is deep and well developed, and early indications are that there is a faster process occurring with species which are not adsorbed in the monolayer, but are interacting with vacant electrode sites. Elucidation of the nature of these non-adsorbed species will certainly be important as all indications are they either don't follow standard diffusion controlled or steady state behavior which current homogeneous TOF calculations rely on, or they are operating at extremely fast rates – in excess of 10^{10} s^{-1} using known methods. Because the pKa, and therefore degree of protonation, of **PDMAEMA-*g*-[2Fe-2S]** is heavily dependent on the concentration of chloride (or other small anions capable of screening the positives charged side chains) it may be possible to investigate the adsorption effect by lowering the chloride ion concentration while keeping other variables the same (pH, buffer concentration, percentage of the buffer in the conjugate acid form) to reduce the polyelectrolyte effect and hopefully inhibit the electrostatic adsorption. If the non-adsorbed rate is truly faster, and there is a significant difference in the adsorption kinetics by lowering the number of **PDMAEMA-*g*-[2Fe-2S]** side chains that are protonated, the rate should increase upon reduction of the chloride ion concentration. This is complicated by the solution confirmation of polyelectrolyte systems which take on a globular spherical confirmation in the presence of a high concentration of screening ions (*i.e.* chloride). Dropping the chloride concentration too much may result in a more open **PDMAEMA-*g*-[2Fe-2S]** structure which could complicate interpretation of the results of this experiment.

Aside from the transient adsorption, there are several other important effects to investigate. The buffer effect is certainly going to be key to understanding not only [2Fe-2S] electrocatalysts, but is likely to be an effect that is general to other HER electrocatalysts as well. In unpublished work which is currently under investigation by Kayla Clary, we have observed that while **PDMAEMA-*g*-[2Fe-2S]** far outclasses **P(OEGMA)-*g*-[2Fe-2S]** in all metrics of catalytic performance when operating in pH 7 sodium phosphate buffer, the story changes in tris buffer. Preliminary CV experiments have actually shown a higher current density for **P(OEGMA)-*g*-[2Fe-2S]** than **PDMAEMA-*g*-[2Fe-2S]** when operating in tris buffer *also at pH 7 with identical buffer concentrations*. This indicates that the pH of the solution is secondary to the identity of the buffer in this case. **PDMAEMA-*g*-[2Fe-2S]** sees significant improvements in catalytic activity when operating in tris over sodium phosphate at an identical concentration, an effect we attributed to the increase in concentration of conjugate acid form of the buffer, which DigiElech simulations indicated was the primary substrate when operating at pH 7. While this seemed straightforward, it

is less clear why **P(OEGMA)-*g*-[2Fe-2S]** is such a poor catalyst in sodium phosphate buffer, but an excellent catalyst in tris buffer. **P(OEGMA)-*g*-[2Fe-2S]** is not a polyelectrolyte, and tris solution does not contain any significant concentration of cations for it to complex which may encourage adsorption on the electrode. One hypothesis is that in sodium phosphate buffer, the high sodium concentration encourages adsorption of **P(OEGMA)-*g*-[2Fe-2S]**, and like **PDMAEMA-*g*-[2Fe-2S]** the adsorbed species has a slower TOF. Under the low cation concentrations of tris buffer however, **P(OEGMA)-*g*-[2Fe-2S]** may be able to resist adsorption, and the increased activity we see is a reflection of the higher TOF of non-adsorbed polymer catalyst species. Competition experiments between **P(OEGMA)-*g*-[2Fe-2S]** and Fe-free P(OEGMA), as well as a full concentration study of **P(OEGMA)-*g*-[2Fe-2S]** using both CV and LSV in both buffers should help determine if differences in the ability of **P(OEGMA)-*g*-[2Fe-2S]** to adsorb or resist adsorption depending on the buffer identity should help prove or disprove this hypothesis. It would also be worthwhile to preform a competition experiment where sodium ions are progressively added to the solution. If activity in tris decreases upon the addition of sodium ions, it would at the very least point towards a complex interaction between **P(OEGMA)-*g*-[2Fe-2S]** and ions in solution. In conjunction with the aforementioned studies, it would be another piece of evidence in favor of a complexation-electrostatic adsorption effect active on **P(OEGMA)-*g*-[2Fe-2S]** in high sodium concentrations.

In conclusion, there is much to be done in this brand new [2Fe-2S]-metallopolymer space. RAFT polymerization should open up a facile method to poly(acrylic acid)-*g*-[2Fe-2S] (PAA-*g*-2[2Fe-2S]) systems which are expected to operate best at lower pH values, but may provide some further insight into the transient adsorption effect as the polymer chain is a negatively charge polyelectrolyte, rather than a positively charged polyelectrolyte like **PDMAEMA-*g*-[2Fe-2S]**. Conducting pH studies will assist in not only determining optimized operating conditions for various metallopolymer-[2Fe-2S] systems, but may also provide insight into whether or not the side chain functional groups (*i.e.* amines in PDMAEMA, carboxylic acids in PAA) are involved in a PCET mechanism with the iron system, or if they merely provide a high local concentration of labile protons. Understanding the transient adsorption effect will be key to moving forward with future publications in this field, but once it is better understood there is a huge amount of structural space in which to experiment and innovate towards better HER catalysts.

References

[1] W. Sheng, H. A. Gasteiger, Y. Shao-Horn, *J. Electrochem. Soc.* **2010**, *157*, B1529.

[2] S. Morra, F. Valetti, S. J. Sadeghi, P. W. King, T. Meyer, G. Gilardi, *Chem. Commun.* **2011**, *47*, 10566.

[3] C. Madden, M. D. Vaughn, I. Di-ez-Perez, K. A. Brown, P. W. King, D. Gust, A. L. Moore, T. A. Moore, *J. Am. Chem. Soc.* **2012**, *134*, 1577–1582.

[4] W. Hieber, J. Gruber, *Z. Anorg. Chem.* **1958**, *296*, 91–103.

[5] R. B. King, P. M. Treichel, F. G. A. Stone, *Sect. Title Organomet. Organometalloidal Compd.* **1961**, *83*, 3600–3604.

[6] G. A. N. Felton, C. A. Mebi, B. J. Petro, A. K. Vannucci, D. H. Evans, R. S. Glass, D. L. Lichtenberger, *J. Organomet. Chem.* **2009**, *694*, 2681–2699.

[7] A. Onoda, T. Hayashi, *Curr. Opin. Chem. Biol.* **2015**, *25*, 133–140.

[8] M. Winkler, M. Senger, J. Duan, J. Esselborn, F. Wittkamp, E. Hofmann, U.-P. Apfel, S. T. Stripp, T. Happe, *Nat. Commun.* **2017**, *8*, 16115.

[9] A. Silakov, B. Wenk, E. Reijerse, W. Lubitz, *Phys. Chem. Chem. Phys.* **2009**, *11*, 6592–6599.

[10] P. Knörzer, A. Silakov, C. E. Foster, F. A. Armstrong, W. Lubitz, T. Happe, *J. Biol. Chem.* **2012**, *287*, 1489–1499.

[11] S. Morra, A. Giraudo, G. Di Nardo, P. W. King, G. Gilardi, F. Valetti, *PLoS One* **2012**, *7*, 1–8.

[12] W. P. Brezinski, M. Karayilan, K. E. Clary, S. Li, L. Fu, K. Matyjaszewski, D. H. Evans, D. L. Lichtenberger, R. S. Glass, J. Pyun, *Angew. Chem. Int. Ed.* **2018**, *Accepted*.

[13] M. Y. Darensbourg, W. Weigand, *Eur. J. Inorg. Chem.* **2011**, 994–1004.

[14] S. Dey, A. Rana, D. Crouthers, B. Mondal, P. K. Das, M. Y. Darensbourg, A. Dey, *J. Am. Chem. Soc.* **2014**, *136*, 8847–8850.

[15] B. Mondal, A. Dey, *Chem. Commun.* **2017**, *53*, 7707–7715.

[16] A. A. Oughli, F. Conzuelo, M. Winkler, T. Happe, W. Lubitz, W. Schuhmann, O. Rüdiger, N. Plumeré, *Angew. Chem. Int. Ed.* **2015**, *54*, 12329–12333.

[17] P. C. K. Vesborg, B. Seger, I. Chorkendorff, *J. Phys. Chem. Lett.* **2015**, *6*, 951–957.

[18] M. Kapsali, J. K. Kaldellis, *Appl. Energy* **2010**, *87*, 3475–3485.

[19] H. B. Gray, *Nat. Chem.* **2009**, *1*, 112–112.

[20] N. S. Lewis, D. G. Nocera, *Proc. Natl. Acad. Sci. U. S. A.* **2006**, *103*, 15729–15735.

[21] J. Y. Yang, R. M. Bullock, W. J. Shaw, B. Twamley, K. Fraze, M. R. DuBois, D. L. DuBois, *Sect. Title Electrochem. Radiational, Therm. Energy Technol.* **2009**, *131*, 5935–5945.

[22] C. Koroneos, A. Dompros, G. Roumbas, N. Moussiopoulos, *Int. J. Hydrogen Energy* **2004**, *29*, 1443–1450.

[23] K. L. Lim, H. Kazemian, Z. Yaakob, W. R. W. Daud, *Chem. Eng. Technol.* **2010**, *33*, 213–226.

[24] D. J. Durbin, C. Malardier-Jugroot, *Int. J. Hydrogen Energy* **2013**, *38*, 14595–14617.

[25] N. Guerrero Moreno, M. Cisneros Molina, D. Gervasio, J. F. Pérez Robles, *Renew. Sustain. Energy Rev.* **2015**, *52*, 897–906.

[26] J. L. Dempsey, J. R. Winkler, H. B. Gray, in *Compr. Inorg. Chem. II*, Elsevier, **2013**, pp. 553–565.

[27] W. Lubitz, H. Ogata, O. Ru, E. Reijerse, *Chem. Rev.* **2014**, *114*, 4081–4148.

[28] Y. Nicolet, C. Piras, P. Legrand, C. E. Hatchikian, J. Fontecilla-Camps, *Structure* **1999**, *7*, 13–23.

[29] Y. Nicolet, A. L. De Lacey, X. Vernède, V. M. Fernandez, E. C. Hatchikian, J. C. Fontecilla-Camps, *J. Am. Chem. Soc.* **2001**, *123*, 1596–1601.

[30] B. Ginovska-Pangovska, A. Dutta, M. L. Reback, J. C. Linehan, W. J. Shaw, *Acc. Chem. Res.* **2014**, *47*, 2621–2630.

[31] D. Schilter, J. M. Camara, M. T. Huynh, S. Hammes-Schiffer, T. B. Rauchfuss, *Chem. Rev.* **2016**, *116*, 8693–8749.

[32] V. Pelmenschikov, J. A. Birrell, C. C. Pham, N. Mishra, H. Wang, C. Sommer, E. Reijerse, C. P. Richers, K. Tamasaku, Y. Yoda, et al., *J. Am. Chem. Soc.* **2017**, *139*, 16894–16902.

[33] E. J. Reijerse, C. C. Pham, V. Pelmenschikov, R. Gilbert-Wilson, A. Adamska-Venkatesh, J. F. Siebel, L. B. Gee, Y. Yoda, K. Tamasaku, W. Lubitz, et al., *J. Am. Chem. Soc.* **2017**, *139*, 4306–4309.

[34] G. A. N. Felton, C. A. Mebi, B. J. Petro, A. K. Vannucci, D. H. Evans, R. S. Glass, D. L. Lichtenberger, *J. Organomet. Chem.* **2009**, *694*, 2681–2699.

[35] H. M. Berman, J. Westbrook, Z. Feng, G. Gilliland, T. N. Bhat, H. Weissig, I. N. Shindyalov, P. E. Bourne, *Nucleic Acids Res.* **2000**, *28*, 235–242.

[36] Y. Li, T. Yu, Y. Zeng, J. Chen, Y. Y. Li, G. Yang, *Angew. Chem. Int. Ed.* **2013**, *52*, 5631–5635.

[37] F. Wang, W. J. Liang, J. X. Jian, C. B. Li, B. Chen, C. H. Tung, L. Z. Wu, *Angew. Chem. Int. Ed.* **2013**, *52*, 8134–8138.

[38] D. Zhu, Z. Xiao, X. Liu, *Int. J. Hydrogen Energy* **2015**, *40*, 5081–5091.

[39] O. In-noi, K. J. Haller, G. B. Hall, W. P. Brezinski, J. M. Marx, T. Sakamoto, D. H. Evans, R. S. Glass, D. L. Lichtenberger, *Organometallics* **2014**, *33*, 5009–5019.

[40] F. Quentel, G. Passard, F. Gloaguen, *Energy Environ. Sci.* **2012**, *5*, 7757–7761.

[41] V. S. Thoi, Y. Sun, J. R. Long, C. J. Chang, *Chem. Soc. Rev.* **2013**, *42*, 2388–2400.

[42] N. Plumeré, O. Rüdiger, A. A. Oughli, R. Williams, J. Vivekananthan, S. Pöller, W. Schuhmann, W. Lubitz, *Nat. Chem.* **2014**, *6*, 822–827.

[43] A. A. Oughli, F. Conzuelo, M. Winkler, T. Happe, W. Lubitz, W. Schuhmann, O. Rüdiger, N. Plumeré, *Angew. Chem. Int. Ed.* **2015**, *54*, 12329–12333.

[44] V. Fourmond, S. Stapf, H. Li, D. Buesen, J. Birrell, O. Rüdiger, W. Lubitz, W. Schuhmann, N. Plumeré, C. Léger, *J. Am. Chem. Soc.* **2015**, *137*, 5494–5505.

[45] W. P. Brezinski, M. Karayilan, K. E. Clary, L. Fu, D. H. Evans, K. Matyjaszewski, R. S. Glass, D. L. Lichtenberger, J. Pyun, *ACS Macro Lett.* **2018**, *In prep.*

[46] M. Wen, X. B. Li, J. X. Jian, X. Z. Wang, H. L. Wu, B. Chen, C. H. Tung, L. Z. Wu, *Sci. Rep.* **2016**, *6*, 1–8.

[47] C. Costentin, M. Robert, J.-M. Saveant, *Acc. Chem. Res.* **2010**, *43*, 1019–1029.

[48] C. Costentin, G. Passard, M. Robert, J.-M. Savéant, *Chem. Sci.* **2013**, *4*, 819–823.

[49] D. K. Bediako, B. H. Solis, D. K. Dogutan, M. M. Roubelakis, A. G. Maher, C. H. Lee, M. B. Chambers, S. Hammes-Schiffer, D. G. Nocera, *Proc. Natl. Acad. Sci.* **2014**, *111*, 15001–15006.

[50] F. A. Armstrong, J. Hirst, *Proc. Natl. Acad. Sci.* **2011**, *108*, 14049–14054.

[51] C. Tard, C. J. Pickett, *Chem. Rev.* **2009**, *109*, 2245–2274.

[52] J.-F. Capon, F. Gloaguen, F. Y. Petillon, P. Schollhammer, J. Talarmin, *Coord. Chem. Rev.* **2009**, *253*, 1476–1494.

[53] V. Artero, G. Berggren, M. Atta, G. Caserta, S. Roy, L. Pecqueur, M. Fontecave, *Acc. Chem. Res.* **2015**, *48*, 2380–2387.

[54] A. Onoda, T. Hayashi, *Curr. Opin. Chem. Biol.* **2015**, *25*, 133–140.

[55] P. Chenevier, L. Mugherli, S. Darbe, L. Darchy, S. Dimanno, P. D. Tran, F. Valentino, M. Iannello, A. Volbeda, C. Cavazza, et al., *Comptes Rendus Chim.* **2013**, *16*, 491–505.

[56] J.-X. Jian, Q. Liu, Z.-J. Li, F. Wang, X.-B. Li, C.-B. Li, B. Liu, Q.-Y. Meng, B. Chen, K. Feng, et al., *Nat. Commun.* **2013**, *4*, 1–9.

[57] M. L. Singleton, J. H. Reibenspies, M. Y. Darensbourg, *J. Am. Chem. Soc.* **2010**, *132*, 8870–8871.

[58] X. Li, M. Wang, D. Zheng, K. Han, J. Dong, L. Sun, *Energy Environ. Sci.* **2012**, *5*, 8220.

[59] M. L. Singleton, D. J. Crouthers, R. P. Duttweiler, J. H. Reibenspies, M. Y. Darensbourg, *Inorg. Chem.* **2011**, *50*, 5015–5026.

[60] T. Yu, Y. Zeng, J. Chen, X. Zhang, G. Yang, Y. Li, *J. Mater. Chem. A* **2014**, *2*, 20500–

20505.

[61] F. Wang, M. Wen, K. Feng, W.-J. Liang, X.-B. Li, B. Chen, C.-H. Tung, L.-Z. Wu, *Chem. Commun.* **2016**, *52*, 457–460.

[62] H. Y. Wang, W. G. Wang, G. Si, F. Wang, C. H. Tung, L. Z. Wu, *Langmuir* **2010**, *26*, 9766–9771.

[63] R. Fritzsch, O. Brady, E. Adair, J. A. Wright, C. J. Pickett, N. T. Hunt, *J. Phys. Chem. Lett.* **2016**, *7*, 2838–2843.

[64] P. W. J. M. Frederix, R. Kania, J. A. Wright, D. A. Lamprou, R. V. Ulijn, C. J. Pickett, N. T. Hunt, *Dalton Trans.* **2012**, *41*, 13112.

[65] R. Fritzsch, O. Brady, E. Adair, J. A. Wright, C. J. Pickett, N. T. Hunt, P. W. J. M. Frederix, R. Kania, J. A. Wright, D. A. Lamprou, et al., *J. Phys. Chem. Lett.* **2012**, *7*, 2838–2843.

[66] V. Tran, Phong D., Fontecave, M., Artero, in *Bioinspired Catal. Met. Complexes* (Ed.: P. Weigand, W., Schollhammer), **2015**, pp. 383–410.

[67] M. L. Singleton, J. H. Reibenspies, M. Y. Darensbourg, *J. Am. Chem. Soc.* **2010**, *132*, 8870–8871.

[68] W.-G. Wang, F. Wang, H.-Y. Wang, G. Si, C.-H. Tung, L.-Z. Wu, *Chem. - An Asian J.* **2010**, *5*, 1796–1803.

[69] K. Feng, N. Xie, B. Chen, L. P. Zhang, C. H. Tung, L. Z. Wu, *Macromolecules* **2012**, *45*, 5596–5603.

[70] Y. Na, J. Pan, M. Wang, L. Sun, *Inorg. Chem.* **2007**, *46*, 3813–3815.

[71] R. Fritzsch, O. Brady, E. Adair, J. A. Wright, C. J. Pickett, N. T. Hunt, *J. Phys. Chem. Lett.* **2016**, *7*, 2838–2843.

[72] R. Goy, L. Bertini, T. Rudolph, S. Lin, M. Schulz, G. Zampella, B. Dietzek, F. H. Schacher, L. De Gioia, K. Sakai, et al., *Chem. - A Eur. J.* **2017**, *23*, 334–345.

[73] H. Production, M. R. Dubois, D. L. Dubois, *Science (80-.).* **2011**, 863–866.

[74] P. Delahay, G. L. Stiehl, *J. Am. Chem. Soc.* **1952**, *74*, 3500–3505.

[75] F. Quentel, G. Passard, F. Gloaguen, *Chem. - A Eur. J.* **2012**, *18*, 13473–13479.

[76] C. M. Thomas, O. Rudiger, T. Liu, C. E. Carson, M. B. Hall, M. Y. Darensbourg, *Organometallics* **2007**, *26*, 3976–3984.

[77] C. M. T. and M. Y. D. Kayla N. Green, Jennifer L. Hess, *Dalton Trans.* **2009**, 4344.

[78] A. K. Jones, B. R. Lichtenstein, A. Dutta, G. Gordon, P. L. Dutton, *J. Am. Chem. Soc.* **2007**, *129*, 14844–14845.

[79] S. Roy, S. Shinde, G. A. Hamilton, H. E. Hartnett, A. K. Jones, *Eur. J. Inorg. Chem.* **2011**, 1050–1055.

[80] A. Roy, C. Madden, G. Ghirlanda, *Chem. Commun.* **2012**, *48*, 9816–9818.

[81] K. Menzel, U. P. Apfel, N. Wolter, R. Rüger, T. Alpermann, F. Steiniger, D. Gabel, S. Förster, W. Weigand, A. Fahr, *J. Liposome Res.* **2014**, *24*, 59–68.

[82] S. Pullen, H. Fei, A. Orthaber, S. M. Cohen, S. Ott, *J. Am. Chem. Soc.* **2013**, *135*, 16997–17003.

[83] K. Sasan, Q. Lin, C. Mao, P. Feng, *Chem. Commun.* **2014**, *50*, 10390–10393.

[84] F. Wang, M. Wen, K. Feng, W.-J. Liang, X.-B. Li, B. Chen, C.-H. Tung, L.-Z. Wu, *Chem. Commun.* **2016**, *52*, 457–460.

[85] S. Pullen, H. Fei, A. Orthaber, S. M. Cohen, S. Ott, *J. Am. Chem. Soc.* **2013**, *135*, 16997–17003.

[86] T. Nann, S. K. Ibrahim, P. M. Woi, S. Xu, J. Ziegler, C. J. Pickett, *Angew. Chem. Int. Ed.* **2010**, *49*, 1574–1577.

[87] F. Wang, W. J. Liang, J. X. Jian, C. B. Li, B. Chen, C. H. Tung, L. Z. Wu, *Angew. Chem. Int. Ed.* **2013**, *52*, 8134–8138.

[88] W. J. Liang, F. Wang, M. Wen, J. X. Jian, X. Z. Wang, B. Chen, C. H. Tung, L. Z. Wu, *Chem. Eur. J.* **2015**, *21*, 3187–3192.

[89] V. Vijaikanth, J. F. Capon, F. Gloaguen, P. Schollhammer, J. Talarmin, *Electrochem. commun.* **2005**, *7*, 427–430.

[90] S. K. Ibrahim, X. Liu, C. Tard, C. J. Pickett, *Chem. Commun.* **2007**, 1535–1537.

[91] J. A. Wright, L. Webster, A. Jablonskyte, P. M. Woi, S. K. Ibrahim, C. J. Pickett, *Sect. Title Enzym.* **2011**, *148*, 359–371.

[92] E. Xu, Z. Xiao, H. Liu, L. Long, L. Li, X. Liu, *RSC Adv.* **2012**, *2*, 10171–10174.

[93] D. Zhu, Z. Xiao, X. Liu, *Int. J. Hydrogen Energy* **2015**, *40*, 5081–5091.

[94] A. Le Goff, V. Artero, R. Metayé, F. Moggia, B. Jousselme, M. Razavet, P. D. Tran, S. Palacin, M. Fontecave, *Int. J. Hydrogen Energy* **2010**, *35*, 10790–10796.

[95] L. Wang, Z. Xiao, X. Ru, X. Liu, *RSC Adv.* **2011**, *1*, 1211–1219.

[96] X. Liu, X. Ru, Y. Li, K. Zhang, D. Chen, *Int. J. Hydrogen Energy* **2011**, *36*, 9612–9619.

[97] E. Xu, Z. Xiao, H. Liu, L. Long, L. Li, X. Liu, *RSC Adv.* **2012**, *2*, 10171–10174.

[98] D. Zhu, Z. Xiao, X. Liu, *Int. J. Hydrogen Energy* **2015**, *40*, 5081–5091.

[99] X. Ru, X. Zeng, Z. Li, D. J. Evans, C. Zhan, Y. Tang, L. Wang, X. Liu, *J. Polym. Sci. Part A Polym. Chem.* **2010**, *48*, 2410–2417.

[100] I. Manners, *Science (80-.).* **2001**, *294*, 1664–1666.

[101] S. Schubert, I. Manners, G. R. Newkome, U. S. Schubert, *Macromol. Rapid Commun.* **2015**, *36*, 585.

[102] G. R. Whittell, M. D. Hager, U. S. Schubert, I. Manners, *Nat. Mater.* **2011**, *10*, 176–188.

[103] G. R. Whittell, I. Manners, *Adv. Mater.* **2007**, *19*, 3439–3468.

[104] J. Xiang, C.-L. Ho, W.-Y. Wong, *Polym. Chem.* **2015**, *6*, 6905–6930.

[105] W. J. Liang, F. Wang, M. Wen, J. X. Jian, X. Z. Wang, B. Chen, C. H. Tung, L. Z. Wu, *Chem. - A Eur. J.* **2015**, *21*, 3187–3192.

[106] X. Zhu, W. Zhong, X. Liu, *Int. J. Hydrogen Energy* **2016**, *41*, 14068–14078.

[107] S. Ibrahim, P. M. Woi, Y. Alias, C. J. Pickett, *Chem. Commun.* **2010**, *46*, 8189.

[108] A. Le Goff, V. Artero, R. Metayé, F. Moggia, B. Jousselme, M. Razavet, P. D. Tran, S. Palacin, M. Fontecave, *Int. J. Hydrogen Energy* **2010**, *35*, 10790–10796.

[109] L. Wang, Z. Xiao, X. Ru, X. Liu, *RSC Adv.* **2011**, *1*, 1211.

[110] Y. Li, W. Zhong, G. Qian, Z. Xiao, X. Liu, *Appl. Organomet. Chem.* **2013**, *27*, 253–260.

[111] D. Heine, C. Pietsch, U. S. Schubert, W. Weigand, *J. Polym. Sci. Part A Polym. Chem.* **2013**, *51*, 2171–2180.

[112] F. Wang, W. G. Wang, X. J. Wang, H. Y. Wang, C. H. Tung, L. Z. Wu, *Angew. Chem. Int. Ed.* **2011**, *50*, 3193–3197.

[113] F. Wang, W. J. Liang, J. X. Jian, C. B. Li, B. Chen, C. H. Tung, L. Z. Wu, *Angew. Chem. Int. Ed.* **2013**, *52*, 8134–8138.

[114] C. A. Tooley, S. Pazicni, E. B. Berda, *Polym. Chem.* **2015**, *6*, 7646–7651.

[115] C. Costentin, S. Drouet, M. Robert, J. M. Savéant, *J. Am. Chem. Soc.* **2012**, *134*, 11235–11242.

[116] H. I. Karunadasa, E. Montalvo, Y. Sun, M. Majda, J. R. Long, C. J. Chang, *Science* **2012**, *335*, 698.

[117] F. F. Quentel, G. Passard, F. Gloaguen, *Energy Environ. Sci.* **2012**, *5*, 7757–7761.

[118] F. Quentel, G. Passard, F. Gloaguen, *Chem. ? A Eur. J.* **2012**, *18*, 13473–13479.

[119] T. Grimaud, K. Matyjaszewski, *Macromolecules* **1997**, *30*, 2216–2218.

[120] K. a Davis, H.-J. Paik, K. Matyjaszewski, *Macromolecules* **1999**, *32*, 1767–1776.

[121] K. Matyjaszewski, J. Xia, *Chem. Rev.* **2001**, *101*, 2921–2990.

[122] B. E. Conway, L. Bai, *J. Electroanal. Chem. Interfacial Electrochem.* **1986**, *198*, 149–175.

[123] U. D. of Energy, **2018**.

[124] P. Knoerzer, A. Silakov, C. E. Foster, F. A. Armstrong, W. Lubitz, T. Happe, *J. Biol. Chem.* **2012**, *287*, 1489–1499.

[125] L. M. Stratton, Ph.D. Dissertation, University of Arizona, **2012**.

[126] D. Beljonne, J. Cornil, R. H. Friend, R. A. J. Janssen, J. L. Brédas, *J. Am. Chem. Soc.* **1996**, *118*, 6453–6461.

[127] S. S. Zade, N. Zamoshchik, M. Bendikov, *Acc. Chem. Res.* **2011**, *44*, 14–24.

[128] J. a. Cabeza, M. A. Martínez-García, V. Riera, D. Ardura, S. García-Granda, *Organometallics* **1998**, *17*, 1471–1477.

[129] C. Zhang, J. Huang, M. L. Trudell, S. P. Nolan, *J. Org. Chem.* **1999**, *64*, 3804–3805.

[130] H. Meng, J. Zheng, A. J. Lovinger, B.-C. Wang, P. G. Van Patten, Z. Bao, *Chem. Mater.* **2003**, *15*, 1778–1787.

[131] E. Bundgaard, F. C. Krebs, *Sect. Title Electrochem. Radiational, Therm. Energy Technol.* **2005**, *5938*, 59380Q/1-59380Q/12.

[132] P. J. Skabara, I. M. Serebryakov, D. M. Roberts, I. F. Perepichka, S. J. Coles, M. B. Hursthouse, *J. Org. Chem.* **1999**, *64*, 6418–6424.

[133] I. A. Wright, P. J. Skabara, J. C. Forgie, A. L. Kanibolotsky, B. Gonzalez, S. J. Coles, S. Gambino, I. D. W. Samuel, *J. Mater. Chem.* **2011**, *21*, 1462–1469.

[134] L. R. Melby, H. D. Hartzler, W. A. Sheppard, *J. Org. Chem.* **1974**, *39*, 2456–2458.

[135] Alexander J. Fatiadi, *Synthesis (Stuttg).* **1976**, 65–104.

[136] Y. Li, T. B. Rauchfuss, *Chem. Rev.* **2016**, *116*, 7043–7077.

[137] M. Jesberger, T. P. Davis, L. Barner, *Synthesis (Stuttg).* **2003**, *13*, 1929–1958.

[138] C.-C. Ho, Y.-C. Liu, S.-H. Lin, W.-F. Su, *Macromol. (Washington, DC, United States)* **2012**, *45*, 813–820.

[139] Y.-J. Cheng, S.-H. Yang, C.-S. Hsu, *Chem. Rev.* **2009**, *109*, 5868–5923.

[140] O. In-Noi, K. J. Haller, G. B. Hall, W. P. Brezinski, J. M. Marx, T. Sakamoto, D. H. Evans, R. S. Glass, D. L. Lichtenberger, *Organometallics* **2014**, *33*, 5009–5019.

[141] G. A. N. Felton, A. K. Vannucci, J. Chen, L. T. Lockett, N. Okumura, B. J. Petro, U. I. Zakai, D. H. Evans, R. S. Glass, D. L. Lichtenberger, *J. Am. Chem. Soc.* **2007**, *129*, 12521–12530.

[142] L. Sun, B. Åkermark, S. Ott, *Coord. Chem. Rev.* **2005**, *249*, 1653–1663.

[143] R. Lomoth, S. Ott, *Dalt. Trans.* **2009**, 9952.

[144] J. F. Capon, F. Gloaguen, P. Schollhammer, J. Talarmin, *J. Electroanal. Chem.* **2004**, *566*, 241–247.

[145] G. A. N. Felton, B. J. Petro, R. S. Glass, D. L. Lichtenberger, D. H. Evans, *J. Am. Chem. Soc.* **2009**, *131*, 11290–11291.

[146] S. Sill, D. L. Lichtenberger, *Diss. Univ. Arizona* **2014**.

[147] S.-S. Sun, N. S. Sariciftci, *Organic Photovoltaics : Mechanism, Materials, and Devices*, Taylor & Francis, Boca Raton, FL, **2005**.

[148] F. Effenberger, F. Wuerthner, F. Steybe, *J. Org. Chem.* **1995**, *60*, 2082–2091.

[149] J. L. Stanley, T. B. Rauchfuss, S. R. Wilson, *Organometallics* **2007**, *26*, 1907–1911.

[150] R. Siebenlist, H. Frühauf, K. Vrieze, W. J. J. Smeets, A. L. Spek, *Eur. J. Inorg. Chem.* **2000**, *2*, 907–919.

[151] Ö. Güzel, A. Salman, *Bioorganic Med. Chem.* **2006**, *14*, 7804–7815.

[152] S. H. Bertz, E. H. Fairchild, I. Denissova, L. Barriault, in *Encycl. Reagents Org. Synth.*, John Wiley & Sons, Ltd, **2001**.

[153] Y. Aso, H. Yamashita, *J. Org. Chem.* **1989**, *87*, 5627–5629.

[154] G. M. Sheldrick, **1996**.

[155] G. M. Sheldrick, **1997**, *97–2*.

[156] G. M. Sheldrick, *Acta Crystallogr. Sect. A* **2007**, *64*, 112–122.

[157] L. J. Barbour, *J. Supramol. Chem.* **2001**, *1*, 189–191.

[158] O. V. Dolomanov, L. J. Bourhis, R. J. Gildea, J. A. K. Howard, H. Puschmann, *J. Appl. Crystallogr.* **2009**, *42*, 339–341.

[159] H. B. Gray, *Nat. Chem.* **2009**, *1*, 112–112.

[160] N. S. Lewis, D. G. Nocera, *Proc. Natl. Acad. Sci.* **2007**, *103*, 15729–15735.

[161] J. R. McKone, S. C. Marinescu, B. S. Brunschwig, J. R. Winkler, H. B. Gray, *Chem. Sci.* **2014**, *5*, 865–878.

[162] G. A. N. Felton, C. A. Mebi, B. J. Petro, A. K. Vannucci, D. H. Evans, R. S. Glass, D. L. Lichtenberger, *J. Organomet. Chem.* **2009**, *694*, 2681–2699.

[163] C. Tard, C. J. Pickett, *Chem. Rev.* **2009**, *109*, 2245–2274.

[164] F. Gloaguen, T. B. Rauchfuss, *Chem. Soc. Rev.* **2009**, *38*, 100–108.

[165] S. Ibrahim, P. M. Woi, Y. Alias, C. J. Pickett, *Chem. Commun.* **2010**, *46*, 8189–8191.

[166] C. A. Tooley, S. Pazicni, E. B. Berda, *Polym. Chem.* **2015**, *6*, 7646–7651.

[167] C. Zhan, X. Wang, Z. Wei, D. J. Evans, X. Ru, X. Zeng, X. Liu, *Dalt. Trans.* **2010**, *39*, 11255.

[168] X. Zhu, W. Zhong, X. Liu, *Int. J. Hydrogen Energy* **2016**, *41*, 14068–14078.

[169] W.-N. Cao, F. Wang, H.-Y. Wang, B. Chen, K. Feng, C.-H. Tung, L.-Z. Wu, *Chem. Commun.* **2012**, *48*, 8081.

[170] U.-P. Apfel, Y. Halpin, M. Gottschaldt, H. Görls, J. G. Vos, W. Weigand, *Eur. J. Inorg. Chem.* **2008**, *2008*, 5112–5118.

[171] G. Caserta, S. Roy, M. Atta, V. Artero, M. Fontecave, *Curr. Opin. Chem. Biol.* **2015**, *25*, 36–47.

[172] N. Coutard, N. Kaeffer, V. Artero, *Chem. Commun.* **2016**, *52*, 13728–13748.

[173] F. Quentel, G. Passard, F. Gloaguen, *Energy Environ. Sci.* **2012**, *5*, 7757–7761.

[174] Y. Na, M. Wang, K. Jin, R. Zhang, L. Sun, *J. Organomet. Chem.* **2006**, *691*, 5045–5051.

[175] A. A. Oughli, F. Conzuelo, M. Winkler, T. Happe, W. Lubitz, W. Schuhmann, O. Rüdiger, N. Plumereré, *Angew. Chem. Ed.* **2015**, *54*, 12329–12333.

[176] V. Fourmond, C. Greco, K. Sybirna, C. Baffert, P.-H. Wang, P. Ezanno, M. Montefiori, M. Bruschi, I. Meynial-Salles, P. Soucaille, et al., *Nat. Chem.* **2014**, *6*, 336–342.

[177] A. Kubas, C. Orain, D. De Sancho, L. Saujet, M. Sensi, C. Gauquelin, I. Meynial-Salles, P. Soucaille, H. Bottin, C. Baffert, et al., *Nat. Chem.* **2016**, *9*, 88–95.

[178] P. Rodríguez-Maciá, J. A. Birrell, W. Lubitz, O. Rüdiger, *Chempluschem* **2016**, 1–6.

[179] S. Dey, A. Rana, D. Crouthers, B. Mondal, P. K. Das, M. Y. Darensbourg, A. Dey, *J. Am. Chem. Soc.* **2014**, *136*, 8847–8850.

[180] B. Mondal, A. Dey, *Chem. Commun.* **2017**, *53*, 7707–7715.

[181] D. W. Wakerley, E. Reisner, *Energy Environ. Sci.* **2015**, *8*, 2283–2295.

[182] B. Kandemir, L. Kubie, Y. Guo, B. Sheldon, K. L. Bren, *Inorg. Chem.* **2016**, *55*, 1355–1357.

[183] S. Dey, A. Rana, D. Crouthers, B. Mondal, P. K. Das, M. Y. Darensbourg, A. Dey, *J. Am. Chem. Soc.* **2014**, *136*, 8847.

[184] D. H. Pool, D. L. DuBois, *J. Organomet. Chem.* **2009**, *694*, 2858–2865.

[185] B. Reuillard, J. Warnan, J. J. Leung, D. W. Wakerley, E. Reisner, *Angew. Chem. Ed.* **2016**, *55*, 3952–3957.

[186] C. A. Downes, S. C. Marinescu, *J. Am. Chem. Soc.* **2015**, *137*, 13740–13743.

[187] G. Berggren, A. Adamska, C. Lambertz, T. R. Simmons, J. Esselborn, M. Atta, S. Gambarelli, J. M. Mouesca, E. Reijerse, W. Lubitz, et al., *Nature* **2013**, *499*, 66–69.

[188] J. D. Lawrence, H. Li, T. B. Rauchfuss, M. Bénard, M. M. Rohmer, *Angew. Chem. Int. Ed.* **2001**, *40*, 1768–1771.

[189] R. M. Bullock, A. M. Appel, M. L. Helm, *Chem. Commun.* **2014**, *50*, 3125–3143.

[190] C. M. Klug, A. Cardenas, R. M. Bullock, M. O'Hagan, E. S. Wiedner, *ACS Catal.* **2018**, *8*, 3286–3296.

[191] T. Liu, D. L. DuBois, R. M. Bullock, *Nat. Chem.* **2013**, *5*, 228–233.

[192] J. Chen, A. K. Vannucci, C. A. Mebi, N. Okumura, S. C. Borowski, M. Swenson, L. T. Lockett, D. H. Evans, R. S. Glass, D. L. Lichtenberger, *Organometallics* **2010**, *29*, 5330–5340.

[193] K. J. Lee, N. Elgrishi, B. Kandemir, J. L. Dempsey, *Nat. Rev. Chem.* **2017**, *1*, 0039.

[194] J. M. Savéant, K. B. Su, *J. Electroanal. Chem. Interfacial Electrochem.* **1984**, *171*, 341–349.

[195] H. Lee, S. H. Son, R. Sharma, Y. Y. Won, *J. Phys. Chem. B* **2011**, *115*, 844–860.

[196] C. Costentin, J.-M. Savéant, *ChemElectroChem* **2014**, *1*, 1226–1236.

[197] C. Costentin, G. Passard, J. M. Savéant, *J. Am. Chem. Soc.* **2015**, *137*, 5461–5467.

[198] L. B. Conway, B E, *J. Electroanal. Chem.* **1986**, *198*, 149–175.

[199] A. Le Goff, V. Artero, B. Jousselme, P. D. Tran, N. Guillet, R. Metaye, A. Fihri, S. Palacin, M. Fontecave, *Science (80-.).* **2009**, *326*, 1384–1387.

[200] M. R. DuBois, D. L. DuBois, *Chem. Soc. Rev.* **2009**, *38*, 62–72.

[201] M. R. DuBois, D. L. DuBois, *Comptes Rendus Chim.* **2008**, *11*, 805–817.

[202] M. L. Helm, M. P. Stewart, R. M. Bullock, M. R. DuBois, D. L. DuBois, *Science (80-.).* **2011**, *333*, 863–866.

[203] S. Raugei, S. Chen, M.-H. Ho, B. Ginovska-Pangovska, R. J. Rousseau, M. Dupuis, D. L. DuBois, R. M. Bullock, *Chem. - A Eur. J.* **2012**, *18*, 6493–6506, S6493/1–S6493/10.

[204] S. Dey, A. Rana, S. G. Dey, A. Dey, *ACS Catal.* **2013**, *3*, 429–436.

[205] G. Berggren, A. Adamska, C. Lambertz, T. R. Simmons, J. Esselborn, M. Atta, S. Gambarelli, J. M. Mouesca, E. Reijerse, W. Lubitz, et al., *Nature* **2013**, *499*, 66–69.

[206] S. K. Ibrahim, X. Liu, C. Tard, C. J. Pickett, *Chem. Commun.* **2007**, 1535–1537.

[207] Y. Y. Li, T. Yu, Y. Zeng, J. Chen, Y. Y. Li, G. Yang, *Angew. Chem. Ed.* **2013**, *52*, 5631–5635.

[208] F. Wang, W.-G. Wang, X.-J. Wang, H.-Y. Wang, C.-H. Tung, L.-Z. Wu, *Angew. Chem. Int. Ed.* **2011**, *50*, 3193–3197.

[209] B. E. Rolfe, I. Blakey, O. Squires, H. Peng, N. R. B. Boase, C. Alexander, P. G. Parsons, G. M. Boyle, A. K. Whittaker, K. J. Thurecht, *J. Am. Chem. Soc.* **2014**, *136*, 2413–2419.

[210] Y. Xue, J. Tian, W. Tian, P. Gong, J. Dai, X. Wang, *J. Phys. Chem. C* **2015**, *119*, 20762–20772.

[211] L. Zhang, J. M. Chan, F. X. Gu, J. W. Rhee, A. Z. Wang, A. F. Radovic-Moreno, F. Alexis, R. Langer, O. C. Farokhzad, *ACS Nano* **2008**, *2*, 1696–1702.

[212] E. Ruiz-Hernández, A. Baeza, M. Vallet-Regí, *ACS Nano* **2011**, *5*, 1259–1266.

[213] J. Kreuter, R. N. Alyautdin, D. A. Kharkevich, A. A. Ivanov, *Brain Res.* **1995**, *674*, 171–174.

[214] D. Zhai, B. Liu, Y. Shi, L. Pan, Y. Wang, W. Li, R. Zhang, G. Yu, *ACS Nano* **2013**, *7*, 3540–3546.

[215] A. J. Gormley, R. Chapman, M. M. Stevens, *Nano Lett.* **2014**, *14*, 6368–6373.

[216] G. Liu, Y. Lin, V. Ostatna, J. Wang, *Chem. Commun.* **2005**, 3481–3483.

[217] S. J. Hart, A. V. Terray, *Appl. Phys. Lett.* **2003**, *83*, 5316–5318.

[218] Q. Wei, Y. Lin, E. R. Anderson, A. L. Briseno, S. P. Gido, J. J. Watkins, *ACS Nano* **2012**, *6*, 1188–1194.

[219] J. Y. Oh, M. Shin, J. B. Lee, J.-H. Ahn, H. K. Baik, U. Jeong, *ACS Appl. Mater. Interfaces* **2014**, *6*, 6954–6961.

[220] D. J. Lipomi, J. A. Lee, M. Vosgueritchian, B. C.-K. Tee, J. A. Bolander, Z. Bao, *Chem. Mater.* **2012**, *24*, 373–382.

[221] M. V Fabretto, D. R. Evans, M. Mueller, K. Zuber, P. Hojati-Talemi, R. D. Short, G. G. Wallace, P. J. Murphy, *Chem. Mater.* **2012**, *24*, 3998–4003.

[222] E. Poverenov, M. Li, A. Bitler, M. Bendikov, *Chem. Mater.* **2010**, *22*, 4019–4025.

[223] Q. Yang, S.-K. Pang, K.-C. Yung, *J. Electroanal. Chem.* **2014**, *728*, 140–147.

[224] A. M. Österholm, D. E. Shen, A. L. Dyer, J. R. Reynolds, *ACS Appl. Mater. Interfaces* **2013**, *5*, 13432–13440.

[225] R. A. Green, R. T. Hassarati, L. Bouchinet, C. S. Lee, G. L. M. Cheong, J. F. Yu, C. W. Dodds, G. J. Suaning, L. A. Poole-Warren, N. H. Lovell, *Biomaterials* **2012**, *33*, 5875–5886.

[226] K. A. L. and N. B. L. and M. D. J. and S. M. R.-B. and J. L. H. and D. R. Kipke, *J. Neural Eng.* **2011**, *8*, 14001.

[227] R. F. Vreeland, C. W. Atcherley, W. S. Russell, J. Y. Xie, D. Lu, N. D. Laude, F. Porreca, M. L. Heien, *Anal. Chem.* **2015**, *87*, 2600–2607.

[228] T. Skotheim, J. R. Reynolds, *Conjugated Polymers: Theory, Synthesis, Properties, and Characterization*, CRC Press, **2006**.

[229] A. Elschner, *PEDOT : Principles and Applications of an Intrinsically Conductive Polymer*, CRC Press ; London, Boca Raton, Fla, **2011**.

[230] N. Massonnet, A. Carella, A. de Geyer, J. Faure-Vincent, J.-P. Simonato, *Chem. Sci.* **2015**, *6*, 412–417.

[231] U. Lang, E. Muller, N. Naujoks, J. Dual, *Adv. Funct. Mater.* **2009**, *19*, 1215–1220.

[232] A. A. Kiss, D. J.-. P. C. Suszwalak, *Sep. Purif. Technol.* **2012**, *86*, 70–78.

[233] D. B. G. Williams, M. Lawton, *J. Org. Chem.* **2010**, *75*, 8351–8354.

[234] K. Fischer, *Angew. Chem.* **1935**, *48*, 394–396.

[235] H. Sun, B. Wang, S. G. DiMagno, *Org. Lett.* **2008**, *10*, 4413–4416.

[236] R. Nußbaum, D. Lischke, H. Paxmann, B. Wolf, *Chromatographia* **2000**, *51*, 119–121.

[237] C. Reichardt, *Chem. Rev.* **1994**, *94*, 2319–2358.

[238] B. Bonillo, T. M. Swager, *J. Am. Chem. Soc.* **2012**, *134*, 18916–18919.

[239] I. Avigal, J. Feitelson, M. Ottolenghi, *J. Chem. Phys.* **1969**, *50*, 2614–2617.

[240] G. A. N. Felton, A. K. Vannucci, J. Chen, L. T. Lockett, N. Okumura, B. J. Petro, U. I. Zakai, D. H. Evans, R. S. Glass, D. L. Lichtenberger, *J. Am. Chem. Soc.* **2007**, *129*,

12521–12530.

[241] C. K. Song, B. J. Eckstein, T. L. D. Tam, L. Trahey, T. J. Marks, *ACS Appl. Mater. Interfaces* **2014**, *6*, 19347–19354.

[242] M. Al-Ibrahim, H. K. Roth, M. Schroedner, A. Konkin, U. Zhokhavets, G. Gobsch, P. Scharff, S. Sensfuss, *Org. Electron. physics, Mater. Appl.* **2005**, *6*, 65–77.

[243] R. Chen, C. Yang, W. Cai, H.-Y. Wang, J. Miao, L. Zhang, S. Chen, B. Liu, *ACS Energy Lett.* **2017**, *2*, 1070–1075.

[244] E. P. Friis, J. E. T. Andersen, L. L. Madsen, N. Bonander, P. Møller, J. Ulstrup, *Electrochim. Acta* **1998**, *43*, 1114–1122.

[245] C. Costentin, G. Passard, J.-M. Saveant, *J. Am. Chem. Soc.* **2015**, *137*, 5461–5467.

[246] N. Kaeffer, A. Morozan, J. Fize, E. Martinez, L. Guetaz, V. Artero, *ACS Catal.* **2016**, *6*, 3727–3737.

[247] H. G. M. van de Steeg, M. A. C. Stuart, A. de keizer, B. H. Bijsterbosch, *Langmuir* **1992**, *8*, 2538–2546.

[248] A. V. Dobrynin, A. Deshkovski, M. Rubinstein, *Macromolecules* **2001**, *34*, 3421–3436.

[249] J. M. Kleijn, D. Barten, M. A. C. Stuart, *Langmuir* **2004**, *20*, 9703–9713.

[250] W. Humphrey, A. Dalke, K. Schulten, *J. Molec. Graph.* **1996**, *14*, 33–38.

[251] K. A. Vincent, A. Parkin, F. A. Armstrong, *Chem. Rev.* **2007**, *107*, 4366–4413.

[252] A. V. Dobrynin, M. Rubinstein, *Prog. Polym. Sci.* **2005**, *30*, 1049–1118.

[253] G. M. Sheldrick, *Acta Crystallogr. Sect. A Found. Crystallogr.* **2007**, *64*, 112–122.

[254] L. J. Barbour, *J. Supramol. Chem.* **2001**, *1*, 189–191.

[255] X. Zhang, J. Xia, K. Matyjaszewski, *Macromolecules* **1998**, *31*, 5167–5169.

[256] H. Dong, K. Matyjaszewski, *Macromolecules* **2008**, *41*, 6868–6870.

[257] R. L. Teoh, K. B. Guice, Y. L. Loo, *Macromolecules* **2006**, *39*, 8609–8615.

[258] K. Matyjaszewski, T. Pintauer, S. Gaynor, *Notes*,
https://www.cmu.edu/maty/chem/fundamentals-atrp/index.html, **2000**, 1476–1478.

[259] J. F. Lutz, *J. Polym. Sci. Part A Polym. Chem.* **2008**, *46*, 3459–3470.

[260] J. F. Lutz, A. Hoth, *Macromolecules* **2006**, *39*, 893–896.

[261] H. Bergenudd, G. Coullerez, M. Jonsson, E. Malmstro, *Macromolecules* **2009**, *42*, 3302–3308.

[262] S.-I. Yamamoto, J. Pietrasik, K. Matyjaszewski, *J. Polym. Sci. Part A Polym. Chem.* **2007**, *46*, 194.

[263] D. Fournier, R. Hoogenboom, H. M. L. Thijs, R. M. Paulus, U. S. Schubert, *Macromolecules* **2007**, *40*, 915–920.